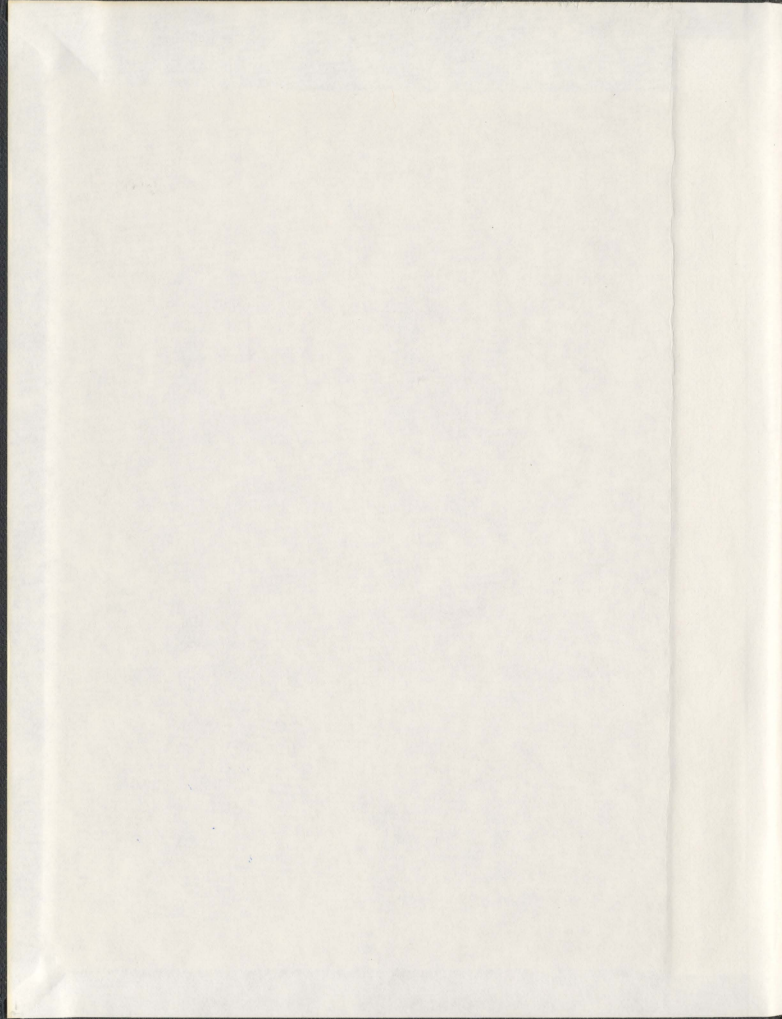


LIGAND DIRECTED SELF-ASSEMBLY OF  
POLYMETALLIC  $[n \times n]$  ( $n = 2, 3, 4$ ) GRID PLATFORMS:  
SYNTHESIS, STRUCTURE AND MAGNETISM

LOUISE N. DAWE



001311





**Ligand Directed Self-Assembly of Polymetallic [n×n] (n = 2, 3, 4) Grid Platforms:  
Synthesis, Structure and Magnetism**

By

© Louise N. Dawe, B. Sc. (Honours), M. Sc., B. Ed.

A thesis submitted to the  
School of Graduate Studies  
in partial fulfillment of the  
requirements for the degree of  
Doctor of Philosophy

Department of Chemistry  
Memorial University of Newfoundland

October, 2008

St. John's

Newfoundland and Labrador

Canada

### Abstract:

Metallo-supramolecular [ $n \times n$ ]  $M_n$  transition metal grid arrays (with  $n = 2, 3$  and  $4$ ) were synthesized by self-assembly reactions with new ditopic imidazole hydrazone, tritopic picolinic dihydrazone and tetratopic pyridazine bis(hydrazone) ligands. Mono-, di-, trinuclear,  $[2 \times 2]$   $M_4$  grid and trigonal-bipyramidal clusters formed by self-assembly reactions between the ditopic ligands and metal salts. Their structural characterizations suggest a possible route to the self-assembly of  $[2 \times 2]$   $M_4$  grid and trigonal-bipyramidal architectures. Homometallic  $[3 \times 3]$   $M_9$  ( $M = \text{Mn(II)}, \text{Co(II)}, \text{Cu(II)}$  and  $\text{Zn(II)}$ ) and heterobimetallic  $[3 \times 3]$   $\text{Mn(II)}_5\text{Cu(II)}_4$ ,  $\text{Mn(II)}_5\text{Zn(II)}_4$  and  $\text{Mn(II)}\text{Cu(II)}_8$  grids, based on a  $[\text{M}_9-(\mu\text{-O})_{12}]$  core framework were synthesized. Their structural characterizations, in particular the identification of the Jahn-Teller axes, leading to strict orbital orthogonality and ferromagnetism in the  $\text{Cu(II)}$  containing complexes, formed the basis for magnetic interpretation and modeling.  $[3 \times 3]$   $\text{Mn(II)}_9$ ,  $\text{Cu(II)}_9$  and  $\text{Co(II)}_5\text{Co(III)}_4$  grids synthesized by self-assembly reactions between metal salts and tritopic ligands with quinoline-type endpieces, leading to extended structural motifs through intermolecular face-to-face and edge-to-face  $\pi$ - $\pi$  interactions are also reported.  $4 \times [2 \times 2]$   $M_{16}$  ( $M = \text{Mn(II)}, \text{Co(II)}, \text{Cu(II)}$  and  $\text{Cu(II)}_{12}\text{Cu(I)}_4$ ) grids were synthesized, and their magnetic properties modeled as compartmental  $[2 \times 2]$   $M_4-(\mu\text{-O}_{\text{hydrazone}})_4$  squares for the  $\text{Mn(II)}_{16}$  and  $\text{Co(II)}_{16}$  complexes. The structural characterization of the Jahn-Teller axes leading to a combination of orthogonal and non-orthogonal orbital connections for both of the  $\text{Cu}_{16}$  grids allowed for fairly simple magnetic models to be devised.

### **Acknowledgements:**

I would like to thank my supervisor, Dr. Laurence Thompson, for his guidance and support. He is a wonderful teacher, and it has been a pleasure learning more about chemistry under his direction.

Thank you to David Miller for many encouraging words and for teaching me about X-ray crystallography. Thank you also to my good friend and fellow crystal enthusiast, Julie Collins, for her patience, insight and support. I am very grateful to have shared in this learning experience with Julie.

I would also like to thank my supervisory committee, Dr. Yuming Zhao and Dr. Christopher Kozak, for their helpful suggestions.

Julie Collins and Dr. Celine Schneider are gratefully acknowledged for help with my NMR data. Thanks are also extended to Linda Windsor for helping me with my mass spectrometry experiments, and to Tareque Abedin for magnetic data collection.

I would like to thank the members of the Thompson research group that I have worked with during my graduate program: Victoria Milway, Tareque Abedin, Peter Blanchard, Corey McClary, Randy Royle, Lisa LeShane, Subrata Dey, Andrew Elliott and Konstantin Shuvaev. I would also like to thank Gary Hancock, David Stirling, Yvette Favaro-Park and Nick Ryan, with whom I demonstrated undergraduate laboratories, for their enthusiasm and professionalism. Working with all of these individuals made for a very enjoyable and enriching graduate experience.

Thanks to my parents, Ken and Marian, and to my brother, Tony, for their love and support, and to my sister, Margot, for being my best friend, always listening to me,

and for keeping me company during many long nights in front of the computer. Finally, thank you to my partner, Craig Steele, for his extraordinary patience, understanding and love.

Dr. Laurence Thompson, Memorial University Department of Chemistry, School of Graduate Studies and CREAT, and NSERC are acknowledged for financial support.

## Table of Contents:

Abstract .....	ii
Acknowledgements .....	iii
List of Tables .....	viii
List of Figures .....	xi
List of Schemes .....	xxvi
List of Symbols and Abbreviations.....	xxvii
List of Appendices .....	xxx
Chapter 1: General Introduction	
1.1: Supramolecular chemistry and self-assembly.....	1
1.2: Metallo-supramolecular arrays and nanotechnology .....	9
1.3: Magnetic interactions in paramagnetic clusters.....	12
1.4: Superexchange.....	14
1.5: Fitting magnetic data for polynuclear clusters.....	17
1.6: Conclusions.....	28
Chapter 2: Ligand synthesis and physical measurements	
2.1: General comments on ligand design and synthesis .....	29
2.2: Methodology .....	35
2.3: Experimental.....	37
2.4: Summary .....	49

Chapter 3: Complete and 'Incomplete' [2×2] grids and pentanuclear clusters by self-assembly with sterically hindered ditopic imidazole hydrazone ligands	
3.1: Preamble .....	50
3.2: Experimental .....	52
3.3: Results and Discussion .....	63
3.4: Summary .....	89
Chapter 4: [3×3] M(II) <sub>9</sub> grids (M = Mn, Co, Cu, Zn) from self-assembly reactions with a picolinic dihydrazone ligand	
4.1: Preamble .....	92
4.2: Experimental .....	96
4.3: Results and Discussion .....	104
4.4: Summary .....	128
Chapter 5: Heterobimetallic [3×3] Mn(II) <sub>1</sub> Cu(II) <sub>8</sub> and Mn(II) <sub>5</sub> M(II) <sub>4</sub> (where M = Ni, Cu and Zn) grid complexes	
5.1: Preamble .....	130
5.2: Experimental .....	132
5.3: Results and Discussion .....	139
5.4: Summary .....	156
Chapter 6: Long range magnetic cooperativity through extended structural motifs? Introducing intermolecular π-π interactions between [3×3] M <sub>9</sub> grids	
6.1: Preamble .....	159
6.2: Experimental .....	165

6.3: Results and Discussion .....	173
6.4: Summary .....	208
Chapter 7: Antiferromagnetic $4 \times [2 \times 2]$ $M_{16}$ grids ( $M = \text{Mn(II)}, \text{Co(II)}$ and $\text{Co(II)/Co(III)}$ ) from self-assembly reactions with pyridazine bis(hydrazone) ligands	
7.1: Preamble .....	211
7.2: Experimental .....	217
7.3: Results and Discussion .....	225
7.4: Summary .....	246
Chapter 8: Homovalent and heterovalent copper complexes from reactions with tetratopic ligands	
8.1: Preamble .....	248
8.2: Experimental .....	252
8.3: Results and Discussion .....	259
8.4: Summary .....	283
Chapter 9: General Conclusions .....	286
References .....	290

## List of Tables:

Table 3.1: Summary of crystallographic data for <b>3.1</b> and <b>3.2</b> .....	59
Table 3.2: Summary of crystallographic data for <b>3.3</b> and <b>3.4</b> .....	60
Table 3.3: Summary of crystallographic data for <b>3.5</b> .....	61
Table 3.4: Summary of crystallographic data for <b>3.6 - 3.8</b> .....	62
Table 3.5: Selected bond distances (Å) and torsion angle (°) for <b>3.1</b> .....	64
Table 3.6: Selected bond distances (Å) and angles (°) for <b>3.2</b> .....	66
Table 3.7: Selected bond distances (Å) and angles (°) for <b>3.3</b> .....	68
Table 3.8: Selected bond distances (Å) and angle (°) for <b>3.4</b> .....	70
Table 3.9: Selected bond distances (Å) and angles (°) for <b>3.5</b> .....	72
Table 3.10: Selected bond distances (Å) and angles (°) for <b>3.6</b> .....	73
Table 3.11: Selected bond distances (Å) and angles (°) for <b>3.7</b> .....	75
Table 3.12: Selected bond distances (Å) and angles (°) for <b>3.8</b> .....	76
Table 3.13: Summary of the magnetic analysis of <b>3.2 - 3.5, 3.7</b> and <b>3.8</b> .....	88
Table 4.1: Summary of crystallographic data for <b>4.1 - 4.2</b> .....	101
Table 4.2: Summary of crystallographic data for <b>4.3 - 4.4</b> .....	102
Table 4.3: Summary of crystallographic data for <b>4.5 - 4.6</b> .....	103
Table 4.4: Selected bond distances (Å) and angles (°) for <b>4.1</b> .....	106
Table 4.5: Selected bond distances (Å) and angles (°) for <b>4.2</b> .....	108
Table 4.6: Selected bond distances (Å) and angles (°) for <b>4.3</b> .....	110
Table 4.7: Selected bond distances (Å) and angles (°) for <b>4.4</b> .....	112
Table 4.8: Selected bond distances (Å) for and angles (°) for <b>4.5</b> .....	113

Table 4.9: Selected bond distances (Å) and angles (°) for <b>4.6</b> .....	116
Table 4.10: Summary of the magnetic analysis of <b>4.2 - 4.3, 4.5 and 4.6</b> .....	127
Table 5.1: Summary of crystallographic data for <b>5.1, 5.2</b> .....	137
Table 5.2: Summary of crystallographic data for <b>5.4</b> .....	138
Table 5.3: Selected bond distances (Å) and angles (°) for <b>5.1</b> .....	141
Table 5.4: Selected bond distances (Å) and angles (°) for <b>5.2</b> .....	143
Table 5.5: Selected bond distances (Å) and angles (°) for <b>5.4</b> .....	145
Table 6.1: Summary of crystallographic data for <b>6.1 - 6.3</b> .....	171
Table 6.2: Summary of crystallographic data for <b>6.4 and 6.6</b> .....	172
Table 6.3: Selected bond distances (Å) and torsion angles (°) for <b>6.1</b> .....	176
Table 6.4: Selected bond distances (Å), angles (°) and torsion angles (°) for <b>6.2</b> .....	181
Table 6.5: Selected bond distances (Å) and angles (°) for <b>6.3</b> .....	186
Table 6.6: Selected bond distances (Å) and angles (°) for <b>6.4</b> .....	191
Table 6.7: Selected bond distances (Å) and angles (°) for <b>6.6</b> .....	195
Table 6.8: Summary of the magnetic analysis of <b>6.2 - 6.6</b> .....	208
Table 7.1: Summary of crystallographic data for <b>7.1 and 7.2a</b> .....	223
Table 7.2: Summary of crystallographic data for <b>7.4</b> .....	224
Table 7.3: Selected bond distances (Å) angles (°) and torsion angles (°) for <b>7.1</b> .....	229
Table 7.4: Selected bond distances (Å) angles (°) and torsion angles (°) for <b>7.2a</b> .....	233
Table 7.5: Selected bond distances (Å) angles (°) and torsion angles (°) for <b>7.4</b> .....	238
Table 8.1: Summary of crystallographic data for <b>8.1 and 8.2</b> .....	257
Table 8.2: Summary of crystallographic data for <b>8.3</b> .....	258

Table 8.3: Selected bond distances (Å) angles (°) and torsion angles (°) for <b>8.1</b> .....	264
Table 8.4: Selected bond distances (Å) angles (°) and torsion angles (°) for <b>8.2</b> .....	274
Table 8.5: Selected bond distances (Å) angles (°) and torsion angles (°) for <b>8.3</b> .....	283

## List of Figures:

Figure 1.1: a) The ligand Hpiv which leads to the formation of b) $[M_8F_8(\text{piv})_{16}]$ and $[M_7M'F_8(\text{piv})_{16}]$ rings ( $R = t\text{Bu}$ ).....	4
Figure 1.2: a) The ditopic ligand <b>L1</b> , with tridentate coordination pockets that adopt b) meridional positions on an octahedral metal ion leading to the formation of c) $[2 \times 2]$ square grids ( $R = t\text{Bu}$ ).....	6
Figure 1.3: a) The ditopic ligand <b>L2</b> . b) The tritopic ligand <b>L3</b> which leads to the formation of c) a $[3 \times 3]$ $M(\text{I})_9$ grid ( $M = \text{Ag}$ ).....	7
Figure 1.4: a) The tetratopic ligand <b>L4</b> which lead to the formation of b) a $(\text{L4})_8\text{Pb}(\text{II})_{16}$ grid .....	8
Figure 1.5: a) The ligand 2poap ( $R = \text{H}$ ) or $\text{Cl}2\text{poap}$ ( $R = \text{Cl}$ ) which leads to the formation of b) $[3 \times 3]$ $M(\text{II})_9$ grids, that subsequently become heterovalent (green circles = $\text{Mn}(\text{III})$ , orange circles = $\text{Mn}(\text{II})$ ) upon chemical or electrochemical oxidation [28,29]. Surface studies on $[\text{Mn}_9(\text{Cl}2\text{poap})_6]^{6+}$ on HOPG gives c) a topographic image, d) a CITS image, and e) a 3D current isopol plot [28].....	10
Figure 1.6: Simple illustration of superexchange via $\sigma$ -bonding in a linear M-O-M system.....	15
Figure 1.7: Other modes of superexchange via $\sigma$ -bonding in a linear M-O-M System.....	15
Figure 1.8: A linear M-O-M system exhibiting strict magnetic orbital orthogonality resulting in ferromagnetism .....	16

Figure 1.9: General scheme for the coupling in a) an equilateral triangle and b) a linear triad of spin centers.....	19
Figure 1.10: The core of a Turbo Basic© routine for evaluating susceptibility as a function of temperature for an equilateral triangle .....	22
Figure 1.11: Magnetic model for an $M_4$ tetrahedron .....	24
Figure 1.12: MAGMUN4.1 input file for $Cu(II)_4$ square model .....	24
Figure 1.13: *.spk file for a $Cu(II)_4$ square. The first column defines the relative energy while the second column defines $2S'$ .....	25
Figure 1.14: Magnetization as a function of field for $g = 2$ , $T = 2$ K and $S = \frac{1}{2}$ (black), $S = \frac{3}{2}$ (solid red), $S = 3 \times \frac{1}{2}$ (dashed red), $S = \frac{5}{2}$ (solid blue), $S = 5 \times \frac{1}{2}$ (dashed blue), $S = \frac{7}{2}$ (solid green) $S = 7 \times \frac{1}{2}$ (dashed green) generated with MAGMUN4.1 .....	27
Figure 2.1: Examples of ditopic ligands suitable for the formation of $[2 \times 2]$ grids. ....	30
Figure 2.2: General representation of possible bonding modes, showing the formation of 5-membered chelate rings. a) $\mu$ -O bonding mode b) $\mu$ -NN bonding mode.....	30
Figure 2.3: Examples of tritopic ligands showing metal coordination, leading to the formation of $[3 \times 3]$ grids .....	32
Figure 2.4: a) <i>Syn</i> enolic rotameric form of a tetratopic diethyl 3,5-pyrazoledicarbohydrazide ligand; b) and with the hydrazone oxygen atoms in a non-coordinating ketonic form .....	34

Figure 2.5: <i>Syn</i> -enolic rotomeric representations of pyridazine based ligands; R = H or R = NH <sub>2</sub> .....	35
Figure 3.1: a) poap (R = NH <sub>2</sub> ), pomp (R = CH <sub>3</sub> ); b) ioap ( <b>2.1</b> ; X = CH), ioapm ( <b>2.2</b> ; X = N).....	50
Figure 3.2: Various ligand conformations; a) dinucleating, hydrazone-bridged; b) mononucleating; c) dinucleating, diazine-bridged; d) mononucleating, imidazole-twisted.....	51
Figure 3.3: Ball-and-stick depiction of the cationic moiety of <b>3.1</b> . Hydrogen atoms omitted for clarity. ....	63
Figure 3.4: a) Ball-and-stick depiction of the cationic moiety <b>3.2</b> . Hydrogen atoms omitted for clarity. b) Core structural representation of <b>3.2</b> . ....	65
Figure 3.5: a) Ball-and-stick depiction of the cationic moiety <b>3.3</b> . Hydrogen atoms omitted for clarity. b) Core structural representation of <b>3.3</b> . ....	67
Figure 3.6: a) Ball-and-stick depiction of the cationic moiety <b>3.4</b> . Hydrogen atoms omitted for clarity. b) Core structural representation of <b>3.4</b> . Arrows highlight the elongated Jahn–Teller axes.....	69
Figure 3.7: a) Ball-and-stick depiction of the cationic moiety <b>3.5</b> . Hydrogen atoms omitted for clarity. b) Core structural representation of <b>3.5</b> . Arrows highlight the elongated Jahn–Teller axes.....	71
Figure 3.8: Ball-and-stick depiction of the cationic moiety of <b>3.6</b> .....	72

Figure 3.9: a) Ball-and-stick depiction of the cationic moiety <b>3.7</b> . Hydrogen atoms omitted for clarity. b) Core structural representation of <b>3.7</b> . Arrows highlight the elongated Jahn–Teller axes.....	74
Figure 3.10: a) Ball-and-stick depiction of the cationic moiety <b>3.8</b> . Hydrogen atoms omitted for clarity. b) Core structural representation of <b>3.8</b> . .....	75
Figure 3.11: Variable temperature magnetic data for <b>3.2</b> ; $g = 2.04(2)$ , $J = -3.03(1)$ $\text{cm}^{-1}$ , $\text{TIP} = 0 \text{ cm}^3 \text{ mol}^{-1}$ , $\rho = 0.01$ , $10^2 R = 0.81$ . .....	78
Figure 3.12: Magnetic exchange models for some polynuclear systems; a) $M_3$ triad b) $M_4$ square c) $M_5$ trigonal bipyramid. ....	79
Figure 3.13: Variable temperature magnetic data for <b>3.3</b> ; $g = 2.25(1)$ , $J = -13.3(8)$ $\text{cm}^{-1}$ , $\theta = -1 \text{ K}$ , $\text{TIP} = 800 \times 10^{-6} \text{ cm}^3 \text{ mol}^{-1}$ , $\rho = 0.04$ , $10^2 R = 1.01$ .....	80
Figure 3.14: Variable temperature magnetic data for <b>3.4</b> . $\chi$ represented by triangles; $\mu$ represented by diamonds. $g = 2.07(0)$ , $J = 7.2(8) \text{ cm}^{-1}$ , $\theta = -0.5 \text{ K}$ , $\text{TIP} = 475 \times 10^{-6} \text{ cm}^3 \text{ mol}^{-1}$ , $10^2 R = 2.14$ .....	82
Figure 3.15: Variable field magnetization data for <b>3.4</b> ; solid line represents simulation with $g = 2.07$ , $T = 2 \text{ K}$ , $S' = 2$ . .....	84
Figure 3.16: a) Variable temperature magnetic data for <b>3.5</b> ; $g = 2.073(7)$ , $J = 7.62(8) \text{ cm}^{-1}$ , $\theta = 0 \text{ K}$ , $\text{TIP} = 210 \times 10^{-6} \text{ cm}^3 \text{ mol}^{-1}$ , $\rho = 0.1$ , $10^2 R = 2.16$ . b) Variable field magnetization data for <b>3.5</b> ; solid line represents simulation with $g = 2.073$ , $T = 2 \text{ K}$ , $S' = 2$ . .....	85

Figure 3.17: a) Variable temperature magnetic data for <b>3.7</b> ; $g = 2.102(3)$ , $J = 7.2(5)$ $\text{cm}^{-1}$ , $\theta = -0.2$ K, $\text{TIP} = 250 \times 10^{-6} \text{ cm}^3 \text{ mol}^{-1}$ , $\rho = 0$ , $10^2 R = 0.44$ . b) Variable field magnetization data for <b>3.7</b> ; solid line represents simulation with $g = 2.1$ , $T = 2$ K, $S' = 2$ . .....	86
Figure 3.18: Variable temperature magnetic data for <b>3.8</b> ; $g = 2.015$ , $J = -2.65 \text{ cm}^{-1}$ , $\theta = 0$ K, $\text{TIP} = 0 \text{ cm}^3 \text{ mol}^{-1}$ , $\rho = 0.0001$ , $10^2 R = 0.44$ . .....	87
Figure 4.1: Examples of tritopic, metal-coordinated, ligands suitable for the formation of [3×3] $M_9$ ( $M = \text{Mn, Fe, Ni, Cu, Zn}$ ) grids. ....	92
Figure 4.2: a) 2pmpop ( <b>2.4</b> ; $Y = \text{N}$ , $R = \text{NH}_2$ , $X = \text{H}$ ), Cl2popp ( $Y = \text{CH}$ , $R = \text{Ph}$ , $X = \text{Cl}$ ); b) the <i>in situ</i> hydrolysis product of 2pmpop (pmpopCOO; $Y = \text{N}$ , $R = \text{NH}_2$ , $X = \text{H}$ ) and of Cl2popp (poppCOO; $Y = \text{CH}$ , $R = \text{Ph}$ , $X = \text{Cl}$ ). .....	96
Figure 4.3: a) Ball-and-stick depiction of the cationic moiety <b>4.1</b> . Hydrogen atoms omitted for clarity. b) Core structural representation of <b>4.1</b> . ....	105
Figure 4.4: a) Ball-and-stick depiction of the cationic moiety <b>4.2</b> . Hydrogen atoms omitted for clarity. b) Core structural representation of <b>4.2</b> . ....	107
Figure 4.5: a) Ball-and-stick depiction of the cationic moiety <b>4.3</b> . Hydrogen atoms omitted for clarity. b) Core structural representation of <b>4.3</b> . ....	109
Figure 4.6: Ball-and-stick depiction of the cationic moiety <b>4.4</b> . ....	111
Figure 4.7: a) Ball-and-stick depiction of the cationic moiety <b>4.5</b> . Hydrogen atoms omitted for clarity. b) Core structural representation of <b>4.5</b> . Arrows highlight the Jahn–Teller axes. ....	112

Figure 4.8: a) Ball-and-stick depiction of the cationic moiety <b>4.6</b> . Hydrogen atoms omitted for clarity. b) Core structural representation of <b>4.6</b> . Arrows highlight the Jahn–Teller axes. ....	114
Figure 4.9: Magnetic exchange models for a [3×3] $M_9$ grid. ....	117
Figure 4.10: Variable temperature magnetic data for <b>4.2</b> ; $g = 2.04$ , $J = -4.8 \text{ cm}^{-1}$ , $TIP = 0 \text{ cm}^3 \text{ mol}^{-1}$ , $\rho = 0.003$ , $10^2R = 2.1$ . ....	119
Figure 4.11: Variable temperature magnetic data for <b>4.3</b> ; $g = 2.263(9)$ , $J = -6.5(2) \text{ cm}^{-1}$ , $TIP = 2200 \times 10^{-6} \text{ cm}^3 \text{ mol}^{-1}$ , $\rho = 0.075$ , $10^2R = 1.9$ . ....	120
Figure 4.12: Variable temperature magnetic data for <b>4.5</b> ; $g = 2.27(1)$ , $J_1 = 1.8(1) \text{ cm}^{-1}$ , $J_2 = -18(1) \text{ cm}^{-1}$ , $TIP = 700 \times 10^{-6} \text{ cm}^3 \text{ mol}^{-1}$ , $\theta = -1 \text{ cm}^{-1}$ , $10^2R = 4.4$ . ....	122
Figure 4.13: Variable temperature magnetic data for <b>4.6</b> ; $g = 2.27(1)$ , $J_1 = 1.52(9) \text{ cm}^{-1}$ , $J_2 = -15.2(9) \text{ cm}^{-1}$ , $TIP = 900 \times 10^{-6} \text{ cm}^3 \text{ mol}^{-1}$ , $10^2R = 3.2$ . ....	125
Figure 4.14: Variable field magnetization data for <b>4.6</b> ; solid red line calculated for $g = 2.27$ , $S' = 7/2$ , $T = 2 \text{ K}$ and dashed blue line calculated for $g = 2.27$ , $S' = 7 \times 1/2$ , $T = 2 \text{ K}$ using the appropriate Brillouin function. ....	127
Figure 5.1: a) <i>N</i> -(2-hydroxybenzyl)-3-amino-1-propanol. b) poap mononuclear precursor ( $M = \text{Fe(III)}$ ). c) 2poapz ( $X = \text{N}$ , $Y = \text{CH}$ , $R = \text{H}$ ); 2pmoap ( $X = \text{CH}$ , $Y = \text{N}$ , $R = \text{H}$ ); Cl2poap ( $X = Y = \text{CH}$ , $R = \text{Cl}$ ) .....	132
Figure 5.2: a) Ball-and-stick depiction of the cationic moiety <b>5.1</b> . Hydrogen atoms omitted for clarity. b) Core structural representation of <b>5.1</b> . ....	139

Figure 5.3: a) Ball-and-stick depiction of the cationic moiety <b>5.2</b> . Hydrogen atoms omitted for clarity. b) Core structural representation of <b>5.2</b> ; arrows highlight the Jahn–Teller axes.....	141
Figure 5.4: a) Ball-and-stick depiction of the cationic moiety <b>5.4</b> . Hydrogen atoms omitted for clarity. b) Core structural representation of <b>5.4</b> ; arrows highlight the Jahn–Teller axes.....	143
Figure 5.5: $[3 \times 3]$ $A(II)_5B(II)_4$ grids with metals sites arranged as for a) <b>5.1</b> (A = Mn, B = Zn) and b) <b>5.2</b> (A = Mn, B = Cu).....	145
Figure 5.6: Magnetic exchange model for a $[3 \times 3]$ $M_9$ grid.....	146
Figure 5.7: Variable temperature magnetic data for <b>5.1</b> ; $g = 2.00(6)$ , $J = -0.148(8) \text{ cm}^{-1}$ , $TIP = 20 \times 10^{-6} \text{ cm}^3 \text{ mol}^{-1}$ , $\rho = 0.10$ , $10^2 R = 2.39$ .....	147
Figure 5.8: Variable temperature magnetic data for <b>5.2</b> .....	149
Figure 5.9: Calculated relative energy as a function of total spin state for <b>5.2</b> ; blue line shows the calculated ground state of $S' = 11/2$ ; red line shows the second lowest lying energy state, $S' = 9/2$ .....	150
Figure 5.10: Variable field magnetization data for <b>5.2</b> ; solid red line calculated for $g = 2.15$ , $S' = 9/2$ , $T = 2 \text{ K}$ , and dashed blue line calculated for $g = 2.15$ , $S' = 11/2$ $T = 2 \text{ K}$ , using the appropriate Brillouin function.....	151
Figure 5.11: Variable temperature magnetic data for <b>5.3</b> . Solid line calculated for $g_{ave} = 2.17$ , $J = -3 \text{ cm}^{-1}$ , $TIP = 750 \times 10^{-6} \text{ cm}^3 \text{ mol}^{-1}$ , $\rho = 0.05$ .....	152

Figure 5.12: Variable temperature magnetic data for <b>5.4</b> ; $g = 2.3(1)$ , $J_1 = 0.45(2) \text{ cm}^{-1}$ , $J_2 = -22.5(2) \text{ cm}^{-1}$ , $TIP = 1000 \times 10^{-6} \text{ cm}^3 \text{ mol}^{-1}$ , $\rho = 0.055$ , $\theta = -0.5$ , $10^2 R = 2.2$ .....	154
Figure 5.13: Variable field magnetization data for <b>5.4</b> ; solid red line represents simulation with $g = 2.3$ , $T = 2 \text{ K}$ , $S' = 3/2$ ; dashed blue line represents $g = 2.3$ , $T = 2 \text{ K}$ , $S' = 5/2$ using the appropriate Brillouin function .....	156
Figure 6.1: a) Direct, repulsive, $\pi$ - $\pi$ overlap. b) Favourable slipped 'face-to-face' and c) 'edge-to-face' $\pi$ - $\pi$ interactions.....	162
Figure 6.2: Stacking of two quinoline rings; black arrow indicates the normal vector to the quinoline plane; red arrow drawn from the centroid of one quinoline-pyridine moiety to the centroid of the other quinoline-arene moiety, off-set by the angle $\alpha$ ; blue arrow drawn from the centroid of one quinoline-pyridine moiety to the centroid of the other quinoline-pyridine moiety, off-set by the angle $\beta$ . .....	163
Figure 6.3: a) The $\mu$ -O and b) $\mu$ -NN bridging modes of 2po56hq ( <b>2.5</b> ).....	164
Figure 6.4: a) 2po56nq ( <b>2.6</b> ) b) 2po34nq ( <b>2.8</b> ) and c) 2po45nq ( <b>2.7</b> ).....	164
Figure 6.5: Ball-and-stick depiction of <b>6.1</b> . Solvent molecules omitted for clarity.....	173
Figure 6.6: Ball-and-stick depiction of <b>6.1</b> a) looking down the b-axis and b) rotated about the c-axis to show the layered arrangement of the ligand cations. ....	174
Figure 6.7: Ball-and-stick depiction of <b>6.1</b> showing face-to-face $\pi$ - $\pi$ contacts between cations in adjacent layers.....	175

Figure 6.8: Ball-and-stick depiction of a) the cationic moiety of <b>6.2</b> . Hydrogen atoms omitted for clarity. b) The unit cell of <b>6.2</b> looking down the a-axis c) Core structural representation of <b>6.2</b> .....	177
Figure 6.9: Ball-and-stick depiction of extended cell of <b>6.2</b> , oriented to show face-to-face intramolecular (orange arrows), intermolecular (green arrow) and intermolecular edge-to-face (purple arrows) $\pi$ - $\pi$ interactions. ....	180
Figure 6.10: Ball-and-stick depiction of a) the cationic moiety <b>6.3</b> . Hydrogen atoms omitted for clarity. b) The unit cell of <b>6.3</b> ; anions omitted for clarity .....	182
Figure 6.11: Ball-and-stick depiction of the core structure of <b>6.3</b> . Arrows highlight the Jahn-Teller axes.....	183
Figure 6.12: Ball-and-stick depiction of <b>6.3</b> ( $0.5 \leq x \leq 1$ , $0 \leq y \leq 1.1$ , $0 \leq z \leq 1$ ) showing face-to-face intramolecular (orange arrows), intermolecular (green arrow) and intermolecular edge-to-face (purple arrows) $\pi$ - $\pi$ interactions.....	185
Figure 6.13: Ball-and-stick depiction of a) the cationic moiety <b>6.4</b> . Hydrogen atoms omitted for clarity. b) The unit cell of <b>6.4</b> , looking down the b-axis; anions omitted for clarity. ....	187
Figure 6.14: Ball-and-stick depiction of the core structure of <b>6.4</b> . Arrows highlight the Jahn-Teller axes.....	188

Figure 6.15: Ball-and-stick depiction of extended cell of <b>6.4</b> looking down the c-axis, showing face-to-face intramolecular (orange arrows), intermolecular (green arrow) and intermolecular edge-to-face (purple arrows) $\pi$ - $\pi$ interactions.....	190
Figure 6.16: Ball-and-stick depiction of a) the cationic moiety <b>6.6</b> . Hydrogen atoms omitted for clarity. b) The unit cell of <b>6.6</b> . c) Core structural representation of <b>6.6</b> .....	192
Figure 6.17: Ball-and-stick depiction of extended half-cell of <b>6.6</b> , looking down the c-axis, showing face-to-face intramolecular (orange arrows), intermolecular (green arrow) and intermolecular edge-to-face (purple arrows) $\pi$ - $\pi$ interactions.....	194
Figure 6.18: Magnetic exchange models for a $3 \times [1 \times 3]$ $M_0$ grid.....	196
Figure 6.19: Variable temperature magnetic data for <b>6.2</b> ; $g = 2.04$ , $J = -1.4 \text{ cm}^{-1}$ , $z = 4/3$ , $J' = -0.4 \text{ cm}^{-1}$ , $TIP = 200 \times 10^{-6} \text{ cm}^3 \text{ mol}^{-1}$ , $10^2 R = 1.56$ .....	197
Figure 6.20: Magnetic exchange model for a $[3 \times 3]$ $M_0$ grid.....	198
Figure 6.21: Variable temperature magnetic data for <b>6.3</b> ; $g = 2.07(1)$ , $J_1 = -0.8(1) \text{ cm}^{-1}$ , $J_2 = -10(1) \text{ cm}^{-1}$ , $TIP = 860 \times 10^{-6} \text{ cm}^3 \text{ mol}^{-1}$ , $\theta = -0.2 \text{ cm}^{-1}$ , $10^2 R = 3.45$ .....	199
Figure 6.22: Variable field magnetization data for <b>6.3</b> ; solid red line calculated for $g = 2.06$ , $S' = 5 \times 1/2$ , $T = 2 \text{ K}$ , and dashed blue line calculated for $g = 2.06$ , $S' = 5/2$ , $T = 2 \text{ K}$ using the appropriate Brillouin function.....	201

Figure 6.23: Variable temperature magnetic data for <b>6.4</b> ; $g = 2.16(2)$ , $J_1 = 2.2(2) \text{ cm}^{-1}$ , $J_2 = -28(3) \text{ cm}^{-1}$ , $TIP = 720 \times 10^{-6} \text{ cm}^3 \text{ mol}^{-1}$ , $\rho = 0.09$ , $\theta = -1 \text{ cm}^{-1}$ , $10^2 R = 2.54$ .....	202
Figure 6.24: Variable field magnetization data for <b>6.4</b> ; solid red line calculated for $g = 2.16$ , $S' = 7/2$ , $T = 2 \text{ K}$ and dashed blue line calculated for $g = 2.16$ , $S' = 7 \times 1/2$ , $T = 2 \text{ K}$ using the appropriate Brillouin function. ....	204
Figure 6.25: Variable temperature magnetic data for <b>6.5</b> ; $g = 2.42$ , $J_2 = -5.92 \text{ cm}^{-1}$ , $TIP = 2000 \times 10^{-6} \text{ cm}^3 \text{ mol}^{-1}$ , $\theta = -2 \text{ K}$ .....	205
Figure 6.26: Variable temperature magnetic data for <b>6.6</b> ; $g = 2.0$ , $J_1 = -4.7 \text{ cm}^{-1}$ , $TIP = 0 \text{ cm}^3 \text{ mol}^{-1}$ , $\theta = -4 \text{ K}$ , $10^2 R = 1.14$ .....	207
Figure 7.1: A hypothetical self-assembled [4×4] grid .....	211
Figure 7.2: a) The complexed ligand <b>L1</b> in its <i>cisoid</i> configuration, leading to b) a hypothetical [5×5] square grid .....	212
Figure 7.3: a) The complexed ligand <b>L1</b> in its <i>transoid</i> configuration, leading to the formation of b) [2×5] $\text{Ag(I)}_{10}$ rectangular subunits .....	213
Figure 7.4: a) The ligand <b>L2</b> (showing metal coordination) used in the synthesis of b) a $4 \times [2 \times 2] \text{ Pb(II)}_{16}$ grid.....	214
Figure 7.5: Tetratopic pyridazine bis(hydrazone) ligands <b>L3</b> ( $R = \text{NH}_2$ ) and <b>L4</b> ( $R = \text{H}$ ), showing metal coordination pockets. ....	215
Figure 7.6: Ball-and-stick model of an $\text{Mn}_{16}(\text{L4})_8(\text{OH})_8$ cation [56]; pink = Mn, red = O, grey = C, blue = N .....	216
Figure 7.7: Tetratopic pyridazine bis(hydrazone) ligand 2pdoapm, <b>2.10</b> .....	217

Figure 7.8: Tetratopic pyridazine bis(hydrazone) ligand 2pdo56hq, <b>2.11</b> .....	217
Figure 7.9: a) Ball-and-stick depiction of the cationic moiety <b>7.1</b> . Hydrogen atoms omitted for clarity. b) The unit cell of <b>7.1</b> , looking down the a-axis; anions omitted for clarity. c) Bifurcation of the M-O core in <b>7.1</b> .....	226
Figure 7.10: Ball-and-stick depiction of the core structure of <b>7.1</b> .....	227
Figure 7.11: a) Ball-and-stick depiction of the cationic moiety <b>7.2a</b> . Hydrogen atoms omitted for clarity. b) The unit cell of <b>7.2a</b> , looking down the a-axis; anions omitted for clarity. c) Bifurcation of the M-O core in <b>7.2a</b> .....	230
Figure 7.12: Ball-and-stick depiction of the core structure of <b>7.2a</b> .....	231
Figure 7.13: Ball-and-stick depiction of the cationic moiety in the unit cell of <b>7.4</b> , viewed down the c-axis. Hydrogen atoms, solvent, anions and O(6) omitted for clarity.....	234
Figure 7.14: Ball-and-stick depiction of the core structure of <b>7.4</b> ; O(6) omitted for clarity. ....	235
Figure 7.15: Ball-and-stick depiction of <b>7.4</b> , viewed down the c-axis ( $0 \leq x \leq 1$ , $0 \leq y \leq 1$ , $0.75 \leq z \leq 1$ ) showing face-to-face intramolecular (orange arrows), intermolecular (green arrow) and intermolecular edge-to-face (purple arrows) $\pi$ - $\pi$ interactions. ....	237
Figure 7.16: Magnetic exchange model for a $4 \times [2 \times 2]$ $M_{16}$ grid. ....	239
Figure 7.17: Variable temperature magnetic data for <b>7.1</b> ; $g = 2.0$ , $J = -0.04 \text{ cm}^{-1}$ , $z = 2$ , $J' = -4.0 \text{ cm}^{-1}$ , $\rho = 0.014$ , $10^2 R = 2.91$ . ....	240

Figure 8.6: Ball-and-stick depiction of the cationic moiety <b>8.1</b> .....	259
Figure 8.7: Bifurcated chains of Cu(II) <sub>2</sub> subunits in <b>8.1</b> .....	261
Figure 8.8: a) Ball-and-stick model of the unit cell of <b>8.1</b> , showing the layered arrangement of cations; b) van der Waals representation showing the close packing between layers. ....	261
Figure 8.9: Variable temperature magnetic data for <b>8.1</b> ; dashed blue line (dinuclear model) $g = 2.02(4)$ , $J = -357(12) \text{ cm}^{-1}$ , $TIP = 100 \times 10^{-6} \text{ cm}^3 \text{ mol}^{-1}$ , $\rho = 0.05$ , $\theta = -3.8 \text{ K}$ , $10^3 R = 3.8$ ; solid red line (alternating chain model) $g = 2.07$ , $J = -187 \text{ cm}^{-1}$ , $\alpha = 0.2$ , $TIP = 50 \times 10^{-6} \text{ cm}^3 \text{ mol}^{-1}$ , $\rho = 0.04$ , $\theta = -4 \text{ K}$ , $10^3 R = 1.6$ .....	262
Figure 8.10: a) Ball-and-stick depiction of the cationic moiety <b>8.2</b> . Hydrogen atoms omitted for clarity. b) The unit cell of <b>8.2</b> , looking down the a-axis; anions omitted for clarity. c) Bifurcation of the M-O core in <b>8.2</b> .....	265
Figure 8.11: Ball-and-stick depiction of the core structure of <b>8.2</b> .....	266
Figure 8.12: The asymmetric unit of <b>8.2</b> ; arrows highlight the Jahn-Teller axes .....	268
Figure 8.13: Variable temperature magnetic data for <b>8.2</b> . $\chi$ represented by triangles; $\mu$ represented by diamonds; solid lines calculated from fitted values of $g_{\text{ave}} = 2.21$ , $J_1 = -45 \text{ cm}^{-1}$ , $J_2 = -350 \text{ cm}^{-1}$ , $TIP = 800 \times 10^{-6} \text{ cm}^3 \text{ mol}^{-1}$ , $10^2 R = 2.3$ .....	270
Figure 8.14: A spin-exchange model for <b>8.2</b> ; $J_1$ = antiferromagnetic coupling via pyridazine $\mu$ -NN only; $J_2$ = antiferromagnetic coupling via both $\mu$ -NN and $\mu$ -O bridges. ....	271

Figure 8.15: Variable field magnetization data for <b>8.2</b> ; $g = 2.21$ , $T = 2$ K, $S' = 4 \times \frac{1}{2}$ .....	274
Figure 8.16: a) Ball-and-stick depiction of the cationic moiety <b>8.3</b> . Hydrogen atoms omitted for clarity. b) The unit cell of <b>8.3</b> , looking down the a-axis; anions omitted for clarity. ....	275
Figure 8.17: Ball-and-stick depiction of the core structure of <b>8.3</b> . ....	276
Figure 8.18: One-quarter of the cationic core of <b>8.3</b> ; arrows highlight the Jahn-Teller axes. ....	278
Figure 8.19: Variable temperature magnetic data for <b>8.3</b> ; $g = 2.072$ , $J = 4.23$ cm <sup>-1</sup> , $z = 2$ , $J' = -0.08$ cm <sup>-1</sup> , $TIP = 1200 \times 10^{-6}$ cm <sup>3</sup> mol <sup>-1</sup> , $\rho = 0.02$ , $10^2 R = 0.636$ . ....	280
Figure 8.20: Magnetic exchange model for <b>8.3</b> . Yellow circles represent Cu(II) ( $S = 1/2$ ) centres and green circles represent Cu(I) ( $S = 0$ ) centres. ....	281
Figure 8.21: Variable field magnetization data for <b>8.3</b> ; solid red line calculated for $g = 2.072$ , $S' = 4 \times 3/2$ , $T = 2$ K and dashed blue line calculated for $g = 2.072$ , $S' = 12/2$ , $T = 2$ K using the appropriate Brillouin function. ....	282

**List of Schemes:**

Scheme 2.1: One possible route to [2×2] M <sub>4</sub> grid self-assembly .....	31
Scheme 2.2: One possible route to [3×3] M <sub>9</sub> grid self-assembly [75].....	33
Scheme 2.3: Synthesis of the pyridazine-based tetratopic ligand precursor.....	36
Scheme 2.4: Synthesis of ioap (2.2) and ioapm (2.3). .....	39
Scheme 2.5: Synthesis of 2pmoap (2.4).....	41
Scheme 2.6: Syntheses of quinoline-type ligands.....	43
Scheme 2.7: Summary of the synthesis of 2pyoapm (2.9). .....	46
Scheme 2.8: Summary of the synthesis of 2pdoapm (2.10) and 2pdo56hq (2.11). .....	47
Scheme 3.1: Possible route to the self-assembly of [2×2] grids and trigonal bipyramidal M <sub>5</sub> clusters. ....	90
Scheme 4.1: Self-assembled [3×3] grid.....	93
Scheme 6.1: General synthesis of Cu(II) <sub>8</sub> L <sub>4</sub> pinwheels. ....	160

### List of Symbols and Abbreviations:

APCI	atmospheric pressure chemical ionization
N	Avogadro's number ( $6.023 \times 10^{23}$ )
$\beta$	Bohr magneton ( $0.9273 \times 10^{-20}$ erg gauss <sup>-1</sup> )
k	Boltzmann's constant ( $1.381 \times 10^{-16}$ erg deg <sup>-1</sup> )
BVS	bond valence sum
Bs(y)	Brillouin function
CD-ROM	compact disk read only memory
T <sub>c</sub>	critical temperature
C	Curie temperature
CITS	current imaging tunneling spectroscopy
$\Omega(S')$	degeneracy of each state, S'
DNA	deoxyribonucleic acid
DMSO-d <sub>6</sub>	deuterated dimethylsulfoxide
DMF	dimethylformamide
$\mu_e$	effective magnetic moment
e.m.u.	electromagnetic unit
E(S')	energy of total spin quantum numbers
Et	ethyl-
H <sub>ex</sub>	exchange Hamiltonian
J	exchange integral

J'	exchange interaction in a molecular field approximation
H	external magnetic field
$\epsilon$	extinction coefficient
FT	Fourier transform
$\rho$	fraction of paramagnetic impurity
FMD	full matrix diagonalization
HOPG	highly oriented pyrolytic graphite
Im	imidazole
IR	infrared
ITO	irreducible tensor operators
g	Landé splitting factor
<i>vide infra</i>	Latin: "seen below"
<i>vide supra</i>	Latin: "see above"
<i>in situ</i>	Latin: "in the reaction mixture"
$\chi$	magnetic susceptibility
M	magnetization
$\tau$	measure of five-coordinate geometric distortion
MLCT	metal-to-ligand charge transfer
Mp	melting point
Me	methyl-
$\chi_M$	molar susceptibility

NBu	n-butyl-
NIR	Near-infrared
nPr	n-propyl-
NMR	Nuclear magnetic resonance
z	number of nearest neighbors in a molecular field approximation
Hpiv	pivalic acid
$\delta_H$	proton chemical shift
Py	pyridine
qubit	quantum bit
$M_s$	saturation magnetization
STM	scanning tunneling microscopy
SMM	single molecule magnet
S	spin quantum number
SQUID	superconducting quantum interference device
TIP	temperature independent paramagnetism
<i>t</i> Bu	tertiary butyl-
$S'$	total spin quantum number
UV-Vis	Ultra-violet visible
VC	vector coupling
$\nu$	wavelength of absorbance (IR)
$\lambda$	wavelength of absorbance (UV-Vis)

$\theta$	Weiss correction
XPS	X-ray photoelectron spectroscopy

### List of Appendices:

#### Appendix 1: Vector coupling approach to magnetic modeling

A1.1: Dinuclear compounds .....	305
A1.2: Trinuclear Compounds.....	308
A1.3: Tetranuclear Compounds.....	312

#### Appendix 2: Magnetic models, OW01.ini files, and spk files

A2.1: Dinuclear Compounds .....	315
A2.2: Trinuclear Complexes.....	317
A2.3: Tetranuclear Complexes .....	319
A2.4: Pentanuclear Clusters.....	320
A2.5: [3 $\times$ 3] M(II) <sub>9</sub> Grids .....	321
A2.6: [3 $\times$ 3] A <sub>5</sub> B <sub>4</sub> Grids .....	326
A2.7: 3 $\times$ [1 $\times$ 3] Mn(II) <sub>9</sub> .....	330
A2.8: 4 $\times$ [2 $\times$ 2] M <sub>16</sub> grids.....	332
A2.9: 4 $\times$ [2 $\times$ 2] M <sub>16</sub> grids with four diamagnetic centres .....	334
A2.10: 4 $\times$ [2 $\times$ 2] Cu(II) <sub>16</sub> grid.....	336

#### Appendix 3: Extended structural data

A3.1: [(ioap-H)(ioap-2H)Co <sub>2</sub> (H <sub>2</sub> O) <sub>4</sub> ](BF <sub>4</sub> ) <sub>2</sub> (H <sub>2</sub> O) <sub>2.75</sub> ( <b>3.1</b> ).....	338
---	-----

A3.2: [(ioap) <sub>2</sub> (ioap-H) <sub>2</sub> Mn <sub>3</sub> (H <sub>2</sub> O) <sub>2</sub> ](NO <sub>3</sub> ) <sub>4</sub> (H <sub>2</sub> O) <b>(3.2)</b> .....	340
A3.3: [(ioap-H) <sub>4</sub> Ni <sub>4</sub> (CF <sub>3</sub> SO <sub>3</sub> )(H <sub>2</sub> O) <sub>3</sub> ](CF <sub>3</sub> SO <sub>3</sub> ) <sub>2</sub> (PF <sub>6</sub> ) <b>(3.3)</b> .....	342
A3.4: [(ioap-H) <sub>4</sub> Cu <sub>4</sub> ](NO <sub>3</sub> ) <sub>4</sub> (CH <sub>3</sub> CN) <sub>4</sub> <b>(3.4)</b> .....	344
A3.5: [(ioap-H) <sub>4</sub> Cu <sub>4</sub> ](PF <sub>6</sub> ) <sub>2.5</sub> (CF <sub>3</sub> SO <sub>3</sub> ) <sub>1.5</sub> (H <sub>2</sub> O) <sub>2</sub> (CH <sub>3</sub> CN) <sub>3.5</sub> <b>(3.5)</b> .....	346
A3.6: [Cu(ioapm)(ClO <sub>4</sub> )(CH <sub>3</sub> CN)](ClO <sub>4</sub> ) <b>(3.6)</b> .....	348
A3.7: [Cu <sub>4</sub> (ioapm-H) <sub>4</sub> ](ClO <sub>4</sub> ) <sub>4</sub> ·3 H <sub>2</sub> O <b>(3.7)</b> .....	350
A3.8: [Mn <sub>5</sub> (ioapm-H) <sub>6</sub> ](ClO <sub>4</sub> ) <sub>4</sub> ·2.5H <sub>2</sub> O <b>(3.8)</b> .....	352
A3.9: [(2pmoap-2H) <sub>6</sub> Zn <sub>9</sub> ](NO <sub>3</sub> ) <sub>6</sub> ·15.5H <sub>2</sub> O <b>(4.1)</b> .....	354
A3.10: [(2pmoap-2H) <sub>6</sub> Mn <sub>9</sub> ](NO <sub>3</sub> ) <sub>6</sub> ·28H <sub>2</sub> O <b>(4.2)</b> .....	356
A3.11: [(2pmoap-2H) <sub>6</sub> Co <sub>9</sub> ](NO <sub>3</sub> ) <sub>6</sub> ·2CH <sub>3</sub> CN·11H <sub>2</sub> O <b>(4.3)</b> .....	358
A3.12: [(pmoapCOO)Cu](NO <sub>3</sub> ) <b>(4.4)</b> .....	360
A3.13: [(2pmoap-2H) <sub>6</sub> Cu <sub>9</sub> ](NO <sub>3</sub> ) <sub>6</sub> ·20.5H <sub>2</sub> O <b>(4.5)</b> .....	362
A3.14: [Cu <sub>9</sub> (2pmoap-2H) <sub>2</sub> (2pmoap-H) <sub>4</sub> ](ClO <sub>4</sub> ) <sub>10</sub> ·13.2H <sub>2</sub> O <b>(4.6)</b> .....	364
A3.15: [(2pmoap-2H) <sub>6</sub> Mn <sub>5</sub> Zn <sub>4</sub> ](NO <sub>3</sub> ) <sub>6</sub> ·14H <sub>2</sub> O <b>(5.1)</b> .....	366
A3.16: [(2pmoap-2H) <sub>6</sub> Mn <sub>5</sub> Cu <sub>4</sub> ](NO <sub>3</sub> ) <sub>6</sub> ·24H <sub>2</sub> O <b>(5.2)</b> .....	368
A3.17: [(2pmoap-2H) <sub>6</sub> Mn <sub>1</sub> Cu <sub>8</sub> ](NO <sub>3</sub> ) <sub>6</sub> ·15H <sub>2</sub> O <b>(5.4)</b> .....	370
A3.18: (2po56hq+2H)(BF <sub>4</sub> ) <sub>2</sub> (CH <sub>3</sub> OH) <sub>1</sub> (H <sub>2</sub> O) <sub>1</sub> <b>(6.1)</b> .....	372
A3.19: [(2po56hq-2H) <sub>6</sub> Mn <sub>9</sub> ](ClO <sub>4</sub> ) <sub>6</sub> <b>(6.2)</b> .....	374
A3.20: [(2po56nq-2H) <sub>6</sub> Cu <sub>9</sub> ](BF <sub>4</sub> ) <sub>6</sub> ·6.4H <sub>2</sub> O <b>(6.3)</b> .....	376
A3.21: [(2po45nq-2H) <sub>6</sub> Cu <sub>8.5</sub> ](CF <sub>3</sub> SO <sub>3</sub> ) <sub>1.4</sub> (PF <sub>6</sub> ) <sub>3.6</sub> ·3H <sub>2</sub> O <b>(6.4)</b> .....	378
A3.22: [(2po34nq-2H) <sub>6</sub> Mn <sub>9</sub> ](CF <sub>3</sub> SO <sub>3</sub> ) <sub>3</sub> (NO <sub>3</sub> ) <sub>3</sub> (H <sub>2</sub> O) <sub>3.8</sub> <b>(6.6)</b> .....	380
A3.23: [(2pdoapm-2H) <sub>8</sub> Mn <sub>16</sub> O <sub>4</sub> (OH) <sub>4</sub> ](PF <sub>6</sub> ) <sub>4</sub> ·21.2H <sub>2</sub> O <b>(7.1)</b> .....	382

A3.24: [(2pdoapm-2H) <sub>8</sub> Co <sub>16</sub> (OH) <sub>8</sub> ](BF <sub>4</sub> ) <sub>8</sub> ·19.8H <sub>2</sub> O ( <b>7.2a</b> ).....	384
A3.25: [(2pdo56hq-2H) <sub>8</sub> Mn <sub>16</sub> O <sub>4</sub> (OH) <sub>4</sub> ](NO <sub>3</sub> ) <sub>4</sub> ·32H <sub>2</sub> O ( <b>7.4</b> ) .....	386
A3.26: [(2pyoapm-H)Cu(OH)](ClO <sub>4</sub> ) <sub>2</sub> ·1.6H <sub>2</sub> O ( <b>8.1</b> ) .....	388
A3.27: [(2pdoapm-2H) <sub>6</sub> (2pdoapm-3H) <sub>2</sub> Cu <sub>16</sub> O <sub>2</sub> (OH) <sub>4</sub> (H <sub>2</sub> O) <sub>2</sub> ] (CF <sub>3</sub> SO <sub>3</sub> ) <sub>6</sub> ·21.4H <sub>2</sub> O ( <b>8.2</b> ) .....	390
A3.28: [(2pdoapm-2H) <sub>8</sub> Cu <sub>16</sub> ](CF <sub>3</sub> SO <sub>3</sub> ) <sub>12</sub> ·2.8H <sub>2</sub> O ( <b>8.3</b> ).....	392

## Chapter 1: General introduction

### 1.1: Supramolecular chemistry and self-assembly:

In 1894 Hermann Emil Fischer unknowingly laid the roots of modern supramolecular chemistry when he described enzyme-substrate interactions in terms of a “lock and key” mechanism [1]. He was later awarded the 1902 Nobel Prize in chemistry “in recognition of the extraordinary services he has rendered by his work on sugar and purine syntheses” [2]. 85 years after this award and 91 years after Fischer’s initial description of what is now called molecular recognition and host-guest chemistry, Donald J. Cram, Jean-Marie Lehn and Charles J. Pedersen were awarded the 1987 Nobel Prize in chemistry for “for their development and use of molecules with structure-specific interactions of high selectivity” [3]. In his subsequent Nobel lecture, Lehn defined supramolecular chemistry as “chemistry beyond the molecule” [4]. This area of study deals with assemblies held together not by covalent forces, but rather by hydrogen bonding, metal coordination, hydrophobic forces, van der Waals forces,  $\pi$ - $\pi$  interactions and/or electrostatic effects [5,6].

An important concept in supramolecular chemistry is molecular self-assembly. In general terms, self-assembly describes the means by which a disordered system of simple molecular components forms a complex organized architecture as a result of local, non-covalent interactions, without external direction. The clusters presented in this thesis were specifically produced by metal-mediated self-assembly methods, and in this context, Stang has defined four components common to all such entities [7]. These are:

1. Components of the architecture are held together by coordinative bonds.

2. The self-assembled entity is the most stable for the optimal combination of its components, and therefore exhibits thermodynamic selectivity.
3. The assembly can be characterized as a distinct entity separate from the individual components.
4. Discrete assemblies, rather than infinite structures, result.

Within the realm of self-assembly, scientists are synthesizing large architectures by both a 'serendipitous' approach and by using rational design. Serendipitous self-assembly is characterized by the use of ligands that can exhibit varying coordination modes, with metals that have flexible coordination geometries [8]. Results are often achieved by creating a mismatch between the coordinating ability of a ligand and the available sites on a metal, or by creating elements of unsaturation about a metal centre by removing ligands from a complex [8]. Winpenny has observed that "You can predict there will be an effect, but cannot predict how that effect will be manifested." (*Dalton Trans.*, **2002**, 2) He also lists three critical factors for the selection of ligands for serendipitous assembly, summarized as follows:

1. Since the usefulness of any one ligand cannot be predicted, synthetically complicated ligands should be avoided. Often, simple molecules available for commercial purchase, that exhibit a variety of bonding modes, are entirely suitable as candidates for serendipitous assembly.
2. Related ligands should be explored as minor changes can lead to large differences in the resulting complex.

3. It is helpful if the ligands are soluble in a range of solvents, as many solvents must be examined for their influence on the formation of complexes.

Serendipitous self-assembly has produced a wide variety of beautiful and complex structures, including the first reported molecular magnet, a mixed oxidation state  $M_4O_4$  butterfly surrounded by an  $Mn_8$  ring [9], a magnetically anisotropic  $Fe(III)_{18}$  cluster with an  $S' = 33/2$  ground state [10] and a  $Mn(III)_{12}Mn(II)_7$  aggregate with a very high  $S' = 83/2$  ground state [11]. Serendipity is the faculty of making fortunate discoveries by accident, and while it is impossible to deny that many metal architectures of current interest have been generated 'accidentally', systematic studies of such assemblies may lead to a greater understanding of relationships between reaction components, solvent conditions, bonding forces and other factors involved in self-assembly processes.

Work from the Winpenny group demonstrates how such a systematic investigation can lead to rational product outcomes, however, this comes only after a great deal of experimental effort. While this group has published several comprehensive studies on the effects of varying the base used in the synthesis of  $Ni(II)$  cages [12], and mixed oxidation state  $Mn(III)/Mn(IV)$  cages [13], their investigation of the synthesis of self-assembled heterometallic wheel compounds bears particular attention. Heterometallic wheels of various sizes and compositions were synthesized based upon the antiferromagnetic, homometallic  $[Cr_8F_8(piv)_{16}]$  ring (see Figures 1.1a for the ligand Hpiv and 1.1b for a sketch of the resulting ring) [14,15].  $[RNH_2][Cr_7MF_8(piv)_{16}]$  wheels (where  $R = Me, Et, nPr, NBu, N$ -octyl and  $M = Ni, Co, Mn, Fe$  or  $Cd$ ) resulted from the addition of excess  $M(II)$  salt to a mixture of  $CrF_3$ , pivalic acid, and a secondary amine

template [16]. Changing the template from secondary to tertiary amines and imidazole subsequently lead to the formation of octa-, nona- and decanuclear rings [17].

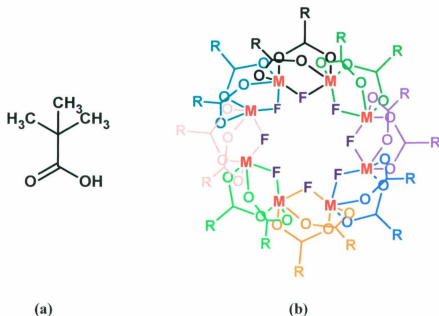


**Figure 1.1:** a) The ligand Hpiv (pivalic acid) which leads to the formation of b)  $[M_8F_8(\text{piv})_{16}]$  and  $[M_7M'F_8(\text{piv})_{16}]$  rings ( $R = t\text{Bu}$ ).

In contrast to serendipitous self-assembly, other researchers are designing rigid multidentate ligands suitable for the achievement of specific synthetic targets, such as racks, ladders, and grids [18]. Such ligands are generally synthetically challenging, incorporate a coordination capacity that matches the requirements of specific metal ions and have donor groups (oxygen or nitrogen atoms for example) built into the backbone in positions suitable for the formation of stable five- or six-membered chelate rings upon interaction with a metal ion. Many such ligands are also planar due to the presence of delocalized  $\pi$ -systems, and moieties such as pyrimidine and pyridine. In the context of this thesis, the design principles behind ligands suitable for the formation of square  $[n \times n]$

grids bear a closer examination. Jean-Marie Lehn and his collaborators laid the groundwork in this area by considering the ‘coordination algorithm’ of a particular metal ion. In the strict sense of the word, an algorithm is a set of rules that specify how to solve a problem. Here, the ‘rules’ entail designing a ligand that considers not only the metal ion’s preferred geometry (for example, four-coordinate tetrahedral or six-coordinate octahedral), but also, the donor capacity of the ligand, and the metal ion’s preference for particular donors.

These principles are best illustrated by a specific example. Figure 1.2a shows a ditopic ligand (**L1**) which self-assembles in a 1:1 ratio with four ligands and four Cu(II) ions to form a  $[2 \times 2]$  (**L1**)<sub>4</sub>Cu(II)<sub>4</sub> square grid complex (Figure 1.2c) [19]. The ligand donor groups are positioned to adopt a *mer* configuration about each metal centre, which encourages coordination by a second ligand molecule, oriented perpendicular to the first. (Figure 1.2b). There is an exact match between the donor capacity of four ligands and the coordination requirements of four six-coordinate, octahedrally-bound Cu(II) ions. The ligands are therefore aligned in two roughly parallel groups above and below the metal pseudo-plane (Figure 1.2c; one group shown in blue, oriented perpendicular to the other group, shown in magenta), and the bridging phenoxide moiety allows for weak antiferromagnetic exchange between neighboring copper ions.

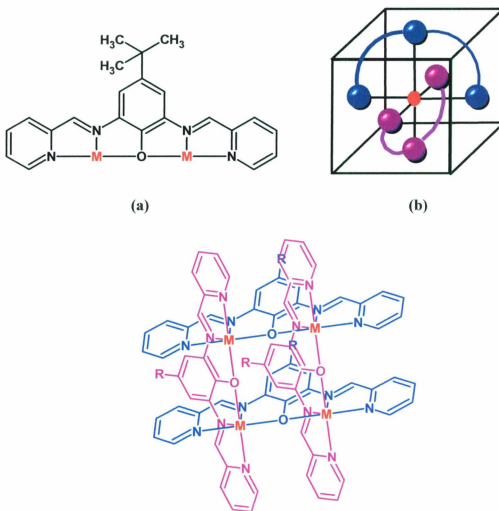


**Figure 1.2:** a) The ditopic ligand **L1**, with tridentate coordination pockets that adopt b) meridional positions on an octahedral metal ion leading to the formation of c)  $[2 \times 2]$  square grids ( $R = t\text{Bu}$ ).

Similar design principles have led to the synthesis of other ditopic (**L2**, Figure 1.3a) [20], tritopic (**L3**, Figure 1.3b) [21] and tetratopic (**L4**, Figure 1.4a) [22] ligands. Note that in **L2**, each pocket is tridentate, which again leads to the formation of a  $[2 \times 2]$  (**L2**)<sub>4</sub>M<sub>4</sub> square grid, in this case with octahedral  $M = \text{Co(II)}$  ions [20].

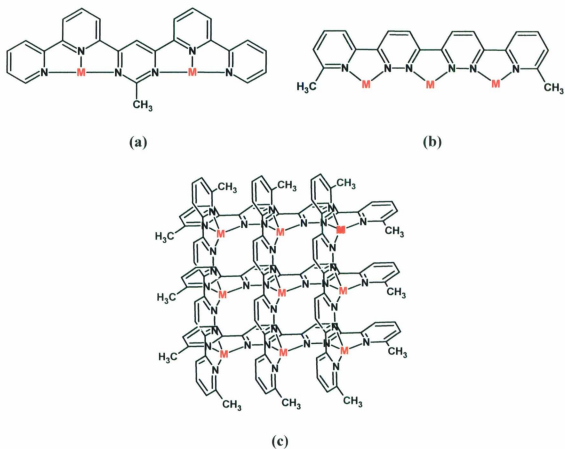


**Figure 1.3:** a) The ditopic ligand **L2**. b) The tritopic ligand **L3** which leads to the formation of c) a  $[3 \times 3] M(I)_9$  grid ( $M = Ag$ ).

Each of the coordination pockets in the tritopic ligand **L3**, however, is bidentate. Here, a congruence exists between the available donor sites, their positions, and the coordination capacity of metals with a tetrahedral geometric preference. Consequently, a  $[3 \times 3] Ag(I)_9$  grid was produced (Figure 1.3c,  $M = Ag(I)$ ), with an exact match between the number of available donor atoms from six ligands, and the coordination requirements of nine tetrahedral  $Ag(I)$  ions [21].

A  $\text{Pb(II)}_{16}$  grid was synthesized *via* a self-assembly reaction between 16 metal ions and eight **L4** ligands [22] (Figure 1.4b) with 16 triflate anions and eight water molecules filling additional sites on the seven-, eight- or nine-coordinate lead ions [22,23].

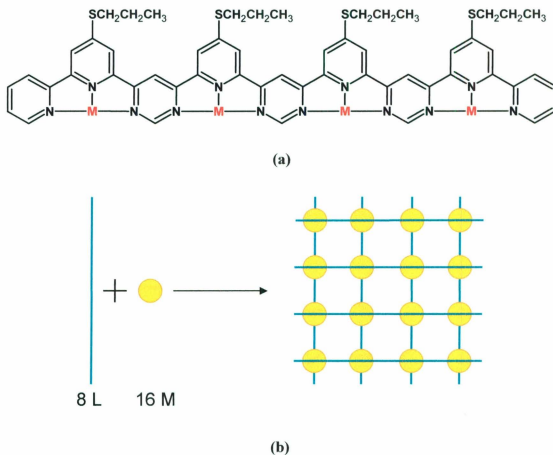


**Figure 1.4:** a) The tetratopic ligand **L4** which lead to the formation of b) a  $(\text{L4})_8\text{Pb(II)}_{16}$  grid.

## 1.2: Metallo-supramolecular arrays and nanotechnology:

A 'bottom-up' approach to the construction of nanoscale materials suitable for application as electronic or computer components is being fueled by the apparent doubling of transistor density every 18 months [24]. Current computer memory devices, such as magnetic disks and CD-ROMs store approximately  $10^8$  bits/cm<sup>2</sup>, while it has been theorized that DNA could store approximately  $10^{10}$  bits/cm<sup>2</sup> [25,26]. In his review of the potential for using grid type molecules as quantum dot cellular automata, Lehn theorizes that based on surface studies of third row transition metal supramolecular arrays with dimensions of 25×25 Å, a self-assembled monolayer consisting of tightly packed two-dimensional arrays of [2×2] grids that stored one bit of data for every grid molecule, could possibly hold up to  $10^{12}$  bits/cm<sup>2</sup> of data [25].

Metallo-supramolecular arrays are suitable for consideration towards this end as they possess magnetic properties, redox properties and spin-state transitions that serve as independent states within a single molecule, in addition to forming two-dimensional arrangements that bear a striking resemblance to cross-bar structures used for conventional information storage and computer processing [27]. Finally, such arrays can be deposited upon surfaces in an ordered manner and metal centres can be addressed uniquely [25, 28]. For example, a solution of the [3×3] grid complex [Mn(II)<sub>9</sub>(Cl<sub>2</sub>poap-2H)<sub>6</sub>](ClO<sub>4</sub>)<sub>6</sub> was deposited on highly oriented pyrolytic graphite (HOPG), and was probed by scanning tunneling microscopy (STM) and current imaging tunneling spectroscopy (CITS) (Figure 1.5a, c-e) [28].

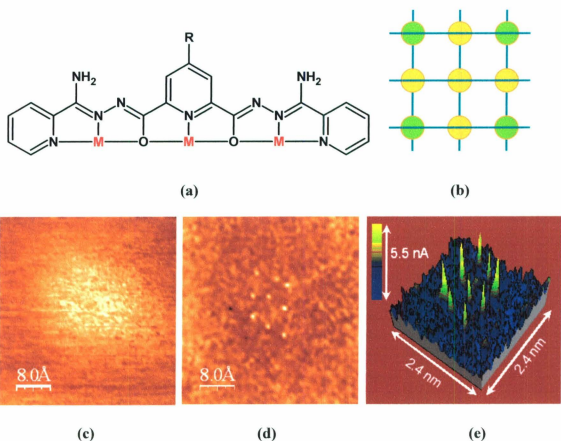


**Figure 1.5:** a) The ligand 2poap (R = H) or Cl<sub>2</sub>poap (R = Cl) which leads to the formation of b) [3×3] M(II)<sub>9</sub> grids, that subsequently become heterovalent (green circles = Mn(III), orange circles = Mn(II)) upon chemical or electrochemical oxidation [28,29]. Surface studies on [Mn<sub>9</sub>(Cl<sub>2</sub>poap)<sub>6</sub>]<sup>6+</sup> on HOPG gives c) a topographic image, d) a CITS image, and e) a 3D current isopol plot [28].

The mixed-oxidation state [3×3] grid complex [Mn(II)<sub>5</sub>Mn(III)<sub>4</sub>(2poap-2H)<sub>6</sub>](ClO<sub>4</sub>)<sub>10</sub> (see Figure 1.5a for 2poap [30]) was produced by bulk electrolysis of the Mn(II)<sub>9</sub> complex [28], with Mn(III) centres present in the corner sites, and Mn(II) elsewhere (Figure 1.5b). It exhibited an  $S = \frac{1}{2}$  magnetic ground state [28,29] which was

in agreement with the presence of the Mn(III) centres ( $S = 2$ ) at the corner sites, coupled antiferromagnetically with the Mn(II) ( $S = 5/2$ ) centres to produce an overall ferrimagnetic effect ( $S = (4 \times 2) + 5/2 - (4 \times 5/2) = 1/2$ ).

Waldmann considered this molecule to be an actual experimental example of a mesoscopic  $S = 1/2$  cluster suitable for consideration as an antiferromagnetic qubit [31]. In general, antiferromagnetic, transition metal rings have potential in the area of nanocomputing, where quantum effects, such as tunneling are very important. For example, such a system would have computing applications were it possible to tunnel between a spin "up" and a spin "down" state without energy transfer; this is known as tunneling coherence [32]. Interactions with nuclear spins, lattice vibrations and with other paramagnetic molecules in the lattice however, can lead to incoherent tunneling between two states. It is predicted, however, that for an antiferromagnetic ring with an odd number of spin centres, tunneling will take place coherently, in part due to the presence of at least one uncompensated spin in the ground state. That is, at a sufficiently low temperature, for the one uncompensated spin to flip *via* a tunneling mechanism, all other spins must similarly reverse their spins in order to maintain the antiferromagnetic interaction. It should also be possible to observe quantum effects for rings with an even number of spin centres provided that there is an excited state that lies sufficiently close to the  $S = 0$  ground state so that upon application of a sufficiently high magnetic field at low temperatures the  $S = 0$  ground state and the low-lying excited state will become reversed in energy *via* quantum tunneling.

Further investigations of this  $\text{Mn(II)}_5\text{Mn(III)}_4$  system, to analyze for possible anisotropy, are required before the ability of the ground state unpaired spin to tunnel from a 'spin up' configuration to a 'spin down' configuration can be assessed. If it is possible for this tunneling to take place without an energy transfer, the system would exhibit tunneling coherence and would be suitable for consideration as a qubit [33].

### 1.3: Magnetic interactions in paramagnetic clusters:

Many excellent general introductions to the magnetic properties of materials have been written [34], and are presented in most senior undergraduate inorganic chemistry textbooks [35]. Therefore, this discussion will begin with a description of diamagnetism and paramagnetism.

Diamagnetic substances contain no unpaired electrons and are weakly repelled by an external magnetic field. Diamagnetic susceptibility values generally range between -1 and  $-100 \times 10^{-6}$  e.m.u. and are independent of field strength and temperature. All substances that contain paired electrons have an associated diamagnetic component which must be corrected for when assessing the paramagnetic properties of a material.

Paramagnetic substances contain unpaired electrons and are attracted into an external magnetic field. Paramagnetic susceptibility values generally range between 100 and  $100,000 \times 10^{-6}$  e.m.u. Paramagnetism is independent of field strength, but exhibits an inverse dependence of susceptibility upon temperature. This relationship can be expressed as:

$$\chi = \frac{N\beta^2\mu_e^2}{3kT} \quad (1.1)$$

Where  $N$  is Avogadro's number =  $6.023 \times 10^{23}$ ,  $\beta$  is the Bohr magneton =  $0.9273 \times 10^{-20}$  erg gauss<sup>-1</sup>,  $k$  is Boltzmann's constant =  $1.381 \times 10^{-16}$  erg deg<sup>-1</sup> and  $T$  is the temperature expressed in Kelvin.  $\mu_e$  is the "effective magnetic moment" and can consequently be expressed in units of Bohr magnetons as:

$$\mu_e = 2.828 \sqrt{\chi T} \quad (1.2)$$

When paramagnetic centres are directly bonded or are bridged by a suitable intervening atom or molecule, the resulting spin-spin interactions may be either ferromagnetic or antiferromagnetic. In ferromagnetic systems, the spin magnetic dipoles of the individual paramagnetic centres align in the same direction below a certain temperature (the Curie temperature). Increasing the thermal energy of the system leads to the randomization of the spins, and above the Curie temperature the system will behave like a simple paramagnetic, in agreement with the Curie-Weiss law (equation 1.3).

$$\chi = \frac{C}{T - \theta} \quad (1.3)$$

Where  $C$  is the Curie temperature, and  $\theta$  is the Weiss correction, which is positive for ferromagnetic systems. Note that ferromagnetic effects are both field- and temperature-dependent.

In antiferromagnetic systems, the spin magnetic dipoles on adjacent paramagnetic centres align antiparallel below a certain temperature (the Néel temperature). This results in a decrease in the observed susceptibility. Increasing the thermal energy of the system leads to the randomization of the spins, and above the Néel temperature the system will behave like a simple paramagnetic, in agreement with the Curie-Weiss law (equation

1.3). The Weiss correction is negative for antiferromagnetic systems. Note that antiferromagnetic effects are temperature-dependent, but field-independent.

A third paramagnetic possibility exists if the unpaired electrons on one centre are opposed to those on another, but the magnitude of the opposing moments is unequal. This results in a ferrimagnetic material where spontaneous magnetization is possible. Finally, if the crystal structure is of low symmetry, the unpaired spins may not line up in either a strictly antiparallel or parallel manner, but instead may be canted. This leads to canted ferro- or antiferromagnetism.

#### **1.4: Superexchange:**

The following discussion of magnetic interactions and superexchange is limited to the types of orbital alignment that are referenced in later chapters of this thesis, and is therefore not comprehensive. A mathematical discussion of the wavefunctions that are involved is also omitted. These topics, which make up the Goodenough-Kanamori-Anderson rules, are reviewed in detail elsewhere [36-41].

When metals in paramagnetic clusters are separated by distances that far exceed their covalent radii, with intervening diamagnetic atoms, anions or molecules, they may exhibit magnetic interactions *via* superexchange ('kinetic' exchange). Consider the very simple illustrated example in Figure 1.6. Here, two metal centres, each with one unpaired d electron (Cu(II) for example) residing in the  $d_{z^2}$  orbital, are bridged by an intervening oxide ( $O^{2-}$ ) ion.

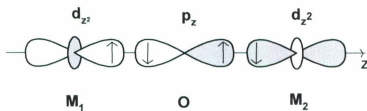


**Figure 1.6:** Simple illustration of superexchange *via*  $\sigma$ -bonding in a linear M-O-M system.

If we assume the unpaired electron on  $M_1$  to be 'spin up' then when the  $d_{z^2}$  orbital admixes with an orbital of suitable symmetry ( $p_z$ ) on the intervening ion, leading to  $\sigma$ -bonding, a  $p_z$  electron will pair and become 'spin down'. The other electron in the  $p_z$  orbital will then be 'spin up', pairing with the unpaired electron on  $M_2$ , which will then be spin down [42]. The overall effect is antiferromagnetic exchange.

Antiferromagnetic exchange in linear M-O-M systems can take place by the admixing of various metal d orbitals and bridging orbitals of appropriate symmetry. Two other examples are shown in Figure 1.7.

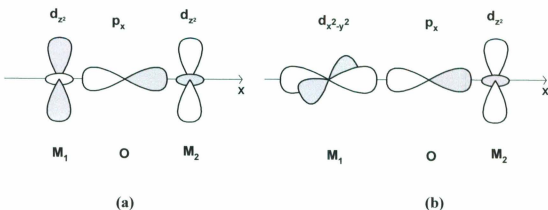


**Figure 1.7:** Other modes of superexchange *via*  $\sigma$ -bonding in a linear M-O-M system.

In Figure 1.7a, the unpaired metal electron again resides in a  $d_{z^2}$  orbital, but these orbitals are now oriented in an orthogonal manner ( $90^\circ$ ) to the intervening oxygen orbital. Antiferromagnetic exchange is still possible *via* the  $d_{z^2}$  lobe in the  $xy$  plane, and the unpaired electrons pair in a ‘spin up’ and ‘spin down’ manner as in the first example. In Figure 1.7b, antiferromagnetic exchange also results from the overlap of a magnetic ground state  $d_{x^2-y^2}$  metal orbital with a  $d_{z^2}$  orbital *via* the intervening  $p$  orbital.

In the case of strict orbital orthogonality, the coupling is *via* direct exchange (‘potential’/Heisenberg exchange), and the coupling constant,  $J$ , is always positive since it results from the repulsive potential energy involved in the electron exchange over the distance separating the two magnetic centres [43]. Figure 1.8 illustrates the orthogonal orientation of two magnetic ground state  $d_{x^2-y^2}$  orbitals to the intervening  $p_z$  orbital.

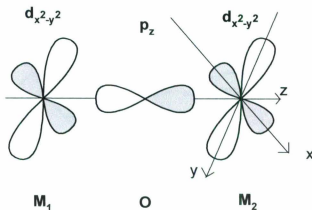


**Figure 1.8:** A linear M-O-M system exhibiting strict magnetic orbital orthogonality resulting in ferromagnetism.

While the potential term is present in all exchange couplings, it is normally very small in the presence of superexchange. The examples presented here illustrated

superexchange by a single atom bridge, however, multiple atom bridges are possible. For example, diazine Cu-NN-Cu systems, with  $d_{x^2-y^2}$  metal magnetic ground states, exhibit both antiferromagnetism (by superexchange) and ferromagnetism (from accidental orbital orthogonality) as a linear function of rotation of the copper magnetic planes about the N-N bond [44,45]. A similar linear relationship was reported by Hatfield [46] between the strength of the exchange coupling ( $2J$ ) and the Cu-O-Cu bond angle in a series of di- $\mu$ -hydroxo-bridged copper(II) complexes. It is only when magnetic orbitals are aligned in an orthogonal manner (either in a strict or accidental sense) that ferromagnetism dominates the exchange behaviour between two centres.

### 1.5: Fitting magnetic data for polynuclear clusters:

The first step in modeling experimental magnetic data is to define a Heisenberg spin Hamiltonian to describe the exchange situation and to determine all of the spin states associated with the system. A general Heisenberg spin Hamiltonian, which includes spin coupling between the paramagnetic centres, ligand field effects, and Zeeman splitting terms is shown in equation 1.4.

$$H = -\sum_{i < j} J_{ij} \cdot S_i \cdot S_j + \sum_i S_i \cdot D_i \cdot S_i + \mu_B \sum_i S_i \cdot g_i \cdot B \quad (1.4)$$

Normally, the ligand field effects ( $\sum_i S_i \cdot D_i \cdot S_i$ ) are ignored and it is assumed that the Landé splitting factor ( $g$ ) effects are identical and isotropic. The Hamiltonian is therefore simplified to give equation 1.5.

$$H = -\sum_{i < j} J_{ij} \cdot S_i \cdot S_j \quad (1.5)$$

The total spin quantum numbers,  $S'$ , and their energies,  $E(S')$ , can now be determined from the exchange Hamiltonian, and can be substituted into the Van Vleck equation to calculate the susceptibility as a function of temperature for the system. Equation 1.6 shows the generalized form of the Van Vleck equation.

$$\chi_M = \frac{N\beta^2 g^2}{3k(T-\theta)} \frac{\sum S'(S'+1)(2S'+1)\Omega(S')e^{-E(S')/kT}}{\sum (2S'+1)\Omega(S')e^{-E(S')/kT}} \quad (1.6)$$

Where  $\Omega(S')$  gives the degeneracy of each state with a particular value of  $S'$ . This is normally corrected to include the fraction of paramagnetic impurity ( $\rho$ ), a temperature independent paramagnetic term (TIP) and a Weiss-like temperature correction,  $\theta$ . The modified Van Vleck equation is expressed in equation 1.7.

$$\chi_M = \frac{N\beta^2 g^2}{3k(T-\theta)} \frac{\sum S'(S'+1)(2S'+1)\Omega(S')e^{-E(S')/kT}}{\sum (2S'+1)\Omega(S')e^{-E(S')/kT}} (1-\rho) + \quad (1.7)$$

$$\frac{N\beta^2 g^2 S(S+1)\rho}{3kT} + TIP$$

The spin states and energies from the exchange Hamiltonian can be determined by three mathematical methods: vector coupling (VC), irreducible tensor operators (ITO) and full matrix diagonalization (FMD) [47]. The vector coupling approach was first used by Kambe [48], and results in closed form susceptibility expressions, that can be conveniently evaluated. This approach is illustrated by considering two possible trinuclear situations, an equilateral triangle and a line (Figure 1.9).

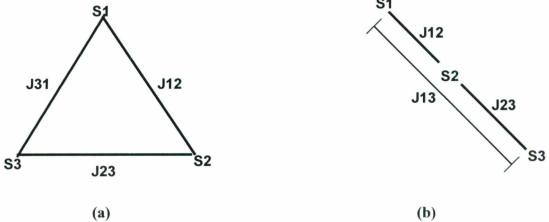


**Figure 1.9:** General scheme for the coupling in a) an equilateral triangle and b) a linear triad of spin centers.

The Hamiltonian to describe either of these cases is:

$$H_{\alpha} = -2[J_{12}(S_1 \cdot S_2) + J_{23}(S_2 \cdot S_3) + J_{31}(S_3 \cdot S_1)] \quad (1.8)$$

Letting  $J = J_{12} = J_{23}$ ;  $\alpha J = J_{31}$

$$H_{\alpha} = -2J[(S_1 \cdot S_2) + (S_2 \cdot S_3) + \alpha(S_3 \cdot S_1)] \quad (1.9)$$

Two summations are now defined in equations 1.10 and 1.11:

$$S' = S_1 + S_2 + S_3 \quad (1.10)$$

and

$$S^* = S_3 + S_1 \quad (1.11)$$

Squaring equation 1.10 leads to:

$$(S_1 + S_2 + S_3)^2 = (S' \cdot S') = 3S(S+1) + 2(S_1 \cdot S_2) + 2(S_2 \cdot S_3) + 2(S_3 \cdot S_1) \quad (1.12)$$

Which can be rearranged to give equation 1.13.

$$2(S_1 \cdot S_2) + 2(S_2 \cdot S_3) = (S' \cdot S') - 3S(S+1) - 2(S_3 \cdot S_1) \quad (1.13)$$

Squaring equation 1.11 leads to:

$$(S_3 + S_1)^2 = (S^* \cdot S^*) = 2S(S+1) + 2(S_3 \cdot S_1) \quad (1.14)$$

Which can be rearranged to give equation 1.15.

$$2(S_3 \cdot S_1) = (S^* \cdot S^*) - 2S(S+1) \quad (1.15)$$

Equations 1.12 and 1.14 can now be substituted back into equation 1.9 to give:

$$H_{\alpha} = -J(S' \cdot S') - 3S(S+1) - (S^* \cdot S^*) + 2S(S+1) + \alpha\{(S^* \cdot S^*) - 2S(S+1)\} \quad (1.16)$$

Gathering terms leads to equation 1.17, which is a general form of a Hamiltonian suitable for addressing either an equilateral triangle or a linear triad.

$$\begin{aligned} H_{\alpha} &= -J\{(S' \cdot S') - (S^* \cdot S^*) - S(S+1)\} + \alpha\{(S^* \cdot S^*) - 2S(S+1)\} \\ &= -J[(S' \cdot S') - (1 - \alpha)(S^* \cdot S^*) - (1 + 2\alpha)S(S+1)] \end{aligned} \quad (1.17)$$

Note that  $S^* = (S_3 + S_1) \dots |S_3 - S_1|$  in integer steps, therefore  $(S^* \cdot S^*)$  will have  $[S^*(S^*+1)]$  eigenvalues and  $S' = (S^* + S) \dots |S^* - S|$  in integer steps, therefore  $(S' \cdot S')$  will have  $[S'(S'+1)]$  eigenvalues.

Finally, for an equilateral triangle where  $J_{31} = J_{12} = J_{23} = J$ ,  $\therefore \alpha = 1$  the Hamiltonian (1.17) simplifies to:

$$H_{\alpha} = -J[(S' \cdot S') - 3(S(S+1))] \quad (1.18)$$

with energies:

$$E = -J[S'(S'+1) - 3S(S+1)] \quad (1.19)$$

And for a linear triad with a negligible 1-3 interaction  $J_{12} = J_{23} = J; J_{31} \approx 0$ ,  $\therefore \alpha \approx 0$  and the Hamiltonian (1.17) simplifies to:

$$H_{ex} = -J[(S'_1 \cdot S'_1) - (S^* \cdot S^*) - (S(S+1))] \quad (1.20)$$

with energies:

$$E = -J[S'_1(S'_1+1) - S^*(S^*+1) - S(S+1)] \quad (1.21)$$

For either case the energies may now be substituted into the modified Van Vleck expression (equation 1.7) in order to evaluate magnetic susceptibility as a function of temperature. Note that the exchange coupling can be expressed by convention as simply  $J$ , or as in the above example, as  $2J$ . While this can lead to some confusion, especially when comparing exchange couplings from different literature sources,  $J$  has been used exclusively in this thesis, except where otherwise explicitly indicated. A closed-form of the equation can be obtained by manually calculating the spin states and energies and then substituting those into the Van Vleck equation, a different approach can also be used to evaluate this problem. A Turbo Basic v. 1.0© (1987; Borland International, Inc.) routine that evaluates the numerator and denominator of the Van Vleck equation separately for each possible energy state by a series of nested loops, and then sums and recombines these to generate a complete susceptibility profile as a function of temperature, can be employed. Figure 1.10 gives the core of this program for an equilateral triangle expression.  $S$  is an input required from the user, which is then defined to be equal to  $S_1$ ,  $S_2$  and  $S_3$ .

```

Evaluate:
Espin=0: muo# = 0: muu# = 0
J1=J1/1.4388
Sstar = S1 + S2
For SK = Sstar to abs(S1-S2) step -1
  hi=SK+S3: lo = SK-S3
  if lo<0 then lo=-lo
  if hi<lo then swap hi,lo
    For ST = hi to lo step -1
      a = ST*(ST+1)
      d= 1+(2*ST)
      Sp=S*(S+1)
      term1= J1*(a-3*Sp)
      Espin = term1
      Espin = Espin/T
      top# = (a*d)*(e^Espin)
      bot# = d*(e^Espin)
      muo# = muo# +top#
      muu# = muu# +bot#
    Next ST
next SK
chi = muo#/muu#
chi=chi*const*g*g/(3*(T-th))
chi=chi*(1-ro)+TIP+ro*const*g*g*S*(S+1)/(3*T)
J1=J1*1.4388
Return

```

**Figure 1.10:** The core of a Turbo Basic© routine for evaluating susceptibility as a function of temperature for an equilateral triangle.

Some other examples of this method are shown in Appendix 1. A limitation of this approach is that the system must have symmetry appropriate for the determination of correct and unique combinations of spin operators [47].

The use of irreducible tensor operators requires the use of fairly complicated mathematics, however, it results in matrices that are sufficiently small to be dealt with by most personal computers, with short computation times when compared to the matrices

generated by FMD. An additional drawback to this method is that it does not easily allow for the inclusion of zero-field splitting or other such effects [47].

Finally, full matrix diagonalization allows for the convenient calculation of spin states and their associated energies for a large variety of systems. Zero-field splitting and other effects can also be included. The Hamiltonian matrix dimensions, however, increase rapidly with the number of paramagnetic centres. For a system with a large number of unpaired spins the resulting matrix calculation can exceed the capabilities of personal computer systems. Full matrix diagonalization is the method used by the software package MAGMUN4.1 [49] for the calculation of spin states and their associated energies.

MAGMUN4.1 is a powerful Windows© based software package for simulating and fitting magnetic data [49]. It can be used to deal with polynuclear clusters with many different nuclearities and geometries, including three dimensional systems, by way of an output file (\*.spk) containing total spin state values and their energies. This is generated from an input file (OW01.ini) which details the model in question, *via* an executable program (OW01.exe) which utilizes the FMD approach. The first step in generating the input file is to define a magnetic model, normally *via* a schematic, in which the paramagnetic centres are numbered and the exchange pathways identified. Figure 1.11 shows such a model for a general tetranuclear cluster.

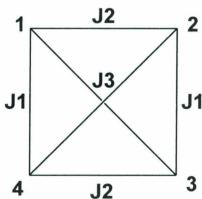


**Figure 1.11:** Magnetic model for an  $M_4$  tetrahedron.

The input file, OW01.ini (Figure 1.12), defines the number of unpaired electrons per paramagnetic centre on the first line, their connectivities on the second line, and the relative strength of the magnetic exchange couplings on the third line. The name of the output file to be generated is given on the fourth line. As an example, it will be assumed that each spin centre is a Cu(II) ion ( $d^9$ , one unpaired electron,  $S = 1/2$ ), though it is not necessary for the cluster to be homometallic. It will also be assumed that there is no cross-coupling exchange ( $J_3 = 0$ ), and that the exchange between each adjacent centre is equal in magnitude and sign ( $J_1 = J_2$ ).

```

Spins: 1 1 1 1      ← four ions, each with one unpaired electron
Couplings: 12 23 34 14  ← definition of adjacent, interacting centres
Strengths: -1 -1 -1 -1  ← couplings equal in sign and magnitude
Output: LND-Cu4

```

**Figure 1.12:** MAGMUN4.1 input file for  $Cu(II)_4$  square model.

The coupling strengths in the above example were assigned as  $-1 \text{ cm}^{-1}$  for mathematical convenience. Once the data are fitted, and the exchange energy,  $J$ , is determined by non linear regression of the data, it is simply multiplied by the coupling

strength as defined in OW01.ini. For a “strength” of  $-1 \text{ cm}^{-1}$ , the actual exchange energy will be a positive multiple of unity for ferromagnetic interactions and a negative multiple of unity for antiferromagnetic interactions.

Once the OW01.ini file is defined and saved, it is used by the executable program OW01.exe to calculate the energies as a function of spin state for the system, eliminating the necessity to derive an exchange equation in order to treat the data. Two output files are generated, with the extensions \*.spk and \*.cig, with the required  $E(S')$  data contained in the \*.spk file. The \*.spk file for the above example of a  $\text{Cu(II)}_4$  square with no cross-coupling exchange is shown in Figure 1.13.

```
MDA 01.00 SPK 00
#PROGRAM:
  Program OW0L, (c) Oliver Waldmann, Version 11.5.01
#HAMILTONIAN:
  Heisenberg Hamiltonian
#SYSTEM:
  Spins = 1/2 1/2 1/2 1/2
  Couplings = 1-2 2-3 3-4 1-4
#PARAMETER:
  Strengths = -1 -1 -1 -1
  Emin = -2
#COMMENT:
  sorted spektrum with classification
#DATA:
0      0      0      ← Magnetic ground state
1      2      0      ← Next lowest lying energy state
2      0      1
2      2      1
2      2      2
3      4      0
```

**Figure 1.13:** \*.spk file for a  $\text{Cu(II)}_4$  square. The first column defines the relative energy while the second column defines  $2S'$ .

Finally, the experimental data, and the \*.spk file can be loaded into MAGMUN4.1, and the data treated by the modified van Vleck equation (equation 1.7). Fitted data can then be exported into a Microsoft Excel© spreadsheet, as columns of “Temperature” and experimental and calculated “ $\chi$ ”, “ $\chi T$ ” and “ $\mu_{mol}$ ”. Appendix 2 contains all the OW01.ini and \*.spk files that were used in this thesis.

The information contained in the \*.spk files can be used in combination with magnetization as a function of field data in order to assess the magnetic ground state of a particular system as well as other related information, such as low lying excited states. For non-zero magnetic ground states, MAGMUN4.1 can be used to model magnetization data using standard Brillouin functions ( $B_S(y)$ ) [50], which describe the dependence of the molar magnetization ( $M$ ) on an external field ( $H$ ) (equations 1.22 - 1.24).

$$M = Ng\beta S B_S(y) \quad (1.22)$$

where

$$B_S(y) = \frac{2S+1}{2S} \coth\left(\frac{2S+1}{2S}y\right) - \frac{1}{2S} \coth\left(\frac{1}{2S}y\right) \quad (1.23)$$

with

$$y = \frac{g\beta SH}{kT} \quad (1.24)$$

When the term  $H/kT$  becomes very large (that is, at high fields and low temperature), the Brillouin function ( $B_S(y)$ ) approaches unity and the magnetization,  $M$ , approaches its saturation value,  $M_s$  (equation 1.25).

$$M_s = Ng\beta S \quad (1.25)$$

Expressing the saturation magnetization in units of  $N\beta$ , means that its value is simply given by  $gS$ . While this holds for a collection of grouped spins in the ground state, when the ground state of a polynuclear system results in isolated residual spins, the  $M_s$  can be calculated from the sum of the individual contributions.

Magnetization profiles can be simulated by MAGMUN4.1 and compared to experimental data loaded from an input with magnetization (in  $N\beta$  units) and field data. Magnetization as a function of field profiles for both grouped and ungrouped ground magnetic spin states, with  $g = 2$  and  $T = 2$  K, are shown in Figure 1.14.

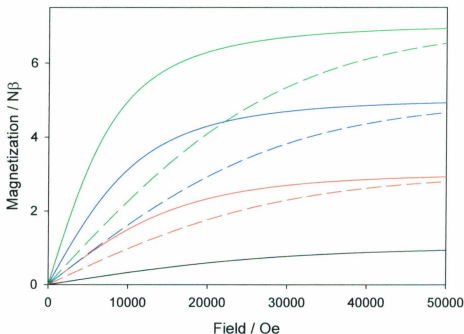


**Figure 1.14:** Magnetization as a function of field for  $g = 2$ ,  $T = 2$  K and  $S = \frac{1}{2}$  (black),  $S = \frac{3}{2}$  (solid red),  $S = 3 \times \frac{1}{2}$  (dashed red),  $S = \frac{5}{2}$  (solid blue),  $S = 5 \times \frac{1}{2}$  (dashed blue),  $S = \frac{7}{2}$  (solid green)  $S = 7 \times \frac{1}{2}$  (dashed green) generated with MAGMUN4.1.

## 1.6: Conclusions:

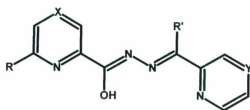
Metallo-supramolecular  $[n \times n]$  arrays synthesized by self-assembly reactions have been introduced and some switchable properties discussed in terms of possible nanotechnological device applications. In the following chapters new classes of  $[n \times n]$   $M_n$  transition metal grid arrays (with  $n = 2, 3$  and  $4$ ) will be presented. These are based on new ditopic imidazole hydrazone, tritopic picolinic dihydrazone and tetratopic pyridazine bis(hydrazone) ligands. Their structures and magnetic properties will be described and discussed in detail.

## Chapter 2: Ligand synthesis and physical measurements

### 2.1: General comments on ligand design and synthesis:

Rigid multidentate ligands suitable for the targeted synthesis of specific  $[n \times n]$  grids upon self-assembly with metal ions are generally synthetically challenging and incorporate a coordination capacity that matches the coordination requirements of a specific metal ion (the metal's "coordination algorithm") [21]. Such ligands have donor groups (oxygen or nitrogen atoms for example) built into the backbone in positions suitable for the formation of stable five- or six-membered chelate rings upon interaction with a metal ion. Many such ligands also have planar conformations due to the presence of delocalized  $\pi$ -systems, and moieties such as pyrimidine, pyridine and pyridazine with examples of self-assembled  $[2 \times 2]$  [51-53],  $[3 \times 3]$  [21],  $[4 \times 4]$  [22,55-57] and  $[5 \times 5]$  [56] grids reported.

Ditopic ligands with one bidentate and one tridentate pocket (Figure 2.1), formed by condensation between an iminoester and a hydrazide, and capable of forming 5-membered chelate rings upon coordination with first-row transition metals, have proven to be suitable for the directed approach to the formation of  $[2 \times 2]$  grids [58-64].



poap: R=H, X=Y=CH, R'=NH<sub>2</sub>;

pzoap: R=H, X=N, Y=CH, R'=NH<sub>2</sub>;

pzoapz: R=H, X=Y=N, R'=NH<sub>2</sub>;

pomp: R=H, X=Y=CH, R'=CH<sub>3</sub>;

poapz: R=H, X=CH, Y=N, R'=NH<sub>2</sub>;

mpoap: R=CH<sub>3</sub>, X=Y=CH, R'=NH<sub>2</sub>

**Figure 2.1:** Examples of ditopic ligands suitable for the formation of [2×2] grids.

Ligands of this type have several rotameric modes, and two can lead to bridging between metal ions through  $\mu$ -O or  $\mu$ -NN connections (Figure. 2.2a and 2.2b). The most common rotamer is the *syn* enolic form, which links two metals through an oxygen bridge (Figure 2.2a).

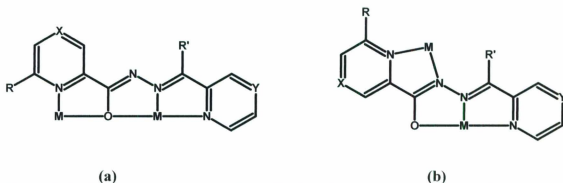
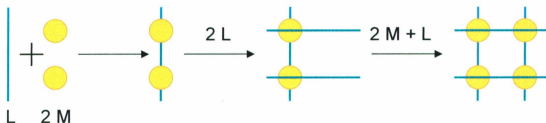


**Figure 2.2:** General representation of possible bonding modes, showing the formation of 5-membered chelate rings. a)  $\mu$ -O bonding mode b)  $\mu$ -NN bonding mode.

In both coordination modes three five-membered chelate rings are formed with metal-ligand bonds that are at approximately right angles, and occupy either *cis*- or *mer*-positions (bidentate or tridentate pocket respectively) of an octahedrally coordinated metal. In mode (a), open coordination sites on the metal positions may then be occupied by two more ligands arranged in a perpendicular fashion which could bind an additional

two metal ions, and finally with a fourth ligand, arranged in a parallel manner to the first, completing the  $[2 \times 2]$  grid (Scheme 2.1).



**Scheme 2.1:** One possible route to  $[2 \times 2]$   $M_4$  grid self-assembly.

Vacant coordination sites for metals incorporated by the bidentate pockets of two perpendicular ligands can be occupied by solvent molecules or anions. In cases, however, where co-ligand competition is limited or eliminated, homoleptic trigonal-bipyramidal clusters of five six-coordinate metal centres and six ligands, with six  $\mu$ -O hydrazone bridges linking the metal ions can also result [61,62,64,65]. Both  $[2 \times 2]$  grids and trigonal-bipyramidal clusters are discussed in Chapter 3.

The same design principles can be employed for the synthesis of tritopic ligands (Figure 2.3) suitable for the formation of  $[3 \times 3]$   $M_9$  ( $M = \text{Mn, Fe, Ni, Cu, Zn}$ ) grids [29,30,66-74]. In their *syn-enolic* conformation, ligands in this class have the potential to create three adjoining, oxygen-bridged meridional pockets that could accommodate a maximum of three six-coordinate metal ions in an approximately linear manner.

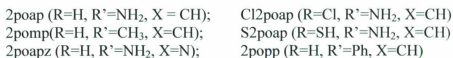
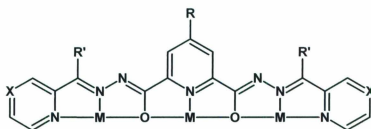
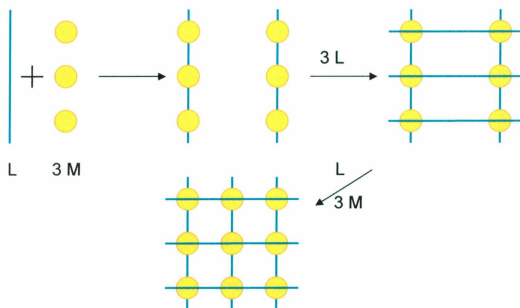


**Figure 2.3:** Examples of tritopic ligands showing metal coordination, leading to the formation of  $[3 \times 3]$  grids.

The open coordination sites on each metal centre in such an arrangement can be occupied by another three ligands, also in their *syn-enolic* rotomer, but arranged in a perpendicular manner to the first ligand. Homoleptic, self-assembled  $[3 \times 3]$  grids finally result from the exact balance of the available number of donor sites provided by the six ligands arranged with three parallel ligands above and below the plane of the nine pseudo-octahedral metal ions (Scheme 2.2).



**Scheme 2.2:** One possible route to  $[3 \times 3] M_9$  grid self-assembly [75].

$[3 \times 3] M_9$  grids exhibit rich electrochemical behaviour [28-30,73,], and mixed-metal systems have also been reported [28]. Work in this thesis reports  $[3 \times 3] M_9$  ( $M = \text{Mn, Co, Cu, Zn}$ ) grids (Chapter 4) and mixed metal systems (Chapter 5) with a new ligand in this class.

The square, essentially flat molecular footprints of the  $[3 \times 3]$  grids, suggests that they could be organized into 2D extended structural motifs. Soft-donor atoms (for example, chlorine and sulfur) have been incorporated into the central pyridine ring of ligands in this class (Figure 2.3) leading to the assembly of grids on gold and graphite surfaces [28,73,76]. Another technique for assembling grids into organized 2D arrays is to enhance the aromatic character of the ligand end-pieces, by incorporating quinoline-type moieties, in order to capitalize upon possible extended  $\pi$ -interactions [77]. This has been achieved and is discussed in Chapter 6.

While altering the ligand end-pieces may result in extended grid interactions, changing the nature of the central aromatic moiety (Figure 2.3; pyridine and substituted derivatives) can result in increased grid nuclearity. For example, pyrazoles and pyridazines are effective dinucleating bridging groups, and so replacing the central ring of ligands capable of forming  $[3 \times 3]$  grids with pyrazole-3,5-dicarbohydrazone [56] or pyridazine-3,6-dicarbohydrazone subunits [55-57] will produce ligands with a potentially tetrapotic capacity (Figure 2.4a and 2.5). A potential problem arises in the pyrazole-based cases, however, in that the large internal angle subtended by the pyrazole-NN metal-ligand bonds could introduce a great deal of strain into any possible  $[4 \times 4]$  systems and so instead an alternate *syn* ligand conformation with the hydrazone oxygen atoms in a non-coordinating ketonic form (Figure 2.4b) is also considered a possibility [56]. Results with a pyrazole-based ligand are further discussed in Chapter 8.

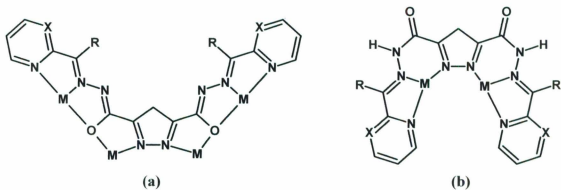


**Figure 2.4:** a) *Syn* enolic rotameric form of a tetrapotic diethyl 3,5-pyrazoledicarbohydrazone ligand; b) and with the hydrazone oxygen atoms in a non-coordinating ketonic form.

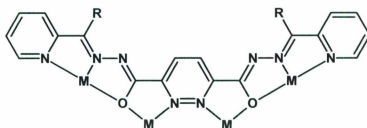


**Figure 2.5:** *Syn-enolic* rotameric representations of pyridazine based ligands; R = H or R = NH<sub>2</sub>.

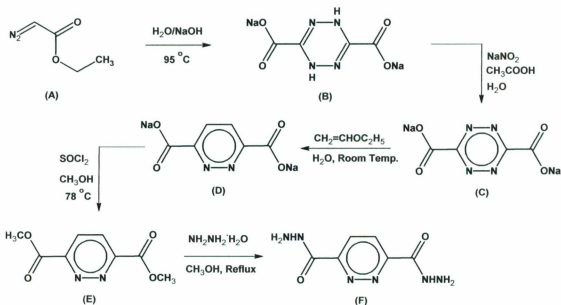
Self-assembled pyridazine-based [4×4] grids with these ligands have been synthesized and have sixteen six-coordinate metal ions held in a grid framework of eight ligands arranged in two roughly parallel groups of four above and below the metal core with adventitious single atom oxygen bridges incorporated from the solvent environment completing vacant sites in the octahedral coordination spheres of the central metals [55-57]. Chapter 7 and 8 report M<sub>16</sub> (M = Mn, Co, Cu) grids with similar [4×4] topologies and from ligands with end-pieces capable of extended  $\pi$ -type interactions.

## 2.2: Methodology:

### 2.2.1: Synthesis of a tetratopic ligand precursor - pyridazine-3,6-dicarbohydrazide

A suitable 3,6-substituted pyridazine precursor for the synthesis of tetratopic ligands is not commercially available, and is instead synthesized in five steps starting from ethyl diazoacetate. The synthesis of the tetratopic ligand precursors is summarized in Scheme 2.3. Briefly, ethyl diazoacetate (**A**) was added dropwise to a hot, concentrated solution of aqueous sodium hydroxide followed by treatment in ethanol to yield sodium dihydrotetrazine-3,6-dicarboxylate (**B**) as a brown solid, which was then slurried in water

with sodium nitrite and kept below 0 °C during the addition of glacial acetic acid. The resulting bright orange slurry was treated with excess methanol to yield sodium s-tetrazine-3,6-dicarboxylate (C) that was then converted to sodium pyridazine-3,6-dicarboxylic acid salt by reaction with ethyl vinyl ether in water at room temperature. The pyridazine acid salt (D) was then converted to the methylester (E) upon treatment in methanol at -78 °C with thionyl chloride. Finally, the dimethyl pyridazine-3,6-dicarboxylate (E) was refluxed in methanol with hydrazine hydrate to produce the required pyridazine-3,6-dicarbohydrazide (F). These precursors are known compounds [78,79], and literature methods were followed, giving comparable yields and purity, therefore the complete procedure for this synthesis is not discussed.



**Scheme 2.3:** Synthesis of the pyridazine-based tetratopic ligand precursor.

## **2.3: Experimental:**

### **2.3.1: Materials:**

Commercially available solvents and chemicals were used without further purification. Perchlorate and azide salts and complexes are potentially explosive and were used and prepared in small quantities, taking appropriate precautions.

### **2.3.2: Physical measurements:**

#### **2.3.2.1: Spectroscopy:**

Infrared spectra were recorded as Nujol mulls between NaCl plates using a Matteson Polaris FT-IR instrument. Solution NMR spectra were obtained with a Bruker AVANCE 500 MHz spectrometer. Solvents used are quoted in the appropriate experimental section. NMR spectra were processed with MestReNova software. UV-Vis-NIR measurements were obtained using a Cary 5E dual beam spectrophotometer in solution in matched quartz cuvettes. The solvents used are quoted in the appropriate experimental section.

#### **2.3.2.2: Mass Spectrometry:**

LCMS measurements were taken on an Agilent 1100 Series LC/MSD in atmospheric pressure chemical ionization positive (APCI+) mode with methanol-acetonitrile mixtures as the solvent.

#### **2.3.2.3: Elemental Analyses:**

Microanalyses were carried out by Canadian Microanalytical service, Delta, B.C., Canada. It should be noted that fluoride and boron have been known to cause

interference in carbon analysis, through the formation of thermostable carbides [80]. This appears to have been a particular problem with some of the results in Chapter 7.

#### **2.3.2.4: Magnetic measurements:**

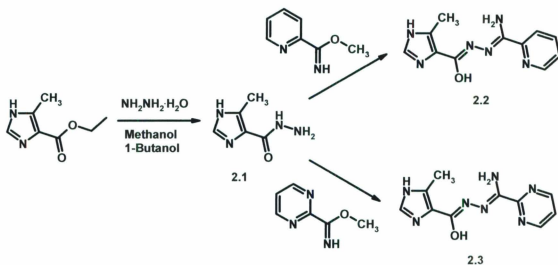
Variable temperature magnetic data were collected with a Quantum Design MPMS5S SQUID magnetometer using field strengths of 1000 Oe for variable temperature experiments, and field strengths in the range 0.1-5 T for magnetization experiments. Background corrections for the sample holder assembly and diamagnetic components of the complexes were applied.

#### **2.3.2.5: Crystallography:**

Data were collected using an AFC8-Saturn 70 single crystal X-ray diffractometer from Rigaku/MSU, equipped with an X-stream 2000 low temperature system, and Crystalclear software for data collection and processing. Further details of the data collection and refinement are located in the experimental section of the appropriate chapters, and Appendix 3.

#### **2.3.3: Synthesis of ligands:**

The syntheses of **2.1 - 2.3** are summarized in Scheme 2.4.



**Scheme 2.4:** Synthesis of ioap (2.2) and ioapm (2.3).

**2.3.3.1:** 5-methyl-1H-imidazole-4-carbohydrazide (2.1). 5-methyl-1H-imidazole-4-carbohydrazide (2.1) was generated by the dropwise addition of hydrazine hydrate (85%) (2.34 g, 46.7 mmol) to a stirred solution of ethyl 4-methyl-5-imidazole carboxylate (3.39 g, 22.0 mmol) in 60 mL of 1-butanol and 25 mL of methanol. The resulting clear, yellow solution was refluxed for 72 hours. Upon cooling a white precipitate formed, which was collected by suction filtration and washed three times with 10 mL of diethyl ether (2.59 g; 84% yield). IR ( $\nu/\text{cm}^{-1}$ ): 3162 ( $\nu\text{NH}$ ), 1627, 1589 ( $\nu\text{CN}$ ,  $\nu\text{CO}$ ).

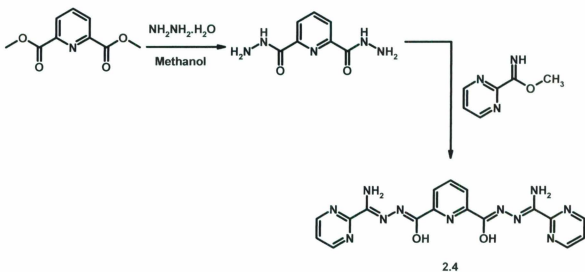
**2.3.3.2:** ioap (2.2). Methyl pyridine-2-carboximidate was generated *in situ* by dissolving 2-pyridinecarbonitrile (2.73 g, 26.2 mmol) in methanol (100 mL) with sodium metal (0.10 g, 4.4 mmol). The flask containing the resulting clear colourless solution was capped with a drying tube and the solution was stirred at room temperature for 8 hours. Acetic acid was then added until a neutral pH was achieved. 5-methyl-1H-imidazole-4-carbohydrazide (2.59 g, 18.5 mmol) was added to the stirred solution of methyl pyridine-

2-carboximidoate, which formed a clear yellow solution that was heated at reflux for 24 hours to give a clear, brown solution. The total volume was reduced to 20 mL under reduced pressure and 50 mL of diethyl ether was added to give a yellow slurry that was stirred for 30 minutes. A yellow powder (**2.2**) was collected by suction filtration, washed three times with 10 mL of diethyl ether, and vacuum dried (quantitative yield). Mp 226-228 °C. *m/z* (APCI-MS<sup>+</sup>): 245.1 (M<sup>+</sup>. C<sub>11</sub>H<sub>12</sub>N<sub>6</sub>O requires 244.3), IR (ν/cm<sup>-1</sup>): 3205 (νNH), 1635, 1519 (νCN, νCO). δ<sub>H</sub>(500 MHz; DMSO-d<sub>6</sub>) 1.78 (3 H, s, CH<sub>3</sub>), 3.34 (1 H, s, OH), 6.79 (2H, s, NH<sub>2</sub>), 7.45 (1H, dd (J=5.43 Hz, 6.84 Hz), Ph), 7.61 (1H, d (J=15.07 Hz), Py), 8.00 (2H, m, Py), 8.62 (1H, t (J=30.84 Hz), Im), 9.94 (1H, s, NH). Anal. Calcd (%) for C<sub>11</sub>H<sub>12</sub>N<sub>6</sub>O·1.2CH<sub>3</sub>OH·0.8H<sub>2</sub>O: C, 49.32 H, 6.24 N, 28.29. Found: C, 49.30; H, 4.95; N, 28.21.

**2.3.3.3: ioapm (2.3).** Methyl pyrimidine-2-carboximidoate was generated *in situ* by dissolving 2-pyrimidinecarbonitrile (2.35 g, 22.4 mmol) in methanol (100 mL) with sodium metal (0.10 g, 4.4 mmol). The flask containing the resulting clear colourless solution was capped with a drying tube and the solution was stirred at room temperature for 8 hours. Acetic acid was then added until a neutral pH was achieved. 5-methyl-1*H*-imidazole-4-carbohydrazide (2.10 g, 15 mmol) was added to the stirred solution of methyl pyrimidine-2-carboximidoate, which formed a clear yellow solution. A yellow precipitate formed upon stirring for 5 min. Methanol was added until a total volume of 250 mL was achieved, and the solution was heated at reflux for 16 hours. Upon heating, the precipitate dissolved. The refluxed solution was cooled to room temperature and remained clear and yellow. The volume was reduced under reduced pressure to 20 mL,

and 100 mL of diethyl ether was added. A yellow precipitate (**2.3**) formed, which was collected by suction filtration, washed twice with 10 mL of methanol, twice with 10 mL of diethyl ether, and vacuum dried (yield 3.4 g, 93 %). Mp 222-225 °C. *m/z* (APCI-MS<sup>+</sup>): 246.1 (*M*<sup>+</sup>). C<sub>10</sub>H<sub>11</sub>N<sub>7</sub>O requires 245.2, IR (ν/cm<sup>-1</sup>): 3332 (νNH), 1654, 1562 (νCN, νCO), 952 (vpym). Anal. Calcd (%) for C<sub>10</sub>H<sub>11</sub>N<sub>7</sub>O·1.5CH<sub>3</sub>OH·1.2H<sub>2</sub>O: C, 43.86 H, 6.17 N, 31.15. Found: C, 43.86; H, 4.80; N, 31.31.

The synthesis of 2pmoap (**2.4**) is summarized in Scheme 2.5.

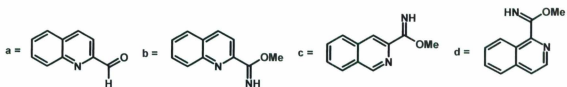
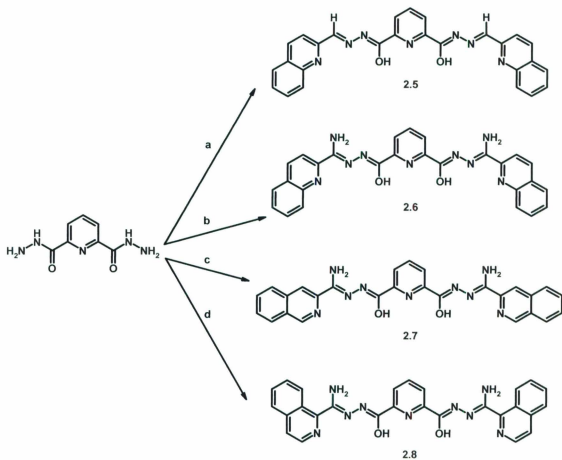


**Scheme 2.5:** Synthesis of 2pmoap (**2.4**).

**2.3.3.4:** 2pmoap (**2.4**). Dimethyl-2,6-pyridinedicarboxylate (10.07 g, 51.60 mmol) was converted to the dihydrazide by reaction with hydrazine hydrate (85%) (2.60 g, 51.9 mmol) in methanol (yield 40 %). Methyl pyrimidine-2-carboximidate was generated *in situ* by dissolving 2-pyrimidinecarbonitrile (1.82 g, 17.3 mmol) in methanol (150 mL) with sodium metal (0.15 g, 6.5 mmol) in a round bottom flask, resulting in a clear

colourless solution. The flask was capped with a drying tube and the solution stirred at room temperature for 8 hours. The solution was then neutralized using acetic acid, and pyridine-2,6-dicarbohydrazide (1.52 g, 7.79 mmol) was added giving a yellow mixture, which was refluxed for 24 hours. A yellow solid was obtained, which was filtered off, washed with methanol and diethyl ether and dried under vacuum. Yield (2.08 g, 66 %).  $m/z$  (APCI-MS<sup>+</sup>): 406 ( $M^+$ .  $C_{17}H_{15}O_2N_{11}$  requires 405.4), IR ( $\nu/cm^{-1}$ ): 3413, 3332, 3181 ( $\nu NH$ ); 1685, 1612 ( $\nu C=O$ ); 1558, 1519 ( $\nu C=N$ ). Anal. Calcd (%) for  $C_{17}H_{15}O_2N_{11} \cdot 2.25CH_3OH$ : C, 48.42; H, 5.06; N, 32.27. Found: C, 48.97; H, 3.71; N 32.27.

The syntheses of ligands **2.5-2.8** are summarized in Scheme 2.6.



**Scheme 2.6:** Syntheses of quinoline-type ligands.

2.3,3.5: 2po56hq (**2.5**). 2-Quinolinecarboxaldehyde (2.05 g, 13.0 mmol) was added to a slurry of pyridine-2,6-dicarbohydrazide (1.29 g, 6.61 mmol) in 300 mL of methanol. The resulting mixture was heated at reflux for 18 hours to produce a yellow powder, which was filtered off and washed with diethyl ether to give 2.32 g (4.90 mmol, 75 % yield) of

**2.5.** This ligand was used without further purification. Mp: 230-232 °C. *m/z* (APCI-MS+): 474 ( $M^+$ .  $C_{27}H_{19}N_7O_2$  requires 473.5). IR ( $\nu/cm^{-1}$ ): 1670 ( $\nu C=O$ ); 1554 ( $\nu C=N$ ).  $\delta_H$ (500 MHz; DMSO- $d_6$ ) 12.61 (2H, s, OH), 9.06 (1H, s, Ar), 8.86 (1H, s, Ar), 8.43 (5H, m, Ar), 7.16 (6H, m, Ar), 7.86 (2H, t ( $J = 7.42$  Hz), Ar), 7.70 (2H, t ( $J = 7.41$  Hz), CH). Anal. Calcd (%) for  $C_{27}H_{19}N_7O_2 \cdot 3H_2O$  (bulk sample): C, 61.47; H, 4.78; N, 18.59. Found: C, 61.05; H, 3.85; N, 19.30.

**2.3.3.6: 2po56nq (2.6).** Methyl quinoline-2-carboximidoate was generated *in situ* by reaction of 2-quinolinecarbonitrile (1.00 g, 6.49 mmol) for 24 hours at room temperature with a solution of sodium methoxide, produced by dissolving sodium metal (0.05 g, 2.17 mmol) in methanol (50 mL). The pH was then adjusted to 7 by addition of glacial acetic acid and pyridine-2,6-dicarbohydrazide (0.62 g, 3.18 mmol) was added. This produced a light yellow slurry that was refluxed for 24 hours, then filtered and washed with diethyl ether (3 x 15 mL) to yield a yellow powder which was used without further purification. Yield (1.49 g, 92.2 %). Mp 259-260 °C. *m/z* (APCI-MS+): 504.1 ( $M^+$ .  $C_{27}H_{21}N_9O_2$  requires 503.5). IR ( $\nu/cm^{-1}$ ): (Nujol): 3406, 3333 ( $\nu NH$ ); 1693, 1605, 1584, 1569 ( $\nu C=O, \nu C=N$ ).  $\delta_H$ (500 MHz; DMSO- $d_6$ ) 11.18 (2H, s, OH), 8.26 (8H, m, Ar), 7.84 (2H, m, Ar), 7.68 (2H, m, Ar), 7.24 (3H, s, Ar). Anal. Calcd (%) for  $C_{27}H_{21}N_9O_2 \cdot 0.25H_2O$ : C, 63.83; H, 4.27; N, 24.81. Found: C, 63.74; H, 4.33; N 24.91.

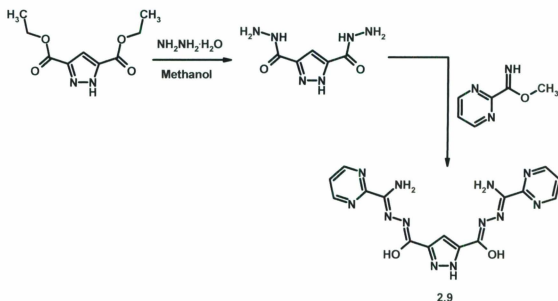
**2.3.3.7: 2po45nq (2.7).** Methyl isoquinoline-3-carboximidoate was generated *in situ* by reaction of 3-isoquinolinecarbonitrile (0.65 g, 4.21 mmol) with a solution of sodium methoxide, produced by dissolving sodium metal (0.10g, 4.35 mmol) in methanol (75 mL). Pyridine-2,6-dicarbohydrazide (0.41 g, 2.10 mmol) was added to the above

solution, followed by an additional 25 mL of methanol and adjustment of pH to 7 by dropwise addition of glacial acetic acid. The resulting white slurry was heated at reflux for 18 hours. This produced a yellow slurry that was filtered and washed with diethyl ether (3 x 15 mL) to yield a yellow powder (**2.7**) which was used without further purification. Yield (0.80 g, 75 %). Mp 267-268 °C. *m/z* (APCI-MS<sup>+</sup>): 504.2 (M<sup>+</sup>. C<sub>27</sub>H<sub>21</sub>N<sub>9</sub>O<sub>2</sub> requires 503.5). IR (ν/cm<sup>-1</sup>): 3417, 3305, 3170 (νNH); 1635, 1581 (νC=O); 1538 (νC=N). δ<sub>H</sub>(500 MHz; DMSO-d<sub>6</sub>) 11.14 (2H, s, OH), 9.53 (1H, s, Ar), 9.32 (1H, s, Ar), 8.72 (1H, s, Ar), 8.23 (6H, m, Ar), 7.81 (3H, m, Ar), 7.2 (3H, m, Ar). Anal. Calcd (%) for C<sub>27</sub>H<sub>21</sub>N<sub>9</sub>O<sub>2</sub>·0.25H<sub>2</sub>O: C, 63.83; H, 4.27; N, 24.81. Found: C, 63.84; H, 4.55; N 24.63.

**2.3.3.8: 2po34nq (2.8).** Methyl isoquinoline-1-carboximidoate was generated *in situ* by reaction of 1-isoquinolinecarbonitrile (0.66 g, 4.28 mmol) for 24 hours at room temperature with a solution of sodium methoxide, produced by dissolving sodium metal (0.10 g, 4.35 mmol) in methanol (75 mL). The pH was then adjusted to 7 by addition of glacial acetic acid and pyridine-2,6-dicarbohydrazide (0.62 g, 3.18 mmol) was added with an additional 25 mL of methanol. This produced a white slurry that turned yellow upon refluxing for 24 hours. The yellow slurry was then filtered and washed with diethyl ether (3 x 15 mL) to yield a yellow powder (**2.8**) that was used without further purification. Yield (0.24 g, 22 %). Mp 277-280 °C. *m/z* (APCI-MS<sup>+</sup>): 504.2 (M<sup>+</sup>. C<sub>27</sub>H<sub>21</sub>N<sub>9</sub>O<sub>2</sub> requires 503.5), 196.0 (C<sub>7</sub>H<sub>9</sub>O<sub>2</sub>N<sub>5</sub> (pyridine-2,6-dicarbohydrazide) requires 195.2). IR (ν/cm<sup>-1</sup>): 3436, 3270 (νNH); 1689, 1635 (νC=O); 1515 (νC=N). Elem. Found: C, 48.99; H, 4.43; N 34.35. An accurate match between the calculated and found

elemental analysis could not be achieved and is likely the result of contamination by the starting material pyridine-2,6-dicarbohydrazide, as indicated by the mass spectral result.

The synthesis of 2pyoapm (**2.9**) is summarized in Scheme 2.7.

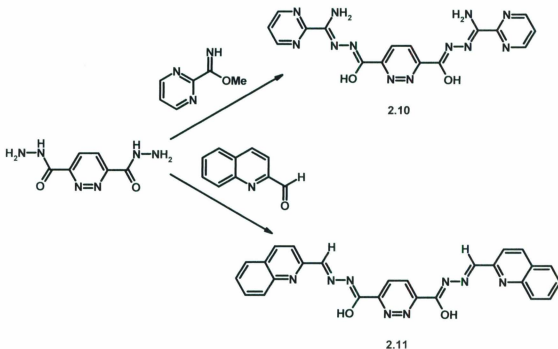


**Scheme 2.7:** Summary of the synthesis of 2pyoapm (**2.9**).

**2.3.3.9: 2pyoapm (2.9).** Hydrazine hydrate (1.06 g, 21.2 mmol) was added to a solution of diethyl 3,5-pyrazoledicarboxylate (1.97 g, 9.28 mmol) in 175 mL of methanol, and the resulting clear, colorless solution was refluxed for 48 hours to produce a white slurry. The resulting white powder (1.54 g, 8.36 mmol), 1H-pyrazole-3,5-dicarbohydrazide, was collected by suction filtration, washed three times with diethyl ether, and added to a neutral solution of methyl pyrimidine-2-carboximidate, produced by the action of sodium in methanol on 1.76 g (16.7 mmol) of 2-cyanopyrimidine in 200 mL of methanol. A white slurry formed, and the mixture was refluxed for 24 h resulting in the formation of a yellow solid. **2.9** (3.29 g, 8.34 mmol, 82% yield overall) was collected by suction

filtration and washed three times with diethyl ether. Mp: >360 °C. *m/z* (APCI-MS+): 391.4 ( $M^+ - 4H$ .  $C_{15}H_{14}N_{12}O_2$  requires 394.3513). IR ( $\nu/cm^{-1}$ ): 3313 ( $\nu NH$ ); 1701 ( $\nu C=O$ ); 1631, 1566 ( $\nu C=N$ ). Anal. Calcd (%) for  $C_{15}H_{14}N_{12}O_2 \cdot 0.5H_2O$  (bulk sample): C, 44.67; H, 3.72; N, 41.69. Found: C, 44.83; H, 3.43; N, 41.95.

The synthesis of 2pdoapm (**2.10**) and 2pdo56hq (**2.11**) are summarized in Scheme 2.8.



**Scheme 2.8:** Summary of the synthesis of 2pdoapm (**2.10**) and 2pdo56hq (**2.11**).

**2.3.3.10:** 2pdoapm (**2.10**). Methyl pyrimidine-2-carboximidate was generated *in situ* by reaction of 2-cyanopyrimidine (0.73 g, 6.96 mmol) with a solution of sodium methoxide, produced by dissolving sodium metal (0.10 g, 4.35 mmol) in methanol (100 mL). Pyridazine-3,6-dicarbohydrazide (0.68 g, 3.45 mmol; prepared from the reaction of

pyridazine-3,6-dicarboxylate[77, 78] with hydrazine hydrate in methanol) was added to the above solution and the pH was adjusted to 7 by dropwise addition of glacial acetic acid. The mixture was refluxed for 18 hours. The resulting yellow slurry was filtered and washed with diethyl ether (3 x 15 mL) to yield a yellow powder, which was used without further purification. Yield (1.24 g, 88%). M.p. >330 °C. *m/z* (APCI-MS+): 391.4 ( $M^+$ -NH<sub>2</sub>. C<sub>16</sub>H<sub>12</sub>N<sub>11</sub>O<sub>2</sub> requires 390.3394), 302.1, 284.1, 149.1. IR (ν/cm<sup>-1</sup>): 3309, 3197 (νNH); 1646 (νC=O); 1600 (νC=N). Anal. Calcd (%) for C<sub>16</sub>H<sub>14</sub>N<sub>12</sub>O<sub>2</sub>·0.5H<sub>2</sub>O (bulk sample): C, 46.27; H, 3.64; N, 40.47. Found: C, 46.44; H, 3.41; N, 40.72.

**2.2.2.11: 2pdo56hq (2.11).** 2-quinolinecarboxaldehyde (1.30 g, 8.27 mmol) was added to a slurry of pyridazine-3,6-dicarbohydrazide (0.78 g, 3.98 mmol; prepared from the reaction of pyridazine-3,6-dicarboxylate [77,78] with hydrazine hydrate in methanol) in 200 mL of methanol, producing a bright yellow slurry that was refluxed for 24 hours. It was then filtered and washed with diethyl ether (3 x 15 mL) to give a beige powder that was used without further purification. Yield (1.78 g, 89.5 %). M.p. 266-267 °C. *m/z* (APCI-MS+): 475.2 ( $M^+$ . C<sub>26</sub>H<sub>18</sub>N<sub>8</sub>O<sub>2</sub> requires 474.5). IR (ν/cm<sup>-1</sup>): 1685 (νC=O). δ<sub>H</sub>(500 MHz; DMSO-d<sub>6</sub>) 13.08 (2H, s, OH), 9.02 (1H, s, Ar), 8.86 (1H, s, Ar), 8.30 (10H, m, Ar), 7.83 (2H, m, Ar), 7.67 (2H, m, CH). Anal. Calcd (%) for C<sub>26</sub>H<sub>18</sub>N<sub>8</sub>O<sub>2</sub>·1.4H<sub>2</sub>O (bulk sample): C, 62.49; H, 4.20; N, 22.42. Found: C, 62.57; H, 4.19; N, 22.42.

#### 2.4: Summary:

The ligands **2.2-2.11** were successfully synthesized. Trinuclear,  $[2 \times 2]$   $M_4$  grid and trigonal-bipyramidal clusters formed by self-assembly reactions with **2.2** and **2.3** are discussed in Chapter 3. Homometallic and heterometallic  $[3 \times 3]$   $M_9$  grid complexes with **2.4** are discussed in Chapter 4 and Chapter 5 respectively.  $[3 \times 3]$   $M_9$  grids with ligands **2.6-2.8**, and a unique  $3 \times [1 \times 3]$   $Mn(II)_9$  rectangle with **2.5** are discussed in Chapter 6. Chapter 7 reports  $[4 \times 4]$   $M_{16}$  ( $M = Mn(II), Co(II),$  and  $Co(II)/Co(III)$ ) grids with **2.10** and **2.11**. Finally, Chapter 8 discusses the synthetic outcomes of reactions between the tetratopic ligands **2.9** and **2.10** with copper(II) salts.

**Chapter 3: Complete and 'Incomplete' [2×2] grids and pentanuclear clusters by self-assembly with sterically hindered ditopic imidazole hydrazone ligands**

**3.1: Preamble:**

The synthetic outcomes of self-assembly reactions are highly dynamic, with metal-ligand interactions influenced by such factors as crystal field effects, metal ion radius, the organizing power of the ligand based on its donor pocket complement and pocket disposition, and the metal ion's preferred coordination number and geometry.

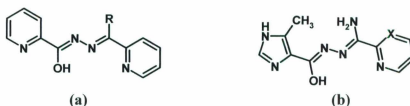


**Figure 3.1:** a) poap (R = NH<sub>2</sub>), pomp (R = CH<sub>3</sub>); b) ioap (**2.1**; X = CH), ioapm (**2.2**; X = N).

Consider the complex synthetic outcomes observed for reactions with the ditopic ligands poap and pomp (Figure 3.1a). Both ligands are suitable for the formation of [2×2] grids, and numerous examples of Mn(II)<sub>4</sub> [64], Co(II)<sub>2</sub>Co(III)<sub>2</sub> [59], Ni(II)<sub>4</sub> [59], Cu(II)<sub>4</sub> [59,62,63], and Zn(II)<sub>4</sub> [61] complexes have been reported. However, other clusters of both lesser and greater metal nuclearity are possible, and have been observed. In a reaction between poap and CuBr<sub>2</sub>, a bromide ion and a water molecule acted as coordinating ligands and inhibited the formation of a [2×2] grid, instead producing a dinuclear M<sub>2</sub>L complex [63]. Trigonal bipyramidal M<sub>5</sub> (M = Mn, Co, Zn) clusters [61, 64, 65] have also been observed, resulting from the exact balance between the complement of six ditopic ligand donor sites and the coordination requirements of five

octahedral metal centres, when solvent and anion competition for metal coordination sites was minimized.

The formation of five-membered chelate rings (Figure 3.2a) upon coordination promotes the formation of a roughly linear M-O-M coordination fragment and the close proximity of the metal ions leads to spin exchange coupling within the grids, with anti-ferromagnetic and ferromagnetic examples.

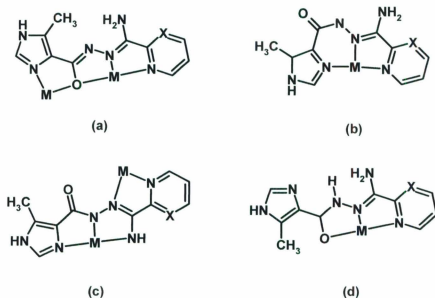


**Figure 3.2:** Various ligand conformations; a) dinucleating, hydrazone-bridged; b) mononucleating; c) dinucleating, diazine-bridged; d) mononucleating, imidazole-twisted.

Herein, the results of the self-assembly reactions between two new sterically hindered ditopic imidazole hydrozone ligands, ioap (**2.1**) and ioamp (**2.2**) (Figure 3.1b), and Mn(II), Co(II), Ni(II) and Cu(II) are reported. Ligands of this nature are capable of a variety of different coordination modes (Figure 3.2), and in addition to other effects that

have been previously observed to influence product nuclearity, the presence of the methyl imidazole moiety leads to steric interference in the assembly of high nuclearity clusters in some cases.

### 3.2: Experimental:

**Note:** In some cases there is a difference between the most reasonable formula based on the elemental analysis (analytical formula), and that obtained from X-ray crystallography. The analytical formulae will be used here.

#### 3.2.1: Complex synthesis:

**3.2.1.1:** [(ioap-H)(ioap-2H)Co<sub>2</sub>(H<sub>2</sub>O)<sub>4</sub>](BF<sub>4</sub>)<sub>2</sub>·9H<sub>2</sub>O (**3.1**). ioap (0.12 g, 0.40 mmol) was added to a solution of Co(BF<sub>4</sub>)<sub>2</sub>·6H<sub>2</sub>O (0.34 g, 1.0 mmol) in methanol:acetonitrile (7.5 mL : 7.5 mL) forming a clear light brown solution that was stirred with gentle heating (55 °C) for 2 hours and kept after filtration for slow evaporation. Air was not excluded. X-ray quality, dark brown, prismatic crystals were collected after 36 days (0.050 g, 25 % yield). Anal. calcd (%) for [(C<sub>11</sub>H<sub>11</sub>ON<sub>6</sub>)(C<sub>11</sub>H<sub>10</sub>ON<sub>6</sub>)Co<sub>2</sub>(H<sub>2</sub>O)<sub>4</sub>](BF<sub>4</sub>)<sub>2</sub>(H<sub>2</sub>O)<sub>9</sub>: C, 26.13; H, 4.69; N, 16.62. Found (%): C, 26.35; H, 3.16; N, 16.53.

**3.2.1.2:** [(ioap)<sub>2</sub>(ioap-H)<sub>2</sub>Mn<sub>3</sub>(H<sub>2</sub>O)<sub>2</sub>](NO<sub>3</sub>)<sub>4</sub>·5H<sub>2</sub>O (**3.2**). ioap (0.10 g, 0.34 mmol) was added to a solution of Mn(NO<sub>3</sub>)<sub>2</sub>·6H<sub>2</sub>O (0.13 g, 0.45 mmol) in methanol:acetonitrile (10 mL : 10 mL) forming initially a clear yellow-orange solution that was stirred for 30 minutes and kept after filtration for slow evaporation (10 days) followed by recrystallization from methanol. X-ray quality, orange, prismatic crystals were collected after eight days (0.040 g, 31% yield). Anal. calcd (%) for [(C<sub>11</sub>H<sub>12</sub>ON<sub>6</sub>)<sub>2</sub>(C<sub>11</sub>H<sub>11</sub>ON<sub>6</sub>)<sub>2</sub>Mn<sub>3</sub>](NO<sub>3</sub>)<sub>4</sub>(H<sub>2</sub>O)<sub>7</sub>: C, 34.91; H, 3.99; N, 25.90. Found (%): C, 34.68; H, 3.79; N, 25.98.

**3.2.1.3:** [(ioap-H)<sub>4</sub>Ni<sub>4</sub>(CF<sub>3</sub>SO<sub>3</sub>)(H<sub>2</sub>O)<sub>3</sub>](CF<sub>3</sub>SO<sub>3</sub>)<sub>2</sub>(PF<sub>6</sub>)<sub>2</sub>·3H<sub>2</sub>O·CH<sub>3</sub>OH (**3.3**). ioap (0.13 g, 0.44 mmol) was dissolved in methanol:acetonitrile (10 mL:10 mL) forming a clear yellow solution to which a solution of Ni(CF<sub>3</sub>SO<sub>3</sub>)<sub>2</sub> (0.040 g; 0.11 mmol) in 2.5 mL of MeOH was added. To the resulting clear green solution was added 20 drops (1 mL) of 1.17 mol/L (1.17 mmol) NaOH(aq) producing a dark brown solution with a neutral pH. This was stirred with gentle heating (55 °C) for 1.5 hours, at which time NH<sub>4</sub>PF<sub>6</sub> (0.08 g; 0.5 mmol) was added. Stirring at room temperature was continued for a further 1.5 hours and the solution was kept after filtration for slow evaporation. X-ray quality, brown, prismatic crystals were collected after 13 days (0.10 g, 46% yield). Anal. calcd (%) for (C<sub>11</sub>H<sub>11</sub>N<sub>6</sub>O)<sub>4</sub>Ni<sub>4</sub>(CF<sub>3</sub>SO<sub>3</sub>)<sub>3</sub>(PF<sub>6</sub>)(H<sub>2</sub>O)<sub>6</sub>(CH<sub>3</sub>OH): C, 29.72; H, 3.12; N, 17.34. Found (%): C, 29.72; H, 2.56; N, 17.13.

**3.2.1.4:** [(ioap-H)<sub>4</sub>Cu<sub>4</sub>](NO<sub>3</sub>)<sub>4</sub>·1.25H<sub>2</sub>O (**3.4**). ioap (0.12 g, 0.40 mmol) was added to a solution of Cu(NO<sub>3</sub>)<sub>2</sub>·3H<sub>2</sub>O (0.14 g, 0.58 mmol) in methanol:acetonitrile (7 mL : 7 mL) forming a clear dark green solution to which was added 4 drops (0.5 mL) of triethylamine. This was stirred with gentle heating (55 °C) for 1.5 hours and the solution was kept after filtration for slow evaporation. X-ray quality, brown, prismatic crystals were collected after 5 days (0.050 g, 33 % yield). Anal. calcd (%) for [(C<sub>11</sub>H<sub>11</sub>O<sub>1</sub>N<sub>6</sub>)<sub>4</sub>Cu<sub>4</sub>](NO<sub>3</sub>)<sub>4</sub>(H<sub>2</sub>O)<sub>1.25</sub>: C, 35.29; H, 3.13; N, 26.19. Found (%): C, 35.16; H, 2.82; N, 26.14.

**3.2.1.5:** [(ioap-H)<sub>4</sub>Cu<sub>4</sub>](CF<sub>3</sub>SO<sub>3</sub>)<sub>1.5</sub>(PF<sub>6</sub>)<sub>2.5</sub>·35H<sub>2</sub>O (**3.5**). ioap (0.14 g, 0.47 mmol) was dissolved in methanol:acetonitrile (10 mL:10 mL) forming a clear yellow solution to which Cu(CF<sub>3</sub>SO<sub>3</sub>)<sub>2</sub> (0.22 g; 0.61 mmol) was added. To the resulting clear green

solution was added 10 drops (0.5 mL) of 1.17 mol/L (0.59 mmol) NaOH(aq) producing a green-brown solution with a pH of 6. This was stirred with gentle heating (55 °C) for 1.5 hours, at which time  $\text{NH}_4\text{PF}_6$  (0.08 g; 0.5 mmol) was added. Stirring and heating was continued for a further 1.5 hours and the solution was kept after filtration for slow evaporation. X-ray quality, brown, prismatic crystals were collected after 41 days (0.21 g, 74 % yield). Anal. calcd (%) for  $(\text{C}_{11}\text{H}_{11}\text{N}_6\text{O}_1)_4\text{Cu}_4(\text{CF}_3\text{SO}_3)_{1.5}(\text{PF}_6)_{2.5}(\text{H}_2\text{O})_{35}$ : C, 22.36; H, 4.70; N, 13.76. Found (%): C, 22.82; H, 2.29; N, 13.76.

**3.2.1.6:**  $[\text{Cu}(\text{ioapm})(\text{ClO}_4)(\text{CH}_3\text{CN})](\text{ClO}_4)$  (**3.6**) and  $[\text{Cu}_4(\text{ioapm-H})_4](\text{ClO}_4)_4 \cdot 3\text{H}_2\text{O}$  (**3.7**). ioapm (0.21 g, 0.86 mmol) was added to a warm solution of  $\text{Cu}(\text{ClO}_4)_2 \cdot 6\text{H}_2\text{O}$  (0.31 g, 0.84 mmol) in methanol:acetonitrile (10 mL:10 mL). Addition of three drops of triethylamine produced a clear, dark green coloured solution, which was stirred for an hour and kept after filtration for crystallization. Dark green crystals, of two different morphologies, (minor component, **3.6**, were flat plates, while major component, **3.7**, were rods) suitable for structural analysis, were obtained by recrystallization from 50:50 methanol:acetonitrile. Only several crystals of **3.6** could be separated from the bulk sample of **3.7** (0.20 g, 59 % yield). Anal. calcd (%) for  $\text{Cu}_4(\text{C}_{10}\text{H}_{10}\text{N}_7\text{O})_4(\text{ClO}_4)_4 \cdot 3\text{H}_2\text{O}$  (bulk dried sample): C, 28.55; H, 2.75; N, 23.30. Found (%): C, 28.63; H, 2.59; N, 23.57.

**3.2.1.7:**  $[\text{Mn}_5(\text{ioapm-H})_6](\text{ClO}_4)_4 \cdot 2.5\text{H}_2\text{O}$  (**3.8**). ioapm (0.10 g, 0.41 mmol) was added to a solution of  $\text{Mn}(\text{ClO}_4)_2 \cdot 6\text{H}_2\text{O}$  (0.17 g, 0.47 mmol) in methanol:acetonitrile (10 mL:10 mL) forming a light yellow clear solution. Addition of 2 drops of triethylamine produced a clear, deep orange coloured solution that was stirred for one hour and kept after filtration for crystallization. X-Ray quality, red, prismatic crystals were collected after

two days (0.040 g, 30 % yield). Anal. calcd (%) for  $(C_{10}H_{10}N_7O)_6Mn_5(ClO_4)_4 \cdot 2.5H_2O$ : C, 33.01; H, 3.00; N, 26.94. Found (%): C, 32.79; H, 2.67; N, 27.40.

### 3.2.2: Crystallography

The diffraction intensities of an orange prismatic crystal of **3.1** having approximate dimensions of  $0.28 \times 0.12 \times 0.10$  mm were collected on a Rigaku Saturn CCD area detector with graphite monochromated Mo-K $\alpha$  radiation at 153(2) K to a maximum  $2\theta$  value of  $61.8^\circ$ . The data were corrected for Lorentz and polarization effects and a correction for secondary extinction [81] was applied. The structure was solved by direct methods [82,83] and expanded using Fourier techniques [84]. The non-hydrogen atoms were refined anisotropically. Hydrogen atoms were refined using the riding model, with isotropic thermal parameters set to twenty percent greater than their bonded partners. Neutral atom scattering factors and anomalous dispersion effects were taken from the usual sources [85-88]. All calculations were performed using the CrystalStructure [89,90] crystallographic software package except for refinement, which was performed using SHELXL-97 [83].

An orange prismatic crystal of **3.2** having approximate dimensions of  $0.32 \times 0.21 \times 0.16$  mm was treated similarly to **3.1**, however, the Platon [91] Squeeze procedure was applied to recover 222.3 electrons per unit cell in one void (total volume  $1001.4 \text{ \AA}^3$ ); that is 111.15 electrons per formula unit. Four badly disordered nitrate ions were present prior to the application of Squeeze, though a good point atom model could not be achieved for these ions. The application of Squeeze gave a good improvement in the data statistics

and allowed for the full anisotropic refinement of the framework structure and one lattice solvent water molecule.

A brown prismatic crystal of **3.3** having approximate dimensions of  $0.61 \times 0.49 \times 0.22$  mm was also treated similarly to **3.1**. The Platon [91] Squeeze procedure was applied to recover 828.5 electrons per unit cell in three voids (total volume  $6820.1 \text{ \AA}^3$ ); that is 46.03 electrons per formula unit. An area of diffuse electron density appeared to be present prior to the application of Squeeze, which was presumed to be the 2/3-occupancy hexafluorophosphate anion (38 electrons) required for charge balance, though a good point atom model could not be achieved for this ion. Protons on water molecules represented by atoms O(5-7) could not be located in the difference map and were hence omitted from the model (6 electrons). The application of Squeeze gave a good improvement in the data statistics and allowed for a full anisotropic refinement of the framework structure and anions.

A green prismatic crystal of **3.4** having approximate dimensions of  $0.37 \times 0.30 \times 0.25$  mm was treated similarly to **3.1**. Hydrogen atoms were introduced in difference map (H(6) and H(7)) or calculated positions with isotropic thermal parameters set twenty percent greater than those of their bonding partners. They were refined on the riding model. All other non-hydrogen atoms were refined anisotropically.

A green prismatic crystal of **3.5** having approximate dimensions of  $0.35 \times 0.14 \times 0.10$  mm was treated similarly to **3.1**. A half-occupancy hexafluorophosphate anion (containing P(4)) overlaps in space with a half-occupancy triflate anion and contains several atoms that were refined isotropically. To account for the space overlap, atom

F(29) was set to an occupancy of 0.944. This accounts for the electron density at this site being a hexafluorophosphate fluoride atom 50 % of the time, and a triflate oxygen atom the other 50 % of the time.

A green platelet crystal **3.6** having approximate dimensions of  $0.36 \times 0.32 \times 0.10$  mm was treated similarly to **3.1**. Hydrogen atoms were introduced in calculated or difference map (H(4) and H(6)) positions with isotropic thermal parameters set twenty percent greater than those of their bonding partners. They were refined on the riding model. The model contains two half-occupancy perchlorate ions which were refined anisotropically. These in fact give one perchlorate ion, disordered over two positions. The model also contains another disordered perchlorate ion. Two chlorine atoms with partial occupancies were used to model this disorder. This ion was also refined anisotropically.

A green prismatic crystal of **3.7** having approximate dimensions of  $0.72 \times 0.17 \times 0.11$  mm was treated similarly to **3.1**. The symmetry expanded model contains two disordered perchlorate anions. The occupancies of the corresponding oxygen atoms were adjusted accordingly and were refined isotropically. Two perchlorate anions are present. They did not exhibit disorder and were refined anisotropically. The symmetry expanded model also contains three acetonitrile molecules as lattice solvent. The terminal carbon of each was refined isotropically, while the other non-hydrogen atoms were refined anisotropically.

A red prism crystal of **3.8** having approximate dimensions of  $0.20 \times 0.20 \times 0.20$  mm was treated similarly to **3.1**. The model contains three well-modeled perchlorate

anions that were refined anisotropically, and one perchlorate anion that was difficult to model; it was refined isotropically. The model contains five partial occupancy water molecules as lattice solvent that were refined isotropically. The occupancies of the five corresponding oxygen atoms were adjusted to reflect this partial occupancy. The corresponding ten hydrogen atoms were not included in the model. The model also included two full-occupancy water molecules as lattice solvent that were refined isotropically. The corresponding four hydrogen atoms could not be located in the difference map and were not included in the model. Abbreviated crystal data for **3.1 - 3.8** are listed in Tables 3.1 - 3.4.

**Table 3.1:** Summary of crystallographic data for **3.1** and **3.2**.

	<b>3.1</b>	<b>3.2</b>
Chemical Formula	C <sub>22</sub> H <sub>34.5</sub> B <sub>2</sub> Co <sub>2</sub> F <sub>8</sub> N <sub>12</sub> O <sub>8.75</sub>	C <sub>44</sub> H <sub>52</sub> Mn <sub>3</sub> N <sub>28</sub> O <sub>19</sub>
M	898.56	1441.96
T(K)	153(2)	113(2)
Crystal System	triclinic	triclinic
Space Group	$\bar{P}1$ (#2)	$\bar{P}1$ (#2)
a (Å)	9.882(2)	10.7348(13)
b (Å)	14.623(3)	13.6851(18)
c (Å)	14.928(4)	23.480(3)
$\alpha$ (°)	107.465(3)	88.283(5)
$\beta$ (°)	107.784(3)	80.327(5)
$\gamma$ (°)	95.447(4)	86.514(5)
V (Å <sup>3</sup> )	1917.6(8)	3393.4(7)
Z	2	2
D <sub>calc</sub> (g/cm <sup>3</sup> )	1.556	1.411
$\mu$ (MoK $\alpha$ ) (cm <sup>-1</sup> )	9.64	6.34
Reflections Total	18471	34286
Reflections Unique	7865	15289
R <sub>int</sub>	0.0453	0.0380
R <sub>1</sub> ( <i>I</i> > 2.00 $\sigma$ ( <i>I</i> ))	0.0988	0.0738
wR <sub>2</sub> (All reflections)	0.2902	0.2393

**Table 3.2:** Summary of crystallographic data for **3.3** and **3.4**.

	<b>3.3</b>	<b>3.4</b>
Chemical Formula	C <sub>47</sub> H <sub>50</sub> F <sub>15</sub> N <sub>24</sub> Ni <sub>4</sub> O <sub>16</sub> P S <sub>3</sub>	C <sub>52</sub> H <sub>56</sub> Cu <sub>4</sub> N <sub>32</sub> O <sub>16</sub>
M	1854.10	1639.45
T(K)	113(2)	153(2)
Crystal System	trigonal	tetragonal
Space Group	$\bar{R}3$ (#148)	I4 <sub>1</sub> /a (#88)
a (Å)	42.677(3)	18.9374(11)
b (Å)	42.677(3)	18.9374(11)
c (Å)	22.0593(15)	18.2748(11)
$\alpha$ (°)	90.00	90.00
$\beta$ (°)	90.00	90.00
$\gamma$ (°)	120.00	90.00
V (Å <sup>3</sup> )	34795(4)	6553.8(7)
Z	18	4
D <sub>calc</sub> (g/cm <sup>3</sup> )	1.593	1.662
$\mu$ (MoK $\alpha$ ) (cm <sup>-1</sup> )	11.70	13.73
Reflections Total	130730	29320
Reflections Unique	16011	3757
R <sub>int</sub>	0.0337	0.0269
R <sub>1</sub> ( $I > 2.00\sigma(I)$ )	0.0883	0.0403
wR <sub>2</sub> (All reflections)	0.2520	0.1070

**Table 3.3:** Summary of crystallographic data for **3.5**.

	<b>3.5</b>
Chemical Formula	C <sub>52.5</sub> H <sub>58.5</sub> Cu <sub>4</sub> F <sub>19.5</sub> N <sub>27.5</sub> O <sub>10.5</sub> P <sub>2.5</sub> S <sub>1.5</sub>
M	1992.89
T(K)	113(2)
Crystal System	orthorhombic
Space Group	Pbca (#61)
a (Å)	26.4718(15)
b (Å)	20.6212(13)
c (Å)	29.8235(18)
α (°)	90.00
β (°)	90.00
γ (°)	90.00
V (Å <sup>3</sup> )	16280.1(17)
Z	8
D <sub>calc</sub> (g/cm <sup>3</sup> )	1.626
μ(MoKα) (cm <sup>-1</sup> )	12.32
Reflections Total	75953
Reflections Unique	16823
R <sub>int</sub>	0.0451
R <sub>1</sub> ( <i>I</i> > 2.00σ( <i>I</i> ))	0.0922
wR <sub>2</sub> (All reflections)	0.2593

**Table 3.4:** Summary of crystallographic data for **3.6 - 3.8**.

	<b>3.6</b>	<b>3.7</b>	<b>3.8</b>
Chemical Formula	C <sub>12</sub> H <sub>14</sub> Cl <sub>2</sub> CuN <sub>8</sub> O <sub>9</sub>	C <sub>46</sub> H <sub>49</sub> Cl <sub>4</sub> Cu <sub>4</sub> N <sub>31</sub> O <sub>20</sub>	C <sub>60</sub> H <sub>74</sub> Cl <sub>4</sub> N <sub>42</sub> Mn <sub>5</sub> O <sub>29</sub>
M	548.75	1752.08	2264.01
T(K)	153(2)	153(2)	153(2)
Crystal System	monoclinic	monoclinic	monoclinic
Space Group	P2 <sub>1</sub> /c (#14)	C 2/c (#15)	P2 <sub>1</sub> /n (#14)
a (Å)	7.6317(6)	22.912(9)	16.8375(19)
b (Å)	9.1727(7)	21.105(7)	23.483(3)
c (Å)	28.531(3)	18.184(7)	23.610(3)
α (°)	90.00	90.00	90.00
β (°)	93.058(2)	128.679(7)	96.970(3)
γ (°)	90.00	90.00	90.00
V (Å <sup>3</sup> )	1994.4(3)	6864(4)	9266.1(18)
Z	4	4	4
D <sub>calc</sub> (g/cm <sup>3</sup> )	1.828	1.695	1.623
μ(MoKα) (cm <sup>-1</sup> )	14.30	14.71	8.77
Reflections Total	18304	37116	32353
Reflections Unique	5449	9417	16107
R <sub>int</sub>	0.0253	0.0821	0.0312
R <sub>1</sub> ( <i>I</i> > 2.00σ( <i>I</i> ))	0.0502	0.1101	0.0979
wR <sub>2</sub> (All reflections)	0.1387	0.2986	0.2906

### 3.3: Results and Discussion:

**Note:** The crystallographically determined formulae are used herein. Colour code for figures: purple = cobalt, magenta = manganese, green = copper, golden = nickel, grey = carbon, blue = nitrogen, red = oxygen, light green = chlorine, yellow = sulphur, pink = fluorine. Crystallographic representations/illustrations were generated using Persistence of Vision Ray Tracer (POV-Ray©) for Windows, version 3.6, with scene description files written by Ortep-3 for Windows (Version 1.08) Copyright© 1997-2003 Louis J. Farrugia.

#### 3.3.1: Description of crystal structures:

##### 3.3.1.1: $[(\text{ioap-H})(\text{ioap-2H})\text{Co}_2(\text{H}_2\text{O})_4](\text{BF}_4)_2(\text{H}_2\text{O})_{2.75}$ (**3.1**)

The structure of the heteroleptic dinuclear cationic fragment of **3.1** is shown in Figure 3.3, and significant bond lengths and angles are listed in Table 3.5.

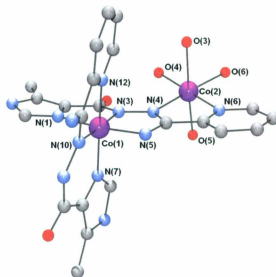


**Figure 3.3:** Ball-and-stick depiction of the cationic moiety of **3.1**. Hydrogen atoms omitted for clarity.

Two octahedral cobalt centres are coordinated by two ligands. One tridentate ligand is mono-deprotonated and arranged as in Figure 3.2b, coordinating only to Co(1), which has short metal ligand bond distances (1.910(4)<sub>av.</sub>) and is assigned as Co(III) (bond valence sum [92], BVS, calculation = 4.33, which is consistent with other high calculated BVS values for Co(III) in similar ligand environments [93]). A second ligand is pentadentate, doubly-deprotonated and twisted (Figure 3.2c), completing the coordination sphere of Co(1) and also coordinating to Co(2). Co(2) has longer metal-ligand bond distances (2.103(5)<sub>av.</sub>) typical of Co(II) (BVS value = 2.147) and is connected to Co(1) by a diazine NN bridge, and completes a *cis*-N<sub>2</sub>O<sub>6</sub> coordination environment with four coordinated water molecules. The Co(1)-N(3)-N(4)-Co(2) torsion angle is 166.2(3)<sup>o</sup>, indicating an almost flat projection of the two metals relative to the pentadentate ligand. The formation of a mixed-oxidation state product indicates the oxygen sensitivity of this reaction.

**Table 3.5:** Selected bond distances (Å) and torsion angle (°) for **3.1**.

Co(1)	N(5)	1.868(5)	Co(2)	N(6)	2.091(6)		
Co(1)	N(3)	1.876(4)	Co(2)	O(4)	2.096(5)		
Co(1)	N(7)	1.925(4)	Co(2)	O(3)	2.114(5)		
Co(1)	N(1)	1.926(5)	Co(2)	N(4)	2.119(5)		
Co(1)	N(12)	1.934(4)	Co(2)	O(6)	2.122(5)		
Co(1)	N(10)	1.934(4)					
Co(2)	O(5)	2.077(6)	Co(1)	N(3)	N(4)	Co(2)	-166.2(3)

**3.3.1.2:** [(ioap)<sub>2</sub>(ioap-H)<sub>2</sub>Mn<sub>3</sub>(H<sub>2</sub>O)<sub>2</sub>](NO<sub>3</sub>)<sub>4</sub>(H<sub>2</sub>O) (**3.2**)

The structure of the trinuclear cationic fragment of **3.2** and its core structural representation are shown in Figure 3.4a and 3.4b respectively, and significant bond lengths and angles are listed in Table 3.6.

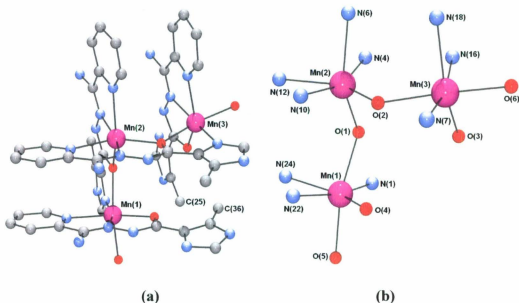


**Figure 3.4:** a) Ball-and-stick depiction of the cationic moiety **3.2**. Hydrogen atoms omitted for clarity. b) Core structural representation of **3.2**.

Three octahedral manganese centres are coordinated to four ligands. Two of the ditopic ligands are mono-deprotonated and arranged as in Figure 3.2a, and both coordinate to two Mn(II) cations (Mn(1)-Mn(2) and Mn(2)-Mn(3)), with intervening hydrazone oxygen bridges. The other two ligands, however, are neutral and in a different twisted conformation as shown in Figure 3.2d, each coordinating one Mn(II) cation (Mn(1) and Mn(3)). Further, the twisted configuration of these two ligands results in steric congestion from the imidazole methyl groups (C(25) and C(36); Figure 3.4a, which prevents a metal from entering the fourth coordination pocket.

The *cis*-MnN<sub>4</sub>O<sub>2</sub> coordination sphere of Mn(2) is occupied fully by ligand based donor atoms with long Mn - N<sub>pyrimidine</sub> bond distances (2.33<sub>av</sub> Å) and shorter remaining Mn - L distances (2.16 - 2.19 Å), while Mn(1) and Mn(3) each have one coordination site

occupied by a water molecule, and *mer*-MnN<sub>3</sub>O<sub>3</sub> coordination spheres with one long Mn - N<sub>pyrimidine</sub> bond (2.32<sub>av.</sub> Å) and shorter remaining Mn - L distances (2.18 - 2.21 Å). Mn - Mn distances fall in the range 3.92 - 3.93 Å, with Mn-O-Mn angles in the range 126.8 - 127.9°. These results are consistent with other reported Mn - L (2.12 - 2.43 Å) and Mn - Mn bond distances (3.865 - 4.01 Å) and angles (126.5 - 131.6°) for [2×2] Mn(II)<sub>4</sub> grids [64] and for pentanuclear Mn(II)<sub>5</sub> clusters [61,64] synthesized with poap, pomp, which also have hydrazone oxygen bridges between metal centres.

**Table 3.6:** Selected bond distances (Å) and angles (°) for **3.2**.

Mn(1) O(5)	2.175(3)	Mn(2) N(12)	2.340(3)
Mn(1) O(1)	2.178(2)	Mn(3) O(6)	2.178(2)
Mn(1) N(22)	2.184(3)	Mn(3) O(3)	2.180(2)
Mn(1) N(1)	2.189(3)	Mn(3) N(7)	2.183(3)
Mn(1) O(4)	2.207(2)	Mn(3) N(16)	2.190(3)
Mn(1) N(24)	2.320(3)	Mn(3) O(2)	2.204(2)
Mn(2) N(10)	2.157(3)	Mn(3) N(18)	2.321(3)
Mn(2) N(4)	2.160(3)		
Mn(2) O(1)	2.181(2)	Mn(1) O(1)	Mn(2) 127.93(10)
Mn(2) O(2)	2.1880(19)	Mn(2) O(2)	Mn(3) 126.77(9)
Mn(2) N(6)	2.325(3)		

**3.3.1.3:** [(ioap-H)<sub>4</sub>Ni<sub>4</sub>(CF<sub>3</sub>SO<sub>3</sub>)(H<sub>2</sub>O)<sub>3</sub>](CF<sub>3</sub>SO<sub>3</sub>)<sub>2</sub>(PF<sub>6</sub>) (**3.3**)

The structure of the tetranuclear cationic fragment of **3.3** and its core structural representation are shown in Figure 3.5a and 3.5b respectively, and significant bond lengths and angles are listed in Table 3.7.

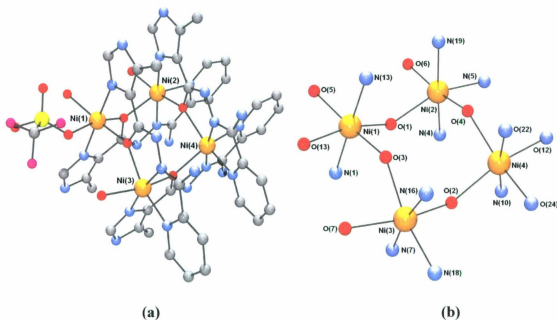


**Figure 3.5:** a) Ball-and-stick depiction of the cationic moiety **3.3**. Hydrogen atoms omitted for clarity. b) Core structural representation of **3.3**.

Four tetradentate ligands are arranged as in Figure 3.2a binding four pseudo-octahedral nickel(II) ions in a hydrazone oxygen bridged  $[2 \times 2]$  grid arrangement, *via* two sets of parallel ligands above and below the square metal pseudo-plane. Each ligand approximately eclipses its set partner and all are mono-deprotonated at the hydrazone oxygen site. The overall charge is balanced by the presence of one hexafluorophosphate and three triflate anions. Ni-Ni distances fall in the range 3.8761(9) - 3.9421(9) Å, with Ni-O-Ni angles in the range 136.21(15) - 136.68(16) $^\circ$ , typical of other hydrazone oxygen bridged  $[2 \times 2]$  Ni(II) $_4$  complexes synthesized from poap (Figure 3.1a), where Ni-O-Ni angles fall in the range 136.2 - 140.1 $^\circ$  and Ni-Ni distances are between 3.91 - 4.03 Å [58]. Nickel-ligand bond distances fall in the range 1.973(5)-2.117(4) Å. The *cis*-NiN $_4$ O $_2$  octahedral coordination sphere of Ni(4) is filled entirely by ligand donor atoms.

Ni(2) and Ni(3) have *mer*-NiN<sub>3</sub>O<sub>3</sub> coordination spheres, with ligand donor atoms filling five-coordination sites and solvent water molecules (O(6) and O(7) respectively) filling the remaining site on each metal centre. Ni(1) has a *trans*-NiN<sub>2</sub>O<sub>4</sub> environment, composed of four ligand donor atoms, one water molecule (O(5)) and a coordinated triflate oxygen atom (O(13)).

**Table 3.7:** Selected bond distances (Å) and angles (°) for **3.3**.

Ni(1)	N(13)	2.019(5)	Ni(3)	O(3)	2.109(4)	
Ni(1)	N(1)	2.021(5)	Ni(3)	O(7)	2.156(4)	
Ni(1)	O(3)	2.064(3)	Ni(3)	N(18)	2.160(4)	
Ni(1)	O(1)	2.072(4)	Ni(4)	N(22)	1.974(4)	
Ni(1)	O(5)	2.094(4)	Ni(4)	N(10)	1.981(4)	
Ni(1)	O(8)	2.174(4)	Ni(4)	N(24)	2.086(4)	
Ni(2)	N(4)	1.973(5)	Ni(4)	O(4)	2.116(3)	
Ni(2)	N(19)	2.020(5)	Ni(4)	N(12)	2.136(4)	
Ni(2)	O(4)	2.085(3)	Ni(4)	O(2)	2.145(3)	
Ni(2)	O(1)	2.133(4)				
Ni(2)	N(6)	2.134(5)	Ni(1)	O(1)	Ni(2)	136.53(17)
Ni(2)	O(6)	2.150(4)	Ni(3)	O(2)	Ni(4)	136.21(15)
Ni(3)	N(16)	1.974(4)	Ni(1)	O(3)	Ni(3)	136.50(17)
Ni(3)	N(7)	2.025(4)	Ni(2)	O(4)	Ni(4)	136.68(16)
Ni(3)	O(2)	2.103(3)				

**3.3.1.4:** [(ioap-H)<sub>4</sub>Cu<sub>4</sub>](NO<sub>3</sub>)<sub>4</sub>(CH<sub>3</sub>CN)<sub>4</sub> (**3.4**)

The structure of the homoleptic tetranuclear cationic fragment of **3.4** and its core structural representation are shown in Figure 3.6a and 3.6b respectively, and significant bond lengths and angles are listed in Table 3.8.

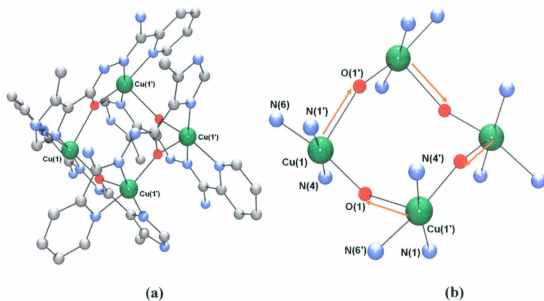


**Figure 3.6:** a) Ball-and-stick depiction of the cationic moiety **3.4**. Hydrogen atoms omitted for clarity. b) Core structural representation of **3.4**. Arrows highlight the elongated Jahn-Teller axes.

Four tetradentate ligands are arranged as in Figure 3.2a coordinating to four distorted square pyramidal copper(II) ions with two sets of ligands aligned in a parallel, but rotated, arrangement above and below the square  $[2 \times 2]$  metal pseudo-plane. Each ligand is mono-deprotonated at the hydrazone oxygen site, and the overall charge is balanced by the presence of four nitrate anions. Cu-Cu distances measure  $4.04(2)$  Å, with Cu-O-Cu angles  $139.49(7)^\circ$ . The basal planes of the distorted copper square pyramids are characterized by short bonds to three ligand donor nitrogen atoms and one oxygen atom ( $1.9005(19)$  -  $2.0557(18)$  Å). Longer bonds to oxygen atoms in the axial position ( $2.3132(14)$  Å) are present for each metal. These define the elongated Jahn-Teller axes (shown in Figure 3.6b) and should result in a  $d_{x^2-y^2}$  magnetic ground state at each copper

centre (though some mixing with  $d_{z^2}$  orbitals is possible due to the distorted geometry). A measure of the distortion at the five coordinate Cu(II) centres is calculated from the  $\tau$  value, expressed in equation 3.1.

$$\tau = \frac{\beta - \alpha}{60} \quad (3.1)$$

In equation 3.1,  $\beta$  is the greater of the basal angles and  $\alpha$  is the angle opposite the axial ligand. For ideal square pyramids  $\alpha = \beta = 180^\circ$  and  $\tau = 0$ , while for ideal trigonal bipyramids,  $\alpha = 120^\circ$ ,  $\beta = 180^\circ$  and  $\tau = 1$  [94]; for **3.4**  $\tau = 0.22$ . The Cu-O bond distances around the square core alternate between equatorial and axial, and link the copper atoms in an orbitally orthogonal manner assuming a  $d_{x^2-y^2}$  ground state. The non-coordinating nitrogen atoms on the imidazole groups provide a means for possible further external metal coordination, but as yet there is no evidence for expansion of the grid nuclearity.

**Table 3.8:** Selected bond distances (Å) and angle ( $^\circ$ ) for **3.4**.

Cu(1)	N(4)	1.9005(19)	Cu(1)	O(1)	Cu(1')	139.49(7)
Cu(1)	N(1')	1.9556(17)				
Cu(1)	O(1)	1.9940(14)				
Cu(1)	N(6)	2.0557(18)				
Cu(1)	O(1')	2.3132(14)				

**3.3.1.5:** [(ioap-H)<sub>4</sub>Cu<sub>4</sub>](PF<sub>6</sub>)<sub>2.5</sub>(CF<sub>3</sub>SO<sub>3</sub>)<sub>1.5</sub>(H<sub>2</sub>O)<sub>2</sub>(CH<sub>3</sub>CN)<sub>3.5</sub> (**3.5**)

The structure of the homoleptic tetranuclear cationic fragment of **3.5** and its core structural representation are shown in Figure 3.7a and 3.7b respectively, and significant bond lengths and angles are listed in Table 3.9.

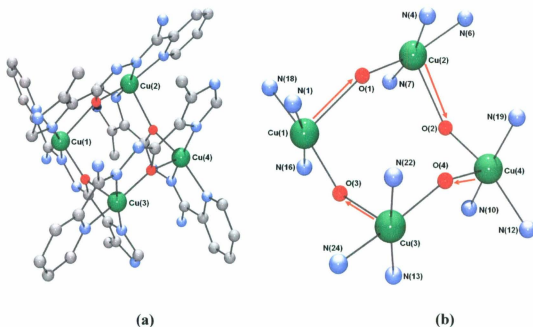


**Figure 3.7:** a) Ball-and-stick depiction of the cationic moiety **3.5**. Hydrogen atoms omitted for clarity. b) Core structural representation of **3.5**. Arrows highlight the elongated Jahn-Teller axes.

Complex **3.5** exhibits the same ligand arrangement as **3.4**, with Cu-Cu distances in the range 3.97 - 4.06 Å, and Cu-O-Cu angles in the range 138.4 - 139.9° ( $\tau_{\text{Cu}(1)} = 0.14$ ,  $\tau_{\text{Cu}(2)} = 0.13$ ,  $\tau_{\text{Cu}(3)} = 0.27$ ,  $\tau_{\text{Cu}(4)} = 0.14$ ). The basal planes of the copper square pyramids are characterized by short bonds to three ligand donor nitrogen atoms and one oxygen atom (1.888(5) - 2.048(5) Å). Longer bonds to oxygen atoms in the axial position (2.282(4) - 2.346(4) Å) are present for each metal. These define the elongated Jahn-Teller axes (shown in Figure 3.7b) and as for **3.4**, result in a  $d_{x^2-y^2}$  magnetic ground state at each copper centre.

**Table 3.9:** Selected bond distances (Å) and angles (°) for **3.5**.

Cu(1) N(16)	1.894(5)	Cu(3) N(24)	2.030(5)
Cu(1) N(1)	1.971(6)	Cu(3) O(3)	2.346(4)
Cu(1) O(3)	1.980(4)	Cu(4) N(10)	1.898(5)
Cu(1) N(18)	2.048(5)	Cu(4) N(19)	1.958(5)
Cu(1) O(1)	2.287(4)	Cu(4) O(2)	1.960(4)
Cu(2) N(4)	1.888(5)	Cu(4) N(12)	2.034(5)
Cu(2) N(7)	1.959(5)	Cu(4) O(4)	2.289(4)
Cu(2) O(1)	2.000(4)		
Cu(2) N(6)	2.040(5)	Cu(2) O(1)	Cu(1) 138.7(2)
Cu(2) O(2)	2.282(4)	Cu(4) O(2)	Cu(2) 138.4(2)
Cu(3) N(22)	1.912(5)	Cu(1) O(3)	Cu(3) 139.1(2)
Cu(3) N(13)	1.959(5)	Cu(3) O(4)	Cu(4) 139.9(2)
Cu(3) O(4)	1.986(4)		

**3.3.1.6:** [Cu(ioapm)(ClO<sub>4</sub>)(CH<sub>3</sub>CN)](ClO<sub>4</sub>) (**3.6**)

The structure of the mononuclear cationic fragment of **3.6** is shown in Figure 3.8, and significant bond lengths and angles are listed in Table 3.10.

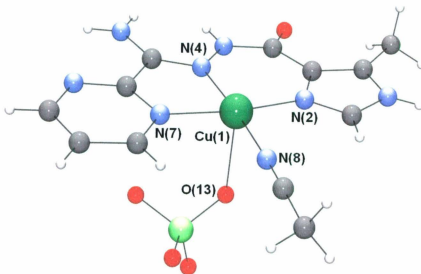


**Figure 3.8:** Ball-and-stick depiction of the cationic moiety of **3.6**.

The basal planes of the square pyramidal copper centre exhibit short bonds to three ligand donor nitrogen atoms, coordinated as in Figure 3.2b, and one short bond to a

coordinated acetonitrile molecule (1.9521(19) - 2.010(2) Å). A longer bond to a perchlorate oxygen atom (O(13)) in the axial position (2.4075(19) Å) is also present. This defines the elongated Jahn-Teller axes and results in a  $d_{x^2-y^2}$  ground state with a calculated  $\tau$  value of 0.04 [94].

**Table 3.10:** Selected bond distances (Å) and angles (°) for **3.6**.

Cu(1)	N(2)	1.9521(19)	N(4) Cu(1) N(8)	174.67(8)
Cu(1)	N(4)	1.9903(19)	N(2) Cu(1) N(7)	172.16(8)
Cu(1)	N(8)	1.996(2)		
Cu(1)	N(7)	2.010(2)		
Cu(1)	O(13)	2.4075(19)		

**3.3.1.7:**  $[\text{Cu}_4(\text{ioapm-H})_4](\text{ClO}_4)_4 \cdot 3 \text{H}_2\text{O}$  (**3.7**)

The structure of the homoleptic tetranuclear cationic fragment of **3.7** and its core structural representation are shown in Figure 3.9a and 3.9b respectively, and significant bond lengths and angles are listed in Table 3.11.

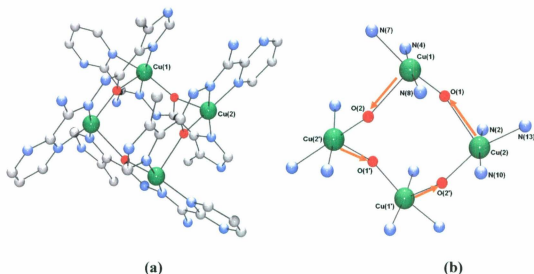


**Figure 3.9:** a) Ball-and-stick depiction of the cationic moiety **3.7**. Hydrogen atoms omitted for clarity. b) Core structural representation of **3.7**. Arrows highlight the elongated Jahn-Teller axes.

Complex **3.7** exhibits the same ligand arrangement as **3.4**, with Cu-Cu distances in the range 4.035 - 4.056 Å, and Cu-O-Cu angles in the range 139.00(19) - 140.42(19)<sup>o</sup> ( $\tau_{\text{Cu}(1)} = \tau_{\text{Cu}(2)} = 0.24$ ). The basal planes of the copper square pyramids are characterized by short bonds to three ligand donor nitrogen atoms and one oxygen atom (1.912(5) - 2.057(5) Å). Longer bonds to oxygen atoms in the axial position (2.318(4) Å) are present for each metal. These define the elongated Jahn-Teller axes (shown in Figure 3.9b) and as for **3.4**, result in a  $d_{x^2-y^2}$  magnetic ground state at each copper centre.

**Table 3.11:** Selected bond distances (Å) and angles (°) for **3.7**.

Cu(1) N(4)	1.912(5)	Cu(1) O(1)	Cu(2)	139.00(19)
Cu(1) N(8)	1.940(5)	Cu(2') O(2)	Cu(1)	140.42(19)
Cu(1) O(1)	1.956(4)			
Cu(1) N(7)	2.057(5)			
Cu(1) O(2)	2.318(4)			
Cu(2) N(10)	1.924(5)			
Cu(2) N(2)	1.967(5)			
Cu(2) O(2')	1.992(4)			
Cu(2) N(13)	2.051(5)			
Cu(2) O(1)	2.349(4)			

**3.3.1.8:**  $[\text{Mn}_5(\text{ioapm-H})_6](\text{ClO}_4)_4 \cdot 2.5\text{H}_2\text{O}$  (**3.8**)

The structure of the homoleptic pentanuclear cationic fragment of **3.8** and its core structural representation are shown in Figure 3.10a and 3.10b respectively, and significant bond lengths and angles are listed in Table 3.12.

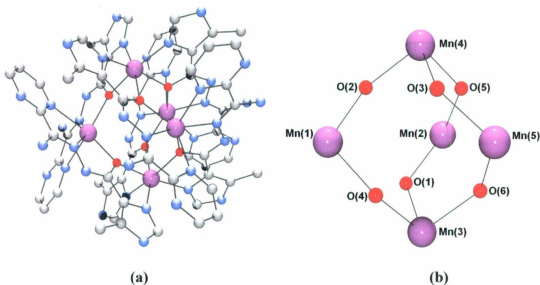


**Figure 3.10:** a) Ball-and-stick depiction of the cationic moiety **3.8**. Hydrogen atoms omitted for clarity. b) Core structural representation of **3.8**.

Six tetradentate ligands are bound in parallel pairs to a trigonal bipyramidal  $Mn_5(\mu-O)_6$  core. The ligands adopt an *anti* arrangement within each pair, and there is an exact match between the bonding capacity of the six ligands and the coordination requirements of the five octahedral manganese ions. Each ligand is mono-deprotonated at the hydrazone oxygen site, and the overall charge is balanced by the presence of four perchlorate anions. Mn-Mn distances fall in the range 3.865-3.950 Å, and Mn-O-Mn angles fall in the range 126.46(17) - 128.69(17)<sup>o</sup>. The outer surface of the cluster is comprised of six pyrimidine and six imidazole subunits, which could be involved in further coordination, though no evidence for this has yet been observed. Again, these results are consistent with other Mn - Mn bond distances and angles for pentanuclear Mn(II)<sub>5</sub> clusters synthesized with poap, pomp [61,64].

**Table 3.12:** Selected bond distances (Å) and angles (°) for **3.8**.

Mn(1) N(25)	2.147(4)	Mn(4) O(3)	2.184(4)
Mn(1) O(2)	2.182(4)	Mn(4) N(9)	2.194(5)
Mn(1) N(11)	2.183(5)	Mn(4) N(30)	2.197(5)
Mn(1) O(4)	2.197(4)	Mn(4) O(5)	2.201(4)
Mn(1) N(14)	2.392(5)	Mn(4) N(16)	2.201(5)
Mn(1) N(28)	2.425(5)	Mn(4) O(2)	2.211(4)
Mn(2) N(32)	2.121(5)	Mn(5) N(18)	2.162(5)
Mn(2) O(1)	2.135(4)	Mn(5) N(39)	2.169(5)
Mn(2) N(4)	2.139(5)	Mn(5) O(6)	2.172(4)
Mn(2) O(5)	2.159(4)	Mn(5) O(3)	2.186(4)
Mn(2) N(7)	2.438(5)	Mn(5) N(21)	2.395(5)
Mn(2) N(34)	2.460(5)	Mn(5) N(41)	2.423(5)
Mn(3) O(4)	2.185(4)		
Mn(3) O(1)	2.194(4)	Mn(1) O(2)	Mn(4) 127.73(17)
Mn(3) N(37)	2.200(5)	Mn(2) O(1)	Mn(3) 126.46(17)
Mn(3) N(2)	2.204(5)	Mn(2) O(5)	Mn(4) 128.18(17)
Mn(3) N(23)	2.206(5)	Mn(3) O(4)	Mn(1) 128.69(17)
Mn(3) O(6)	2.207(4)	Mn(4) O(3)	Mn(5) 127.50(17)
		Mn(5) O(6)	Mn(3) 128.61(18)

### 3.3.2: Magnetic Properties:

The variable temperature magnetic properties of **3.1** show an essentially constant moment from room temperature (approximately  $4.5 \mu_B$ ) to about 100 K, with a drop to  $3.41 \mu_B$  at 2 K. This is consistent with the presence of one high spin Co(II) ( $S = 3/2$ ) centre and one low spin diamagnetic Co(III) ( $S = 0$ ) centre (though Co(III) is nearly “fully” diamagnetic due to second order Zeeman effects). The slight drop below 100 K is associated with zero field splitting effects.

Compound **3.2** consists of a Mn(II) trinuclear array with each Mn(II) centre bridged by single hydrazone oxygen atoms, with large, similar Mn-O-Mn angles. The magnetic profile for **3.2** is shown in Figure 3.11 as a plot of moment per mole as a function of temperature. The moment drops from  $10.0 \mu_B$  at 300 K to  $5.94 \mu_B$  at 2 K and the profile is characteristic of the presence of intramolecular antiferromagnetic exchange. The low temperature value indicates the presence of one uncoupled Mn(II) centre in the ground state ( $S = 5/2$ ), and is associated with the odd number of spin centres in the cluster.

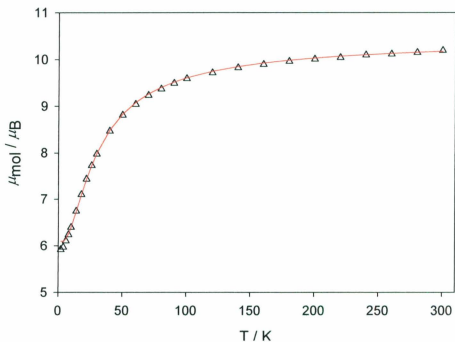


**Figure 3.11:** Variable temperature magnetic data for **3.2**;  $g = 2.04(2)$ ,  $J = -3.03(1) \text{ cm}^{-1}$ ,  $\text{TIP} = 0 \text{ cm}^3 \text{ mol}^{-1}$ ,  $\rho = 0.01$ ,  $10^2 R = 0.81$ .

The variable temperature magnetic data were fitted to an exchange expression by using vector addition principles [43,48] to derive the total spin states ( $S'$ ) and their energies ( $E(S')$ ) which were then substituted into the Van Vleck equation (equation 3.3), using the isotropic exchange Hamiltonian (equation 3.2) for a trinuclear arrangement of three  $S = 5/2$  metal centres (Figure 3.12a, where  $J = J_{12} = J_{23}$  and  $J_{13}$  is assumed negligible.)  $\chi_M$  is the molar susceptibility,  $\rho$  is the fraction of paramagnetic impurity, TIP is the temperature independent paramagnetism,  $\theta$  is a Weiss-like temperature correction and all other terms have their usual significance.

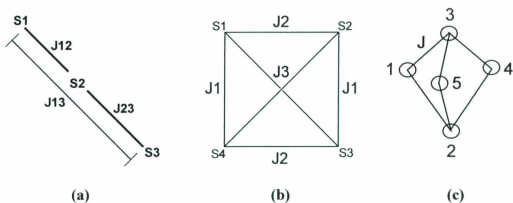


**Figure 3.12:** Magnetic exchange models for some polynuclear systems; a)  $M_3$  triad b)  $M_4$  square c)  $M_5$  trigonal bipyramid.

$$H_{\text{ex}} = -J(S_1 \cdot S_2 + S_2 \cdot S_3) \quad (3.2)$$

$$\chi M = \frac{N\beta^2 g^2}{3k(T - \theta)} \frac{\sum S'(S'+1)(2S'+1)e^{-E(S')/kT}}{\sum (2S'+1)e^{-E(S')/kT}} (1 - \rho) + \frac{N\beta^2 g^2 S(S+1)\rho}{3kT} + TIP \quad (3.3)$$

The experimental magnetic data were fitted by non-linear regression within MAGMUN4.1 [49] to give  $g = 2.04(2)$ ,  $J = -3.03(1) \text{ cm}^{-1}$ ,  $TIP = 0 \text{ cm}^3 \text{ mol}^{-1}$ ,  $\rho = 0.01$  ( $10^2 R = 0.81$ ;  $R = [\sum(\chi_{\text{obs}} - \chi_{\text{calc}})^2 / \sum \chi_{\text{obs}}^2]^{1/2}$ ). The solid line in Figure 3.11 was calculated with these parameters which are in excellent agreement with previously reported examples of antiferromagnetic  $[2 \times 2]$   $Mn_4$  squares [64] and  $Mn_5$  pentanuclear clusters [61, 64, 65], resulting from self-assembly reactions with poap and pomp (Figure 3.1a) that also exhibit hydrazone oxygen bridges between metal centres with similar M-O-M bond angles (approximately  $126 - 130^\circ$ ).

Compound **3.3**, a [2×2] Ni<sub>4</sub>(II) grid with large Ni-O-Ni bond angles, displays a maximum in the  $\chi_M$  versus temperature profile at 26 K (Figure 3.13), indicative of intramolecular antiferromagnetic coupling.

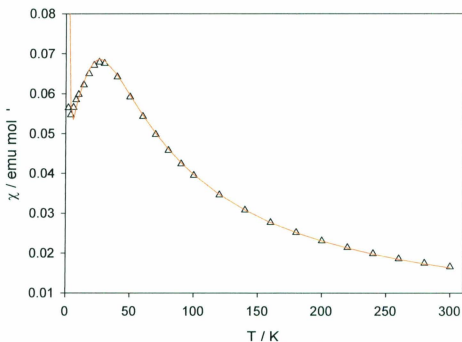


**Figure 3.13:** Variable temperature magnetic data for **3.3**;  $g = 2.25(1)$ ,  $J = -13.3(8) \text{ cm}^{-1}$ ,  $\theta = -1 \text{ K}$ ,  $\text{TIP} = 800 \times 10^{-6} \text{ cm}^3 \text{ mol}^{-1}$ ,  $\rho = 0.04$ ,  $10^2 R = 1.01$ .

The magnetic properties of tetranuclear clusters are addressed in a thorough manner in a review by Murray [47]. Here, the variable temperature magnetic data were fitted to an exchange expression by using vector addition principles [48,43] to derive the total spin states ( $S'$ ) and their energies ( $E(S')$ ) which were then substituted into equation 3.3 using the isotropic exchange Hamiltonian (equation 3.4) for a square arrangement of four  $S = 1$  metal centres (Figure 3.12b):

$$H_{\alpha} = -J(S_1 \cdot S_2 + S_2 \cdot S_3 + S_3 \cdot S_4 + S_1 \cdot S_4) \quad (3.4)$$

Where  $J = J_1 = J_2$  and  $J_3$  is considered negligible and  $E(S', S_{13}, S_{24}) = -J[S'(S'+1) - S_{13}(S_{13}+1) - S_{24}(S_{24}+1)]$  where  $S_{13} = S1 + S3$ ;  $S_{24} = S2 + S4$ ;  $S' = S1 + S2 + S3 + S4$ . The experimental magnetic data were fitted by non-linear regression within MAGMUN4.1 [49] to give  $g = 2.25(1)$ ,  $J = -13.3(8) \text{ cm}^{-1}$ ,  $\theta = -1 \text{ K}$ ,  $\text{TIP} = 800 \times 10^{-6} \text{ cm}^3 \text{ mol}^{-1}$ ,  $\rho = 0.04$  ( $10^2 R = 1.01$ ). The solid line in Figure 3.13 was calculated with these parameters. The observed antiferromagnetic exchange is in agreement with similar compounds [58] with the four octahedral Ni(II) centres bridged by hydrazone oxygen groups with Ni-O-Ni angles in the range  $136.21(15) - 136.68(16)^\circ$ .

Unlike **3.3**, complex **3.4**, a  $[2 \times 2] \text{ Cu}_4(\text{II})$  grid shows a slight decrease in moment from  $3.91 \mu_B$  at 300 K to  $3.70 \mu_B$  at 80 K, followed by a sharp increase to  $4.65 \mu_B$  at 2 K (Figure 3.14), which is characteristic of a system dominated by intramolecular ferromagnetic coupling.

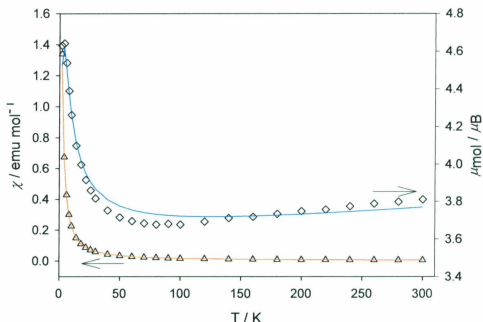


**Figure 3.14:** Variable temperature magnetic data for **3.4**.  $\chi$  represented by triangles;  $\mu$  represented by diamonds.  $g = 2.07(0)$ ,  $J = 7.2(8) \text{ cm}^{-1}$ ,  $\theta = -0.5 \text{ K}$ ,  $\text{TIP} = 475 \times 10^{-6} \text{ cm}^3 \text{ mol}^{-1}$ ,  $10^2 R = 2.14$ .

The variable temperature magnetic data were fitted by non-linear regression within MAGMUN4.1 [49] to an exchange expression (equation 3.3) using the isotropic exchange Hamiltonian (equation 3.4) for a square arrangement of four  $S = 1/2$  metal centres (Figure 3.12b) where  $J = J_1 = J_2$  and  $J_3$  is considered negligible, to give a best fit with  $g = 2.07(0)$ ,  $J = 7.2(8) \text{ cm}^{-1}$ ,  $\theta = -0.5 \text{ K}$ ,  $\text{TIP} = 475 \times 10^{-6} \text{ cm}^3 \text{ mol}^{-1}$  ( $10^2 R = 2.14$ ). The solid lines in Figure 3.14 were calculated with these parameters.

The structure of **3.4** shows that all the connections between the copper centres can be considered orthogonal (*vide supra*; Figure 3.6b), on the assumption that the ground state is 100%  $d_{x^2-y^2}$ . This agrees in general with the observed exchange situation, where

intramolecular ferromagnetic coupling clearly dominates. Similar fitted parameters have been reported for other [2×2] Cu<sub>4</sub> grids [58,62,64,95] exhibiting ferromagnetic exchange due to orthogonal connections between metal centres. However, despite the best fit, there is clearly some deviation from the experimental data, which involves the slight decrease in moment down to 80 K. This cannot be modeled successfully without including an unrealistically high TIP contribution, and can possibly be attributed instead to a small antiferromagnetic component which is reasonably explained on the basis of the mixing of a small d<sub>z<sup>2</sup></sub> component into the dominant d<sub>x<sup>2</sup>-y<sup>2</sup></sub> magnetic ground state, due to the observed distortion of the copper coordination spheres ( $\tau = 0.22$ ). Magnetization (M) versus field data (Figure 3.15) show a rise in M to a value of approximately 3.77 N $\beta$  at 5.0 T. A simulation of the data (solid line, Figure 3.15) was generated using the appropriate Brillouin function with  $g = 2.07$  for  $T = 2$  K, and  $S' = 2$ , and again it shows a slight deviation from the experimental data, as expected, due to the possible mixing of magnetic states.

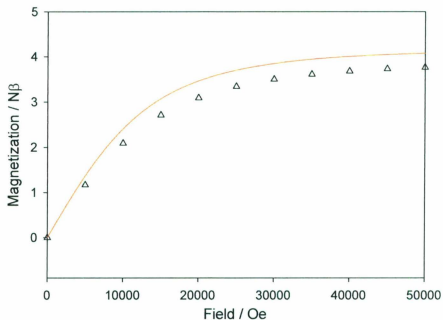
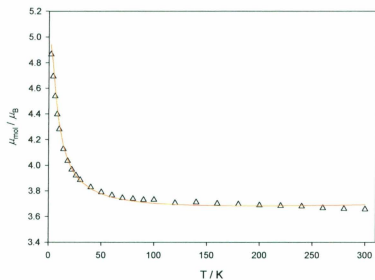
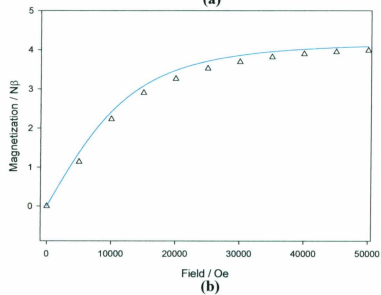


**Figure 3.15:** Variable field magnetization data for **3.4**; solid line represents simulation with  $g = 2.07$ ,  $T = 2$  K,  $S' = 2$ .

Complexes **3.5** (Figure 3.16) and **3.7** (Figure 3.17) were both treated by the same magnetic model, exchange expression and isotropic exchange Hamiltonian as **3.4**. All three exhibit dominant intramolecular ferromagnetic coupling and dominant  $d_{x^2-y^2}$  magnetic ground states for the distorted square pyramidal Cu(II) centres. Fitted exchange values are summarized in Table 3.13.

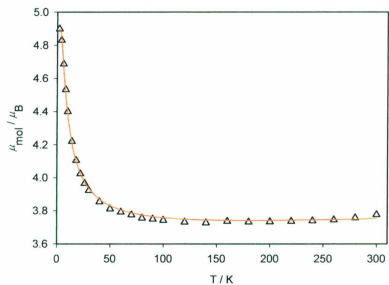


(a)

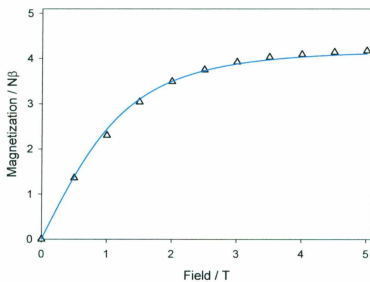


(b)

**Figure 3.16:** a) Variable temperature magnetic data for **3.5**;  $g = 2.073(7)$ ,  $J = 7.62(8) \text{ cm}^{-1}$ ,  $\theta = 0 \text{ K}$ ,  $\text{TIP} = 210 \times 10^{-6} \text{ cm}^3 \text{ mol}^{-1}$ ,  $\rho = 0.1$ ,  $10^2 R = 2.16$ . b) Variable field magnetization data for **3.5**; solid line represents simulation with  $g = 2.073$ ,  $T = 2 \text{ K}$ ,  $S' = 2$ .



(a)



(b)

**Figure 3.17:** a) Variable temperature magnetic data for **3.7**;  $g = 2.102(3)$ ,  $J = 7.2(5) \text{ cm}^{-1}$ ,  $\theta = -0.2 \text{ K}$ ,  $\text{TIP} = 250 \times 10^{-6} \text{ cm}^3 \text{ mol}^{-1}$ ,  $\rho = 0$ ,  $10^2 R = 0.44$ . b) Variable field magnetization data for **3.7**; solid line represents simulation with  $g = 2.1$ ,  $T = 2 \text{ K}$ ,  $S' = 2$ .

Compound **3.8** consists of a Mn(II) trigonal bipyramidal cluster with each Mn(II) centre bridged by single hydrazone oxygen atoms, with large, similar Mn-O-Mn angles. The magnetic profile for **3.8** is shown in Figure 3.18 as a plot of moment per mole as a function of temperature. The moment drops from 12.8  $\mu_B$  at 300 K to 5.9  $\mu_B$  at 2 K and the profile is characteristic of the presence of intramolecular antiferromagnetic exchange. The low temperature value indicates the presence of one uncompensated Mn(II) centre in the ground state ( $S = 5/2$ ), and is associated with the odd number of spin centres in the cluster.

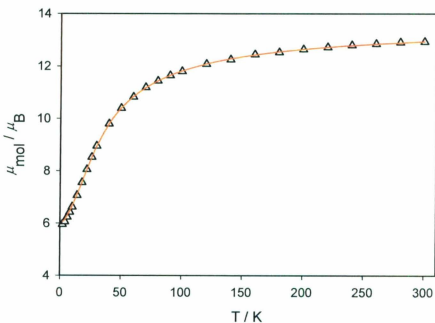


**Figure 3.18:** Variable temperature magnetic data for **3.8**;  $g = 2.015$ ,  $J = -2.65 \text{ cm}^{-1}$ ,  $\theta = 0$  K,  $\text{TIP} = 0 \text{ cm}^3 \text{ mol}^{-1}$ ,  $\rho = 0.0001$ ,  $10^2 R = 0.44$ .

The magnetic exchange model for **3.8** involves six exchange pathways (Figure 3.12c), all of which are considered of equal magnitude based on the similarity of the Mn-O-Mn bond angles. The isotropic exchange Hamiltonian (equation 3.5) describes the exchange situation:

$$\begin{aligned}
 H_{ex} &= -J(S_1 \cdot S_3 + S_4 \cdot S_3 + S_5 \cdot S_3 + S_1 \cdot S_2 + S_5 \cdot S_2 + S_4 \cdot S_2) & (3.5) \\
 &= -J\{S_3(S_1 + S_4 + S_5) + S_2(S_1 + S_5 + S_4)\} \\
 &= -J\{(S_2 + S_3)(S_1 + S_4 + S_5)\} \\
 &= -J(S_{23} \cdot S_{145}) \\
 &= -J/2(S^2 - S_{23}^2 - S_{145}^2)
 \end{aligned}$$

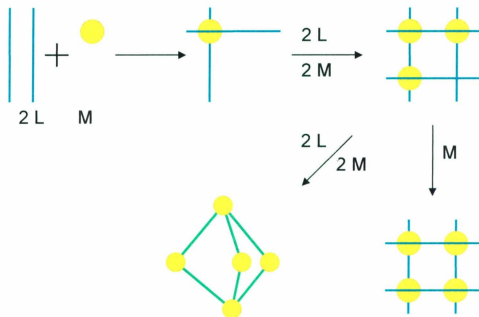
Where  $S_{23} = S_2 + S_3$ ;  $S_{15} = S_1 + S_5$ ;  $S_{145} = S_{15} + S_4$ ;  $S = S_{23} + S_{145}$  ( $S = S_n$  ( $n = 1-5) = 5/2$ ) with eigenvalues  $E(S, S_{23}, S_{145}) = J/2[S(S+1) - S_{23}(S_{23}+1) - S_{145}(S_{145}+1)]$ . The allowed values of  $S$ ,  $S_{23}$  and  $S_{145}$ , and their appropriate energies, were then substituted into the Van Vleck equation (equation 3.3) to create a susceptibility profile as a function of temperature. The experimental magnetic data were fitted by non-linear regression within MAGMUN4.1 [49] to give  $g = 2.015$ ,  $J = -2.65 \text{ cm}^{-1}$ ,  $\theta = -1 \text{ K}$ ,  $\text{TIP} = 0 \text{ cm}^3 \text{ mol}^{-1}$ ,  $\rho = 0.0001$  ( $10^2 R = 0.44$ ). The solid line in Figure 3.18 was calculated with these parameters. The magnitude of the observed antiferromagnetic exchange is in agreement with similar pentanuclear clusters [58,61,64,65].

**Table 3.13:** Summary of the magnetic analysis of **3.2 - 3.5, 3.7** and **3.8**.

Compound	g	J (cm <sup>-1</sup> )	Ground State Spin (S')
<b>3.2</b> (Mn(II) <sub>3</sub> cluster)	2.04(2)	-3.03(1)	2.5
<b>3.3</b> (Ni(II) <sub>4</sub> square grid)	2.25(1)	-13.3(8)	0
<b>3.4</b> (Cu(II) <sub>4</sub> square grid)	2.07(0)	7.2(8)	2
<b>3.5</b> (Cu(II) <sub>4</sub> square grid)	2.073(7)	7.62(8)	2
<b>3.7</b> (Cu(II) <sub>4</sub> square grid)	2.102(3)	7.2(5)	2
<b>3.8</b> (Mn(II) <sub>5</sub> trigonal bipyramid)	2.015	-2.65	2.5

### 3.4: Summary:

The mononuclear and trinuclear complexes **3.6** and **3.2** can be envisaged as possible components in the assembly of a full grid, but for **3.2**, because of the particular orientation of the ligands at the fourth empty site (congruence of two methyl imidazole groups), the steric congestion prevents additional metal coordination. Compound **3.1** shows that two ligands can coordinate to one metal, but then embrace a second metal, in what again could be a component in grid assembly. This case is complicated by the redox instability of the reaction mixture with oxidation of one cobalt(II) site. This has been observed before, but in a fully assembled [2×2] grid [59]. Complexes **3.3-3.5** and **3.7** are complete grids, with the ligands arranged so that steric congestion associated with the imidazole methyl groups is eliminated, while **3.8** is a trigonal bipyramid which reasonably results from an exact match between the number of available donor sites from six ligands and the coordination requirements of five octahedral Mn(II) centres, in the presence of a weakly coordinating anion (perchlorate). This illustrates the dynamic and flexible nature of the coordination process in terms of the available ligand conformational options, and the influence of the thermodynamic stability of the [2×2] grid arrangement in the nickel and copper cases. A possible route to self-assembly, based on structural evidence from **3.1-3.8**, is presented in Scheme 3.1.



**Scheme 3.1:** Possible route to the self-assembly of  $[2 \times 2]$  grids and trigonal bipyramidal  $M_5$  clusters.

Another important factor to consider in grid assembly is the presence of the largely repulsive face-to-face  $\pi$ - $\pi$  interactions associated with the parallel and eclipsed arrangement of the terminal pyridine/pyrimidine rings. While these interactions are minimized in **3.3** by a slightly offset pseudo-eclipsed parallel ligand arrangement, for the  $[2 \times 2]$   $Cu(II)_4$  grids (**3.4**, **3.5** and **3.7**) and the trigonal bipyramidal  $Mn(II)_5$  cluster (**3.8**) they are considerably reduced since each terminal pyridine/pyrimidine ring is instead in parallel alignment with an imidazole ring.

Where direct hydrazone oxygen bridges exist with non-orthogonal magnetic orbital overlap between metal centres, antiferromagnetic exchange occurs, but in the case of the copper(II)  $[2 \times 2]$  grids, ferromagnetic exchange results because of the orthogonal

bridging pathways. The observed magnetic properties are in agreement with structural characterization, and in particular the identification of Jahn-Teller axes leading to ferromagnetism in 3.4, 3.5 and 3.7.

**Chapter 4: [3×3] M(II)<sub>9</sub> grids (M = Mn, Co, Cu, Zn) from self-assembly reactions  
with a picolinic dihydrazone ligand**

**4.1: Preamble:**

Tritopic picolinic dihydrazone ligands capable of forming five-membered chelate rings upon self-assembly with first-row transition metals (Figure 4.1) have led to the synthesis of [3×3] M<sub>9</sub> (M = Mn, Fe, Ni, Cu, Zn) grids [29,30,66-74,96].

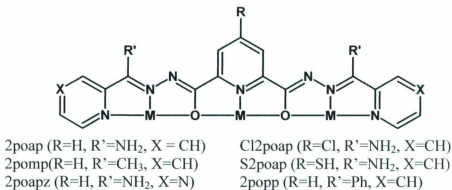
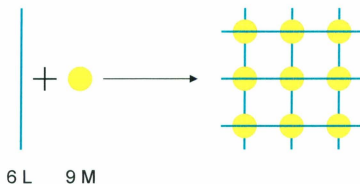


**Figure 4.1:** Examples of tritopic, metal-coordinated, ligands suitable for the formation of [3×3] M<sub>9</sub> (M = Mn, Fe, Ni, Cu, Zn) grids.

Homoleptic, self-assembled [3×3] grids result from the exact balance of the available number of donor sites provided by the six ligands arranged with three parallel ligands above and below a plane of nine pseudo-octahedral  $\mu$ -O-bridged metal ions (Scheme 4.1).



**Scheme 4.1:** Self-assembled [3×3] grid.

Complexes of this nature have attracted much attention for their possible suitability for a ‘bottom-up’ approach to the construction of nanoscale materials for application as electronic or computer components. Before such materials can be developed however, there are two criteria that must be met by molecules under consideration:

1. Two or more distinguishable states with unique physical and chemical properties that can be accessed by external probes must exist.
2. These states and their external probes must be applicable on the nanoscale.

[3×3] grids are suitable for consideration as they possess unique magnetic and redox properties that could possibly serve as independent states within a single molecule, in addition to forming two-dimensional arrangements that bear a remarkable likeness to existing cross-bar structures used in conventional information storage and computer processing. Finally, they have been shown to assemble in an ordered manner upon deposition onto surfaces which provides an opportunity for individual molecules and individual metal centres to be addressed uniquely [25].

Antiferromagnetic examples of  $[3 \times 3]$  grids are most common, with Mn, Fe and Ni cases reported [29,30,69,70,73], while  $\text{Cu(II)}_9$  grids exhibit magnetic orbital orthogonality resulting from the perpendicular orientation of the Jahn-Teller axes in the outer-ring of eight metal centres, leading to dominant ferromagnetic exchange [66,69,71,96]. Torque magnetometry and inelastic neutron scattering studies performed on  $\text{Mn(II)}_9$  grid systems have also shown field-induced level crossing and a change of the magnetic anisotropy from easy-axis to hard-axis type [97,98].

$[3 \times 3]$   $\text{Mn(II)}_9$  grids exhibit a series of oxidation waves upon application of a suitable potential [29,30,73]. Cyclic voltammetry and differential pulse voltammetry were performed on a solution of  $[\text{Mn}_9(2\text{poap-2H})_6](\text{ClO}_4)_6 \cdot 18\text{H}_2\text{O}$  in acetonitrile and showed five quasi-reversible waves with oxidation peaks present at approximately +0.61 V, +0.92 V, +1.13 V, +1.33 V and +1.53 V [29,30]. Coulometry showed that the first wave corresponded to a four-electron oxidation, followed by four one-electron processes. Each was assigned as an oxidation from  $\text{Mn(II)}$  to  $\text{Mn(III)}$ , with the first wave assigned as the oxidation of the corner sites, with each successive one-electron oxidation corresponding to the oxidation of the side sites. It was also shown that upon application of a 20 V potential in a bulk electrolysis experiment that the mixed-oxidation complex  $[\text{Mn}^{\text{II}}_5\text{Mn}^{\text{III}}_4(2\text{poap-2H})_6](\text{ClO}_4)_{10} \cdot 10\text{H}_2\text{O}$  could be isolated and characterized [29]. The  $\text{Mn(III)}$  sites were present in the corner positions of this grid. Variable temperature and magnetization data indicate an  $S = \frac{1}{2}$  ground state, consistent with a model in which the  $\text{Mn(III)}$  ( $S = 2$ ) centres couple antiferromagnetically with the  $\text{Mn(II)}$  ( $S = 5/2$ ) centres to produce an overall ferrimagnetic state.

Waldmann considered this molecule to be an actual experimental example of a mesoscopic  $S = \frac{1}{2}$  cluster suitable for consideration as an antiferromagnetic qubit cluster [31]. While further anisotropic studies are required to assess the ability of the unpaired spin in the ground state to tunnel from a 'spin up' to a 'spin down' configuration, were it possible for this tunneling to take place without energy transfer, the system would exhibit tunneling coherence and would be suitable for consideration as a qubit [33].

Scanning tunneling microscopy (STM) and current imaging tunneling spectroscopy (CITS) studies were conducted on a surface deposition of a  $[3 \times 3]$  Mn(II)<sub>9</sub> grid, formed from the reaction of Cl<sub>2</sub>poap (Figure 4.1) with Mn(ClO<sub>4</sub>)<sub>2</sub>·6H<sub>2</sub>O [70], on highly oriented pyrolytic graphite (HOPG) [28,99]. A drop of Mn(II)<sub>9</sub> grid in acetonitrile was deposited on an HOPG surface and allowed to evaporate. STM imaging was performed to reveal several different motifs, including a line, ribbons, arrays and various associations of random molecules. CITS studies revealed molecular dimensions of 2.4×2.4 nm, and nine regularly spaced peaks separated by 0.4 nm, in agreement with the Mn-Mn separation in the X-ray structure.

In this chapter, self-assembly reactions between 2pmoap (**2.4**; Figure 4.2a), and Zn(II), Mn(II), Co(II), and Cu(II) salts to produce  $[3 \times 3]$  M<sub>9</sub> grids are reported. One example of a ligand hydrolysis (pmoapCOO, Figure 4.2b) complex is also reported as a side-reaction upon recrystallization of a Cu(II)<sub>9</sub> grid from an aqueous solution. This type of *in situ* ligand hydrolysis has been previously reported for Cl<sub>2</sub>popp (Figure 4.2) [100]. While the terminal pyrimidine moiety was chosen to encourage secondary coordination

of homo- or heterometal ions on outside of the predicted  $[3 \times 3] M_9$  grids, reactions towards this end instead produced heterometallic grids, discussed in Chapter 5.

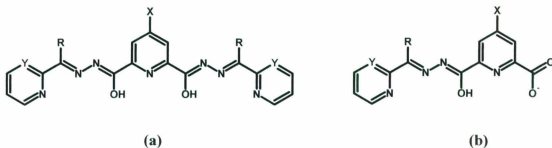


**Figure 4.2:** a) 2pmoap (**2.4**; Y=N, R=NH<sub>2</sub>, X=H), Cl2popp (Y=CH, R=Ph, X=Cl); b) the *in situ* hydrolysis product of 2pmoap (pmpoapCOO; Y=N, R=NH<sub>2</sub>, X=H) and of Cl2popp (poppCOO; Y=CH, R=Ph, X=Cl).

#### 4.2: Experimental:

**Note:** In some cases there is a difference between the most reasonable formula based on the elemental analysis (analytical formula), and that obtained from X-ray crystallography. The analytical formulae will be used here.

##### 4.2.1: Complex synthesis:

**4.2.1.1:**  $[(2\text{pmoap-H})_6\text{Zn}_9](\text{NO}_3)_{12} \cdot 12\text{H}_2\text{O}$  (**4.1**). 2pmoap (0.15 g, 0.37 mmol) was added to a solution of  $\text{Zn}(\text{NO}_3)_2 \cdot 6\text{H}_2\text{O}$  (0.17 g, 0.57 mmol) in methanol:acetonitrile (7 mL : 7 mL) forming a clear yellow solution to which three drops of triethylamine was added. This was left to stir with gentle heating for 4 hours. The solution was filtered and allowed to stand at room temperature. X-ray quality, yellow prismatic crystals formed after 14 days. (0.04 g, 17 % yield). Anal. calcd (%) for  $(\text{C}_{17}\text{H}_{14}\text{N}_{11}\text{O}_2)_6\text{Zn}_9(\text{NO}_3)_{10}(\text{H}_2\text{O})_{12}$  (bulk dried sample): C, 30.82; H, 2.73; N, 27.49. Found (%): C, 30.97; H, 2.61; N, 27.28.

**4.2.1.2:**  $[\text{Mn}_9(2\text{pmoap-2H})_6](\text{NO}_3)_6 \cdot 13(\text{H}_2\text{O})$  (**4.2**). 2pmoap (0.49 g, 1.2 mmol) was added to a solution of excess  $\text{Mn}(\text{NO}_3)_2 \cdot 6\text{H}_2\text{O}$  (1.01 g, 3.50 mmol) in methanol: acetonitrile (20 mL:20 mL) initially forming a clear, light yellow solution. This was left to stir with gentle heating for 2 hours. It was then filtered and solvent was removed from the filtrate to yield 0.96 g of a yellow powder. This was dissolved in methanol: acetonitrile (10 mL:10 mL) to give a clear, yellow solution.  $\text{NH}_4\text{CH}_3\text{COO}$  (0.040 g, 0.51 mmol) was added producing a clear, deep red coloured solution that was stirred with gentle heating ( $\sim 55^\circ\text{C}$ ) for 1 hour, and at room temperature for three hours. This solution was filtered and allowed to stand at room temperature. X-ray quality, red prismatic crystals formed after three days (0.86 g, 96% yield). Anal. calcd (%) for  $(\text{C}_{17}\text{H}_{13}\text{N}_{11}\text{O}_2)_6\text{Mn}_9(\text{NO}_3)_6(\text{H}_2\text{O})_{13}$  (bulk dried sample): C, 34.78; H, 2.98; N, 28.65. Found (%): C, 34.35; H, 2.70; N, 28.94.

**4.2.1.3:**  $[(2\text{pmoap-2H})_6\text{Co}_9](\text{NO}_3)_6 \cdot 24\text{H}_2\text{O}$  (**4.3**). 2pmoap (0.12 g, 0.30 mmol) was added to  $\text{Co}(\text{NO}_3)_2 \cdot 6\text{H}_2\text{O}$  (0.13 g, 0.45 mmol) in 20 mL of 1:1 methanol:acetonitrile. This produced a clear, orange-brown solution that was stirred with gentle heating ( $\sim 55^\circ\text{C}$ ) for 3 hours and at room temperature for another 2 hours. The solution was filtered and the filtrate was preserved for crystallization. Crystals formed after 13 days, and were recrystallized from methanol and acetonitrile to give red prismatic crystals, suitable for X-ray diffraction, upon standing for an additional 17 days (0.15 g; 67% yield). Air was not excluded. Anal. calc. (%) for  $[(\text{C}_{17}\text{H}_{13}\text{N}_{11}\text{O}_2)_6\text{Co}_9](\text{NO}_3)_6 \cdot 24\text{H}_2\text{O}$ : C, 32.63; H, 3.38; N, 26.89. Found (%): C, 32.06; H, 2.77; N 27.43.

**4.2.1.4:** [(pmoapCOO)Cu](NO<sub>3</sub>) (**4.4**) and [(2pmoap-2H)<sub>6</sub>Cu<sub>9</sub>](NO<sub>3</sub>)<sub>6</sub>·35H<sub>2</sub>O (**4.5**).

2pmoap (0.11 g, 0.27 mmol) was added to a solution of excess Cu(NO<sub>3</sub>)<sub>2</sub>·6H<sub>2</sub>O (0.22 g, 0.74 mmol) in methanol:acetonitrile (7.5 mL:7.5 mL) forming a clear dark green solution that was stirred at room temperature for 18 hours. It was then filtered and a green powder was collected (0.09 g). This was redissolved in 20 mL of water with stirring at room temperature, then filtered and allowed to stand at room temperature. Crystals of two different morphologies, (blue (**4.4**) and brown (**4.5**) prisms) suitable for structural analysis were observed after 39 days. **4.4**: 0.011 g, 35 % yield; **4.5**: 0.050 g, 37 % yield (based on an assumption of a 1:3 ratio of products). Anal. calcd (%) for **4.4** (C<sub>12</sub>H<sub>9</sub>CuN<sub>6</sub>O<sub>3</sub>)(NO<sub>3</sub>)(H<sub>2</sub>O)<sub>0.25</sub> (bulk dried sample): C, 34.71; H, 2.31; N, 23.61. Found (%): C, 34.54; H, 2.08; N, 23.90. Anal. calcd (%) for **4.5**(C<sub>17</sub>H<sub>13</sub>N<sub>11</sub>O<sub>2</sub>)<sub>6</sub>Cu<sub>9</sub>(NO<sub>3</sub>)<sub>6</sub>(H<sub>2</sub>O)<sub>35</sub> (bulk dried sample): C, 30.67; H, 3.73; N, 25.25. Found (%): C, 30.66; H, 2.13; N, 25.91.

**4.2.1.5:** [Cu<sub>9</sub>(2pmoap-2H)<sub>2</sub>(2pmoap-H)<sub>4</sub>](ClO<sub>4</sub>)<sub>10</sub>·14H<sub>2</sub>O·7CH<sub>3</sub>OH (**4.6**). 2pmoap (0.12 g, 0.30 mmol) was added to a warm solution of Cu(ClO<sub>4</sub>)<sub>2</sub>·6H<sub>2</sub>O (0.13 g, 0.35 mmol) in methanol:acetonitrile (10 mL : 10 mL). A clear, dark green solution formed. The solution remained clear and dark green upon the addition of 3 drops of triethylamine. It was stirred with gentle heating for 45 minutes and kept after filtration for crystallization. X-ray quality, green prismatic crystals formed after standing at room temperature for two weeks (0.030 g, 15% yield). Anal. calcd (%) for (C<sub>17</sub>H<sub>13</sub>N<sub>11</sub>O<sub>2</sub>)<sub>2</sub>(C<sub>17</sub>H<sub>14</sub>N<sub>11</sub>O<sub>2</sub>)<sub>4</sub>Cu<sub>9</sub>(ClO<sub>4</sub>)<sub>10</sub>(H<sub>2</sub>O)<sub>14</sub>(CH<sub>3</sub>OH)<sub>7</sub> (bulk sample): C, 29.31; H, 3.11; N, 20.69. Found (%): C, 29.31; H, 2.34; N, 20.91.

#### 4.2.2: Crystallography

The diffraction intensities of a yellow prismatic crystal of **4.1** having approximate dimensions of  $0.39 \times 0.35 \times 0.24$  mm were collected on a Rigaku Saturn CCD area detector with graphite monochromated Mo-K $\alpha$  radiation at 113(2) K to a maximum  $2\theta$  value of  $62.2^\circ$ . The data were corrected for Lorentz and polarization effects and a correction for secondary extinction [81] was applied. The structure was solved by direct methods [82,83] and expanded using Fourier techniques [84]. Hydrogen atoms were introduced in calculated positions with isotropic thermal parameters set twenty percent greater than those of their bonding partners. They were refined on the riding model. O(17), O(18) and one nitrate ion were refined isotropically, while all other non-hydrogen atoms were refined anisotropically. Neutral atom scattering factors and anomalous dispersion effects were taken from the usual sources [85-88]. All calculations were performed using the Crystal Structure [89,90] crystallographic software package except for refinement, which was performed using SHELXL-97 [83].

The chip of a red crystal of **4.2** having approximate dimensions of  $0.23 \times 0.20 \times 0.17$  mm was treated similarly to **4.1**. Hydrogen atoms were introduced in calculated positions with isotropic thermal parameters set twenty percent greater than those of their bonding partners. They were refined on the riding model. All non-hydrogen atoms were refined anisotropically except one half-occupancy nitrate anion and seven partial occupancy lattice water molecules that were refined isotropically.

A red prismatic crystal of **4.3** having approximate dimensions of  $0.64 \times 0.60 \times 0.53$  mm was treated similarly to **4.1**. All hydrogen atoms were introduced in calculated

positions with isotropic thermal parameters set twenty percent greater than those of their bonding partners. They were refined on the riding model. Two lattice acetonitriles were refined isotropically, while all other non-hydrogen atoms were refined anisotropically. A Platon [91] check suggested that a symmetry element was missed and that this should be solved in tetragonal space group  $I4_1/acd$  (#142), however, the reflections failed a tetragonal Laue check, and instead passed a Laue check as F-centred orthorhombic.

An irregular, blue crystal of **4.4** having approximate dimensions of  $0.20 \times 0.19 \times 0.18$  mm was treated similarly to **4.1**. Hydrogen atoms were introduced in calculated or difference map (H(4)) positions with isotropic thermal parameters set twenty percent greater than those of their bonding partners. They were refined on the riding model. All non-hydrogen atoms were refined anisotropically.

A brown, prismatic crystal of **4.5** having approximate dimensions of  $0.50 \times 0.24 \times 0.19$  mm was treated similarly to **4.1**. Hydrogen atoms were introduced in calculated positions with isotropic thermal parameters set twenty percent greater than those of their bonding partners. They were refined on the riding model. One half-occupancy nitrate ion was refined isotropically and positional-refinement of its N(19) was not performed in the final round of least squares, 5.125 water solvent molecules were refined isotropically while all other non-hydrogen atoms were refined anisotropically.

A brown, prismatic crystal of **4.6** having approximate dimensions of  $0.17 \times 0.11 \times 0.09$  mm was treated similarly to **4.1**. Hydrogen atoms were introduced in calculated or difference map positions (H(21)) with isotropic thermal parameters set twenty percent greater than those of their bonding partners. They were refined on the riding model. The

model contains one half occupancy perchlorate anion and seven partial occupancy water molecules as lattice solvent which was refined isotropically. All other non-hydrogen atoms were refined anisotropically. Abbreviated crystal data for **4.1 - 4.6** are listed in Tables 4.1 - 4.3.

**Table 4.1:** Summary of crystallographic data for **4.1 - 4.2**.

	<b>4.1</b>	<b>4.2</b>
Chemical Formula	C <sub>102</sub> H <sub>109</sub> N <sub>72</sub> O <sub>45.5</sub> Zn <sub>9</sub>	C <sub>102</sub> H <sub>134</sub> Mn <sub>9</sub> N <sub>72</sub> O <sub>58</sub>
M	3659.94	3791.07
T(K)	113(2)	153(2)
Crystal System	tetragonal	tetragonal
Space Group	I4 <sub>1</sub> /acd (#142)	I4 <sub>1</sub> /acd (#142)
a (Å)	27.668(4)	27.9255(13)
b (Å)	27.668(4)	27.9255(13)
c (Å)	38.890(7)	40.217(2)
α (°)	90.00	90.00
β (°)	90.00	90.00
γ (°)	90.00	90.00
V (Å <sup>3</sup> )	29770(8)	31362(3)
Z	8	8
D <sub>calc</sub> (g/cm <sup>3</sup> )	1.633	1.606
μ(MoKα) (cm <sup>-1</sup> )	15.28	8.09
Reflections Total	104796	151450
Reflections Unique	6545	11887
R <sub>int</sub>	0.0584	0.0591
R <sub>1</sub> (I > 2.00σ(I))	0.1275	0.1278
wR <sub>2</sub> (All reflections)	0.3481	0.3049

**Table 4.2:** Summary of crystallographic data for 4.3 - 4.4.

	4.3	4.4
Chemical Formula	$C_{106}H_{106}Co_9N_{74}O_{41}$	$C_{12}H_9CuN_7O_6$
M	3602.87	410.80
T(K)	153(2)	113(2)
Crystal System	orthorhombic	monoclinic
Space Group	Fddd (#70)	$P2_1/n$ (#14)
a (Å)	39.369(3)	8.6190(18)
b (Å)	39.416(3)	9.1399(17)
c (Å)	39.411(3)	18.120(4)
$\alpha$ (°)	90.00	90.00
$\beta$ (°)	90.00	94.220(5)
$\gamma$ (°)	90.00	90.00
V (Å <sup>3</sup> )	61157(8)	1423.6(5)
Z	16	4
D <sub>calc</sub> (g/cm <sup>3</sup> )	1.565	1.917
$\mu$ (MoK $\alpha$ ) (cm <sup>-1</sup> )	10.51	15.89
Reflections Total	133536	21924
Reflections Unique	15853	3280
R <sub>int</sub>	0.0415	0.0273
R <sub>1</sub> ( $I > 2.00\sigma(I)$ )	0.0988	0.0405
wR <sub>2</sub> (All reflections)	0.2877	0.0998

**Table 4.3:** Summary of crystallographic data for **4.5 - 4.6**.

	<b>4.5</b>	<b>4.6</b>
Chemical Formula	C <sub>102</sub> H <sub>119</sub> Cu <sub>9</sub> N <sub>72</sub> O <sub>50.5</sub>	C <sub>102</sub> H <sub>108.4</sub> Cl <sub>10</sub> Cu <sub>9</sub> N <sub>66</sub> O <sub>65.2</sub>
M	3733.43	4228.43
T(K)	113(2)	153(2)
Crystal System	tetragonal	tetragonal
Space Group	I4 <sub>1</sub> /acd (#142)	P4 <sub>2</sub> /n (#86)
a (Å)	27.841(2)	20.9857(14)
b (Å)	27.841(2)	20.9857(14)
c (Å)	38.298(3)	17.3731(12)
α (°)	90.00	90.00
β (°)	90.00	90.00
γ (°)	90.00	90.00
V (Å <sup>3</sup> )	29686(4)	7651.1(9)
Z	8	2
D <sub>calc</sub> (g/cm <sup>3</sup> )	1.671	1.834
μ(MoKα) (cm <sup>-1</sup> )	13.72	15.17
Reflections Total	60270	75957
Reflections Unique	7277	10853
R <sub>int</sub>	0.0403	0.0535
R <sub>1</sub> (I > 2.00σ(I))	0.1055	0.1023
wR <sub>2</sub> (All reflections)	0.3060	0.2479

### 4.3: Results and Discussion:

**Note:** The crystallographically determined formulae are used herein. Colour code for figures: purple = cobalt, magenta = manganese, green = copper, yellow = zinc, grey = carbon, blue = nitrogen, red = oxygen. Crystallographic representations/illustrations were generated using Persistence of Vision Ray Tracer (POV-Ray©) for Windows, version 3.6, with scene description files written by Ortep-3 for Windows (Version 1.08) Copyright© 1997-2003 Louis J. Farrugia.

4.3.1: Description of crystal structures:

#### 4.3.1.1: [(2pmpoa-2H)<sub>6</sub>Zn<sub>9</sub>](NO<sub>3</sub>)<sub>6</sub>·15.5H<sub>2</sub>O (**4.1**)

The structure of the cationic fragment of **4.1** and its core structural representation are shown in Figures 4.3a and 4.3b respectively, and significant bond lengths and angles are listed in Table 4.4.

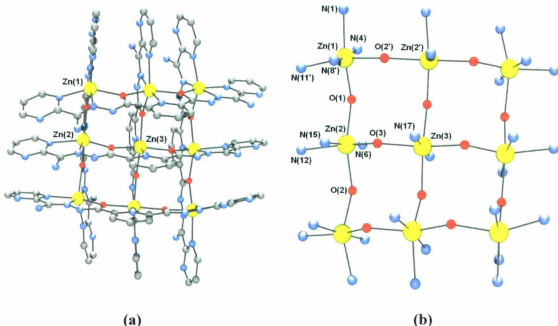


**Figure 4.3:** a) Ball-and-stick depiction of the cationic moiety **4.1**. Hydrogen atoms omitted for clarity. b) Core structural representation of **4.1**.

The structure has tetragonal crystallographic symmetry, which is manifested as four-fold symmetry within the grid cation (Figure 4.3a). The homoleptic grid arrangement results from the roughly parallel arrangement of three heptadentate ligands arranged above and another three below a  $[Zn_9-(\mu-O)_{12}]$  core composed of nine metal ions bridged by twelve hydrazone oxygen atoms (Figure 4.3b). Zn-Zn distances fall in the range 3.945(2) - 4.0985(17) Å, with Zn-O-Zn angles in the range 135.1(3) - 136.4(3) $^\circ$  and distances between corner Zn(II) centres (overall metal-metal grid dimensions) of 8.0185(19) Å. The corner Zn(II) centres have *cis*-ZnN<sub>4</sub>O<sub>2</sub> coordination environments, while the side centres have *mer*-ZnN<sub>3</sub>O<sub>3</sub> environments, and the centre Zn(II) ion has a *trans*-ZnN<sub>2</sub>O<sub>4</sub> coordination environment. Corner and side Zn centres display long Zn-N distances to the external pyrimidine rings (2.147(9) - 2.299(9) Å), likely due to the

stretching of the ligands over the nonanuclear core, with shorter remaining Zn-N contacts (1.980(8) - 2.037(7)Å). Significant  $\pi$ -interactions between the pyrimidine and pyridine rings within the cation are indicated by their arrangement in an approximately parallel fashion with short inter-ring separations of 3.765(7) - 3.825(7) Å (pyrimidine) and 3.612(5) Å (pyridine).

**Table 4.4:** Selected bond distances (Å) and angles (°) for **4.1**.

Zn(1)	O(1)	2.137(6)	Zn(2)	N(15)	1.980(8)	
Zn(1)	O(2)	2.213(6)	Zn(3)	O(3)	2.166(6)	
Zn(1)	N(1)	2.208(10)	Zn(3)	N(17)	2.031(9)	
Zn(1)	N(4)	1.994(9)	Zn(1)	Zn(2)	3.9917(23)	
Zn(1)	N(8)	1.995(9)	Zn(1)	Zn(2')	4.0985(17)	
Zn(1)	N(11)	2.147(9)	Zn(2)	Zn(3)	3.945(2)	
Zn(2)	O(1)	2.183(6)	Zn(1)	O(1)	Zn(2)	135.1(3)
Zn(2)	O(2)	2.207(6)	Zn(2)	O(2)	Zn(1)	136.1(3)
Zn(2)	O(3)	2.083(6)	Zn(2)	O(3)	Zn(3)	136.4(3)
Zn(2)	N(6)	2.037(7)				
Zn(2)	N(12)	2.299(9)				

**4.3.1.2:** [(2pmoap-2H)<sub>6</sub>Mn<sub>9</sub>](NO<sub>3</sub>)<sub>6</sub>·28H<sub>2</sub>O (**4.2**)

The structure of the cationic fragment of **4.2** and its core structural representation are shown in Figures 4.4a and 4.4b respectively, and significant bond lengths and angles are listed in Table 4.5.

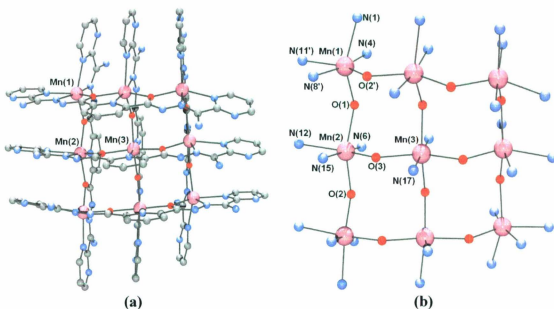


**Figure 4.4:** a) Ball-and-stick depiction of the cationic moiety **4.2**. Hydrogen atoms omitted for clarity. b) Core structural representation of **4.2**.

Complex **4.2** also has tetragonal crystallographic symmetry, and four-fold symmetry within the grid cation (Figure 4.4a). Ligands are arranged, three above and three below, a  $[\text{Mn}_9-(\mu\text{-O})_{12}]$  hydrazone oxygen-bridged core of nine distorted octahedral metals (Figure 4.4b). Mn-Mn distances fall in the range 3.9117(11) - 3.9684(11) Å, with Mn-O-Mn angles in the range 127.61(17) - 128.65(15)° and distances between corner Mn(II) centres (the metal-metal grid footprint) of 7.7972(11) Å. The corner Mn(II) centres have *cis*- $\text{MnN}_4\text{O}_2$  coordination environments, while the side centres have *mer*- $\text{MnN}_3\text{O}_3$  environments, and the centre Mn(II) ion has a *trans*- $\text{MnN}_2\text{O}_4$  coordination environment. Corner and side Mn centres display long Mn-N distances to the external pyrimidine rings (2.280(5) - 2.373(5) Å), with shorter remaining Mn-N contacts (2.135(5) - 2.183(4) Å). Significant  $\pi$ -interactions between the pyrimidine and pyridine

rings are indicated by short inter-ring separations of 3.761(3) - 3.784(3) Å (pyrimidine) and 3.625(2) Å (pyridine). These values are similar to those reported for the parent complex  $[\text{Mn}_9(\text{2poap-2H})_6](\text{ClO}_4)_6$  (see Figure 4.1 for 2poap) [30]. Each terminal, non-coordinating pyrimidine nitrogen atom and the amine  $\text{NH}_2$  groups of each ligand are in a suitable binding mode for possible secondary metal ion coordination, with  $N_{\text{amine}}\text{-C-C-N}_{\text{pyrimidine}}$  torsional angles between 176.5 and 179.3°. Reactions between **4.2** and other metal salts (Cu(II), Ni(II), Zn(II)) have instead, so far produced only heterometallic [3×3] grids with Mn atom site substitution (see Chapter 5).

**Table 4.5:** Selected bond distances (Å) and angles (°) for **4.2**.

Mn(1) O(1)	2.200(4)	Mn(2) N(15)	2.145(4)
Mn(1) O(2)	2.162(4)	Mn(3) O(3)	2.199(3)
Mn(1) N(1)	2.280(5)	Mn(3) N(17)	2.182(5)
Mn(1) N(4)	2.145(5)	Mn(1) Mn(2)	3.9684(11)
Mn(1) N(8)	2.135(5)	Mn(1) Mn(2')	3.9117(11)
Mn(1) N(11)	2.309(5)	Mn(2) Mn(3)	3.924(2)
Mn(2) O(1)	2.222(4)		
Mn(2) O(2)	2.197(4)	Mn(1) O(1)	Mn(2) 127.64(17)
Mn(2) O(3)	2.155(4)	Mn(1) O(2)	Mn(2) 127.61(17)
Mn(2) N(6)	2.183(4)	Mn(2) O(3)	Mn(3) 128.65(15)
Mn(2) N(12)	2.373(5)		

**4.3.1.3:**  $[(\text{2pmoap-2H})_6\text{Co}_9](\text{NO}_3)_6 \cdot 2\text{CH}_3\text{CN} \cdot 11\text{H}_2\text{O}$  (**4.3**)

The structure of the cationic fragment of **4.3** and its core structural representation are shown in Figures 4.5a and 4.5b respectively, and significant bond lengths and angles are listed in Table 4.6.

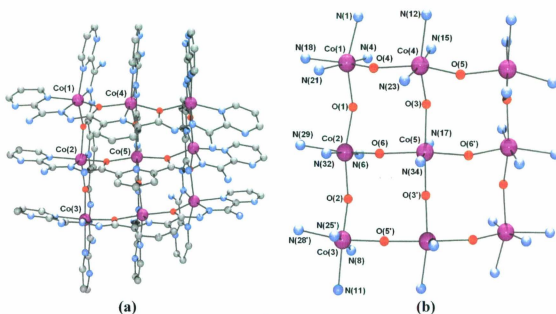


**Figure 4.5:** a) Ball-and-stick depiction of the cationic moiety **4.3**. Hydrogen atoms omitted for clarity. b) Core structural representation of **4.3**.

Unlike **4.1** and **4.2**, **4.3** has orthorhombic crystallographic symmetry, which is manifested as two-fold symmetry within the grid cation (Figure 4.5a). As in the other structures, however, **4.3** exhibits the expected arrangement of three heptadentate ligands arranged above and another three below a  $[\text{Co}_9-(\mu\text{-O})_{12}]$  core (Figure 4.5b). Co-Co distances fall in the range 3.9601(11) - 4.0384(11) Å, with Co-O-Co angles in the range 135.22(19) - 136.3(2)° and distances between corner Co(II) centres (metal-metal grid dimensions) of 7.9169(11) - 7.9181(11) Å. BVS (bond valence sum) values fall in the range 2.17-2.37, typical of Co(II) with this type of ligand [59,93]. The corner, side and central Co(II) centres have *cis*- $\text{CoN}_4\text{O}_2$ , *mer*- $\text{CoN}_3\text{O}_3$  and *trans*- $\text{CoN}_2\text{O}_4$  coordination environments, respectively. Significant  $\pi$ -interactions between the pyrimidine and pyridine rings are present with short inter-ring separations of 3.832(4) - 3.840(4) Å (pyrimidine) and 3.594(3) Å (pyridine).

**Table 4.6:** Selected bond distances (Å) and angles (°) for **4.3**

Co(1) O(1)	2.177(4)	Co(4) N(12)	2.212(6)
Co(1) O(4)	2.120(4)	Co(4) N(15)	2.009(5)
Co(1) N(1)	2.127(5)	Co(4) N(23)	2.041(5)
Co(1) N(4)	2.011(5)	Co(5) N(34)	2.020(7)
Co(1) N(18)	2.213(5)	Co(5) N(17)	2.029(7)
Co(1) N(21)	2.010(5)	Co(5) O(3)	2.151(4)
Co(2) O(1)	2.188(4)	Co(5) O(6)	2.154(4)
Co(2) O(2)	2.162(4)	Co(1) Co(2)	4.0375(11)
Co(2) O(6)	2.123(4)	Co(1) Co(4)	3.9601(11)
Co(2) N(6)	2.045(5)	Co(2) Co(3)	3.9601(11)
Co(2) N(29)	2.213(6)	Co(2) Co(5)	3.9701(8)
Co(2) N(32)	2.004(5)	Co(3) Co(4')	4.0384(11)
Co(3) O(2)	2.119(4)	Co(4) Co(5)	3.9696(8)
Co(3) O(5)	2.178(4)		
Co(3) N(8)	2.011(5)	Co(1) O(1) Co(2)	135.3(2)
Co(3) N(11)	2.217(5)	Co(1) O(4) Co(4)	135.22(19)
Co(3) N(25)	2.009(5)	Co(2) O(6) Co(5)	136.3(2)
Co(3) N(28)	2.125(5)	Co(3) O(2) Co(2)	135.36(19)
Co(4) O(3)	2.126(4)	Co(3) O(5) Co(4)	135.13(19)
Co(4) O(4)	2.163(4)	Co(4) O(3) Co(5)	136.3(2)
Co(4) O(5)	2.190(4)		

**4.3.1.4:** [(pmoapCOO)Cu](NO<sub>3</sub>) (**4.4**)

The structure of the mononuclear cationic fragment of **4.4** is shown in Figure 4.6, and significant bond lengths and angles are listed in Table 4.7.

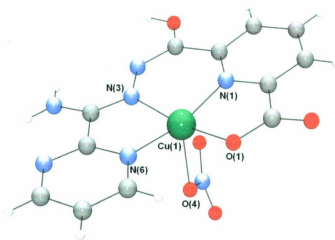


**Figure 4.6:** Ball-and-stick depiction of the cationic moiety **4.4**.

The structure of **4.4** is reminiscent of **3.6**, except that the coordinated acetonitrile molecule in **3.6** has been replaced by a carboxylate moiety resulting from the *in situ* hydrolysis of 2pmpop. A similar *in situ* ligand hydrolysis reaction for Cl2popp (Figure 4.2a) has been previously reported producing the ligand ClpoppCOO (Figure 4.2b) upon reaction of [(Cl2popp-2H)Ni] with  $\text{Cu}(\text{NO}_3)_2 \cdot 3\text{H}_2\text{O}$ , leading to the formation of [(ClpoppCOOCu)<sub>2</sub>Cu(H<sub>2</sub>O)<sub>2</sub>](NO<sub>3</sub>)<sub>2</sub>(H<sub>2</sub>O)<sub>3</sub>(CH<sub>3</sub>OH), a trinuclear Cu(II)<sub>3</sub> chain complex [100]. The basal plane of the square pyramidal copper centre in complex **4.4** exhibits short bonds to three ligand donor nitrogen atoms, and one short bond to a carboxylate oxygen atom (1.946(2) - 1.985(2) Å). A longer bond to an oxygen atom (O(4)) of a nitrate anion in the axial position (2.2476(18) Å) is also present. This defines the elongated Jahn-Teller axis and results in a  $d_{x^2-y^2}$  ground state with a calculated  $\tau$  value of 0.05 (ideal  $\tau$  values are 0 for square pyramids and 1 for trigonal bipyramids) [94].

**Table 4.7:** Selected bond distances (Å) and angles (°) for **4.4**.

Cu(1) O(1)	1.9553(18)	N(3) Cu(1) O(1)	168.14(8)
Cu(1) O(4)	2.2476(18)	N(1) Cu(1) N(6)	164.91(8)
Cu(1) N(1)	1.946(2)		
Cu(1) N(3)	1.9525(19)		
Cu(1) N(6)	1.985(2)		

**4.3.1.5:** [(2pmoap-2H)<sub>6</sub>Cu<sub>9</sub>](NO<sub>3</sub>)<sub>6</sub>·20.5H<sub>2</sub>O (**4.5**)

The structure of the cationic fragment of **4.5** and its core structural representation are shown in Figures 4.7a and 4.7b respectively, and significant bond lengths and angles are listed in Table 4.8.

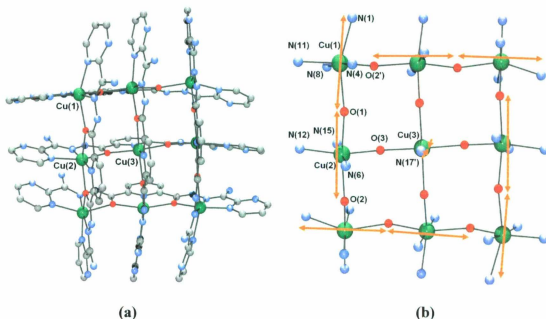


**Figure 4.7:** a) Ball-and-stick depiction of the cationic moiety **4.5**. Hydrogen atoms omitted for clarity. b) Core structural representation of **4.5**. Arrows highlight the Jahn-Teller axes.

Complex **4.5** also has tetragonal crystallographic symmetry, which is manifested as four-fold symmetry within the grid cation (Figure 4.7a). Three heptadentate ligands

are arranged above and another three below a  $[\text{Cu}_9-(\mu\text{-O})_{12}]$  core composed of nine metal ions bridged by twelve hydrazone oxygen atoms (Figure 4.7b). Cu-Cu distances fall in the range 4.0346(13) - 4.2970(11) Å, with Cu-O-Cu angles in the range 138.4(2) - 142.7(2)° and distances between corner Cu(II) centres of 8.2800(11). Each copper ion in the outer eight-membered ring has a Jahn-Teller distorted, axially elongated octahedral geometry (highlighted by the arrows in Figure 4.7b). Cu(1) has a  $d_{x^2-y^2}$  magnetic ground state as defined by short contacts to N(4), N(8), N(11), and O(2) (1.930(7) - 2.090(7)Å) with long axial contacts to N(1) and O(1) (2.215(7) - 2.323(5)Å). Cu(2) also exhibits a  $d_{x^2-y^2}$  ground state with short contacts to N(6), N(12), N(15), and O(3) (1.904(6) - 2.137(6)Å) and long axial contacts to O(1) and O(2) (2.243(5) - 2.266(5)Å). Cu(3) has axially compressed geometry ( $d_{z^2}$  magnetic ground state), with long contacts to O(3) and its symmetry related atoms (2.214(4) Å), and short bonds to N(17) and its symmetry related counterpart (1.933(7) Å). This arrangement sets up orbitally orthogonal magnetic connections in the outer ring of eight Cu(II) ions, with non-orthogonal connections between Cu(3) and its neighbors, and is characteristic of other  $\text{Cu}_9$  grids [66,69,71,96].

**Table 4.8:** Selected bond distances (Å) for and angles (°) for 4.5.

Cu(1)	O(1)	2.323(5)	Cu(2)	N(15)	1.904(6)	
Cu(1)	O(2)	2.072(5)	Cu(3)	O(3)	2.214(4)	
Cu(1)	N(1)	2.215(7)	Cu(3)	N(17)	1.933(7)	
Cu(1)	N(4)	1.995(7)	Cu(1)	Cu(2)	4.2970(11)	
Cu(1)	N(8)	1.930(7)	Cu(1)	Cu(2')	4.0346(13)	
Cu(1)	N(11)	2.090(7)	Cu(2)	Cu(3)	4.074(3)	
Cu(2)	O(1)	2.266(5)				
Cu(2)	O(2)	2.243(5)	Cu(1)	O(2')	Cu(2')	138.4(2)
Cu(2)	O(3)	2.086(4)	Cu(2)	O(1)	Cu(1)	138.9(2)
Cu(2)	N(6)	1.992(5)	Cu(2)	O(3)	Cu(3)	142.7(2)
Cu(2)	N(12)	2.137(6)				

#### 4.3.1.6: $[\text{Cu}_9(2\text{pmoap}-2\text{H})_2(2\text{pmoap}-\text{H})_4](\text{ClO}_4)_{10}\cdot 13.2\text{H}_2\text{O}$ (**4.6**)

The structure of the Cu(II)<sub>9</sub> grid fragment of **4.6** and its core structural representation are shown in Figures 4.8a and 4.8b respectively, and significant bond lengths and angles are listed in Table 4.9.

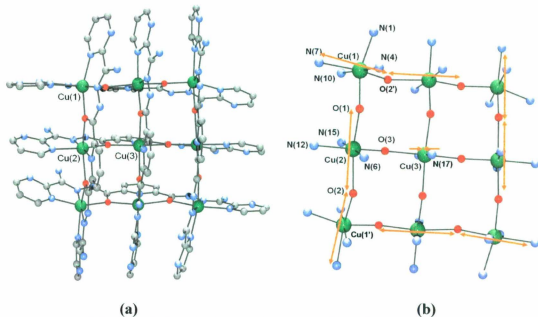


**Figure 4.8:** a) Ball-and-stick depiction of the cationic moiety **4.6**. Hydrogen atoms omitted for clarity. b) Core structural representation of **4.6**. Arrows highlight the Jahn-Teller axes.

Complex **4.6** also has tetragonal crystallographic symmetry, (Figure 4.8a) and a  $[\text{Cu}_9-(\mu\text{-O})_{12}]$  core (Figure 4.8b). Cu-Cu distances fall in the range 4.053(3) - 4.2555(8) Å, with Cu-O-Cu angles in the range 136.50(18) - 142.53(17)<sup>o</sup> and distances between corner Cu(II) centres of 8.2878(8) Å. Each copper ion in the outer eight-membered ring has a Jahn-Teller distorted, axially elongated octahedral geometry (highlighted by the arrows in Figure 4.7b). Cu(1) has a  $d_{x^2-y^2}$  magnetic ground state as defined by short

contacts to N(1), N(4), N(10), and O(1) (1.920(4) - 2.106(5) Å) with long axial contacts to N(7) and O(2) (2.248(5) - 2.298(4) Å). Cu(2) also exhibits a  $d_{x^2-y^2}$  ground state with short contacts to N(6), N(12), N(15), and O(3) (1.908(4) - 2.109(4) Å) and long axial contacts to O(1) and O(2) (2.251(4) - 2.294(4) Å). Cu(3) has axially compressed geometry ( $d_{z^2}$  magnetic ground state), with long contacts to O(3) and its symmetry related atoms (2.203(3) Å), and short bonds to N(17) and its symmetry related counterpart (1.936(6) Å). As in **4.5**, this arrangement sets up orbitally orthogonal magnetic connections in the outer ring of eight copper ions, with non-orthogonal connections to Cu(3).

Ten perchlorate anions are present for each grid which is uncommon (normally each ligand loses two protons, and so six anions are present to balance the +6 charge of the grid cation), but not unprecedented. For example, the complex  $[\text{Cu}_9(2\text{poap-H})_6](\text{NO}_3)_{12}\cdot 9\text{H}_2\text{O}$ , contains six mono-deprotonated ligands, hence the grid cation carries a charge of +12, balanced by the presence of twelve nitrate anions [66]. Unlike more typical  $[3\times 3]$  M(II)<sub>9</sub> grids, **4.6** has a proton (H(21)), located in difference maps, on a non-coordinated diazine nitrogen atom (N(11)). In the symmetry expanded model, this corresponds to four protons, hence there are four mono-deprotonated ligands and two doubly-deprotonated ligands present, and the cation charge is +10. The CO group adjacent to N(21) (C(12)-O(2)) bridges Cu(1) and Cu(2<sup>+</sup>) with long, axial contacts (2.298(4) Å, 2.294(4) Å) respectively, and a short C-O distance (1.241(6) Å) consistent with its identification as a neutral carbonyl C=O group. In contrast the C(23)-O(3) CO group bridges Cu(2) and Cu(3) with short equatorial (Cu(2)-O(3); 2.077(3) Å) and long (Cu(3)-O(3); 2.203(3) Å) equatorial contacts respectively, and has a much longer C-O

bond distance (1.307(6) Å), indicative of a single bond with a formal charge of -1 on the bridging oxygen atom.

**Table 4.9:** Selected bond distances (Å) and angles (°) for **4.6**.

Cu(1) O(1)	2.070(4)	Cu(2) N(15)	1.908(4)
Cu(1) O(2')	2.298(4)	Cu(3) O(3)	2.203(3)
Cu(1) N(1)	2.106(5)	Cu(3) N(17)	1.936(6)
Cu(1) N(4)	1.920(4)	Cu(1) Cu(2)	4.0749(8)
Cu(1) N(7)	2.248(5)	Cu(1) Cu(2')	4.2555(8)
Cu(1) N(10)	2.020(4)	Cu(2) Cu(3)	4.053(3)
Cu(2) O(1)	2.251(4)		
Cu(2) O(2)	2.294(4)	Cu(1) O(1)	Cu(2) 141.13(18)
Cu(2) O(3)	2.077(3)	Cu(2) O(2)	Cu(1') 136.50(18)
Cu(2) N(6)	1.993(4)	Cu(2) O(3)	Cu(3) 142.53(17)
Cu(2) N(12)	2.109(4)		

#### 4.3.2: Magnetic Properties:

Compound **4.1** is a diamagnetic  $[3 \times 3]$  Zn(II)<sub>9</sub> grid, while the variable temperature magnetic properties of **4.4**, a mononuclear Cu(II) complex, show an essentially constant moment (approximately  $1.9 \mu_B$ ) from room temperature to 2 K, consistent with the presence of one Cu(II) ( $S = 1/2$ ) centre.

Compounds **4.2-4.3**, **4.5** and **4.6** are  $[3 \times 3]$  M(II)<sub>9</sub> grids that can be described by a magnetic model where exchange between neighboring metal centres in the outer ring of eight metals (Figure 4.9) is assumed to be the same ( $J_1$ ), based on the structural observation of similar M-O-M bridge angles. Exchange between the central metal ion and its adjacent metals is assumed to be slightly different ( $J_2$ ).

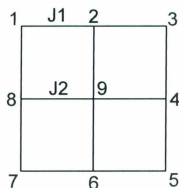


**Figure 4.9:** Magnetic exchange models for a  $[3 \times 3]$   $M_9$  grid.

A Hamiltonian to describe this exchange situation includes just two exchange integrals and is expressed in equation 4.1.

$$H_{ex} = -J1\{S_1 \cdot S_2 + S_2 \cdot S_3 + S_3 \cdot S_4 + S_4 \cdot S_5 + S_5 \cdot S_6 + S_6 \cdot S_7 + S_7 \cdot S_8 + S_1 \cdot S_8\} \\ - J2\{S_2 \cdot S_9 + S_4 \cdot S_9 + S_6 \cdot S_9 + S_8 \cdot S_9\} \quad (4.1)$$

Compound **4.2** is a  $[3 \times 3]$   $Mn(II)_9$  grid, where all metal centres are  $S = 5/2$ , and presents challenges in using a vector coupling approach [74] in order to deal with the exchange situation. Overall, this is a 45-electron problem and involves enormous matrix calculations to generate the total spin state profile for a two J ( $J_1, J_2$ ) system. The largest matrix dimension is 88 900, which can be reduced to a quarter by applying  $D_4$  spatial symmetry, but the resulting calculation still exceeds the capacity of personal computers, and even larger computers/clustered systems [98].

The approach used here to model **4.2** is based on the Fisher model (equations 4.2 - 4.4) and is an approximation that treats the outer ring of eight metals as a spin coupled chain, isolated from the central metal ion (that is,  $J_2$  is assumed to be zero, reducing this to a one J problem) [73,74].  $\chi$  is the susceptibility,  $\rho$  is the fraction of paramagnetic

impurity, TIP is the temperature independent paramagnetism,  $\theta$  is a Weiss-like temperature correction and all other terms have their usual significance.

$$\chi_{mol} = \left( \frac{8 \times \chi_{Mn} + 1.094 \times g^2}{T - \theta} \right) \times (1 - \rho) + \left( \frac{1.094 \times g^2}{T} \right) \times \rho + TIP \quad (4.2)$$

$$u = \coth \left[ \frac{JS(S+1)}{kT} \right] - \left[ \frac{kT}{JS(S+1)} \right] \quad (4.3)$$

$$\chi_{Mn} = \frac{Ng^2 \beta^2 S(S+1)(1+u)}{3kT(1-u)} \quad (4.4)$$

The magnetic profile for 4.2 is shown in Figure 4.10 as a plot of moment per mole as a function of temperature. The Fisher Model approach is justified on the basis that at 2 K the observed moment is  $6.7 \mu_B$ , which indicates that the ground state is effectively  $S = 5/2$ , resulting from intragrid antiferromagnetic exchange (ie. isolation of the central ion), and that divergence from the fully isotropic exchange model would be relatively small for small values of J.

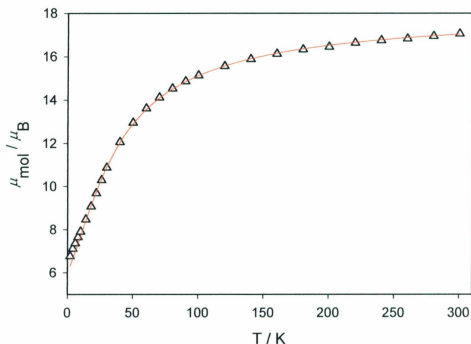


**Figure 4.10:** Variable temperature magnetic data for **4.2**;  $g = 2.04$ ,  $J = -4.8 \text{ cm}^{-1}$ ,  $TIP = 0 \text{ cm}^3 \text{ mol}^{-1}$ ,  $\rho = 0.003$ ,  $10^2 R = 2.1$ .

The room temperature value for **4.2** is  $17.0 \mu_B$ , typical of other  $\text{Mn(II)}_9$  grids. The data were fitted to equation 4.2 to give  $g = 2.04$ ,  $J = -4.8 \text{ cm}^{-1}$ ,  $\rho = 0.003$ ,  $TIP = 0 \text{ cm}^3 \text{ mol}^{-1}$ ,  $10^2 R = 2.1$  ( $R = [\sum(\chi_{\text{obs}} - \chi_{\text{calc}})^2 / \sum \chi_{\text{obs}}^2]^{1/2}$ ). The solid line in Figure 4.10 was calculated with these parameters and the exchange coupling is consistent with other  $\text{Mn(II)}_9$  grids [73,74]. It should be noted, however, that  $J_2$  is in fact likely to be non-zero and hence this is not a rigorous model, but rather serves to give a reasonable estimate of  $J_1$ . As a comparison,  $[\text{Mn(II)}_5\text{Mn(III)}_4(2\text{poap})_6](\text{ClO}_4)_{10}$ , (discussed in the Preamble) involves a sufficiently small matrix calculation for the full isotropic two  $J$  problem that it can be completed on a personal computer with enough (2 GB) RAM [98].  $J_1$  ( $\text{Mn(II)-O-}$

Mn(III)) was reported as  $-8.3 \text{ cm}^{-1}$  and  $J_2$  (Mn(II)-O-Mn(II)) was  $-4.5 \text{ cm}^{-1}$  which is comparable to that obtained for **4.2** using the chain model.

Compound **4.3** is a  $[3 \times 3]$  Co(II)<sub>9</sub> grid and its magnetic profile is shown in Figure 4.11 as a plot of moment per mole as a function of temperature. The moment drops from  $12.8 \mu_B$  at 300 K to  $5.7 \mu_B$  at 2 K and the profile is characteristic of the presence of intramolecular antiferromagnetic exchange.

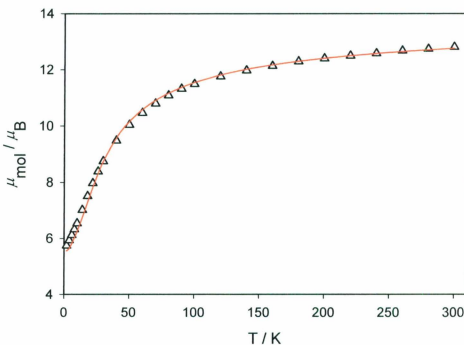


**Figure 4.11:** Variable temperature magnetic data for **4.3**;  $g = 2.263(9)$ ,  $J = -6.5(2) \text{ cm}^{-1}$ ,  $\text{TIP} = 2200 \times 10^{-6} \text{ cm}^3 \text{ mol}^{-1}$ ,  $\rho = 0.075$ ,  $10^2 R = 1.9$ .

The room temperature moment is consistent with nine high spin Co(II) centres while the residual moment at 2 K is slightly larger than expected for a single Co(II) ion. Modelling of the magnetic properties of Co(II) complexes is complicated by spin orbit

coupling and by zero field splitting considerations, however, the single ion effects can be estimated from the dinuclear Co(III)/Co(II) complex [(ioap-H)(ioap-2H)Co<sub>2</sub>(H<sub>2</sub>O)<sub>4</sub>](BF<sub>4</sub>)<sub>2</sub> (**3.1**). Complex **3.1** contains a single Co(II) center in a bidentate N<sub>2</sub> pocket of the ligand ioap (Figure 3.1b), with an N<sub>2</sub>O<sub>4</sub> coordination sphere. The magnetic moment of this compound shows a decrease from 4.5  $\mu_B$  at 300 K to 3.4  $\mu_B$  at 2 K, which would scale up to 13.5  $\mu_B$  to 10.2  $\mu_B$  for a putative Co(II)<sub>9</sub> grid with no exchange in the same temperature range. It is clear, therefore, that antiferromagnetic exchange is a very significant component of the magnetic properties of **4.3** and so, a simple isotropic exchange model for nine  $S = 3/2$  spin centres, assuming  $J_1 = J_2$  (Figure 4.9), was used. The total spin state/energy ( $S/E$ ) profiles could be calculated since the matrix dimensions are considerably smaller than for a [3×3] Mn(II)<sub>9</sub> case, and the experimental data were successfully modeled to equation 4.1 using MAGMUN4.1 [49] to give  $g = 2.263(9)$ ,  $J = -6.5(2) \text{ cm}^{-1}$ ,  $\text{TIP} = 2200 \times 10^{-6} \text{ cm}^3 \text{ mol}^{-1}$ ,  $\rho = 0.075$ ,  $10^2 R = 1.9$ . The solid line in Figure 4.11 was calculated with these parameters. The magnitude of the exchange is consistent with values reported for [2×2] Co(II)<sub>4</sub> grids formed by self-assembly reactions with poapz and pzoapz ( $J = -7$  and  $-6.95(4) \text{ cm}^{-1}$  respectively; see Figure 2.1 for ligands), where similar Co-O-Co bridge angles exist [59].

Compound **4.5** is a [3×3] Cu(II)<sub>9</sub> grid and its magnetic profile is shown in Figure 4.12 as a plot of moment per mole as a function of temperature. The moment drops from 6.24  $\mu_B$  at 300 K to a minimum value of 5.34  $\mu_B$  at 22 K, suggesting an antiferromagnetic exchange component, followed by a rise to 6.63  $\mu_B$  at 2 K, indicative of a second, ferromagnetic, exchange contribution.

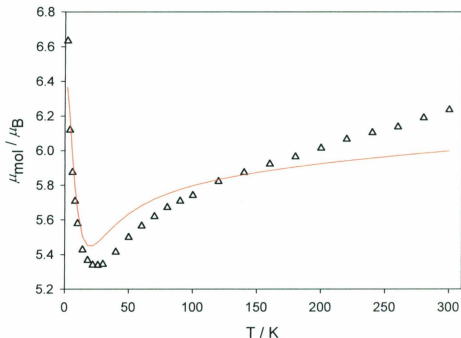


**Figure 4.12:** Variable temperature magnetic data for **4.5**;  $g = 2.27(1)$ ,  $J_1 = 1.8(1) \text{ cm}^{-1}$ ,  $J_2 = -18(1) \text{ cm}^{-1}$ ,  $\text{TIP} = 700 \times 10^{-6} \text{ cm}^3 \text{ mol}^{-1}$ ,  $\theta = -1 \text{ cm}^{-1}$ ,  $10^2 R = 4.4$ .

Compound **4.5** exhibits four-fold symmetry within the grid cation, as seen from the crystal structure, which is useful in the interpretation of the magnetic connectivity and modeling of the experimental data. The corner and side distorted octahedral copper centres (Cu(1) and Cu(2); Figure 4.7b) exhibit Jahn-Teller elongation that defines their magnetic ground states as  $d_{x^2-y^2}$ . The long axis for Cu(1) points towards O(1) with a short connection directed towards O(2), while for Cu(2) the long axis is directed towards both O(1) and O(2) with a short connection to O(3) (Figure 4.7b). Based upon the directionality of the Jahn-Teller axes in the outer  $\text{Cu}(\text{II})_8$  ring, the Cu(1)-O(1)-Cu(2) and Cu(2)-O(2)-Cu(1') connections are orthogonal, while the Cu(2)-O(3)-Cu(3) connection is

not. These structural features should allow only for ferromagnetic coupling between Cu(1) and Cu(2) centres (and their symmetry related counter-parts), and a single exchange constant can be used to model the contribution of the ring to the observed magnetic properties ( $J_1$ , Figure 4.9). Note, however, that two ferromagnetic  $J$  values might also be considered on the basis of the slightly different connections between Cu(1) and Cu(2) (Cu(1)-Cu(2) separation, bridged *via* O(1), is 4.2970(11) Å while Cu(1)-Cu(2'), bridged *via* O(2), is 4.0346(13) Å) though this approach was not taken since the M-O-M bond angles are so similar (138.4(2)- 138.9(2) $^\circ$ ), and fitting magnetic data for ferromagnetically coupled systems can be challenging.

The central distorted octahedral copper (Cu(3); Figure 4.7b) exhibits Jahn-Teller compression that defines its magnetic ground states as  $d_{z^2}$ . The  $d_{z^2}$  orbital does have some electron density in the  $xy$  plane (as defined by the four long connections between Cu(2) to O(3) and its symmetry related counterparts) and therefore a small antiferromagnetic exchange between Cu(3) and the Cu(2) centres is possible. The magnitude of this exchange, normally expected to be rather large based solely upon the large Cu(3)-O(3)-Cu(2) angle (142.7(2) $^\circ$ ), should be quite small due to the limited electron density available in the plane defined by Cu(3)-O(3) and the symmetry related oxygen atoms.

Unlike **4.2**, where large matrix dimensions restricted full isotropic modeling of the exchange situation, for **4.5** the vector coupling approach is challenged by the independent evaluation of two  $J$  values. Instead, **4.5** was fitted using the non-linear regression routines built into the MAGMUN4.1 [49] software by evaluating  $J_2$  as a fraction of  $J_1$  in order to obtain the total spin state/energy ( $S/E$ ) profiles. For example, if

input values are expressed as  $J_1 = -0.1$  and  $J_2 = 1$ , then  $-J_2/J_1 = 10$  and the fitted  $J$  determined by non-linear regression will be a factor by which both  $J_1$  and  $J_2$  must be multiplied. Similar to **4.2**, this is not a completely rigorous approach, however, applied in the context of a sensible analysis of the exchange situation based upon the structure, useful information on the magnitude of the coupling can be obtained.

A fit for **4.5** was obtained after many trial comparisons varying the ratio of  $-J_2/J_1$  to give a best fit with  $g = 2.27(1)$ ,  $J_1 = 1.8(1) \text{ cm}^{-1}$ ,  $J_2 = -18(1) \text{ cm}^{-1}$ ,  $\text{TIP} = 700 \times 10^{-6} \text{ cm}^3 \text{ mol}^{-1}$ ,  $\theta = -1 \text{ cm}^{-1}$ ,  $10^3 R = 4.4$ . The solid line in Figure 4.12 was calculated with these parameters and the exchange coupling is consistent with other  $[3 \times 3] \text{ Cu(II)}_9$  grids [66,69,71,96]. A closer fit ( $10^3 R = 0.423$ ) was obtained for  $g = 2.199(2)$ ,  $J_1 = 0.73(1) \text{ cm}^{-1}$ ,  $J_2 = -20.8(3) \text{ cm}^{-1}$ ,  $\text{TIP} = 2800 \times 10^{-6} \text{ cm}^3 \text{ mol}^{-1}$ , however, the very high TIP value is unrealistic and not consistent with the presence of only nine Cu(II) centres.

Compound **4.6** is also a  $[3 \times 3] \text{ Cu(II)}_9$  grid and its magnetic profile is shown in Figure 4.13 as a plot of moment per mole as a function of temperature, and is similar to that of **4.5**. The moment drops from  $6.24 \mu_B$  at 300 K to a minimum value of  $5.58 \mu_B$  at 40 K, suggesting an antiferromagnetic exchange component, followed by a rise to  $7.26 \mu_B$  at 2 K, indicative of a second, ferromagnetic, exchange contribution.

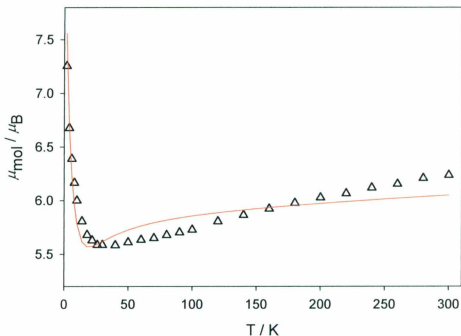


**Figure 4.13:** Variable temperature magnetic data for **4.6**;  $g = 2.27(1)$ ,  $J_1 = 1.52(9) \text{ cm}^{-1}$ ,  $J_2 = -15.2(9) \text{ cm}^{-1}$ ,  $TIP = 900 \times 10^{-6} \text{ cm}^3 \text{ mol}^{-1}$ ,  $10^2 R = 3.2$ .

Compound **4.6** also exhibits four-fold symmetry within the grid cation, as seen from the crystal structure, with corner and side distorted octahedral copper centres (Cu(1) and Cu(2)) exhibiting Jahn-Teller elongation, as seen in Figure 4.8b. Again, based upon the directionality of the Jahn-Teller axes in the outer  $\text{Cu(II)}_8$  ring, the Cu(1)-O(1)-Cu(2) and Cu(2)-O(2)-Cu(1') connections are orthogonal, while the Cu(2)-O(3)-Cu(3) connection is not, and only ferromagnetic coupling between Cu(1) and Cu(2) centres (and their symmetry related counter-parts) is expected. The central distorted octahedral copper (Cu(3)) again exhibits Jahn-Teller compression that defines its magnetic ground states as  $d_{z^2}$  and a small antiferromagnetic exchange between Cu(3) and the Cu(2) centres is

reasonable. Using the same approach as discussed for 4.5, the solid line in Figure 4.13 was obtained with  $g = 2.27(1)$ ,  $J_1 = 1.52(9) \text{ cm}^{-1}$ ,  $J_2 = -15.2(9) \text{ cm}^{-1}$ ,  $\text{TIP} = 900 \times 10^{-6} \text{ cm}^3 \text{ mol}^{-1}$ ,  $10^2 R = 3.2$ .

The variable temperature data for 4.6 suggests that the exchange situation is dominated by ferromagnetism at low temperatures, hence a magnetization versus field study was carried out at 2 K (Figure 4.14). The experimental data rise smoothly with increasing field up to a plateau value of  $8.2 N\beta$  at 50 000 Oe. The solid line was calculated for  $g = 2.27$ ,  $S' = 7/2$ ,  $T = 2 \text{ K}$  using the appropriate Brillouin function while the dashed line was calculated for  $g = 2.27$ ,  $S' = 7 \times 1/2$ ,  $T = 2 \text{ K}$ . The comparison between the experimental data and the simulations shows that the experimental profile is consistent with the variable temperature magnetic model for a grouped set of ferromagnetically-dominated interacting copper(II) centres resulting in a  $7/2$  ground state and not with isolated spin centres.

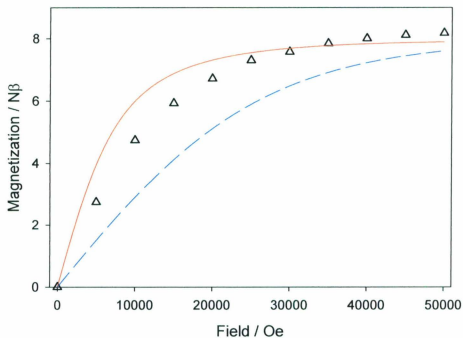


**Figure 4.14:** Variable field magnetization data for **4.6**; solid red line calculated for  $g = 2.27$ ,  $S' = 7/2$ ,  $T = 2$  K and dashed blue line calculated for  $g = 2.27$ ,  $S' = 7 \times \frac{1}{2}$ ,  $T = 2$  K using the appropriate Brillouin function.

A summary of the magnetic results for **4.2-4.3**, **4.5** and **4.6** is presented in Table 4.10.

**Table 4.10:** Summary of the magnetic analysis of **4.2 - 4.3**, **4.5** and **4.6**.

Compound	$g$	$J1$ ( $\text{cm}^{-1}$ )	$J2$ ( $\text{cm}^{-1}$ )	Ground State Spin ( $S'$ )
<b>4.2</b> ( $\text{Mn(II)}_9$ grid)	2.04	-4.8	0	5/2
<b>4.3</b> ( $\text{Co(II)}_9$ grid)	2.263(9)	-6.5(2)	-6.5(2)	3/2
<b>4.5</b> ( $\text{Cu(II)}_9$ grid)	2.27(1)	1.8(1)	-18(1)	7/2
<b>4.6</b> ( $\text{Cu(II)}_9$ grid)	2.27(1)	1.52(9)	-15.2(9)	7/2

#### 4.4: Summary:

[3×3] Mn(II)<sub>9</sub>, Cu(II)<sub>9</sub> and Zn(II)<sub>9</sub> grids synthesized by self-assembly reactions between metal salts and 2pmoap (**2.4**) were characterized and found to be structurally similar to previously reported Mn(II)<sub>9</sub> [30, 69,70,73,29], Cu(II)<sub>9</sub> [66,69, 71,96] and Zn(II)<sub>9</sub> [70] grids. The structural characterizations are of particular importance in the Mn(II)<sub>9</sub> and Cu(II)<sub>9</sub> cases, as these provide the basis for magnetic interpretation and modeling. In the Mn(II)<sub>9</sub> case (**4.2**), large, similar Mn-O-Mn bridging angles lead to antiferromagnetic exchange between metal centres throughout the grid, but due to difficulties associated with enormous matrix calculations, a simplified magnetic model was used in the interpretation of experimental data. For the Cu(II)<sub>9</sub> cases (**4.5** and **4.6**), the effect of large Cu-O-Cu bridging angles for the ring of eight metal centres was negated by the presence of Jahn-Teller distortions leading to magnetic orbital orthogonality and dominant ferromagnetic exchange. A second magnetic effect was also present, and supported by the structural characterization of a d<sub>2</sub> Jahn-Teller distortion for the central Cu(II) ion, leading to some electron density in the Cu-O plane and antiferromagnetic exchange between the central Cu(II) ion and the side metal sites. The matrix calculations for this system are considerably smaller than those for the Mn(II)<sub>9</sub> system, and the experimental data were modeled with two different exchange constants that were independently varied in an iterative ratio to obtain a best fit.

A side product was characterized upon recrystallization of the self-assembly reaction between Cu(NO<sub>3</sub>)<sub>2</sub> and 2pmoap. This mononuclear Cu(II) compound (**4.4**) is not unprecedented; similar *in situ* ligand scission products have been observed upon further

reaction of 'full-ligand' compounds [100]. The bonding motif adopted by the hydrolyzed ligand is similar to that observed for **3.6**, a mononuclear Cu(II) complex synthesized from the reaction between the ditopic ligand ioapm (**2.2**) and  $\text{Cu}(\text{ClO}_4)_2$ .

The first  $[3 \times 3]$   $\text{Co}(\text{II})_9$  grid suitable for both structural and magnetic characterization was produced, and exhibits the same  $[\text{M}_9-(\mu\text{-O})_{12}]$  framework as other reported  $[3 \times 3]$   $\text{M}_9$  grids. Since no other  $\text{Co}(\text{II})_9$  complexes are available for comparison, the magnetic properties of **4.3** were compared to previously reported  $\text{Co}(\text{II})_4$  grids with similar Co-O-Co bridge angles [59]. The magnitude of the coupling constant was found to be consistent with these compounds, which supports the simple isotropic magnetic exchange model that was used to fit the experimental data.

## Chapter 5: Heterobimetallic [3×3] Mn(II)<sub>1</sub>Cu(II)<sub>8</sub> and Mn(II)<sub>5</sub>M(II)<sub>4</sub> (where M = Ni, Cu and Zn) grid complexes

### 5.1: Preamble:

In most magnetic molecules, behaviour is dominated by intramolecular effects; unpaired electrons on one centre in a molecule interacting with unpaired electrons on another centre in the same molecule (see Chapter 1). As temperatures are lowered, the intermolecular interactions between molecules becomes increasingly significant and just above the critical temperature,  $T_c$ , the correlation length becomes very large. At  $T_c$ , the correlation length becomes infinite and three-dimensional magnetic ordering is expected [101]. This ordering is such that all unpaired spins on neighboring molecules are oriented in a parallel manner if the interaction is ferromagnetic in nature, or antiparallel if the interaction is antiferromagnetic. A third possibility exists if the unpaired electrons on one atom are opposed in spin to those on another, but the magnitude of the opposing moments is unequal, resulting in a ferrimagnetic material where spontaneous magnetization is possible.

Single molecule magnets (SMMs) are systems where permanent magnetization and magnetic hysteresis can be achieved as a one-molecule phenomenon. Molecules must exhibit a high spin ground state and high zero-field-splitting (D), resulting from large magnetic anisotropy. In the development of molecular magnets most research is directed toward the development of ferri- or ferromagnetic systems [102], which could potentially exhibit single molecular magnetic behaviour.

The work presented in this chapter is focused on spin amplification achieved through the non-compensation of spins in ferrimagnetic polynuclear systems exhibiting intramolecular antiferromagnetic exchange. Numerous reports of heterobimetallic complexes exhibiting SMM-like behaviours exist [103-110], in part because highest spin-states can more readily be stabilized in some of these systems by strict orthogonality of the magnetic orbitals [111], with the most pronounced examples of high spin ground states existing when there is a large spin difference between the magnetic subunits [112].

Methods for achieving heterometallic systems include designing a ligand with unequal pockets (that is, with different sizes and/or donor atoms) suitable for the accommodation of different metal coordination preferences [113,114], or employing the "ligand complex" method, where a metal complex with additional available donor sites is further reacted with another metal ion source [115,116]. The first method has led to the report of a  $\text{Mn(III)}_2\text{Ni(II)}_2$  incomplete face-sharing double cube with the ligand *N*-(2-hydroxy-benzyl)-3-amino-1-propanol (Figure 5.1a), that exhibits a high spin ground state of  $S' = 6$ , resulting from the non-compensating effect of Ni(II) ( $S = 1$ ) on Mn(III) ( $S = 2$ ) [117]. "Ligand-complex" reactions have produced a suite of incomplete double-cubane molecules with  $[\text{Mn(III)}_2\text{M(II)}_2\text{O}_6]$  cores ( $M = \text{Mn, Ni, Cu and Zn}$ ) that exhibit spin frustration, and when  $M = \text{Cu}$  ( $S = 1/2$ ) a high spin ground state of  $S' = 3$  results [118]. A high spin molecular square ( $S' = 4$ ) with square pyramidal Co(II) and tetrahedral Mn(II) corners has also been reported [119].

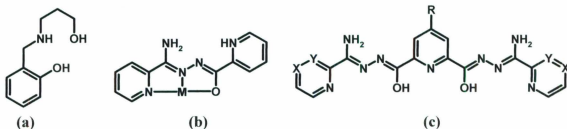


**Figure 5.1:** a) *N*-(2-hydroxybenzyl)-3-amino-1-propanol. b) poap mononuclear precursor ( $M = \text{Fe(III)}$ ). c) 2poapz ( $X = \text{N}$ ,  $Y = \text{CH}$ ,  $R = \text{H}$ ); 2pmoap ( $X = \text{CH}$ ,  $Y = \text{N}$ ,  $R = \text{H}$ ); Cl2poap ( $X = Y = \text{CH}$ ,  $R = \text{Cl}$ ).

Mixed metal square  $[2 \times 2]$   $\text{Cu(II)}_3\text{Fe(III)}$  and  $\text{Fe(III)}_2\text{Ni(II)}_2$  grids with poap have been reported using a “ligand complex”  $\text{Fe(III)}$  mononuclear precursor (Figure 5.1b) [60,120]. The *mer*-bis-ligand coordination environment at the precursor’s  $\text{Fe(III)}$  ion leads to open secondary coordination sites, which take part in grid formation, and leads to a high spin ( $S' = 3$ ) ground state for the  $\text{Fe(III)}_2\text{Ni(II)}_2$  grid. A mixed-metal  $[3 \times 3]$  grid,  $[\text{Mn(II)}_8\text{Co(II)}(2\text{poapz-2H})_6](\text{ClO}_4)_6$ , was also achieved by first reacting 2poapz (Figure 5.1c) with  $\text{Co}(\text{ClO}_4)_2$  followed by the *in situ* addition of  $\text{Mn}(\text{ClO}_4)_2$  [28]. The location of the  $\text{Co(II)}$  ion could not be determined structurally, however, an  $S' = 3/2$  ground state was found experimentally. This is consistent with  $\text{Co(II)}$  at the centre site leading to the observed non-compensation of spins in an antiferromagnetically coupled grid. A similar approach is described here and produces  $[3 \times 3]$   $\text{Mn(II)}_5\text{M(II)}_4$  grids (where  $M = \text{Zn}$ ,  $\text{Cu}$  and  $\text{Ni}$ ), and a  $[3 \times 3]$   $\text{Mn(II)}_1\text{Cu(II)}_8$  complex.

## 5.2: Experimental:

**Note:** In some cases there is a difference between the most reasonable formula based on the elemental analysis (analytical formula), and that obtained from X-ray crystallography. The analytical formulae will be used here.

### 5.2.1: Complex synthesis:

**5.2.1.1:** [(2pmoap-2H)<sub>6</sub>Mn<sub>5</sub>Zn<sub>4</sub>](NO<sub>3</sub>)<sub>6</sub>·33H<sub>2</sub>O·20CH<sub>3</sub>OH (**5.1**). 2pmoap (0.15 g, 0.31 mmol) was added to a solution of Mn(NO<sub>3</sub>)<sub>2</sub>·6H<sub>2</sub>O (0.13 g, 0.45 mmol) in methanol:acetonitrile (15 mL:5 mL) forming a clear, light yellow solution that was stirred for five minutes. Zn(CH<sub>3</sub>COO)<sub>2</sub>·2H<sub>2</sub>O (0.060 g, 0.27 mmol) was added and the solution became clear and orange. It was stirred at room temperature for ten minutes and with gentle heating for 30 minutes, then kept after filtration for slow evaporation. Weakly diffracting, orange, prismatic crystals were collected after six days (0.023 g, 7.5 % yield). Anal. calcd (%) for [(C<sub>17</sub>H<sub>13</sub>N<sub>11</sub>O<sub>2</sub>)<sub>6</sub>Mn<sub>5</sub>Zn<sub>4</sub>](NO<sub>3</sub>)<sub>6</sub>(H<sub>2</sub>O)<sub>33</sub>(CH<sub>3</sub>OH)<sub>20</sub>: C, 32.11; H, 4.95; N, 22.10. Found (%): C, 32.20; H, 2.83; N, 22.02.

**5.2.1.2:** [(2pmoap-2H)<sub>6</sub>Mn<sub>5</sub>Cu<sub>4</sub>](NO<sub>3</sub>)<sub>6</sub>·15H<sub>2</sub>O·2CH<sub>3</sub>OH (**5.2**). [Mn<sub>9</sub>(2pmoap-2H)<sub>6</sub>](NO<sub>3</sub>)<sub>6</sub>·13H<sub>2</sub>O (**4.2**) (0.12 g, 0.034 mmol) was dissolved in methanol:acetonitrile (7 mL : 7 mL) to give a clear dark orange solution, that was treated with 0.1 mol/L NaOH until a neutral pH was achieved. A solution of Cu(NO<sub>3</sub>)<sub>2</sub>·6H<sub>2</sub>O (0.050 g, 0.17 mmol) dissolved in methanol:acetonitrile (5 mL:5 mL), was added to give a clear brown solution. The pH was tested and four drops of triethylamine were added to maintain a neutral pH. The solution was stirred with gentle heating for one hour, and then filtered. Crystals suitable for X-ray analysis formed in six days (0.030 g, 24 % yield). Anal. calcd (%) for [(C<sub>17</sub>H<sub>13</sub>N<sub>11</sub>O<sub>2</sub>)<sub>6</sub>Mn<sub>5</sub>Cu<sub>4</sub>](NO<sub>3</sub>)<sub>6</sub>(H<sub>2</sub>O)<sub>15</sub>(CH<sub>3</sub>OH)<sub>2</sub>: C, 34.17; H, 3.19; N, 27.59; Found C, 34.15; H, 2.47; N, 27.64.

**5.2.1.3:** [(2pmoap-2H)<sub>6</sub>Mn<sub>5</sub>Ni<sub>4</sub>](NO<sub>3</sub>)<sub>6</sub>·60H<sub>2</sub>O·3CH<sub>3</sub>OH (**5.3**). 2pmoap (0.20 g, 0.42 mmol) was added to a solution of Mn(NO<sub>3</sub>)<sub>2</sub>·6H<sub>2</sub>O (0.32 g, 1.1 mmol) in

methanol:acetonitrile (10 mL:10 mL) forming a clear, light yellow solution that was stirred for 5 minutes. A solution of  $\text{Ni}(\text{CH}_3\text{COO})_2 \cdot 4\text{H}_2\text{O}$  (0.19 g, 0.76 mmol in 10 mL of methanol) was then added dropwise to produce a brown solution that was stirred with gentle heating for 35 minutes and kept after filtration for slow evaporation. The resulting brown powder was recrystallized from ethanol-methanol-acetonitrile (10 mL:5 mL:5 mL) after 21 days. Brown microcrystals, unsuitable for X-ray analysis were collected after 41 days (0.050 g, 16 % yield). Anal. calcd (%) for  $[(\text{C}_{17}\text{H}_{13}\text{N}_{11}\text{O}_2)_6\text{Mn}_3\text{Ni}_4](\text{NO}_3)_6(\text{H}_2\text{O})_{60}(\text{CH}_3\text{OH})_3$ : C, 28.16; H, 4.72; N, 22.52. Found (%): C, 28.24; H, 2.45; N, 22.45.

**5.2.1.4:**  $[(2\text{pmoap-2H})_6\text{Mn}_1\text{Cu}_8](\text{NO}_3)_6 \cdot 23\text{H}_2\text{O}$  (**5.4**).  $\text{Cu}(\text{NO}_3)_2 \cdot 6\text{H}_2\text{O}$  (0.10 g, 0.34 mmol) was added to a solution of  $[\text{Mn}_9(2\text{pmoap-2H})_6](\text{NO}_3)_6 \cdot 13\text{H}_2\text{O}$  (**4.2**) (0.050 g, 0.014 mmol) in methanol:acetonitrile (5 mL:5 mL) to give a clear green-brown solution that was gently refluxed for one hour and kept after filtration for slow evaporation. Brown, prismatic crystals were collected after 13 days (0.020 g, 38 % yield). Anal. calcd (%) for  $[(\text{C}_{17}\text{H}_{13}\text{N}_{11}\text{O}_2)_6\text{Mn}_1\text{Cu}_8](\text{NO}_3)_6(\text{H}_2\text{O})_{23}$ : C, 32.50; H, 3.32; N, 26.75. Found (%): C, 32.04; H, 2.52; N, 27.29.

### 5.2.2: Crystallography

The diffraction intensities of an orange prismatic crystal of **5.1** having approximate dimensions of  $0.20 \times 0.20 \times 0.20$  mm were collected on a Rigaku Saturn CCD area detector with graphite monochromated  $\text{Mo-K}\alpha$  radiation at 153(2) K to a maximum  $2\theta$  value of  $62.0^\circ$ . The data were corrected for Lorentz and polarization effects and a correction for secondary extinction [81] was applied. The structure was solved by direct methods [82,83] and expanded using Fourier techniques [84]. Hydrogen atoms

were introduced in calculated positions with isotropic thermal parameters set twenty percent greater than those of their bonding partners. They were refined on the riding model. Neutral atom scattering factors and anomalous dispersion effects were taken from the usual sources [85-88]. All calculations were performed using the Crystal Structure [89,90] crystallographic software package except for refinement, which was performed using SHELXL-97 [83]. The Platon [91] Squeeze procedure was applied to recover 1523.4 electrons per unit cell in one void (total volume 9028.0 Å<sup>3</sup>); that is 190.43 electrons per formula unit. A disordered nitrate anion was present in the asymmetric unit prior to the application of Squeeze, though a good point atom model could not be achieved. This accounts for 50 electrons per formula unit. Disordered solvent was also present (14 lattice water molecules; 140 electrons per formula unit). The application of Squeeze gave a good improvement in the data statistics and allowed for a full anisotropic refinement of the framework structure.

A chunk of a brown crystal of **5.2** having approximate dimensions of 0.20 × 0.20 × 0.20 mm was treated similarly to **5.1**. Hydrogen atoms were introduced in calculated positions with isotropic thermal parameters set twenty percent greater than those of their bonding partners. They were refined on the riding model. The model contains one full-occupancy disordered nitrate anion that was refined anisotropically. The occupancies of the corresponding oxygen atoms reflect the disorder. The model also contains one difficult to model, half-occupancy nitrate anion and a total of six water molecules as lattice solvent, which were refined isotropically. The occupancies of the water oxygen were adjusted to reflect their partial occupancy, and make up 24 oxygen atoms per

formula unit, in the symmetry expanded model. The corresponding hydrogen atoms were not included in the model.

A chunk of a brown crystal of **5.4** having approximate dimensions of  $0.30 \times 0.30 \times 0.15$  mm was treated similarly to **5.1**. **5.4** was collected only out to a maximum  $2\theta$  value was  $46.4^\circ$ . Employing Bragg's law (equation 5.1):

$$n\lambda = 2d \sin \theta \quad (5.1)$$

with  $\lambda = 0.7107 \text{ \AA}$  (Mo-K $\alpha$  radiation) and  $\theta = 23.2^\circ$ , the minimum atomic separation that can be resolved is  $0.9021 \text{ \AA}$ . For this reason, this structure is not suitable for journal publication, however, since the protons were introduced in calculated positions, and all other atoms were separated by more than  $0.9021 \text{ \AA}$ , this structure is suitable for discussion here. All non-hydrogen atoms were refined anisotropically while all hydrogen atoms were refined on the riding model with isotropic thermal parameters set twenty percent greater than those of their bonding partners. The asymmetric unit contains 3.75 water molecules as lattice solvent. Their corresponding hydrogen atoms could not be located in the difference map and were therefore omitted from the model. Abbreviated crystal data for **5.1**, **5.2** and **5.4** are listed in Table 5.1 and 5.2.

**Table 5.1:** Summary of crystallographic data for 5.1, 5.2.

	5.1	5.2
Chemical Formula	C <sub>102</sub> H <sub>106</sub> Mn <sub>5</sub> N <sub>72</sub> O <sub>42</sub> Zn <sub>4</sub>	C <sub>102</sub> H <sub>126</sub> Cu <sub>4</sub> Mn <sub>5</sub> N <sub>72</sub> O <sub>54</sub>
M	3548.63	3753.44
T(K)	153(2)	153(2)
Crystal System	tetragonal	tetragonal
Space Group	I4 <sub>1</sub> /acd (#142)	I4 <sub>1</sub> /acd (#142)
a (Å)	27.958(3)	27.6101(16)
b (Å)	27.958(3)	27.6101(16)
c (Å)	39.801(4)	40.319(2)
α (°)	90.00	90.00
β (°)	90.00	90.00
γ (°)	90.00	90.00
V (Å <sup>3</sup> )	31112(5)	30736(3)
Z	8	8
D <sub>calc</sub> (g/cm <sup>3</sup> )	1.515	1.622
μ(MoKα) (cm <sup>-1</sup> )	10.94	10.47
Reflections Total	96366	65432
Reflections Unique	7665	7972
R <sub>int</sub>	0.0992	0.0386
R <sub>1</sub> (I > 2.00σ(I))	0.1168	0.0812
wR <sub>2</sub> (All reflections)	0.2855	0.2378

**Table 5.2:** Summary of crystallographic data for **5.4**.

	<b>5.4</b>
Chemical Formula	C <sub>102</sub> H <sub>120</sub> Cu <sub>8</sub> Mn N <sub>72</sub> O <sub>45</sub>
M	3637.83
T(K)	153(2)
Crystal System	tetragonal
Space Group	I4 <sub>1</sub> /acd (#142)
a (Å)	27.889(3)
b (Å)	27.889(3)
c (Å)	39.039(4)
$\alpha$ (°)	90.00
$\beta$ (°)	90.00
$\gamma$ (°)	90.00
V (Å <sup>3</sup> )	30365(5)
Z	8
D <sub>calc</sub> (g/cm <sup>3</sup> )	1.591
$\mu$ (MoK $\alpha$ ) (cm <sup>-1</sup> )	12.80
Reflections Total	36621
Reflections Unique	4959
R <sub>int</sub>	0.0296
R <sub>1</sub> ( $I > 2.00\sigma(I)$ )	0.1079
wR <sub>2</sub> (All reflections)	0.3702

### 5.3: Results and Discussion:

**Note:** The crystallographically determined formulae are used herein. Colour code for figures: magenta = manganese, green = copper, yellow = zinc, grey = carbon, blue = nitrogen, red = oxygen. Crystallographic representations/illustrations were generated using Persistence of Vision Ray Tracer (POV-Ray©) for Windows, version 3.6, with scene description files written by Ortep-3 for Windows (Version 1.08) Copyright© 1997-2003 Louis J. Farrugia.

#### 5.3.1: Description of crystal structures:

##### 5.3.1.2: $[(2\text{pmpoaap-2H})_6\text{Mn}_5\text{Zn}_4](\text{NO}_3)_6 \cdot 14\text{H}_2\text{O}$ (**5.1**)

The structure of the cationic fragment of **5.1** and its core structural representation are shown in Figures 5.2a and 5.2b respectively, and significant bond lengths and angles are listed in Table 5.3.

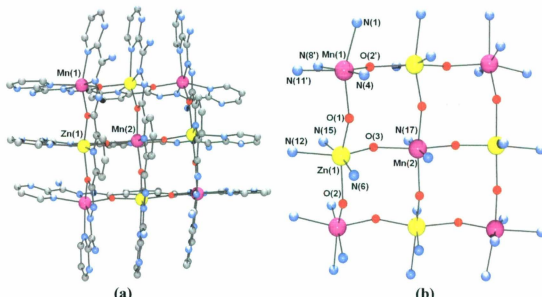


**Figure 5.2:** a) Ball-and-stick depiction of the cationic moiety **5.1**. Hydrogen atoms omitted for clarity. b) Core structural representation of **5.1**.

The structure has tetragonal crystallographic symmetry, which is manifested as four-fold symmetry within the grid cation (Figure 5.1a). The homoleptic grid arrangement results from the roughly parallel arrangement of three heptadentate ligands arranged above and another three below a  $[M_9-(\mu-O)_{12}]$  core composed of nine metal ions bridged by twelve hydrazone oxygen atoms (Figure 5.1b). Metal assignment was done based on a comparison of bond distances to the previously reported  $[3 \times 3]$  Zn(II)<sub>9</sub> (**4.1**) and Mn(II)<sub>9</sub> (**4.2**) grids, and upon a sensible magnetic analysis, all which agree with the presence of Mn(II) ions at the centre and corner sites of **5.1**, and Zn(II) at the side sites.

Zn-Mn distances fall in the range 3.9238(11) - 3.9871(15) Å, with Zn-O-Mn angles in the range 131.1(2) - 134.0(3)°. Distances between corner Mn(II) centres (that is, the overall metal-metal grid dimensions) are 7.8866(15) Å. The corner Mn(II) centres have *cis*-MnN<sub>4</sub>O<sub>2</sub> coordination environments, while the side Zn(II) centres have *mer*-ZnN<sub>3</sub>O<sub>3</sub> environments, and the centre Mn(II) ion has a *trans*-MnN<sub>2</sub>O<sub>4</sub> coordination environment.

The side Zn centres display long Zn-N distances to the external pyrimidine rings (2.345(7) Å), with shorter remaining Zn-N contacts (2.071(6) - 2.106(6) Å), similar to those reported for **4.1** (2.299(9) and 1.980(8) - 2.037(7) respectively), while corner Mn centres display long Mn-N distances to the external pyrimidine rings (2.235(8) - 2.315(9) Å), with shorter remaining Mn-N contacts (2.004(8) - 2.016(7) Å), similar to those reported for **4.2** (2.280(5) - 2.309(5) and 2.135(5) - 2.145(5) respectively). The central Mn centre has Mn-N and Mn-O bond distances of 2.167(8) and 2.194(5), again, comparable to those for **4.2** (2.182(5) and 2.199(3) respectively).

**Table 5.3:** Selected bond distances (Å) and angles (°) for **5.1**.

Zn(1) N(15)	2.071(6)	Mn(1) N(11')	2.315(9)
Zn(1) N(6)	2.106(6)	Mn(2) N(17)	2.167(8)
Zn(1) O(3)	2.116(5)	Mn(2) O(3)	2.194(5)
Zn(1) O(1)	2.183(5)	Mn(1) Zn(1)	3.9871(15)
Zn(1) O(2)	2.212(6)	Mn(1) Zn(1')	3.9612(15)
Zn(1) N(12)	2.345(7)	Zn(1) Mn(2)	3.9238(11)
Mn(1) N(4)	2.004(8)		
Mn(1) N(8')	2.016(7)	Mn(1) O(1)	Zn(1) 134.0(3)
Mn(1) O(2')	2.116(5)	Mn(1) O(2')	Zn(1') 132.4(3)
Mn(1) O(1)	2.149(5)	Zn(1) O(3)	Mn(2) 131.1(2)
Mn(1) N(1)	2.235(8)		

**5.3.1.2:**  $[(2\text{pmoap-}2\text{H})_6\text{Mn}_5\text{Cu}_4](\text{NO}_3)_6 \cdot 24\text{H}_2\text{O}$  (**5.2**)

The structure of the cationic fragment of **5.2** and its core structural representation are shown in Figures 5.3a and 5.3b respectively, and significant bond lengths and angles are listed in Table 5.4.

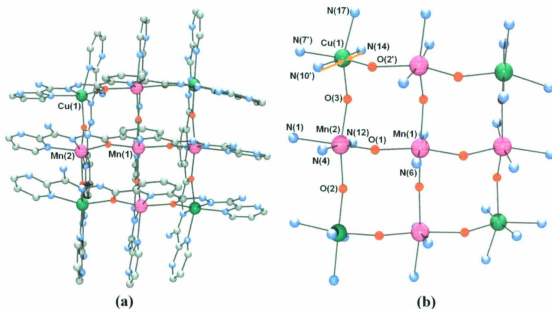


**Figure 5.3:** a) Ball-and-stick depiction of the cationic moiety **5.2**. Hydrogen atoms omitted for clarity. b) Core structural representation of **5.2**; arrows highlight the Jahn-Teller axes.

Complex **5.2** exhibits tetragonal crystallographic symmetry, and four-fold symmetry within the grid cation (Figure 5.3a). A typical [3×3] grid arrangement, with a [M<sub>9</sub>-(μ-O)<sub>12</sub>] core is revealed (Figure 5.3b) with *cis*-CuN<sub>4</sub>O<sub>2</sub> coordination environments for corner centres, *mer*-MnN<sub>3</sub>O<sub>3</sub> environments for the side centres, and a *trans*-MnN<sub>2</sub>O<sub>4</sub> coordination environment for the central Mn(II) ion. Metal assignment was done by comparison of bond lengths to that of the parent compound (**4.2**; a [3×3] Mn(II)<sub>9</sub> grid) and to a Cu(II)<sub>9</sub> grid with 2pmoap that crystallized in the same space group (**4.5**).

Metal-metal distances fall in the range 3.9723(5) - 4.0836(8) Å, with M-O-M angles in the range 130.10(14) - 134.35(16)°. The overall metal-metal grid dimensions are 8.0401(8) Å. Side Mn centres display long Mn-N distances to the external pyrimidine rings (2.327(4) Å), with shorter remaining Mn-N contacts (2.096(4) and 2.155(4) Å), similar to those reported for **4.2** (2.373(5) and 2.145(4) - 2.183(4) respectively), while the central Mn ion has Mn-N and Mn-O bond distances of 2.198(5) and 2.226(3), also comparable to those for **4.2** (2.182(5) and 2.199(3) respectively).

Cu(1) has axially compressed geometry resulting in a d<sub>z<sup>2</sup></sub> magnetic ground state, with long contacts to N(7'), N(17), O(2') and O(3) (2.134(3) - 2.244(5) Å), and short bonds to N(10) and N(14) (1.970(5) and 1.931(5) Å). For comparison, the central copper(II) ion for **4.5** also exhibits axial compression with four long contacts measuring 2.214(4) Å, and two short measuring 1.933(7) Å.

**Table 5.4:** Selected bond distances (Å) and angles (°) for **5.2**.

Cu(1) N(14)	1.931(5)	Mn(2) O(2)	2.193(4)
Cu(1) N(10 <sup>''</sup> )	1.970(5)	Mn(2) O(3)	2.211(3)
Cu(1) O(3)	2.134(3)	Mn(2) N(1)	2.327(4)
Cu(1) N(17)	2.169(4)	Cu(1) Mn(2)	4.0011(7)
Cu(1) O(2 <sup>'</sup> )	2.237(3)	Cu(1) Mn(2 <sup>'</sup> )	4.0836(8)
Cu(1) N(7 <sup>'</sup> )	2.244(5)	Mn(1) Mn(2 <sup>'</sup> )	3.9723(5)
Mn(1) N(6)	2.198(5)		
Mn(1) O(1)	2.226(3)	Mn(2) O(1)	Mn(1) 130.10(14)
Mn(2) N(4)	2.096(4)	Mn(2) O(2)	Cu(1 <sup>'</sup> ) 134.35(16)
Mn(2) O(1)	2.155(3)	Cu(1) O(3)	Mn(2) 134.12(16)
Mn(2) N(12)	2.155(4)		

**5.3.1.3:** [(2pmoap-2H)<sub>6</sub>Mn<sub>1</sub>Cu<sub>8</sub>](NO<sub>3</sub>)<sub>6</sub>·15H<sub>2</sub>O (**5.4**)

The structure of the cationic fragment of **5.4** and its core structural representation are shown in Figures 5.4a and 5.4b respectively, and significant bond lengths and angles are listed in Table 5.5.

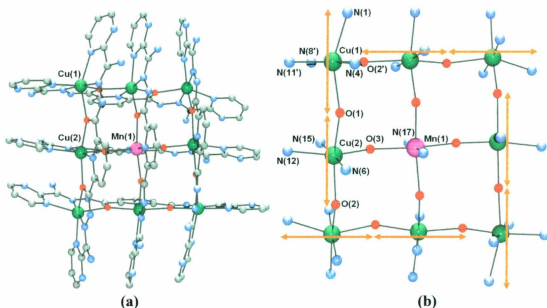


**Figure 5.4:** a) Ball-and-stick depiction of the cationic moiety **5.4**. Hydrogen atoms omitted for clarity. b) Core structural representation of **5.4**; arrows highlight the Jahn-Teller axes.

Complex **5.4** exhibits the normal  $[3 \times 3]$  grid arrangement with tetragonal crystallographic symmetry, and four-fold symmetry within the grid cation (Figure 5.4a). Metal assignment was done by comparison of bond lengths to that of the parent compound (**4.2**; a  $[3 \times 3]$  Mn(II)<sub>9</sub> grid) and to the all Cu(II)<sub>9</sub> grid, **4.5**, and from a sensible magnetic analysis. All agree with the presence of a Mn(II) ion at the centre of **5.4**, and Cu(II) at the side and corner sites.

Metal-metal distances fall in the range 4.0139(11) - 4.2491(15) Å, with M-O-M angles in the range 135.7(3) - 138.3(3)° and distances between corner Cu(II) centres of 8.2406(15) Å. Each copper ion has a Jahn-Teller distorted, axially elongated octahedral geometry (highlighted by the arrows in Figure 5.4b). Cu(1) has a  $d_{x^2-y^2}$  magnetic ground state as defined by short contacts to N(4), N(8'), N(11'), and O(2') (2.035 Å<sub>ave</sub>) with long axial contacts to N(1) and O(1) (2.271 Å<sub>ave</sub>). Cu(2) also exhibits a  $d_{x^2-y^2}$  ground state with short contacts to N(6), N(12), N(15), and O(3) (2.067 Å<sub>ave</sub>) and long axial contacts to O(1) and O(2) (2.251 Å<sub>ave</sub>). These values are comparable to those for the Cu(II) ions in the outer ring of **4.5** which also have  $d_{x^2-y^2}$  magnetic ground states (2.026 Å<sub>ave</sub> short and 2.262 Å<sub>ave</sub> axial). Mn(1) exhibits bond lengths that are consistent with those observed for the central Mn ion in **4.2**. This arrangement sets up orbitally orthogonal magnetic connections in the outer ring of eight copper ions, with non-orthogonal connections between Mn(1) and its neighbors, leading to the ferrimagnetic behaviour reported in Section 5.3.2.

**Table 5.5:** Selected bond distances (Å) and angles (°) for **5.4**.

Cu(1) N(8')	1.918(8)	Cu(2) O(1)	2.263(6)
Cu(1) N(4)	2.034(8)	Mn(1) N(17)	2.126(9)
Cu(1) O(2')	2.072(6)	Mn(1) O(3)	2.224(5)
Cu(1) N(11')	2.116(8)	Cu(1) Cu(2')	4.0288(15)
Cu(1) N(1)	2.253(8)	Cu(2) Cu(1)	4.2491(15)
Cu(1) O(1)	2.289(6)	Cu(2) Mn(1)	4.0139(11)
Cu(2) N(15)	1.942(7)		
Cu(2) N(6)	2.023(7)	Cu(1) O(2')	Cu(2') 138.3(3)
Cu(2) O(3)	2.110(6)	Cu(2) O(1)	Cu(1) 138.0(3)
Cu(2) N(12)	2.193(8)	Cu(2) O(3)	Mn(1) 135.7(3)
Cu(2) O(2)	2.238(6)		

### 5.3.2: Magnetic Properties:

The description of a magnetic exchange model for **5.1 - 5.3**,  $[3 \times 3] \text{Mn(II)}_5\text{M(II)}_4$  grids, requires that both metal identity, M (where  $M = \text{Zn, Cu or Ni}$ ), and position within the grid, be considered (Figure 5.5).

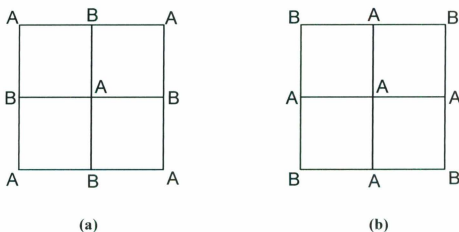


**Figure 5.5:**  $[3 \times 3] \text{A(II)}_5\text{B(II)}_4$  grids with metals sites arranged as for a) **5.1** ( $A = \text{Mn, B} = \text{Zn}$ ) and b) **5.2** ( $A = \text{Mn, B} = \text{Cu}$ ).

The heterometal arrangement presented in Figure 5.5a can be treated by an exchange Hamiltonian (equation 5.2) with a single  $J$  value since all magnetic

exchange interactions are between adjacent AB centres with similar A-O-B angles (Figure 5.6;  $J = J_1 = J_2$ ).

$$H_{ex} = -J\{S_1 \cdot S_2 + S_2 \cdot S_3 + S_3 \cdot S_4 + S_4 \cdot S_5 + S_5 \cdot S_6 + S_6 \cdot S_7 + S_7 \cdot S_8 + S_8 \cdot S_9 + S_1 \cdot S_8 + S_2 \cdot S_9 + S_4 \cdot S_9 + S_6 \cdot S_9 + S_8 \cdot S_9\} \quad (5.2)$$

This arrangement of metal atoms could lead to antiferromagnetically coupled systems with high spin ground states through the non-compensation of spins. For example, the largest spin difference for first row transition metal ions is between Mn(II) ( $S = 5/2$ ) and Cu(II) ( $S = 1/2$ ), and so a ground state spin of  $S' = 15/2$  results when A = Cu(II) and B = Mn(II) (Figure 5.5a). If the metal identities are reversed, the ground state would instead be  $S' = 21/2$ .

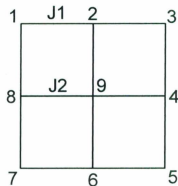


**Figure 5.6:** Magnetic exchange model for a  $[3 \times 3]$   $M_9$  grid.

The arrangement presented in Figure 5.5b would be better treated with a model that accounts for two different magnetic exchange interactions; one for the eight metal centres in the outer-ring (Figure 5.6;  $J_1$ ), where exchange is between different metal ions (A-B), and a second for the exchange between the central metal ion and its adjacent homometallic (A-A) centres (Figure 5.6;  $J_2$ ).

A Hamiltonian to describe this exchange situation is expressed in equation 5.3.

$$H_{ex} = -J1\{S_1 \cdot S_2 + S_2 \cdot S_3 + S_3 \cdot S_4 + S_4 \cdot S_5 + S_5 \cdot S_6 + S_6 \cdot S_7 + S_7 \cdot S_8 + S_1 \cdot S_8\} \\ - J2\{S_2 \cdot S_9 + S_4 \cdot S_9 + S_6 \cdot S_9 + S_8 \cdot S_9\} \quad (5.3)$$

This Hamiltonian can equally be used to describe the exchange situation that would occur if the eight metal ions in the outer-ring were one type (A), while the ninth metal ion in the centre was different (B).  $J1$  would then reflect the sign and magnitude of the exchange between A-A, while  $J2$  would be a reflection of the exchange between A-B.

Compound **5.1** is a  $[3 \times 3]$   $Mn(II)_5Zn(II)_4$  grid, with metal sites arranged as in Figure 5.5a, with A = Mn(II) ( $S = 5/2$ ) and B = Zn(II) ( $S = 0$ ). Its magnetic profile is shown in Figure 5.7 as a plot of moment per mole as a function of temperature.

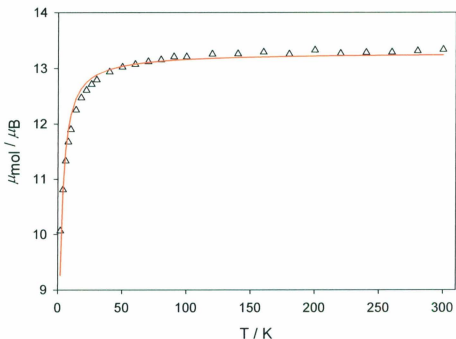


**Figure 5.7:** Variable temperature magnetic data for **5.1**;  $g = 2.006(6)$ ,  $J = -0.148(8) \text{ cm}^{-1}$ ,  $TIP = 20 \times 10^{-6} \text{ cm}^3 \text{ mol}^{-1}$ ,  $\rho = 0.10$ ,  $10^2 R = 2.39$ .

The moment drops from 13.3  $\mu_B$  at 300 K to 12.9  $\mu_B$  at 40 K, consistent with the presence of five isolated, non-interacting Mn(II) ions, followed by a rapid decrease to 10.1  $\mu_B$  at 2 K. This decrease could be attributed to zero-field splitting effects, however, these are normally quite small for Mn(II), and instead is due to weak, long-range antiferromagnetic coupling between Mn(II) centres *via* the intervening Zn(II) sites (Figure 5.2, Mn(1)-O(1)-Zn(1)-O(2)-Mn(1') and Mn(1)-O(2')-Zn(1')-O(3')-Mn(2)). The isotropic exchange Hamiltonian that describes this  $M_5$  exchange situation is expressed in equation 5.4 (see Figure 5.6 for site numbering):

$$H_{ex} = -J(S_1 \cdot S_7 + S_1 \cdot S_9 + S_1 \cdot S_3 + S_3 \cdot S_7 + S_3 \cdot S_9 + S_5 \cdot S_3) \quad (5.4)$$

The experimental magnetic data were fitted by non-linear regression within MAGMUN4.1 [49] to give  $g = 2.006(6)$ ,  $J = -0.148(8) \text{ cm}^{-1}$ ,  $TIP = 20 \times 10^{-6} \text{ cm}^3 \text{ mol}^{-1}$ ,  $\rho = 0.10$ ,  $10^2 R = 2.39$  ( $R = [\sum(\chi_{obs} - \chi_{calc})^2 / \sum \chi_{obs}^2]^{1/2}$ ). The solid line in Figure 5.7 was calculated with these parameters. These values are consistent with the small long-range magnetic exchange expected between the Mn-Mn centres and are comparable to the results obtained for an incompletely metalated Fe(III)<sub>5</sub> square grid formed from self-assembly with Cl2poap (Figure 5.1c) [70]. In this  $L_6M_5$  grid, ligands adopt the normal configuration for a  $[3 \times 3]$  grid, however, Fe(III) ions ( $S = 5/2$ ; the same as for Mn(II)) occupy only the centre and corner grid positions; the side metal sites are vacant. Data were fitted to an Fe(III)<sub>5</sub> (4+1) model, since no exchange pathway between the corner and central metals was present, to give  $g = 2.015$ ,  $J = -0.2 \text{ cm}^{-1}$ ,  $TIP = 200 \times 10^{-6} \text{ cm}^3 \text{ mol}^{-1}$ .

5.2 is a  $[3 \times 3]$   $\text{Mn(II)}_3\text{Cu(II)}_4$  grid with metal sites arranged as in Figure 5.5b, with A = Mn(II) ( $S = 5/2$ ) and B = Cu(II) ( $S = 1/2$ ). Its magnetic profile is shown in Figure 5.8 as a plot of moment per mole as a function of temperature.

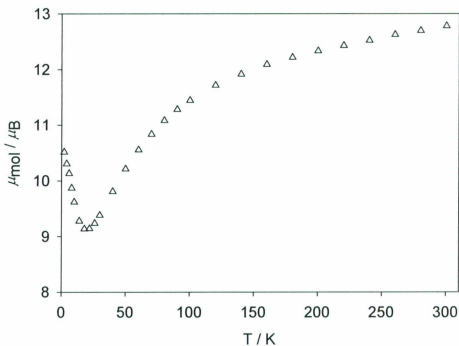


**Figure 5.8:** Variable temperature magnetic data for 5.2.

The moment drops from  $12.8 \mu_{\text{B}}$  at 300 K to to about  $9.14 \mu_{\text{B}}$  at approximately 20 K, followed by a rise at lower temperature, which is indicative of intramolecular antiferromagnetic exchange, and a high spin ground state. This results from the ferrimagnetic non-compensation of spins between the dissimilar metal ions. Theoretical calculations show the expected ground state to be  $S' = 11/2$ , however, the low temperature (2 K) moment suggests a slightly smaller ground state, and

depending on the choice of coupling constants, the  $S' = 9/2$  spin state is energetically close to the  $S' = 11/2$  state (Figure 5.9, with  $J_1 = J_2 = -1 \text{ cm}^{-1}$ ).

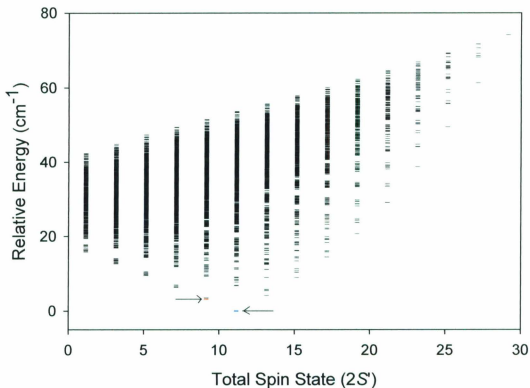


**Figure 5.9:** Calculated relative energy as a function of total spin state for 5.2; blue line shows the calculated ground state of  $S' = 11/2$ ; red line shows the second lowest lying energy state,  $S' = 9/2$ .

It is possible that at the lower temperature limit the real ground state is not being populated, but could be populated at some temperature below 2 K. This is supported by the magnetization data at 2 K, shown in Figure 5.10.

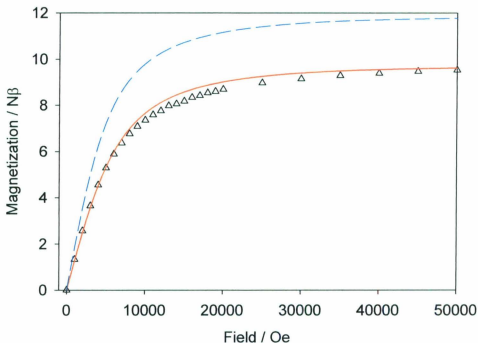


**Figure 5.10:** Variable field magnetization data for **5.2**; solid red line calculated for  $g = 2.15$ ,  $S' = 9/2$ ,  $T = 2$  K, and dashed blue line calculated for  $g = 2.15$ ,  $S' = 11/2$ ,  $T = 2$  K, using the appropriate Brillouin function.

The magnetization data show a sharp rise to an almost saturation value of  $9.5 N\beta$  at 5 T. Assuming an average  $g$  value of 2.15, the appropriate Brillouin function was used to simulate the data for an  $S' = 9/2$  ground state (Figure 5.10, solid red line) and for an  $S' = 11/2$  ground state (Figure 5.10, dashed blue line), clearly showing the close match between the experimental data and that expected for an  $S' = 9/2$  ground state. A hysteresis experiment was also performed, however, the loop was closed and exhibited no discernible coercive field.

The magnetic profile of **5.3**, a  $\text{Mn(II)}_5\text{Ni(II)}_4$  grid, is shown in Figure 5.11 and shows a moment at room temperature of  $15.4 \mu_B$ , which drops on lowering the

temperature to  $9.3 \mu_B$  at 2 K indicative of intramolecular antiferromagnetic exchange between metal centres.

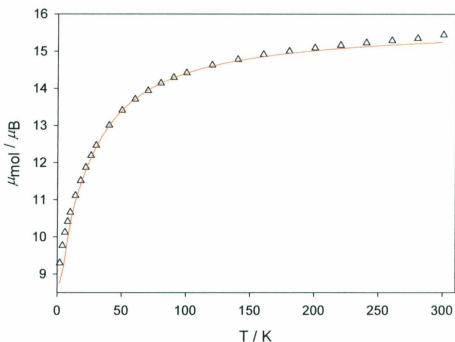


**Figure 5.11:** Variable temperature magnetic data for **5.3**. Solid line calculated for  $g_{\text{ave}} = 2.17$ ,  $J = -3 \text{ cm}^{-1}$ ,  $\text{TIP} = 750 \times 10^{-6} \text{ cm}^3 \text{ mol}^{-1}$ ,  $\rho = 0.05$ .

While structural characterization of **5.3** has not been possible, theoretical calculations show that within an antiferromagnetically coupled grid framework, with metal sites arranged as in Figure 5.5b, with A = Mn(II) ( $S = 5/2$ ) and B = Ni(II) ( $S = 1$ ), the expected ground state for **5.3** would be  $S' = 7/2$ , in agreement with the experimental value at 2 K. As a comparison, if instead the metals were arranged as in Figure 5.5a, with A = Mn(II) and B = Ni(II), the expected ground state would be  $S' = 17/2$ , which is not consistent with the experimental data. Total spin state/energy ( $S'/E$ ) calculations can be carried out on a personal computer with 2 GB of RAM, however 58644 energy states

result, which exceeds the number of lines that can be read by MAGMUN4.1 [49], and so fitting by least squares regression of the experimental data was not performed. Imposing D4 spin rotational symmetry on the system to simplify the problem does allow for the generation of susceptibility profile simulations [121]. While this is not a fit, fixing the exchange variables with sensible values does allow for a close approximation of the experimental data. As a comparison, for the [2×2] Ni(II)<sub>4</sub> square, **3.3**, the fitted values  $g = 2.25(1)$ ,  $J = -13.3(8) \text{ cm}^{-1}$ ,  $\text{TIP} = 800 \times 10^{-6} \text{ cm}^3 \text{ mol}^{-1}$  were obtained (Ni-O-Ni  $136.48^\circ_{\text{ave}}$ ), while for the trigonal bipyramidal Mn(II)<sub>5</sub> cluster, **3.8**, the fitted values  $g = 2.015$ ,  $J = -2.65 \text{ cm}^{-1}$ ,  $\text{TIP} = 0 \text{ cm}^3 \text{ mol}^{-1}$ , were obtained (Mn-O-Mn  $127.53^\circ_{\text{ave}}$ ). It would therefore be reasonable to assume that for **5.3**,  $g$  should be intermediate between those obtained for **3.3** and **3.8**, while TIP should reflect the presence of four Ni(II) ions. After numerous simulations were generated and compared 'by sight' to each other and to the experimental data, a good match for **5.3** was obtained with  $g_{\text{ave}} = 2.17$ ,  $J = -3 \text{ cm}^{-1}$ ,  $\text{TIP} = 750 \times 10^{-6} \text{ cm}^3 \text{ mol}^{-1}$ ,  $\rho = 0.05$  (solid line in Figure 5.11).

Compound **5.4** is a [3×3] Mn(II)<sub>1</sub>Cu(II)<sub>8</sub> grid and its magnetic profile is shown in Figure 5.12 as a plot of moment per mole as a function of temperature. The moment drops from  $8.67 \mu_B$  at 300 K to a plateau value of approximately  $5.2 \mu_B$  between 18 K and 2 K, suggesting an antiferromagnetic exchange component, followed by a second, weak, ferromagnetic exchange contribution.

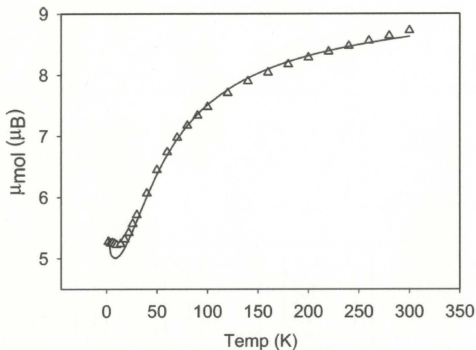


**Figure 5.12:** Variable temperature magnetic data for **5.4**;  $g = 2.3(1)$ ,  $J_1 = 0.45(2) \text{ cm}^{-1}$ ,  $J_2 = -22.5(2) \text{ cm}^{-1}$ ,  $\text{TIP} = 1000 \times 10^{-6} \text{ cm}^3 \text{ mol}^{-1}$ ,  $\rho = 0.055$ ,  $\theta = -0.5$ ,  $10^2 R = 2.2$ .

Compound **5.4** exhibits four-fold symmetry within the grid cation, as seen from the crystal structure, which is useful in the interpretation of the magnetic connectivity and modeling of the experimental data. The corner and side distorted octahedral copper centres (Cu(1) and Cu(2); Figure 5.4b) exhibit Jahn-Teller elongation that defines their magnetic ground states as  $d_x^2-y^2$ . The long axis for Cu(1) points towards O(1) with a short connection directed towards O(2), while for Cu(2) the long axis is directed towards both O(1) and O(2) with a short connection to O(3) (Figure 5.4b). Based upon the directionality of the Jahn-Teller axes in the outer  $\text{Cu(II)}_8$  ring, the  $\text{Cu(1)-O(2')-Cu(2')}$  and  $\text{Cu(2)-O(1)-Cu(1)}$  connections are orthogonal, while the  $\text{Cu(2)-O(3)-Mn(1)}$  connection is not. These structural features should allow only for ferromagnetic coupling between Cu(1) and Cu(2) centres (and their symmetry related counter-parts), and a single

exchange constant can be used to model the ring's contribution to the observed magnetic properties ( $J_1$ , Figure 5.6). Unlike the Jahn-Teller distorted Cu(II) centres, the central Mn(II) ion is magnetically isotropic, with electron density along all axes, leading to antiferromagnetic exchange between the Cu(2) centres and Mn(1) ( $J_2$ , Figure 5.6) via the non-orthogonal Cu(2)-O(3) connection.

**5.4** was fitted in a manner similar to the homometallic Cu(II)<sub>9</sub> grids, **4.5** and **4.6** by using the non-linear regression routines built into the MAGMUN4.1 [49] software to evaluate  $J_2$  as a fraction of  $J_1$ . This is not a completely rigorous approach since it does not allow for an independent regression analysis of the 2J model. However, based upon the structure, useful information on the magnitude of the couplings can be obtained.

A fit for **5.4** was obtained after many trial comparisons varying the ratio of  $-J_2/J_1$  to give  $g_{\text{ave}} = 2.3(1)$ ,  $J_1 = 0.45(2) \text{ cm}^{-1}$ ,  $J_2 = -22.5(2) \text{ cm}^{-1}$ ,  $\text{TIP} = 1000 \times 10^{-6} \text{ cm}^3 \text{ mol}^{-1}$ ,  $\rho = 0.055$ ,  $\theta = -0.5$ ,  $10^2 R = 2.2$ . The solid line in Figure 5.12 was calculated with these parameters and the exchange coupling is consistent with the ferromagnetic ring contribution of other [3×3] Cu(II)<sub>9</sub> grids [66,69,71,96], while the sign and magnitude of the exchange between Cu(2) and Mn(1) agrees with that expected from the structural analysis.

A magnetization versus field study for **5.4** was carried out at 2 K. The experimental data rise smoothly with increasing field from 0 N $\beta$  to 4.73 N $\beta$  at 50000 Oe. The calculated ground state is  $S = 3/2$ , and so a solid line was calculated for  $g_{\text{ave}} = 2.2$ ,  $T = 2 \text{ K}$ ,  $S' = 3/2$  (Figure 5.13, solid red line) using the appropriate Brillouin function. A clear discrepancy is observed between the predicted ground state and that observed

experimentally, and may be associated with the presence of some Mn(II)-rich impurity. A second simulation with  $S' = 5/2$  was calculated (Figure 5.13, dashed blue line), and further supports that the experimental ground state is not strictly  $S = 3/2$ .

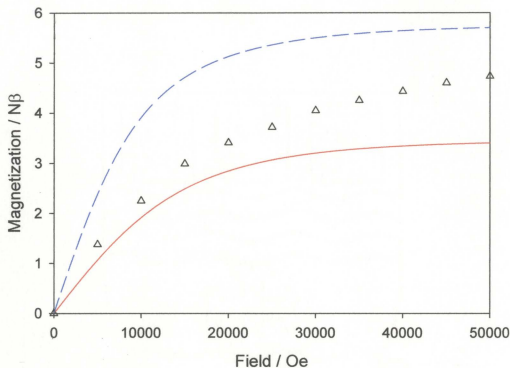


**Figure 5.13:** Variable field magnetization data for **5.4**; solid red line represents simulation with  $g = 2.3$ ,  $T = 2$  K,  $S' = 3/2$ ; dashed blue line represents  $g = 2.3$ ,  $T = 2$  K,  $S' = 5/2$  using the appropriate Brillouin function.

#### 5.4: Summary:

Mixed metal square  $[3 \times 3]$   $\text{Mn(II)}_5\text{M(II)}_4$  grids (where  $M = \text{Zn}$  (**5.1**),  $\text{Cu}$  (**5.2**) and  $\text{Ni}$  (**5.3**)), as well as a  $[3 \times 3]$   $\text{Mn(II)}_1\text{Cu(II)}_8$  grid (**5.4**) complex were synthesized, and characterized structurally (except **5.3**) and magnetically.

Compounds **5.1** and **5.3** were produced by self-assembly reactions between two different metal salts and the ligand 2pmoap. The magnetic properties of both are dominated by antiferromagnetic exchange. For **5.1**, Mn(II) ( $S = 5/2$ ) ions occupy the corner and centre positions in the grid framework, while the side sites are occupied by diamagnetic Zn(II) ions. The magnitude of the antiferromagnetic exchange between Mn(II) centres is very weak, consistent with the absence of direct bridging pathways between Mn(II) ions. Fitted values for the magnetic data are also consistent with the analogous Fe(III) ( $S = 5/2$ )  $L_6M_5$  incompletely metalated square grid, where side metal positions were vacant [70]. No structural characterization was possible for **5.3**, however, the magnetic profile and calculated ground state are consistent with the presence of four Ni(II) ions at the corner sites in the grid and five Mn(II) ions in the side and centre grid positions.  $D_4$  spin rotational symmetry was imposed on the system and a simulation was generated that closely matched the experimental data.

Compounds **5.2** and **5.4** were produced by substitutions reactions, through gentle heating of the parent  $[3 \times 3]$   $[Mn_9(2pmoap-2H)_6](NO_3)_6 \cdot 13H_2O$  grid (**4.2**) with  $Cu(NO_3)_2$  to give a  $[3 \times 3]$   $Mn(II)_5Cu(II)_4$  grid (**5.2**), or by refluxing with  $Cu(NO_3)_2$  to give a  $[3 \times 3]$   $Mn(II)_1Cu(II)_8$  grid (**5.4**). A high spin ground state was exhibited by **5.2**, resulting from the non-compensation of spins due to the ferrimagnetic effect from the intramolecular antiferromagnetic exchange between the heterometallic ions. While calculations gave  $S' = 11/2$  as the predicted ground state, a smaller,  $S' = 9/2$ , ground state was observed experimentally, likely due to the real ground state not being populated at the experimental low temperature limit (2 K). For **5.4**, the presence of Jahn-Teller distortions in the outer

ring of eight Cu(II) ions leads to magnetic orbital orthogonality and ferromagnetic exchange. An antiferromagnetic exchange contribution was also present, between the central Mn(II) ion and the side Cu(II) sites. The experimental data were modeled with two different exchange constants that were independently varied in an iterative ratio to obtain a best fit.

The corner-site selective substitution upon gentle heating, for **5.2**, followed by substitution of the full outer-ring upon refluxing, for **5.4**, suggests that these positions are particularly labile. Site-specific oxidations have also been experimentally observed and characterized for  $[\text{Mn}_9(\text{2poap-2H})_6](\text{ClO}_4)_6 \cdot 18\text{H}_2\text{O}$  [29,30,73]. A bulk electrolysis experiment produced the mixed-oxidation state complex  $[\text{Mn}(\text{II})_5\text{Mn}(\text{III})_4(\text{2poap-2H})_6](\text{ClO}_4)_{10} \cdot 10\text{H}_2\text{O}$  and structural characterization showed the Mn(III) sites were present in the corner positions of this grid [29]. Cyclic and differential pulse voltammetry showed five quasi-reversible waves [29,30], with the first wave corresponding to a four electron oxidation (assigned as the oxidation of the corner sites), followed by four one-electron processes (oxidation of the side sites). These electrochemical results, and the substitution reaction results for **5.2** and **5.4**, show that within a normal  $[3 \times 3]$  Mn(II) grid framework the corner *cis*- $\text{MnN}_4\text{O}_2$  sites are the most labile and susceptible to both oxidation and substitution, with the side *mer*- $\text{MnN}_3\text{O}_3$  sites requiring more forcing reactions conditions, while the centre *trans*- $\text{MnN}_2\text{O}_4$  ion has yet to show any affinity for oxidation or substitution.

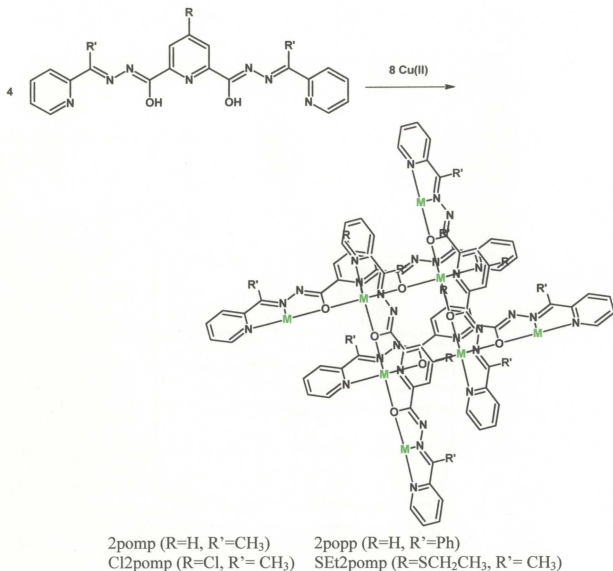
## Chapter 6: Long range magnetic cooperativity through extended structural motifs?

### Introducing intermolecular $\pi$ - $\pi$ interactions between [3 $\times$ 3] M<sub>9</sub> grids

#### 6.1: Preamble:

Supramolecular chemistry, as discussed in Chapter 1, is concerned primarily with weak, non-covalent bonding interactions. Many such 'bonds' are possible, including ion-ion (250 kJ mol<sup>-1</sup>; *versus* the homolytic cleavage of a covalent bond which requires 100 - 400 kJ mol<sup>-1</sup>), ion-dipole (50 - 200 kJ mol<sup>-1</sup>), dipole-dipole (5 - 50 kJ mol<sup>-1</sup>), hydrogen bonding (10 - 65 kJ mol<sup>-1</sup>) and van der Waals force interactions (less than 5 kJ mol<sup>-1</sup>) [122, 123]. A detailed understanding of these interactions, as exhibited by molecules suitable for use as building blocks, or 'synthons', in theory allows for the synthesis of new crystalline materials in a predictable and rational manner, and is an area of active research among crystal engineers [124].

As an alternative to [3 $\times$ 3] Cu(II)<sub>9</sub> grids,  $\mu$ -O and  $\mu$ -NN bridged Cu(II)<sub>8</sub>L<sub>4</sub> (L = 2pomp, 2popp, Cl2pomp and SEt2pomp) ferromagnetic 'pinwheels' have been synthesized, and possess open coordination sites on the Cu(II) ions in the 'arms' of the pinwheels (Scheme 6.1) [96, 125]. These open sites make secondary coordination to a suitable bridging co-ligand or anion (synthon) possible, and introduce a logical route to materials that could exhibit long-range magnetic cooperativity.



**Scheme 6.1:** General synthesis of Cu(II)<sub>8</sub>L<sub>4</sub> pinwheels.

For example, the pinwheel complex [(2pomp-2H)<sub>4</sub>Cu<sub>8</sub>Br<sub>6</sub>](CuBr<sub>4</sub>)(H<sub>2</sub>O)<sub>11</sub> has been reported [125], with bromide ions bridging the external Cu(II) centres of four adjacent pinwheels, leading to the formation of a two-dimensional network, with cavities filled by hydrogen-bonded CuBr<sub>4</sub><sup>2-</sup> guests, though no evidence for intermolecular magnetic communication was detected. In the complex [(Cl2pomp-2H)<sub>4</sub>Cu<sub>8</sub>(N(CN)<sub>2</sub>)<sub>8</sub>](H<sub>2</sub>O)<sub>9</sub>(CH<sub>3</sub>CN), however, dicyanamide ions bound to the external Cu(II) centres

interacted with the central chlorine atoms on ligands of adjacent pinwheels, leading to the formation of stacked clusters, with evidence for weak long-range magnetic interactions [125].

Intermolecular  $\pi$ - $\pi$  interactions ( $50 \text{ kJ mol}^{-1}$ ) are another type of non-covalent 'bond' that can act as a powerful organizing force for extended lattice interactions [122, 123]. Elegantly stated by Claessens and Stoddart,  $\pi$ - $\pi$  interactions "...define and rule the self-assembly processes that lead to the formation of the desired molecular and supramolecular architectures, and thereafter they still govern the dynamic processes occurring within the self-assembled structures and superstructures." [126] Significant and broad  $\pi$ - $\pi$  interactions have been identified in biological systems [127], for example stacked nucleotide-base pairs (aromatic pyrimidine and purine groups) separated by  $3.5 \text{ \AA}$  help to stabilize the DNA double-helix [128]. Supramolecular chemists have employed concave (electron donating) - convex (electron withdrawing)  $\pi$ - $\pi$  interactions in novel host-guest systems to synthesize inclusion complexes of  $\text{C}_{60}$  with corannulene derivatives [129-131].

The term  $\pi$ - $\pi$  interaction is normally used to describe parallel, stacked aromatic groups, separated by distances between  $3.3 - 3.8 \text{ \AA}$ , where interactions of approximately  $3.3 \text{ \AA}$  are considered strong, those greater than  $3.6 \text{ \AA}$  are considered weaker, and  $3.8 \text{ \AA}$  is the approximate maximum value that can be considered the limit of a real interaction [132]. The limiting forms of such interactions are the largely repulsive 'face-to-face' stacked conformation, and the enthalpically favorable 'edge-to-face' C-H -  $\pi$  interactions (Figure 6.1a and c, respectively).

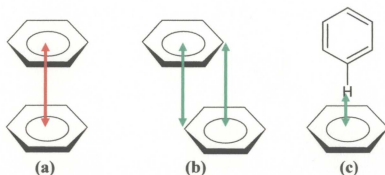


**Figure 6.1:** a) Direct, repulsive,  $\pi$ - $\pi$  overlap. b) Favourable slipped 'face-to-face' and c) 'edge-to-face'  $\pi$ - $\pi$  interactions.

Hunter and Sanders [133,134] have proposed rules that qualitatively account for the charge distribution in a non-polarized  $\pi$ -system by separating the  $\sigma$ -framework and the  $\pi$ -electrons. These rules state that:

1. In a face-to-face  $\pi$ -stacked geometry (Figure 6.1a)  $\pi$ - $\pi$  repulsions dominate.
2. In an edge-on geometry (Figure 6.1c)  $\pi$ - $\sigma$  attractions dominate.
3. In a slipped or off-set  $\pi$ -stacked geometry (Figure 6.1b)  $\pi$ - $\sigma$  attractions dominate.

The introduction of substituents or heteroatoms alters the uniform charge distribution in non-polarized  $\pi$ -systems, and introduces electrostatic dipole-dipole and dipole-induced-dipole interactions, and in some cases, electrostatic considerations (that is, the Hunter-Sanders rules) cannot satisfactorily explain binding trends for edge-to-face interactions [135,136]. However, the introduction of electron-withdrawing groups (like the nitrogen atom in pyridine) does increase face-to-face  $\pi$ - $\pi$  interactions by decreasing the  $\pi$ -electron density in the aromatic ring, and reducing repulsive effects [132]. Furthermore, if the aromatic heteroatom is involved in metal coordination, the electron-

withdrawing effect will be increased, as will the tendency for such systems to exhibit  $\pi$ - $\pi$  stacking.

Janiak [132] performed a Cambridge Structural Database search on the interaction between two transition-metal quinoline fragments and found several types of possible  $\pi$ - $\pi$  stacking interactions. Three prominent motifs were the approach of the two pyridine rings, or the two arene rings or the arene to the pyridine ring. Analysis was done for centroid-centroid distances out to 3.8 Å, with 718 structures that satisfied his search criteria giving 980 data sets (as several structures contained multiple contacts). It was found that a preference for the pyridine-arene interaction existed, followed by the arene-arene approach and that pyridine-pyridine interactions were significantly less common. For all real  $\pi$ - $\pi$  interactions, displacement angles of approximately  $20^\circ$  were found (Figure 6.2,  $\alpha$ -angle).

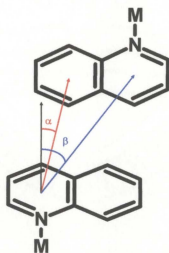


**Figure 6.2:** Stacking of two quinoline rings; black arrow indicates the normal vector to the quinoline plane; red arrow drawn from the centroid of one quinoline-pyridine moiety to the centroid of the other quinoline-arene moiety, off-set by the angle  $\alpha$ ; blue arrow

drawn from the centroid of one quinoline-pyridine moiety to the centroid of the other quinoline-pyridine moiety, off-set by the angle  $\beta$ .

Given the tendency for metal coordinated quinoline rings to form extended lattice motifs [132,137-141], ligands with a variety of quinoline-type endpieces were synthesized in an attempt to organize grid molecules into extended arrays (Figure 6.3 and 6.4).

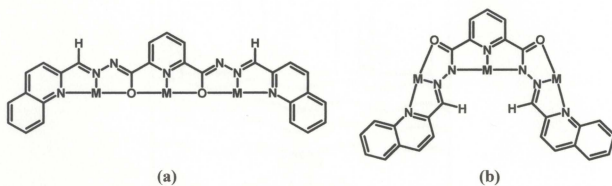


**Figure 6.3:** a) The  $\mu$ -O and b)  $\mu$ -NN bridging modes of 2po56hq (2.5).

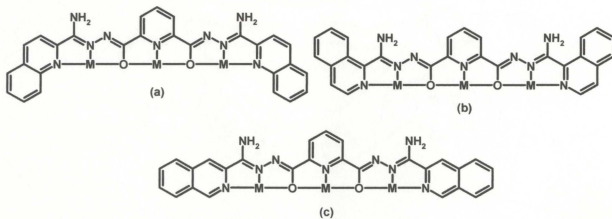


**Figure 6.4:** a) 2po56nq (2.6); b) 2po34nq (2.8); c) 2po45nq (2.7).

Upon self-assembly with appropriate metal salts, a regular  $[3 \times 3]$  Mn(II)<sub>9</sub> grid was produced, as well as a unique  $3 \times [1 \times 3]$  Mn(II)<sub>9</sub> rectangle and two  $[3 \times 3]$  Cu(II)<sub>9</sub> grids that

exhibit intermolecular face-to-face and edge-to-face  $\pi$ - $\pi$  interactions. In one case, the typical octahedral Cu(II) Jahn-Teller distortions are altered, resulting in a distinctive antiferromagnetic  $[3 \times 3] \text{Cu(II)}_9$  grid. These results are presented here.

## 6.2: Experimental:

**Note:** In some cases there is a difference between the most reasonable formula based on the elemental analysis (analytical formula), and that obtained from X-ray crystallography. The analytical formulae will be used here.

### 6.2.1: Complex synthesis:

**6.2.1.1:**  $(2\text{po56hq}+2\text{H})(\text{BF}_4)_2(\text{H}_2\text{O})_{1.6}$  (**6.1**).  $2\text{po56hq}$  (**2.5**; 0.12 g, 0.25 mmol) was added to a warm solution of  $\text{Zn}(\text{BF}_4)_2 \cdot x\text{H}_2\text{O}$  (0.14 g, 0.40 mmol) in  $\text{CH}_3\text{OH}:\text{CH}_3\text{CN}$  (10:10 mL) producing a clear yellow-green solution. The flask was equipped with a condenser and allowed to stir with gentle heating for 24 hours and at room temperature for 48 hours. The solution was kept after filtration for crystallization. Yellow prismatic crystals, suitable for X-ray analysis, formed upon standing for 6 days (yield 0.01 g, 8 %). Anal. Calcd (%) for  $(\text{C}_{27}\text{H}_{21}\text{N}_7\text{O}_2)(\text{BF}_4)_2 \cdot 1.6\text{H}_2\text{O}$  (bulk sample): C, 47.83; H, 3.60; N, 14.46. Found (%): C, 47.95; H, 3.89; N, 14.31. No further product could be cleanly isolated from the mother liquor, though it is presumed that a zinc complex remained therein.

**6.2.1.2:**  $[(2\text{po56hq}-2\text{H})_6\text{Mn}_9](\text{ClO}_4)_6 \cdot 8\text{H}_2\text{O}$  (**6.2**).  $2\text{po56hq}$  (**2.5**; 0.12 g, 0.25 mmol) was added to a warm solution of  $\text{Mn}(\text{ClO}_4)_2 \cdot 6\text{H}_2\text{O}$  (0.14 g, 0.55 mmol) in  $\text{CH}_3\text{OH}:\text{CH}_3\text{CN}$  (10:10 mL). A cloudy, white suspension formed. The addition of 2 drops of triethylamine produced a dark orange solution, which was stirred with gentle heating for 2 hours and

kept after filtration for crystallization. Red prismatic crystals, suitable for X-ray analysis, formed upon standing for two weeks (yield 0.30 g, 30 %). Anal. Calcd (%) for  $[(C_{27}H_{17}N_7O_2)_6Mn_9](ClO_4)_6 \cdot 8H_2O$  (bulk sample): C, 47.89; H, 2.91; N, 14.89. Found (%): C, 47.87; H, 2.85; N, 14.41.

**6.2.1.3:**  $[(2po56nq-2H)_6Cu_9](BF_4)_6 \cdot 6H_2O$  (**6.3**). 2po56nq (**2.6**; 0.12 g, 0.35 mmol) was added to a warm solution of  $Cu(CH_3COO)_2 \cdot H_2O$  (0.08 g, 0.4 mmol) in 20 mL of 1:1  $CH_3OH:CH_3CN$ . This produced a clear, dark brown solution that was stirred with gentle heating for 20 minutes.  $NaBF_4$  (0.030 g, 0.27 mmol) was then added (solution appearance remained unchanged), and heating and stirring was continued for four hours. The filtrate was kept after filtration for crystallization. Very small, weakly diffracting red prismatic crystals formed upon standing, covered, for five months (yield 0.030 g, 16 %). Anal. calcd (%) for  $[(C_{27}H_{19}N_9O_2)_6Cu_9](BF_4)_6 \cdot 6H_2O$ : C, 46.22; H, 3.02; N, 17.97. Found (%): C, 46.28; H, 3.09; N 17.86.

**6.2.1.4:**  $[(2po45nq-2H)_6Cu_9](CF_3SO_3)_2(PF_6)_4 \cdot 22H_2O$  (**6.4**). 2po45nq (**2.7**; 0.12 g, 0.35 mmol) was added to a warm solution of  $Cu(CF_3SO_3)_2$  (0.13 g, 0.36 mmol) in 20 mL of 1:1  $CH_3OH:CH_3CN$ . This produced a clear, dark brown solution that was stirred with gentle heating (equipped with a condenser) for 24 hours, followed by stirring at room temperature for an additional 24 hours. The dark brown filtrate was kept after filtration for crystallization producing a brown powder that was recrystallized from 10 mL of 1:1  $CH_3OH:CH_3CN$  with the addition of  $NH_4PF_6$  (0.040 g, 0.25 mmol). This solution was again filtered and the filtrate kept for crystallization, forming green crystals suitable for X-ray diffraction upon standing for seven days (yield 0.030 g, 15 %). Anal. Calcd (%) for

$[(C_{27}H_{19}N_9O_2)_6Cu_9](CF_3SO_3)_2(PF_6)_4 \cdot 22H_2O$ : C, 40.57; H, 3.28; N, 15.58. Found (%): C, 40.68; H, 2.39; N 15.31.

**6.2.1.5:**  $[(2po45nq-2H)_6Co_9](BF_4)_{10} \cdot 3CH_3OH \cdot 8H_2O$  (**6.5**).  $Co(BF_4)_2 \cdot 6H_2O$  (0.12 g, 0.35 mmol) was added to a slurry of 2po45nq (**2.7**; 0.12 g, 0.24 mmol) in 20 mL of 1:1  $CH_3OH:CH_3CN$ . This produced a clear, brown solution that was stirred with gentle heating for 24 hours and then at room temperature for another 36 hours, at which time a brown precipitate formed. The reaction mixture was filtered and a brown powder was collected (0.12g; 75 % yield). Air was not excluded during this preparation. Anal. Calcd (%) for  $[(C_{27}H_{19}N_9O_2)_6Co_9](BF_4)_{10} \cdot 3CH_3OH \cdot 8H_2O$ : C, 42.64; H, 3.08; N, 16.27. Found (%): C, 42.94; H, 3.12; N 16.43.

**6.2.1.6:**  $[(2po34nq-2H)_6Mn_9](CF_3SO_3)_6 \cdot 23H_2O$  (**6.6**).  $Mn(CF_3SO_3)_2 \cdot xH_2O$  (2 mL of a  $0.09 \text{ g mL}^{-1}$  solution in  $CH_3OH$ ; 0.5 mmol) was added to a slurry of 2po34nq (**2.8**; 0.090 g, 0.18 mmol) in 20 mL of 1:1  $CH_3OH:CH_3CN$  to give an orange slurry.  $NH_4CH_3COO$  (0.04 g, 0.5 mmol) was added, producing no change in the appearance of the mixture, which was then stirred with gentle heating for four hours. The reaction mixture was filtered and the clear, orange filtrate was preserved for crystallization. After six days dark red crystals were observed, but were unsuitable for analysis by X-ray diffraction. These were redissolved in 14 mL of 1:1  $CH_3OH:CH_3CN$  with the addition of  $NaNO_3$  (0.030 g, 0.35 mmol) and the resulting clear red solution was stirred with gentle heating for one hour and then filtered, with the filtrate again preserved for crystallization. Red crystals suitable for X-ray analysis formed upon standing, covered, for 3 months (0.01 g;

7 % yield). Anal. Calcd (%) for  $[(C_{27}H_{19}N_9O_2)_6Mn_9](CF_3SO_3)_6 \cdot 23H_2O$ : C, 41.93; H, 3.35; N, 15.72. Found (%): C, 41.99; H, 2.61; N 15.50.

### 6.2.2: Crystallography

The diffraction intensities of a colourless prismatic crystal of **6.1** having approximate dimensions of  $0.48 \times 0.20 \times 0.20$  mm were collected on a Rigaku Saturn CCD area detector with graphite monochromated Mo-K $\alpha$  radiation at 153(2) K to a maximum  $2\theta$  value of  $61.8^\circ$ . The data were corrected for Lorentz and polarization effects and a correction for secondary extinction [81] was applied. The structure was solved by direct methods [82,83] and expanded using Fourier techniques [84]. Hydrogen atoms were introduced in calculated positions, except H(22,23,27), which were introduced in difference map positions, with isotropic thermal parameters set twenty percent greater than those of their bonding partners. They were refined on the riding model. All non-hydrogen atoms were refined anisotropically. Neutral atom scattering factors and anomalous dispersion effects were taken from the usual sources [85-88]. All calculations were performed using the Crystal Structure [89,90] crystallographic software package except for refinement, which was performed using SHELXL-97 [83].

A red prismatic crystal of **6.2** having approximate dimensions of  $0.20 \times 0.20 \times 0.20$  mm was treated similarly to **6.1**. Hydrogen atoms were introduced in calculated positions with isotropic thermal parameters set twenty percent greater than those of their bonding partners. They were refined on the riding model. The Platon [91] Squeeze procedure was applied to recover 396.7 electrons per unit cell in four voids ( $3203.8 \text{ \AA}^3$ ); that is 99.2 electrons per formula unit. Disordered solvent water and acetonitrile

molecules appeared to be present prior to the application of Squeeze, though a good point atom model could not be achieved. The application of Squeeze gave a good improvement in the data statistics and allowed for a full anisotropic refinement of the framework structure and counterions.

A red prismatic crystal of **6.3** having approximate dimensions of  $0.60 \times 0.49 \times 0.41$  mm was treated similarly to **6.1**. Hydrogen atoms were introduced in calculated positions with isotropic thermal parameters set twenty percent greater than those of their bonding partners. They were refined on the riding model. The Platon [91] Squeeze procedure was applied to recover 396.7 electrons per unit cell in one void ( $62258.5 \text{ \AA}^3$ ); that is 187.45 electrons per formula unit. Evidence for three tetrafluoroborate anions and several solvent water molecules was present prior to the application of Squeeze, though a good point atom model could not be achieved. The application of Squeeze gave a good improvement in the data statistics and allowed for a full anisotropic refinement of the framework cationic structure and three tetrafluoroborate anions.

A brown prismatic crystal of **6.4** having approximate dimensions of  $0.39 \times 0.38 \times 0.28$  mm was treated similarly to **6.1**. Hydrogen atoms were introduced in calculated positions with isotropic thermal parameters set twenty percent greater than those of their bonding partners. They were refined on the riding model. All non-hydrogen atoms were refined anisotropically. Six ligands were present in the core structure; each with a charge of -2, for a total charge of -12. 8.5 copper(II) atoms were also present, contributing a charge of +17. The charge is therefore balanced by the presence of 3.6 hexafluorophosphate and 1.4 triflate anions which make up a charge of -5. 0.75 water

molecules were present in the asymmetric unit, contributing 3 molecules per formula unit. The protons on these could not be located in the difference map and hence were omitted from the model.

A red prismatic crystal of **6.6** having approximate dimensions of  $0.68 \times 0.36 \times 0.35$  mm was treated similarly to **6.1**. Hydrogen atoms were introduced in calculated positions with isotropic thermal parameters set twenty percent greater than those of their bonding partners. They were refined on the riding model. The Platon [91] Squeeze procedure was applied to recover 553.4 electrons per unit cell in one void ( $3765.5 \text{ \AA}^3$ ); that is 276.7 electrons per formula unit. A total of two disordered/partial occupancy triflate anions, three nitrate anions and some lattice water appeared to be present prior to the application of Squeeze, though a good point atom model could not be achieved. The application of Squeeze gave a good improvement in the data statistics and allowed for a full anisotropic refinement of the framework structure. An additional full occupancy triflate anion that was not disordered is present in the asymmetric unit and was not removed in the application of Squeeze. Abbreviated crystal data for **6.1** - **6.4** and **6.6** are listed in Tables 6.1 and 6.2.

**Table 6.1:** Summary of crystallographic data for **6.1 - 6.3**.

	<b>6.1</b>	<b>6.2</b>	<b>6.3</b>
Chemical Formula	C <sub>28</sub> H <sub>27</sub> B <sub>2</sub> F <sub>8</sub> N <sub>7</sub> O <sub>4</sub>	C <sub>162</sub> H <sub>102</sub> Cl <sub>6</sub> Mn <sub>9</sub> N <sub>42</sub> O <sub>36</sub>	C <sub>162</sub> H <sub>126.80</sub> B <sub>6</sub> Cu <sub>9</sub> F <sub>24</sub> N <sub>54</sub> O <sub>18.40</sub>
M	699.17	3920.01	4217.07
T(K)	153(2)	153(2)	138(2)
Crystal System	triclinic	monoclinic	triclinic
Space Group	P $\bar{1}$ (#2)	P2 <sub>1</sub> /n (#14)	P $\bar{1}$ (#2)
a (Å)	9.1217(8)	20.908(4)	15.604(3)
b (Å)	10.1336(8)	27.102(4)	23.135(4)
c (Å)	17.6705(19)	32.492(5)	26.411(5)
$\alpha$ (°)	77.640(8)	90.00	93.403(4)
$\beta$ (°)	82.793(9)	98.239(4)	100.014(5)
$\gamma$ (°)	68.011(6)	90.00	90.626(5)
V (Å <sup>3</sup> )	1477.6(2)	18222(5)	9371(3)
Z	2	4	2
D <sub>calc</sub> (g/cm <sup>3</sup> )	1.571	1.429	1.494
$\mu$ (MoK $\alpha$ ) (cm <sup>-1</sup> )	1.39	7.72	10.99
Reflections Total	20929	137797	81553
Reflections Unique	6703	37263	33798
R <sub>int</sub>	0.0308	0.0513	0.0445
R <sub>1</sub> ( <i>I</i> > 2.00 $\sigma$ ( <i>I</i> ))	0.0647	0.0936	0.0987
wR <sub>2</sub> (All reflections)	0.1741	0.2597	0.3167

**Table 6.2:** Summary of crystallographic data for **6.4** and **6.6**.

	<b>6.4</b>	<b>6.6</b>
Chemical Formula	$C_{163.4}H_{120}Cu_{8.5}F_{25.8}N_{54}O_{19.2}P_{3.6}S_{1.4}$	$C_{163}H_{121.60}F_{9}N_{57}Mn_9O_{33.80}S_3$
M	4333.79	4181.12
T(K)	113(2)	113(2)
Crystal System	tetragonal	triclinic
Space Group	$P4_2/n$ (#86)	$P\bar{1}$ (#2)
a (Å)	20.580(3)	20.514(5)
b (Å)	20.580(3)	20.643(4)
c (Å)	22.970(4)	25.948(6)
$\alpha$ (°)	90.00	90.917(4)
$\beta$ (°)	90.00	108.365(7)
$\gamma$ (°)	90.00	90.517(6)
V (Å <sup>3</sup> )	9729(3)	10426(4)
Z	2	2
D <sub>calc</sub> (g/cm <sup>3</sup> )	1.479	1.332
$\mu$ (MoK $\alpha$ ) (cm <sup>-1</sup> )	10.53	6.41
Reflections Total	75221	97528
Reflections Unique	9535	42546
R <sub>int</sub>	0.0410	0.0576
R <sub>1</sub> ( $I > 2.00\sigma(I)$ )	0.1174	0.0889
wR <sub>2</sub> (All reflections)	0.3717	0.2794

### 6.3: Results and Discussion:

**Note:** The crystallographically determined formulae are used herein. Colour code for figures: magenta = manganese, green = copper, grey = carbon, blue = nitrogen, red = oxygen, light green = boron, yellow = fluorine. Crystallographic representations/illustrations were generated using Persistence of Vision Ray Tracer (POV-Ray©) for Windows, version 3.6, with scene description files written by Ortep-3 for Windows (Version 1.08) Copyright© 1997-2003 Louis J. Farrugia.

#### 6.3.1: Description of crystal structures:

##### 6.3.1.1: $(2p056hq+2H)(BF_4)_2(CH_3OH)_1(H_2O)_1$ (6.1)

The structure of 6.1 is shown in Figure 6.5, and significant bond lengths and angles are listed in Table 6.3.

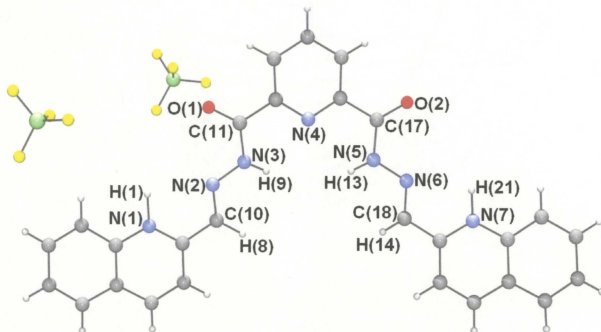


**Figure 6.5:** Ball-and-stick depiction of 6.1. Solvent molecules omitted for clarity.

**6.1** is a doubly-protonated 2po56hq ligand-tetrafluoroborate salt. The cation is in its ketonic form, with short hydrazone C-O distances exhibiting double-bond character (C(11)-O(1) 1.231(2) Å; C(17)-O(2) 1.223(2) Å) and longer adjacent C-N bonds (C(11)-N(3) 1.356(3) Å; C(17)-N(5) 1.360(3) Å), more characteristic of single bonds. C(10)-N(2)-N(3)-C(11) and C(17)-N(5)-N(6)-C(18) torsion angles ( $176.5^\circ$  and  $174.9^\circ$  respectively) reveal the nearly planar configuration of the ligand cation. Figure 6.6a shows a view of the unit cell normal to (0,1,0), while Figure 6.6b is rotated about the c-axis to show the layered arrangement of the cations.

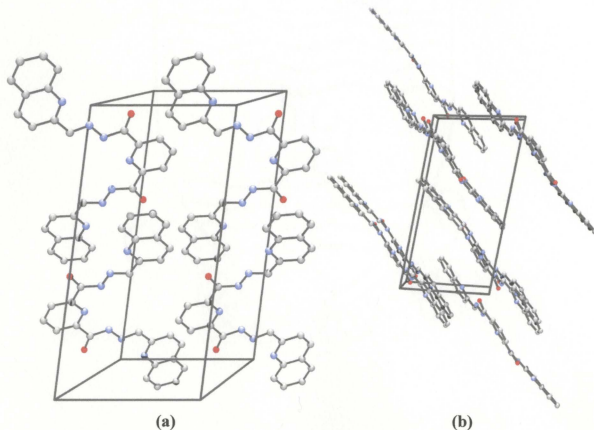


**Figure 6.6:** Ball-and-stick depiction of **6.1** a) looking down the b-axis and b) rotated about the c-axis to show the layered arrangement of the ligand cations.

Face-to-face  $\pi$ - $\pi$  interactions are present between the central pyridine ring of the cation and both the pyridine and arene moieties of the terminal quinoline ring (Figure 6.7). The distance between the pyridine centroids (orange arrows in Figure 6.7) is 3.68 Å, with an off-set angle of only 22.7°, and an angle between planes of 5.4°, while the distance between the central pyridine to arene-moiety centroid (green arrows in Figure 6.7) is 3.54 Å, with an off-set angle of 16.5°, and an angle between planes of 4.6°

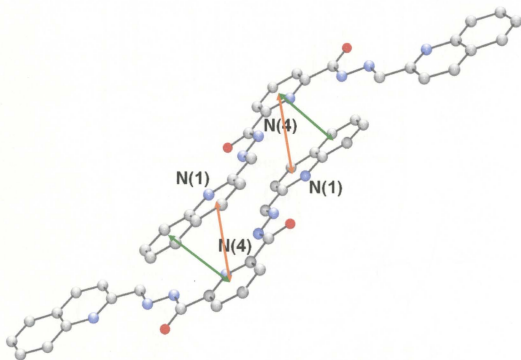


**Figure 6.7:** Ball-and-stick depiction of **6.1** showing face-to-face  $\pi$ - $\pi$  contacts between cations in adjacent layers.

**Table 6.3:** Selected bond distances (Å) and torsion angles (°) for **6.1**.

N(2)	C(10)	1.276(3)	N(5)	N(6)	1.367(2)		
N(2)	N(3)	1.359(2)	N(6)	C(18)	1.274(3)		
N(3)	C(11)	1.356(3)					
O(1)	C(11)	1.231(2)	C(10)	N(2)	N(3)	C(11)	176.5
O(2)	C(17)	1.223(2)	C(17)	N(5)	N(6)	C(18)	174.9
N(5)	C(17)	1.360(3)					

**6.3.1.2:** [(2po56hq-2H)<sub>6</sub>Mn<sub>9</sub>](ClO<sub>4</sub>)<sub>6</sub> (**6.2**)

The structure of the cationic fragment of **6.2**, its unit cell and core structural representation are shown in Figures 6.8a, b and c respectively, and significant bond lengths and angles are listed in Table 6.4.

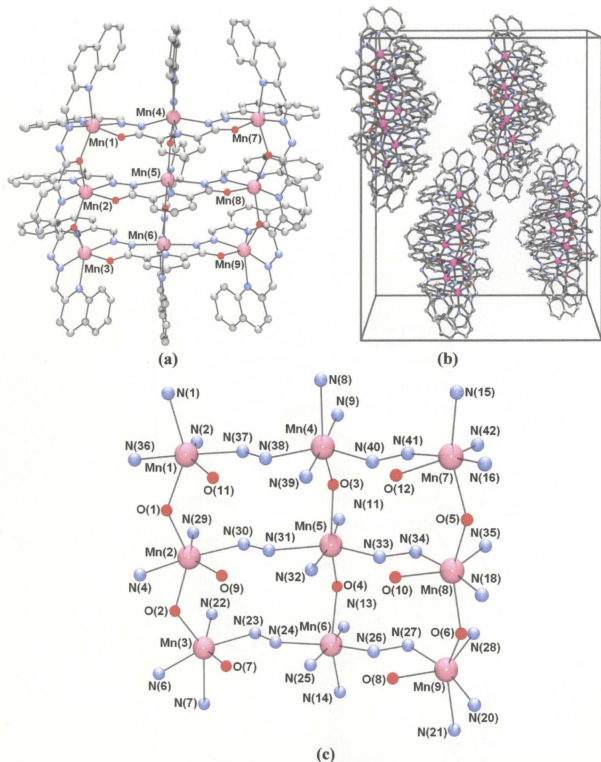


**Figure 6.8:** Ball-and-stick depiction of a) the cationic moiety of **6.2**. Hydrogen atoms omitted for clarity. b) The unit cell of **6.2** looking down the *a*-axis c) Core structural representation of **6.2**.

This  $3 \times [1 \times 3]$  rectangular structure, the first example of this motif, results from self-assembly between Mn(II) ions and 2po56hq (Figure 6.8a). The grid is subdivided into three groups of  $[\text{Mn}_3(\mu_2\text{-O})_2]$  linear subunits, which are connected across the rectangle by  $\mu_2\text{-N}_2$  diazine bridges. This leads to short Mn-Mn distances (4.1417(10) - 4.1819(12) Å) within the  $\mu\text{-O}$  triads, and long Mn-Mn distances (5.2159(10) - 5.6163(9) Å) within the  $\mu\text{-N}_2$  triads. Three ligands in the *cisoid* NN-bridging mode wrap around the metal core in an approximately parallel manner (Figure 6.3b and 6.7c), spanning the long rectangle dimensions (10.417<sub>ave</sub> Å) and linking together the Mn(1)-Mn(4)-Mn(7), Mn(2)-Mn(5)-Mn(8), and Mn(3)-Mn(6)-Mn(9) metal groupings. The end  $\mu\text{-O}$ -bridging ligands lie on one side of the metal core, while the middle one lies on the other side (Figure 6.3a and 6.7a), spanning the short rectangle dimensions (8.297<sub>ave</sub> Å) and linking together the Mn(1)-Mn(2)-Mn(3), Mn(6)-Mn(5)-Mn(4), and Mn(7)-Mn(8)-Mn(9) triads. Normal Mn<sub>9</sub> square grids have all  $\mu\text{-O}$  bridges, however the  $\mu\text{-NN}$  bridging mode has been previously observed in octanuclear Cu<sub>8</sub>(2pomp)<sub>4</sub> [96,125] and Cu<sub>8</sub>(Cl2pomp)<sub>4</sub> [125] pinwheel clusters and in incomplete Ni<sub>6</sub>(Cl2poap)<sub>5</sub>, Ni<sub>6</sub>(SEt2poap)<sub>5</sub> and Co<sub>7</sub>(2poap)<sub>5</sub> grid oligomers [93].

Corner sites (Mn(1,3,7,9)) have *cis*-MnN<sub>4</sub>O<sub>2</sub> environments, while 'short' side sites (Mn(2,8)) have *mer*-MnN<sub>3</sub>O<sub>3</sub> environments, 'long' side sites (Mn(4,6)) have MnN<sub>5</sub>O<sub>1</sub> environments and the central Mn ion (Mn(5)) is *trans*-MnN<sub>4</sub>O<sub>2</sub> coordinated. Corner Mn centres display very long Mn-N distances to the external quinoline rings of the  $\mu\text{-O}$ -bridging ligands (2.378(4) - 2.449(4) Å), due to the stretching of the ligands over the

nonanuclear core, with shorter remaining Mn-L contacts (2.126(5) - 2.231(4) Å). The quinoline end-pieces of 2po56hq present a significantly larger aromatic component than the terminal rings normally present in this ligand-type, and as the ligands approach each other in the typical grid arrangement, the  $\pi$ -interactions are considerably greater. The metal ions are arranged further apart in the  $\mu$ -NN bridging mode than in the  $\mu$ -O mode and give the  $\mu$ -O bridging ligand end pieces a greater separation, leading to the formation of a rectangle and not a square. Mn-O-Mn angles are in the range 132.33(15) - 134.37(18) $^\circ$  with Mn-NN-Mn torsion angles between 160.6 - 179.1 $^\circ$ , which suggests that the magnetic exchange situations should be dominated by intramolecular antiferromagnetic exchange [28,29,45,70,73,96].

One of the characteristic traits of the [3 $\times$ 3]  $M_9$  square grids is the alignment of the ligands, in two roughly parallel groups of three above and below the grid metal pseudoplane. The ligands of **6.2** in the  $\mu$ -NN bridging mode are still aligned in an approximately parallel manner, with distances between the quinoline-pyridine centroids of 3.61 - 3.71 Å, off-set by 7.8 - 20.9 $^\circ$ , and between quinoline-arene centroids of 3.53 - 3.72 Å, off-set by 13.5 - 23.4 $^\circ$  (Figure 6.9, orange arrows). Intermolecular face-to-face  $\pi$ - $\pi$  interactions are also present between the quinoline-arene moieties of adjacent grids (Figure 6.9, green arrows), separated by a distance of 3.57 - 3.58 Å, off-set by 14.8 - 24.8 $^\circ$ . Additional close intermolecular edge-to-face contacts (purple arrows; 3.08 - 3.69 Å) between the planes of the  $\mu$ -O bridging ligands and the terminal moieties of the  $\mu$ -NN bridging ligands are also present. These close contacts constitute an effective organizational force within the grid layers.

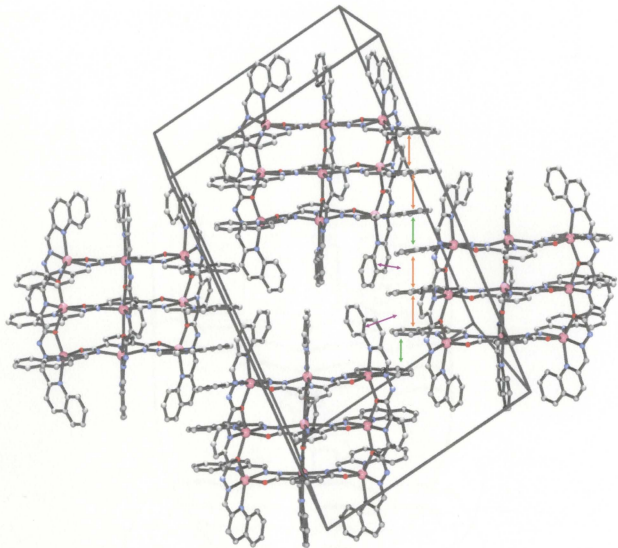


**Figure 6.9:** Ball-and-stick depiction of extended cell of **6.2**, oriented to show face-to-face intramolecular (orange arrows), intermolecular (green arrow) and intermolecular edge-to-face (purple arrows)  $\pi$ - $\pi$  interactions.

**Table 6.4:** Selected bond distances (Å), angles (°) and torsion angles (°) for **6.2**

Mn(1) N(2)	2.135(5)	Mn(4) N(9)	2.124(4)	Mn(7) N(16)	2.126(5)
Mn(1) N(37)	2.167(4)	Mn(4) N(39)	2.185(4)	Mn(7) N(41)	2.165(4)
Mn(1) N(36)	2.228(5)	Mn(4) N(38)	2.200(4)	Mn(7) O(5)	2.221(4)
Mn(1) O(1)	2.228(3)	Mn(4) N(40)	2.208(4)	Mn(7) O(12)	2.227(4)
Mn(1) O(11)	2.231(4)	Mn(4) O(3)	2.244(3)	Mn(7) N(42)	2.259(5)
Mn(1) N(1)	2.441(4)	Mn(4) N(8)	2.435(4)	Mn(7) N(15)	2.397(5)
Mn(2) O(9)	2.147(4)	Mn(5) N(11)	2.176(4)	Mn(8) O(10)	2.156(3)
Mn(2) N(4)	2.162(4)	Mn(5) N(32)	2.200(4)	Mn(8) N(18)	2.184(4)
Mn(2) N(30)	2.259(4)	Mn(5) O(4)	2.266(3)	Mn(8) N(35)	2.254(4)
Mn(2) N(29)	2.262(4)	Mn(5) O(3)	2.272(3)	Mn(8) N(34)	2.257(4)
Mn(2) O(1)	2.304(3)	Mn(5) N(33)	2.373(4)	Mn(8) O(6)	2.283(3)
Mn(2) O(2)	2.327(3)	Mn(5) N(31)	2.441(4)	Mn(8) O(5)	2.321(4)
Mn(3) N(6)	2.136(4)	Mn(6) N(13)	2.134(4)	Mn(9) N(20)	2.142(5)
Mn(3) N(23)	2.178(4)	Mn(6) N(25)	2.184(4)	Mn(9) N(27)	2.161(4)
Mn(3) O(7)	2.187(4)	Mn(6) N(26)	2.200(4)	Mn(9) O(8)	2.224(4)
Mn(3) O(2)	2.242(4)	Mn(6) N(24)	2.253(4)	Mn(9) O(6)	2.240(4)
Mn(3) N(22)	2.248(4)	Mn(6) O(4)	2.262(3)	Mn(9) N(28)	2.258(5)
Mn(3) N(7)	2.417(4)	Mn(6) N(14)	2.378(4)	Mn(9) N(21)	2.449(4)
Mn(1) O(1)	Mn(2) 134.37(18)	Mn(1) N(37)	N(38) Mn(4) -165.0		
Mn(3) O(2)	Mn(2) 132.49(16)	Mn(2) N(30)	N(31) Mn(5) 178.3		
Mn(4) O(3)	Mn(5) 133.30(15)	Mn(3) N(23)	N(24) Mn(6) 163.4		
Mn(6) O(4)	Mn(5) 132.33(15)	Mn(4) N(40)	N(41) Mn(7) 160.6		
Mn(7) O(5)	Mn(8) 133.11(16)	Mn(5) N(33)	N(34) Mn(8) 179.1		
Mn(9) O(6)	Mn(8) 133.56(15)	Mn(6) N(26)	N(27) Mn(9) -162.8		

**6.3.1.3:** [(2po56nq-2H)<sub>6</sub>Cu<sub>9</sub>](BF<sub>4</sub>)<sub>6</sub>·6.4H<sub>2</sub>O (**6.3**)

The structure of the cationic fragment of **6.3** and its unit cell are shown in Figures 6.10a and b respectively, and significant bond lengths and angles are listed in Table 6.5.

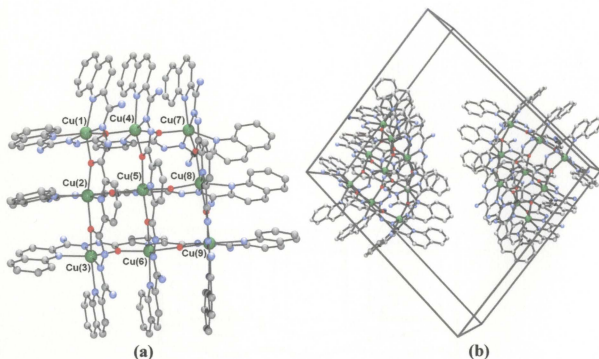


**Figure 6.10:** Ball-and-stick depiction of a) the cationic moiety **6.3**. Hydrogen atoms omitted for clarity. b) The unit cell of **6.3**; anions omitted for clarity.

Complex **6.3** crystallized in a triclinic space group and consists of three heptadentate ligands arranged above and another three below a  $[\text{Cu}_9-(\mu\text{-O})_{12}]$  core composed of nine metal ions bridged by twelve hydrazone oxygen atoms (Figure 6.10a). Cu-Cu distances fall in the range 4.0582(9) - 4.1896(9) Å, with Cu-O-Cu angles in the range 139.8(2) - 144.02(18)° and overall, almost square, metal core dimensions measuring 8.1716(3) Å<sub>ave</sub>. Unlike all other reported  $\text{Cu}(\text{II})_9$  grids [66,69,71,96], where each copper ion in the outer eight-membered ring has a Jahn-Teller distorted, axially elongated octahedral geometry and a  $d_{x^2-y^2}$  magnetic ground state, **6.3** is the first example of a  $\text{Cu}(\text{II})_9$  grid in which all copper ions exhibit axially compressed octahedral geometry leading to a  $d_{z^2}$  magnetic ground state (highlighted by the arrows in Figure 6.11).

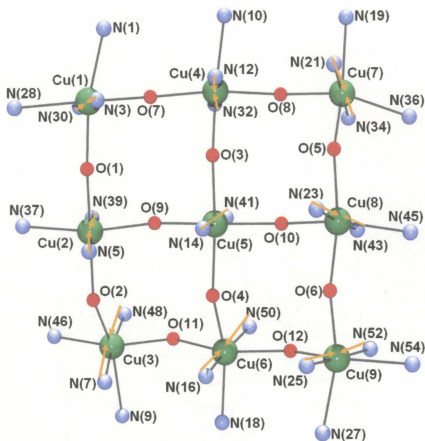


**Figure 6.11:** Ball-and-stick depiction of the core structure of **6.3**. Arrows highlight the Jahn-Teller axes.

For each copper ion, the Jahn-Teller axes are ‘pinned’ in the same direction as defined by short contacts to the central pyridine, and diazine ligand donor atoms (1.896(4) - 1.978(6) Å), while the long contacts are to the bridging hydrazone oxygen atoms and the terminal quinoline moieties (2.113(4) - 2.426(5) Å). For previously reported Cu(II)<sub>9</sub> grids, orbitally orthogonal magnetic connections are present in the outer ring of eight Cu(II) ions, with non-orthogonal connections between the central Cu(II) ion and its neighbors [66,69,71,96], however, for **6.3**, all magnetic connections are non-orthogonal, and the magnetic exchange situation should be dominated by antiferromagnetism.

Within each grid, the ligands are aligned in an approximately parallel manner, with intramolecular distances between terminal quinoline-pyridine centroids of 3.77 - 4.12 Å, off-set by 13.7 - 28.8 °, and terminal quinoline-arene centroids of 3.88 - 4.83 Å, off-set by 8.9 - 27.5 ° (Figure 6.12, orange arrows). Examination of the extended lattice structure (Figure 6.12) reveals that the aromatic quinoline moieties organize the grids in a three dimensional array, with both face-to-face quinoline-arene to quinoline-pyridine interactions (Figure 6.12, green arrow, 3.70 - 4.03 Å, off-set by 21.5 - 35.4°) and perpendicular edge-to-face (Figure 6.12, purple arrows, 3.09 - 3.56 Å) interactions. One exception is present for the quinoline-moiety that contains N(1), where the  $\pi$ - $\pi$  overlap is instead an arene-arene interaction (3.64 Å, off-set by 24.9°, versus a pyridine-arene distance of 4.67 Å, off-set by 45.9°).

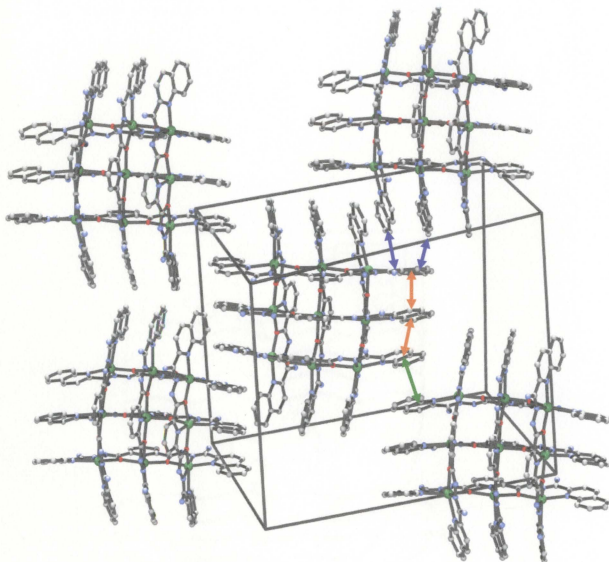


**Figure 6.12:** Ball-and-stick depiction of **6.3** ( $0.5 \leq x \leq 1$ ,  $0 \leq y \leq 1.1$ ,  $0 \leq z \leq 1$ ) showing face-to-face intramolecular (orange arrows), intermolecular (green arrow) and intermolecular edge-to-face (purple arrows)  $\pi$ - $\pi$  interactions.

**Table 6.5:** Selected bond distances (Å) and angles (°) for **6.3**.

Cu(1) N(3)	1.904(6)	Cu(4) N(12)	1.901(5)	Cu(7) N(34)	1.913(6)
Cu(1) N(30)	1.951(6)	Cu(4) N(32)	1.978(6)	Cu(7) N(21)	1.925(5)
Cu(1) O(1)	2.117(4)	Cu(4) O(3)	2.170(4)	Cu(7) O(8)	2.132(5)
Cu(1) O(7)	2.209(5)	Cu(4) O(7)	2.171(5)	Cu(7) O(5)	2.209(4)
Cu(1) N(1)	2.288(5)	Cu(4) O(8)	2.208(5)	Cu(7) N(36)	2.280(6)
Cu(1) N(28)	2.400(6)	Cu(4) N(10)	2.345(5)	Cu(7) N(19)	2.392(5)
Cu(2) N(39)	1.912(5)	Cu(5) N(41)	1.913(4)	Cu(8) N(43)	1.904(5)
Cu(2) N(5)	1.957(5)	Cu(5) N(14)	1.928(4)	Cu(8) N(23)	1.945(5)
Cu(2) O(9)	2.155(4)	Cu(5) O(9)	2.157(4)	Cu(8) O(10)	2.154(4)
Cu(2) O(2)	2.158(3)	Cu(5) O(10)	2.162(4)	Cu(8) O(5)	2.180(4)
Cu(2) O(1)	2.207(4)	Cu(5) O(3)	2.176(4)	Cu(8) O(6)	2.223(4)
Cu(2) N(37)	2.309(4)	Cu(5) O(4)	2.222(3)	Cu(8) N(45)	2.298(5)
Cu(3) N(48)	1.919(5)	Cu(6) N(16)	1.896(4)	Cu(9) N(25)	1.898(6)
Cu(3) N(7)	1.933(4)	Cu(6) N(50)	1.970(5)	Cu(9) N(52)	1.954(5)
Cu(3) O(11)	2.077(3)	Cu(6) O(4)	2.095(4)	Cu(9) O(6)	2.113(4)
Cu(3) N(46)	2.208(4)	Cu(6) O(12)	2.199(4)	Cu(9) O(12)	2.231(4)
Cu(3) O(2)	2.245(3)	Cu(6) O(11)	2.241(3)	Cu(9) N(27)	2.267(5)
Cu(3) N(9)	2.408(4)	Cu(6) N(18)	2.256(4)	Cu(9) N(54)	2.426(5)
Cu(1) O(1)	Cu(2) 139.8(2)	Cu(4) O(7)	Cu(1) 142.3(2)		
Cu(2) O(2)	Cu(3) 140.22(16)	Cu(7) O(8)	Cu(4) 142.4(2)		
Cu(4) O(3)	Cu(5) 142.86(18)	Cu(2) O(9)	Cu(5) 142.33(17)		
Cu(6) O(4)	Cu(5) 141.14(17)	Cu(8) O(10)	Cu(5) 144.02(18)		
Cu(8) O(5)	Cu(7) 141.2(2)	Cu(3) O(11)	Cu(6) 140.01(17)		
Cu(9) O(6)	Cu(8) 142.4(2)	Cu(6) O(12)	Cu(9) 142.1(2)		

**6.3.1.4:** [(2po45nq-2H)<sub>6</sub>Cu<sub>8.5</sub>](CF<sub>3</sub>SO<sub>3</sub>)<sub>1.4</sub>(PF<sub>6</sub>)<sub>3.6</sub>·3H<sub>2</sub>O (**6.4**)

The structure of the cationic fragment of **6.4** and its core structural representation are shown in Figures 6.13a and 6.12b respectively, and significant bond lengths and angles are listed in Table 6.6.

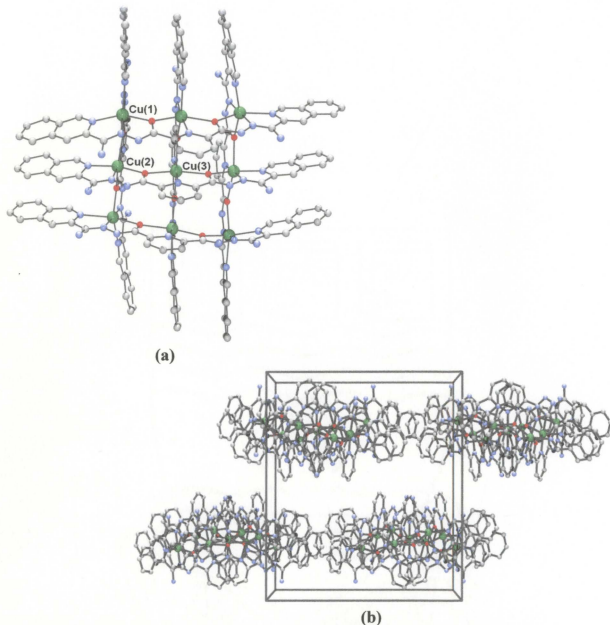


**Figure 6.13:** Ball-and-stick depiction of a) the cationic moiety **6.4**. Hydrogen atoms omitted for clarity. b) The unit cell of **6.4**, looking down the b-axis; anions omitted for clarity.

Complex **6.4** has tetragonal crystallographic symmetry, which is manifested as four-fold symmetry within the grid cation (Figure 6.13a), and four cationic moieties are

present in the unit cell (Figure 6.13b). Three heptadentate ligands are arranged above and another three below a  $[\text{Cu}_{8.5}(\mu\text{-O})_{12}]$  core (Figure 6.14).

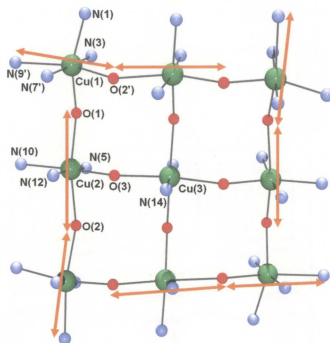


**Figure 6.14:** Ball-and-stick depiction of the core structure of **6.4**. Arrows highlight the Jahn-Teller axes.

Cu-Cu distances fall in the range 4.0413(8) - 4.3611(8) Å, with Cu-O-Cu angles in the range 139.28(18) - 144.20(17)° and distances between corner Cu(II) centres of 8.3683(8) Å. **6.4** exhibits the same Jahn-Teller distorted, axially elongated octahedral geometry of each copper ion in the outer eight-membered ring (highlighted by the arrows in Figure 6.14) as seen in **4.5**, **4.6** and other  $\text{Cu}_9$  grids [66,69,71,96]. Cu(1) has a  $d_{x^2-y^2}$  magnetic ground state as defined by short contacts to N(1), N(3), N(7'), and O(1) (1.898(5) - 2.064(4) Å) with long axial contacts to O(2') and N(9') (2.312(4) - 2.336(5) Å). Cu(2) also exhibits a  $d_{x^2-y^2}$  ground state with short contacts to N(5), N(10), N(12), and

O(3) (1.891(5) - 2.067(5) Å) and long axial contacts to O(1) and O(2) (2.266(4) - 2.327(4) Å).

Cu(3) is present at one-half occupancy, though the bulk magnetic properties are consistent with the site being fully occupied. It has axially compressed geometry ( $d_{z^2}$  magnetic ground state), with long contacts to O(3) and its symmetry related atoms (2.234(4) Å), and short bonds to N(17) and its symmetry related counterpart (1.908(6) Å). This arrangement sets up orbitally orthogonal magnetic connections in the outer ring of eight Cu(II) ions, with non-orthogonal connections between Cu(3) and its neighbors, as further discussed in Section 6.3.2.

The ligands of **6.4** are aligned in an approximately parallel manner, with distances between terminal quinoline-pyridine centroids of 3.82 - 3.96 Å, off-set by 12.7 - 23.5°, and terminal quinoline-arene centroids of 3.68 - 3.86 Å, off-set by 13.2 - 28.4° (Figure 6.15, orange arrows). Examination of the extended lattice structure (Figure 6.15) reveals that the aromatic quinoline moieties extend in a two-dimensional array, with each grid interlocked with two others through both face-to-face quinoline-arene to quinoline-pyridine interactions (Figure 6.15, green arrow, 3.69 Å, off-set by 12.0 - 23.3°) and perpendicular edge-to-face interactions (Figure 6.15, purple arrows, 3.09 - 3.56 Å).

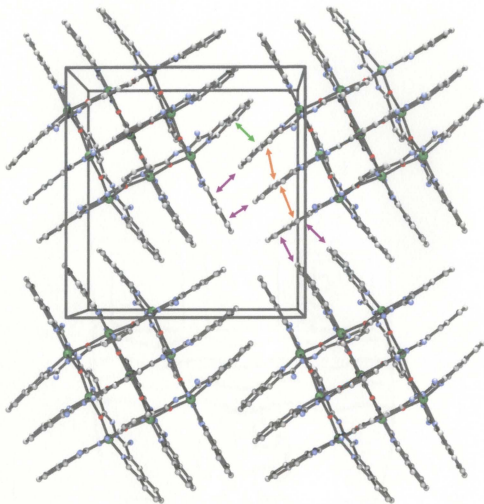


**Figure 6.15:** Ball-and-stick depiction of extended cell of **6.4** looking down the c-axis, showing face-to-face intramolecular (orange arrows), intermolecular (green arrow) and intermolecular edge-to-face (purple arrows)  $\pi$ - $\pi$  interactions.

**Table 6.6:** Selected bond distances (Å) and angles (°) for **6.4**.

Cu(1) N(3)	1.898(5)	Cu(2) N(12)	1.891(5)	
Cu(1) N(7')	1.997(4)	Cu(2) N(5)	1.998(4)	
Cu(1) O(1)	2.043(4)	Cu(2) O(3)	2.063(4)	
Cu(1) N(1)	2.064(4)	Cu(2) N(10)	2.067(5)	
Cu(1) O(2')	2.312(4)	Cu(2) O(1)	2.266(4)	
Cu(1) N(9')	2.336(5)	Cu(2) O(2)	2.327(4)	
Cu(3) N(14)	1.908(6)	Cu(1) O(1)	Cu(2)	139.28(18)
Cu(3) O(3)	2.234(4)	Cu(1) O(2')	Cu(2')	140.14(17)
		Cu(2) O(3)	Cu(3)	144.20(17)

**6.3.1.5:** [(2po34nq-2H)<sub>6</sub>Mn<sub>9</sub>](CF<sub>3</sub>SO<sub>3</sub>)<sub>3</sub>(NO<sub>3</sub>)<sub>3</sub>(H<sub>2</sub>O)<sub>3.8</sub> (**6.6**)

The structure of the cationic fragment of **6.6**, its unit cell and core structural representation are shown in Figures 6.16a, b and c respectively, and significant bond lengths and angles are listed in Table 6.7.

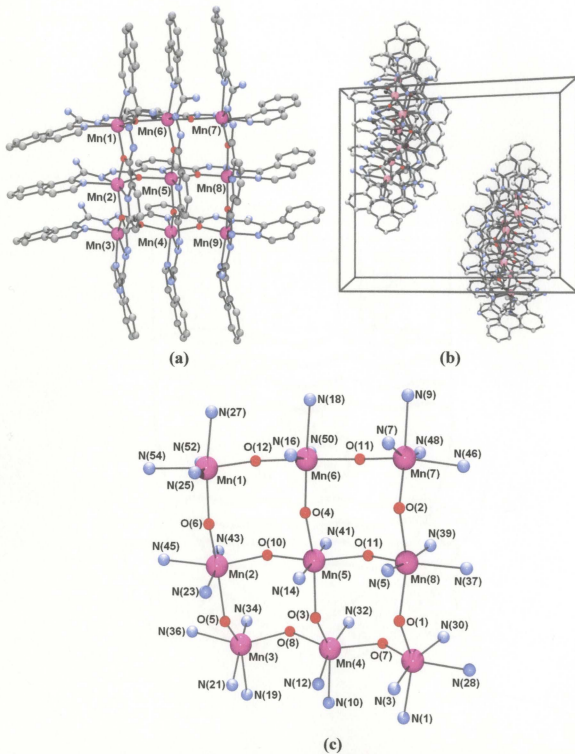


**Figure 6.16:** Ball-and-stick depiction of a) the cationic moiety **6.6**. Hydrogen atoms omitted for clarity. b) The unit cell of **6.6**. c) Core structural representation of **6.6**.

Complex **6.6** is a [3×3] Mn<sub>9</sub> grid with ligands arranged, three above and three below, a [Mn<sub>9</sub>-(μ-O)<sub>12</sub>] hydrazone oxygen-bridged core of nine distorted octahedral metals (Figure 6.16a). Mn-Mn distances fall in the range 3.8450(9) - 3.9607(8) Å, with Mn-O-Mn angles in the range 124.63(14) - 129.72(14)° and overall side dimensions measuring 7.6868(5) Å<sub>ave</sub>. The corner Mn(II) centres have *cis*-MnN<sub>4</sub>O<sub>2</sub> coordination environments, while the side centres have *mer*-MnN<sub>3</sub>O<sub>3</sub> environments, and the centre Mn(II) ion has a *trans*-MnN<sub>2</sub>O<sub>4</sub> coordination environment. Corner and side Mn centres display long Mn-N distances to the external quinoline rings (2.277(4) - 2.331(4) Å), with shorter remaining Mn-L contacts (2.129(4) - 2.226(3) Å).

The ligands are aligned in an approximately parallel manner, with intramolecular distances between terminal quinoline-pyridine centroids of 3.64 - 3.93 Å, off-set by 13.8 - 30.3°, and terminal quinoline-arene centroids of 3.58 - 4.06 Å, off-set by 17.7 - 35.4° (Figure 6.17, orange arrows). Examination of the extended lattice structure reveals that the aromatic quinoline moieties organize the grids into a chain-like motif parallel to the *a*-axis by interlocking each grid with two others through both face-to-face quinoline-arene to quinoline-pyridine interactions (Figure 6.17, green arrow, 3.49 - 3.65 Å, off-set by 18.2 - 20.4°) and perpendicular edge-to-face interactions (Figure 6.17, purple arrows, 3.57 - 3.63 Å).

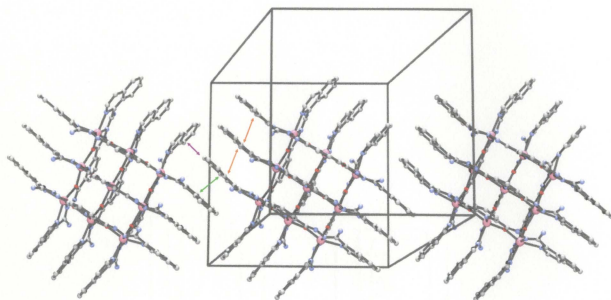


**Figure 6.17:** Ball-and-stick depiction of extended half-cell of **6.6**, looking down the *c*-axis, showing face-to-face intramolecular (orange arrows), intermolecular (green arrow) and intermolecular edge-to-face (purple arrows)  $\pi$ - $\pi$  interactions.

**Table 6.7:** Selected bond distances (Å) and angles (°) for **6.6**.

Mn(1) N(52)	2.143(4)	Mn(4) O(3)	2.138(3)	Mn(7) N(48)	2.129(4)
Mn(1) N(25)	2.148(4)	Mn(4) N(12)	2.140(4)	Mn(7) N(7)	2.147(4)
Mn(1) O(6)	2.161(3)	Mn(4) N(32)	2.176(4)	Mn(7) O(2)	2.159(3)
Mn(1) O(12)	2.163(3)	Mn(4) O(8)	2.187(3)	Mn(7) O(11)	2.165(3)
Mn(1) N(27)	2.281(4)	Mn(4) O(7)	2.192(3)	Mn(7) N(46)	2.319(4)
Mn(1) N(54)	2.329(4)	Mn(4) N(10)	2.316(4)	Mn(7) N(9)	2.325(4)
Mn(2) O(10)	2.143(3)	Mn(5) N(14)	2.141(4)	Mn(8) N(39)	2.146(4)
Mn(2) N(43)	2.153(4)	Mn(5) N(41)	2.156(4)	Mn(8) O(9)	2.152(3)
Mn(2) O(6)	2.185(3)	Mn(5) O(3)	2.183(3)	Mn(8) N(5)	2.167(4)
Mn(2) O(5)	2.190(3)	Mn(5) O(9)	2.186(3)	Mn(8) O(1)	2.194(3)
Mn(2) N(23)	2.205(4)	Mn(5) O(4)	2.193(3)	Mn(8) O(2)	2.195(3)
Mn(2) N(45)	2.331(4)	Mn(5) O(10)	2.220(3)	Mn(8) N(37)	2.317(4)
Mn(3) N(34)	2.138(4)	Mn(6) O(4)	2.154(3)	Mn(9) N(30)	2.139(4)
Mn(3) O(8)	2.144(3)	Mn(6) N(16)	2.161(4)	Mn(9) N(3)	2.141(4)
Mn(3) N(21)	2.147(4)	Mn(6) O(11)	2.208(3)	Mn(9) O(1)	2.156(3)
Mn(3) O(5)	2.148(3)	Mn(6) N(50)	2.216(4)	Mn(9) O(7)	2.164(3)
Mn(3) N(36)	2.286(4)	Mn(6) O(12)	2.226(3)	Mn(9) N(1)	2.277(4)
Mn(3) N(19)	2.306(4)	Mn(6) N(18)	2.317(4)	Mn(9) N(28)	2.305(4)
Mn(9) O(1)	Mn(8) 126.57(15)	Mn(9) O(7)	Mn(4) 124.63(14)		
Mn(7) O(2)	Mn(8) 126.47(16)	Mn(3) O(8)	Mn(4) 125.15(14)		
Mn(4) O(3)	Mn(5) 128.06(13)	Mn(8) O(9)	Mn(5) 128.03(15)		
Mn(6) O(4)	Mn(5) 126.89(14)	Mn(2) O(10)	Mn(5) 129.72(14)		
Mn(3) O(5)	Mn(2) 126.12(15)	Mn(7) O(11)	Mn(6) 127.42(15)		
Mn(1) O(6)	Mn(2) 126.72(15)	Mn(1) O(12)	Mn(6) 128.34(15)		

### 6.3.2: Magnetic Properties

Complex **6.2** is a  $3 \times [1 \times 3]$  Mn(II)<sub>9</sub> rectangular grid comprised of three  $[M_3-(\mu-O)_2]$  subunits separated by  $\mu$ -NN bridges. As discussed in section 4.3.2, full matrix calculation on this 45-electron problem is not possible because of the immensity of the calculations involved. Therefore, a simpler model that treats the system as a composite of three linear trinuclear subunits was considered (Figure 6.18).

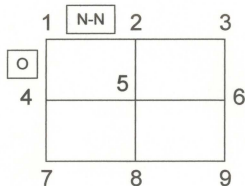


**Figure 6.18:** Magnetic exchange models for a  $3 \times [1 \times 3]$   $M_9$  grid.

A Hamiltonian to describe this exchange situation is expressed in equation 6.1.

$$H_{ex} = -J\{S_1 \cdot S_4 + S_4 \cdot S_7\} \quad (6.1)$$

A correction for weak intramolecular interactions between the trinuclear subunits is included by introducing a molecular field approximation [142] into the susceptibility expression (6.2):

$$\chi_{mol} = \frac{N\beta^2 g^2}{3k(T - zJ' \chi_{trimer})} \frac{\sum S'(S'+1)(2S'+1)e^{-E(S')/kT}}{\sum (2S'+1)e^{-E(S')/kT}} (1 - \rho) + \frac{N\beta^2 g^2 S(S+1)\rho}{3kT} + TIP \quad (6.2)$$

Where  $z$  is the number of nearest neighbours around a magnetic moiety and  $J'$  is the exchange interaction between the two nearest neighbours.

Variable-temperature magnetic data for **6.2** are shown in Figure 6.19, with a drop in moment from  $17.7 \mu_B$  at 300 K to  $6.4 \mu_B$  at 2K, consistent with the presence of nine Mn(II) centres within an antiferromagnetically coupled grid.

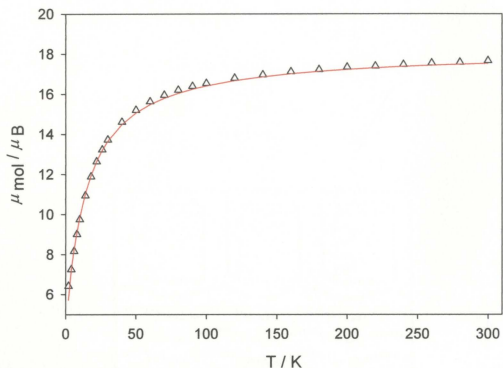


**Figure 6.19:** Variable temperature magnetic data for **6.2**;  $g = 2.04$ ,  $J = -1.4 \text{ cm}^{-1}$ ,  $z = 4/3$ ,  $J' = -0.4 \text{ cm}^{-1}$ ,  $\text{TIP} = 200 \times 10^{-6} \text{ cm}^3 \text{ mol}^{-1}$ ,  $10^2 R = 1.56$ .

The data were fitted to equation 6.2 to give  $g = 2.04$ ,  $J = -1.4 \text{ cm}^{-1}$ ,  $z = 4/3$ ,  $J' = -0.4 \text{ cm}^{-1}$ ,  $\text{TIP} = 200 \times 10^{-6} \text{ cm}^3 \text{ mol}^{-1}$ ,  $10^2 R = 1.56$  ( $R = [\sum(\chi_{\text{obs}} - \chi_{\text{calc}})^2 / \sum \chi_{\text{obs}}^2]^{1/2}$ ). The solid line in Figure 6.19 was calculated with these parameters. The negative sign of both  $J$  and  $J'$  are consistent with the large Mn-O-Mn bond and Mn-NN-Mn torsional angles, leading to the observed antiferromagnetic exchange. Similar Mn-O-Mn bond angles are present in the Mn(II)<sub>3</sub> cluster, **3.2**, with comparable fitted values of  $g = 2.04(2)$  and  $J = -3.03(1) \text{ cm}^{-1}$ .

Compounds **6.3-6.6** are  $[3 \times 3]$  M(II)<sub>9</sub> grids that can be described by the same magnetic model employed to treat similar grids in Chapters 4 and 5. Briefly, exchange between neighboring metal centres in the outer ring of eight metals (Figure 6.20) is

assumed to be the same ( $J_1$ ) while exchange between the central metal ion and its adjacent metals is assumed to be slightly different ( $J_2$ ).

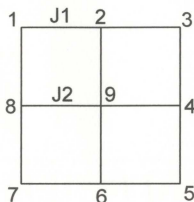


**Figure 6.20:** Magnetic exchange model for a  $[3 \times 3] M_9$  grid.

A Hamiltonian to describe this exchange situation includes two exchange integrals and is expressed in equation 6.3.

$$H_{ex} = -J_1\{S_1 \cdot S_2 + S_2 \cdot S_3 + S_3 \cdot S_4 + S_4 \cdot S_5 + S_5 \cdot S_6 + S_6 \cdot S_7 + S_7 \cdot S_8 + S_1 \cdot S_8\} \quad (6.3) \\ - J_2\{S_2 \cdot S_9 + S_4 \cdot S_9 + S_6 \cdot S_9 + S_8 \cdot S_9\}$$

Compound **6.3** is a  $[3 \times 3]$   $Cu(II)_9$  grid and its magnetic profile is shown in Figure 6.21 as a plot of moment per mole as a function of temperature. The moment drops from  $5.58 \mu_B$  at 300 K to a minimum value of  $4.36 \mu_B$  at 2 K, indicative of antiferromagnetic exchange.

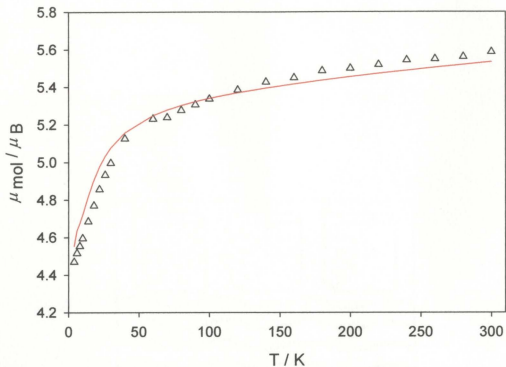


**Figure 6.21:** Variable temperature magnetic data for **6.3**;  $g = 2.07(1)$ ,  $J_1 = -0.8(1) \text{ cm}^{-1}$ ,  $J_2 = -10(1) \text{ cm}^{-1}$ ,  $\text{TIP} = 860 \times 10^{-6} \text{ cm}^3 \text{ mol}^{-1}$ ,  $\theta = -0.2 \text{ cm}^{-1}$ ,  $10^2 R = 3.45$ .

All nine octahedral copper centres exhibit Jahn-Teller compression (Figure 6.11), which defines their magnetic ground states as  $d_{z^2}$ . The  $d_{z^2}$  orbital does have some electron density in the  $xy$  plane and therefore antiferromagnetic exchange, *via* the hydrazone oxygen bridges, is expected. Compound **6.3** was fitted using the non-linear regression routines built into the MAGMUN4.1 [49] software by evaluating  $J_2$  as a fraction of  $J_1$ . As discussed in Chapters 4 and 5, this is not a completely rigorous approach, however, applied in the context of a sensible analysis of the exchange situation based upon the structure, useful information on the magnitude of the coupling can be obtained.

A fit for **6.3** was obtained after many trial comparisons varying the ratio of  $-J_2/J_1$  to give a best fit with  $g = 2.07(1)$ ,  $J_1 = -0.8(1) \text{ cm}^{-1}$ ,  $J_2 = -10(1) \text{ cm}^{-1}$ ,  $\text{TIP} = 860 \times 10^{-6}$

$\text{cm}^3 \text{mol}^{-1}$ ,  $\theta = -0.2 \text{ cm}^{-1}$ ,  $10^2 R = 3.45$ . The solid line in Figure 6.21 was calculated with these parameters and the sign of the exchange couplings is consistent with the expected antiferromagnetism from a structural analysis.

If the magnitude of the antiferromagnetic exchange for both the external ring of eight centres (Figure 6.20, sites 1-8) and for the central 'cross' of five metal centres (Figure 6.20, site 2, 4, 6, 8 and 9) was equal, calculations show that the expected ground state should be  $S' = \frac{1}{2}$ . The variable temperature data for **6.3** is not consistent for that situation, and instead shows a residual moment of  $4.36 \mu_B$  at 2 K, which suggests that at low temperature the exchange situation is dominated by  $J_2$ , and that the contribution from  $J_1$  is negligible. Theoretical calculation then give that  $S'_{\text{cross}} = \frac{1}{2}$  for the central cross, with each corner Cu(II) centre contributing  $S_{\text{Cu}} = \frac{1}{2}$ , giving an overall ground state for **6.3** as  $S' = S'_{\text{cross}} + 4 \times S_{\text{Cu}} = 5 \times \frac{1}{2}$ . A magnetization versus field study was carried out at 2 K (Figure 6.22) and shows a smooth rise in the experimental data with increasing field up to a value of  $4.84 \text{ N}\beta$  at 50 000 Oe. The solid line was calculated for  $g = 2.06$ ,  $S' = 5 \times \frac{1}{2}$ ,  $T = 2 \text{ K}$  using the appropriate Brillouin function while the dashed line was calculated for  $g = 2.06$ ,  $S' = 5/2$ ,  $T = 2 \text{ K}$ . It is clear that the experimental data is consistent with the proposed ground state of  $S' = 5 \times \frac{1}{2}$ , and that there is no significant exchange between the residual spins at 2 K, as might be expected if an  $S' = 5/2$  had been observed.

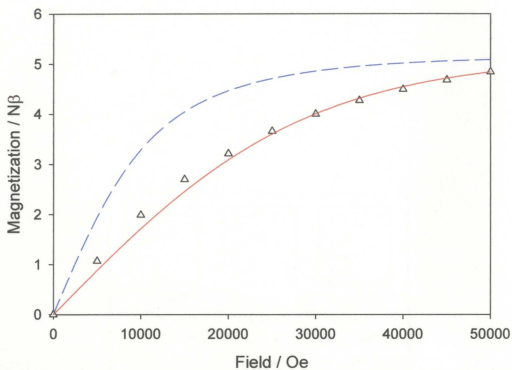


**Figure 6.22:** Variable field magnetization data for **6.3**; solid red line calculated for  $g = 2.06$ ,  $S' = 5 \times \frac{1}{2}$ ,  $T = 2$  K, and dashed blue line calculated for  $g = 2.06$ ,  $S' = 5/2$ ,  $T = 2$  K using the appropriate Brillouin function.

Compound **6.4** is also a  $[3 \times 3]$   $\text{Cu(II)}_9$  grid and its magnetic profile is shown in Figure 6.23 as a plot of moment per mole as a function of temperature. The moment drops from  $5.71 \mu_B$  at 300 K to a minimum value of  $5.37 \mu_B$  at 30 K, suggesting an antiferromagnetic exchange component, followed by a rise to  $6.35 \mu_B$  at 2 K, indicative of a second, ferromagnetic, exchange contribution.

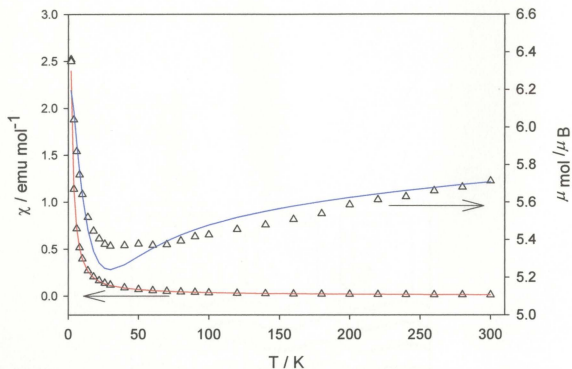


**Figure 6.23:** Variable temperature magnetic data for **6.4**;  $g = 2.16(2)$ ,  $J_1 = 2.2(2) \text{ cm}^{-1}$ ,  $J_2 = -28(3) \text{ cm}^{-1}$ ,  $\text{TIP} = 720 \times 10^{-6} \text{ cm}^3 \text{ mol}^{-1}$ ,  $\rho = 0.09$ ,  $\theta = -1 \text{ cm}^{-1}$ ,  $10^2 R = 2.54$ .

Compound **6.4** exhibits four-fold symmetry within the grid cation, with corner and side distorted octahedral copper centres (Cu(1) and Cu(2)) displaying Jahn-Teller elongation (Figure 6.14). Based upon the directionality of the Jahn-Teller axes in the outer  $\text{Cu(II)}_8$  ring, the Cu(1)-O(1)-Cu(2) and Cu(1)-O(2')-Cu(2') connections are orthogonal, while the Cu(2)-O(3)-Cu(3) connection is not. Therefore, ferromagnetic coupling between Cu(1) and Cu(2) centres (and their symmetry related counter-parts) is predicted. Cu(3), the central distorted octahedral copper, exhibits Jahn-Teller compression (magnetic ground state is  $d_{z^2}$ ) and antiferromagnetic exchange between the Cu(3) and Cu(2) centres is expected.

Using the same approach as discussed for 6.3, the solid line in Figure 6.23 was obtained with  $g = 2.16(2)$ ,  $J_1 = 2.2(2) \text{ cm}^{-1}$ ,  $J_2 = -28(3) \text{ cm}^{-1}$ ,  $\text{TIP} = 720 \times 10^{-6} \text{ cm}^3 \text{ mol}^{-1}$ ,  $\rho = 0.09$ ,  $\theta = -1 \text{ cm}^{-1}$ ,  $10^2 R = 2.54$ . The variable temperature data for 6.4 is dominated by ferromagnetism at low temperature, therefore a magnetization versus field study was carried out at 2 K (Figure 6.24). The experimental data rise smoothly with increasing field up to a value of  $7.75 \text{ N}\beta$  at 50 000 Oe. The solid line was calculated for  $g = 2.16$ ,  $S' = 7/2$ ,  $T = 2 \text{ K}$  using the appropriate Brillouin function while the dashed line was calculated for  $g = 2.16$ ,  $S' = 7 \times 1/2$ ,  $T = 2 \text{ K}$ . Examination of the experimental data and simulations shows that the experimental profile is more consistent with the model for a grouped set of ferromagnetically-dominated, interacting copper(II) centres approaching an  $S' = 7/2$  ground state.

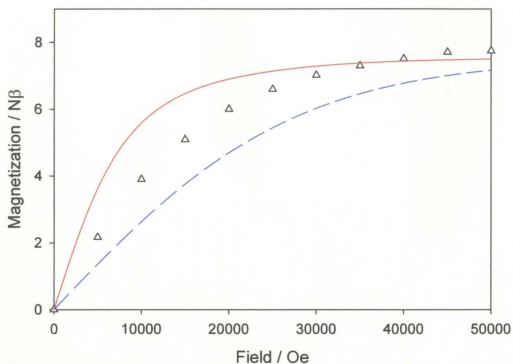


**Figure 6.24:** Variable field magnetization data for 6.4; solid red line calculated for  $g = 2.16$ ,  $S' = 7/2$ ,  $T = 2$  K and dashed blue line calculated for  $g = 2.16$ ,  $S' = 7 \times 1/2$ ,  $T = 2$  K using the appropriate Brillouin function.

Variable temperature magnetic data for 6.5 are shown in Figure 6.25. The moment drops from  $10.93 \mu_B$  at 300 K to a minimum value of  $8.43 \mu_B$  at 22 K, followed by a rise to a maximum of  $10.73 \mu_B$  at 8 K, with a further drop at lower temperatures. Such behaviour is typical of a ferrimagnetic system, with a non-compensated ground state spin due to intramolecular antiferromagnetic exchange (Chapter 5).

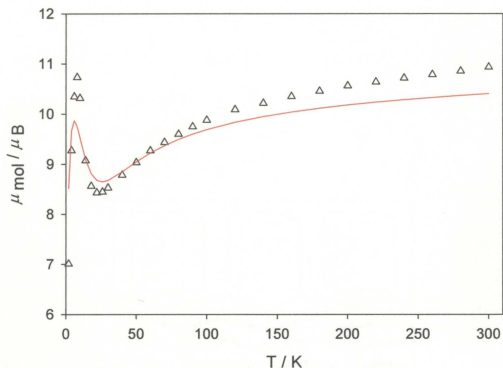


**Figure 6.25:** Variable temperature magnetic data for **6.5**;  $g = 2.42$ ,  $J_2 = -5.92 \text{ cm}^{-1}$ ,  $\text{TIP} = 2000 \times 10^{-6} \text{ cm}^3 \text{ mol}^{-1}$ ,  $\theta = -2 \text{ K}$ .

A model which reasonably accounts for this behaviour in an antiferromagnetic  $[3 \times 3]$   $\text{Co}_9$  grid involves oxidation of the four corner metal sites from  $\text{Co(II)}$  ( $S = 3/2$ ) to diamagnetic  $\text{Co(III)}$  (Figure 6.20; sites 1,3,5,7). An accurate reproduction of the magnetic data for **6.5** cannot be achieved using a strictly isotropic  $S = 3/2$  model for the five  $\text{Co(II)}$  sites (with a predicted ground state of  $S' = 9/2$ ), however, the shape of the profile can be reproduced with maxima and minima at the appropriate temperatures for  $g = 2.42$ ,  $J_2 = -5.92 \text{ cm}^{-1}$ ,  $\text{TIP} = 2000 \times 10^{-6} \text{ cm}^3 \text{ mol}^{-1}$ ,  $\theta = -2 \text{ K}$  (solid line, Figure 6.25). While no other  $\text{Co(II)}_5\text{Co(III)}_4$  grid has been reported for comparison, a  $\mu\text{-O}_{\text{hydrazone}}$  bridged  $[2 \times 2]$   $\text{Co(II)}_4$  grid gave fitted values of  $g = 2.42(1)$ ,  $J = -6.95(4) \text{ cm}^{-1}$  [59], which supports the reasonable values used to generate the simulation for **6.5**.

Complex **6.6** is a  $[3 \times 3]$   $\text{Mn(II)}_9$  grid, and as was the challenge with **4.2**, and all other reported  $[3 \times 3]$   $\text{Mn(II)}_9$  grids [73,74], a vector coupling approach cannot be used to model the variable temperature magnetic data due to the enormity of the required matrix calculations [98]. An adaptation of the Fisher model (equations 4.2 - 4.4) was used to approximate the outer ring of eight metals as a spin coupled chain, isolated from the central metal ion (Figure 6.20, with  $J_2$  assumed to be zero) [73,74]. The magnetic profile for **6.6** is shown in Figure 6.26 as a plot of moment per mole as a function of temperature. The moment drops from  $16.7 \mu_B$  at 300 K to a minimum value of  $6.3 \mu_B$  at 2 K. The Fisher Model approach is justified on the basis that at 2 K the observed moment is consistent for  $S' = 5/2$ , resulting from intragrid antiferromagnetic exchange and the non-compensation of the spin of the central ion in the ground state.

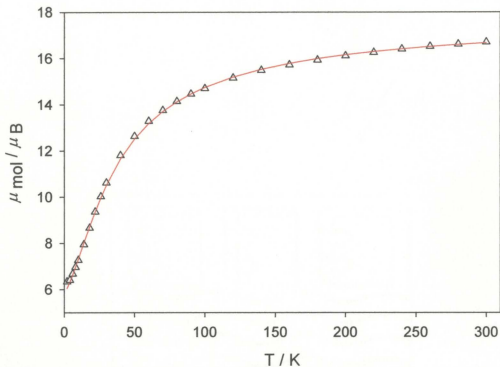


**Figure 6.26:** Variable temperature magnetic data for **6.6**;  $g = 2.0$ ,  $J_1 = -4.7 \text{ cm}^{-1}$ ,  $TIP = 0 \text{ cm}^3 \text{ mol}^{-1}$ ,  $\theta = -4 \text{ K}$ ,  $10^2 R = 1.14$ .

The data were fitted to equation 4.2 to give  $g = 2.0$ ,  $J_1 = -4.7 \text{ cm}^{-1}$ ,  $TIP = 0 \text{ cm}^3 \text{ mol}^{-1}$ ,  $\theta = -4 \text{ K}$ ,  $10^2 R = 1.14$  ( $R = [\sum(\chi_{\text{obs}} - \chi_{\text{calc}})^2 / \sum \chi_{\text{obs}}^2]^{1/2}$ ). The solid line in Figure 6.26 was calculated with these parameters and the exchange coupling is consistent with other  $\text{Mn(II)}_9$  grids [73,74], though as previously discussed for **4.2**, this is not a rigorous model and it is likely that  $J_2$  is non-zero, which is possibly reflected by the negative  $\theta$ -corrections. A summary of the magnetic results for **6.2 - 6.6** is presented in Table 6.8.

**Table 6.8:** Summary of the magnetic analysis of 6.2 - 6.6.

Compound	g	J1 (cm <sup>-1</sup> )	J2 (cm <sup>-1</sup> )	Ground State Spin (S')
6.2 (3×[1×3] Mn(II) <sub>9</sub> rectangle)	2.04	-1.4	-0.4*	5/2
6.3 (Cu(II) <sub>9</sub> grid)	2.07(1)	-0.8(1)	-10(1)	5 × ½
6.4 (Cu(II) <sub>9</sub> grid)	2.16(2)	2.2(2)	-28(3)	7/2
6.5 (Co(II) <sub>5</sub> Co(III) <sub>4</sub> grid)**	2.42	0	-5.92	9/2
6.6 (Mn(II) <sub>9</sub> grid)	2.0	-4.7	0	5/2

\*Molecular Field Correction with  $z = 4/3$ ,  $J' = -0.4 \text{ cm}^{-1}$

\*\*Simulation; data not fitted

#### 6.4: Summary:

[3×3] Mn(II)<sub>9</sub>, Cu(II)<sub>9</sub> and Co(II)<sub>5</sub>Co(III)<sub>4</sub> grids were synthesized by self-assembly reactions between metal salts and 2po45nq (2.7) and 2po34nq (2.8). A Cu(II)<sub>9</sub> grid (6.4), and a Mn(II)<sub>9</sub> grid (6.6), were characterized and their intramolecular properties (structure and magnetism) were found to be similar to those previously reported for ferromagnetic Cu(II)<sub>9</sub> [66,69,71,96] and antiferromagnetic Mn(II)<sub>9</sub> [30,69,70,73,29] grids. Single crystals, suitable for structural characterization, could not be obtained for 6.5, the mixed oxidation state Co(II)<sub>5</sub>Co(III)<sub>4</sub> grid, however, its magnetic profile is typical of intramolecular ferrimagnetic exchange, and the assignment of the oxidation sites as those in the grid corners is consistent with that previously observed in the case of Mn(II)<sub>9</sub> grid oxidation [29,30,73]. The data could not be fitted using an isotropic exchange model, however, the shape of the profile could be simulated using an exchange constant that is consistent for a [2×2] Co(II)<sub>4</sub> complex [59], presumed to have similar Co-O-Co bond angles.

Compound 6.3 is also a [3×3] Cu(II)<sub>9</sub> grid, with the ligand 2po56nq (2.6), however, unlike all other previously reported examples [66,69,71,96 and in Chapter 4,

compounds **4.5** and **4.6**], each Cu(II) centre exhibits axial compression and a  $d_{z^2}$  magnetic ground state, leading to antiferromagnetic coupling due to the large Cu-O-Cu bridging angles between both the ions in the ring and between the central ion and its neighbors. The experimental data were modeled with two different exchange constants that were independently varied in an iterative ratio to obtain a best fit, in the same manner as for other reported Cu(II)<sub>9</sub> grids, however both J1 and J2 were negative, consistent with antiferromagnetic exchange dominating both exchange pathways.

A unique antiferromagnetic  $3 \times [1 \times 3]$  Mn(II)<sub>9</sub> rectangle (**6.2**) was synthesized using the ligand 2po56hq (**2.5**), which differs from **2.6-2.8**, in that it does not possess an amine group neighboring both the diazine bridge and the terminal quinoline moiety. Without this additional steric factor, an alternative, enthalpically favoured ligand conformation was adopted around the metal core, presumably in order to minimize electrostatic repulsive effects between quinoline groups. The magnetic properties of **6.2** were successfully modeled using a linear triad to represent the  $\mu$ -O<sub>hydrazone</sub> bridged Mn(II) centres, and a molecular field correction to account for the interaction between triads *via* the  $\mu$ -NN<sub>diazine</sub> bridges.

Intermolecular  $\pi$ - $\pi$  interactions were observed in the extended lattice motifs of **6.1-6.4** and **6.6**. These effects organized the cations of **6.1** into layers *via* face-to-face interactions. The extended lattice of **6.6** showed that the cationic grid moieties were organized into chains, while the cations of **6.2** and **6.4** exhibited two-dimensional, layered arrangements, and **6.3** displayed a three-dimensional network ordering. Edge-to-face and face-to-face contacts between terminal quinoline moieties were found in all cases, and the

distances of separation and off-set angles were consistent with those reported by Janiak [132] from his Cambridge Structural Database search on the interactions between transition-metal quinoline fragments. While long-range structural ordering was observed in all cases, no corresponding long-range magnetic interactions were present. This is perhaps not surprising due to the weak nature of  $\pi$ - $\pi$  interactions, long distances between metal centres in adjacent grids, and the lack of direct bridges between these metals.

**Chapter 7: Antiferromagnetic  $4 \times [2 \times 2]$   $M_{16}$  grids ( $M = \text{Mn(II)}, \text{Co(II)}$  and  $\text{Co(II)/Co(III)}$ ) from self-assembly reactions with pyridazine bis(hydrazone) ligands**

**7.1: Preamble:**

Self-assembly is a reversible process in which one or more components of a system associate in a reversible manner to produce the most thermodynamically stable aggregate, held together by non-covalent forces [143], as discussed in detail in Chapter 1. The synthesis of large  $[n \times n]$   $M_n$  grid systems ( $n > 2$ ; see Figure 7.1 for  $n = 4$ ) is complicated by many factors, including the identity of the metal ion ( $M$ ) and any associated crystal field stabilization energy, the pH of the synthetic reaction, simultaneous or subsequent metal redox behaviour, and the possibility that other oligomers may form preferentially (that is, act as a thermodynamic sink) over the intended target [75].

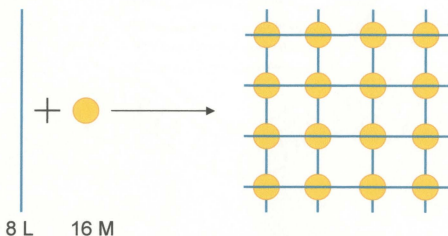
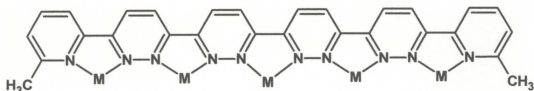


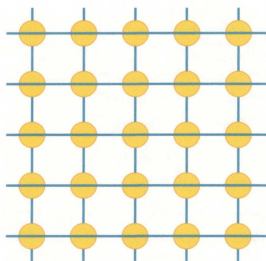
**Figure 7.1:** A hypothetical self-assembled  $[4 \times 4]$  grid.

Despite many complicating factors, grids of greater size and nuclearity are desirable goals in the pursuit of quantum arrays with nanometric dimensions. Towards

this end, the pentatopic ligand **L1** (Figure 7.2a) was synthesized, programmed with the coordination elements necessary for the formation of a self-assembled  $[5 \times 5]$   $M_{25}$  grid [144].



(a)



(b)

**Figure 7.2:** a) The complexed ligand **L1** in its *cisoid* configuration, leading to b) a hypothetical  $[5 \times 5]$  square grid.

While **L1** contains five pockets suitable for the formation of five-membered chelate rings upon coordination with a metal ion, and therefore could be envisaged to lead to the desired target upon assembly of ten ligands with 25 metal ions (Figure 7.2b), this result was not achieved. Instead, the ligand adopted a *transoid*  $N=C-C=N$  configuration about the central pyridazine-pyridazine bond (Figure 7.3a), leading to the

formation of a compartmental  $2 \times [2 \times 5]$   $\text{Ag(I)}_{20}$  grid with nine ligands (Figure 7.3b) [144].

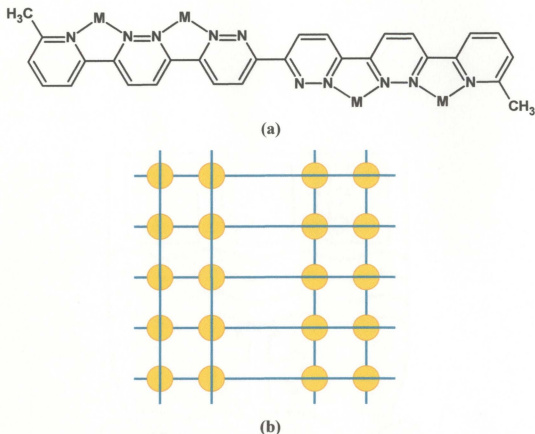


**Figure 7.3:** a) The complexed ligand **L1** in its *transoid* configuration, leading to the formation of b)  $2 \times 5$   $\text{Ag(I)}_{10}$  rectangular subunits.

A non-magnetic  $\text{Pb(II)}_{16}$  grid was synthesized *via* a self-assembly reaction between 16 metal ions and eight ligands [22] (**L2**, Figure 7.4a) with 16 triflate anions and eight water molecules filling additional sites on the lead ions, which adopted coordination numbers of seven, eight or nine [22,23]. The ligands were arranged with two perpendicular sets of four outer (Figure 7.4b, blue) and four inner (Figure 7.4, magenta) ligands, which does not result in a regular  $4 \times 4$  grid, but instead another

compartmentalized arrangement, this one consisting of four  $[2 \times 2]$  subunits, that is, a  $4 \times [2 \times 2]$   $\text{Pb(II)}_{16}$  grid (Figure 7.4b) [23].

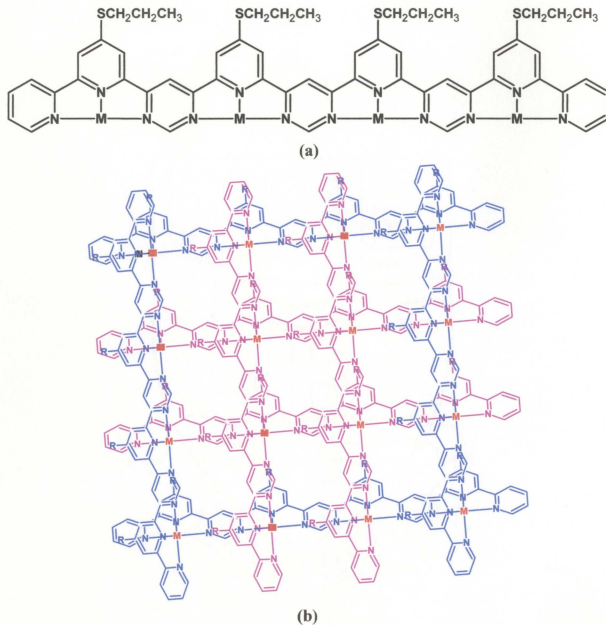


**Figure 7.4:** a) The ligand **L2** (showing metal coordination) used in the synthesis of b) a  $4 \times [2 \times 2]$   $\text{Pb(II)}_{16}$  grid.

Tetrapotic ligands based on a central dinucleating pyridazine bis(hydrazone) fragment (Figure 7.5), suitable for the formation of  $[4 \times 4]$   $\text{M}_{16}$  grids, have been

synthesized. Initial reports, however, included only the lower nuclearity complexes  $\text{Ni(II)}_3(\mathbf{L3})_3$ , a linear, trinuclear helix [145] and  $\text{Cu(II)}_{12}(\mathbf{L3})_8$ , an incomplete 'picture frame' [146], in which some of the potential coordination sites were vacant.

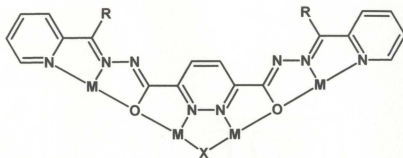


**Figure 7.5:** Tetratopic pyridazine bis(hydrazone) ligands **L3** ( $\text{R} = \text{NH}_2$ ) and **L4** ( $\text{R} = \text{H}$ ), showing metal coordination pockets.

Compartmental  $4 \times [2 \times 2]$   $\text{Mn(II)}_{16}$  grids were subsequently reported [55,56], consisting of six-coordinate metal ions in an arrangement of four  $[2 \times 2]$   $\text{Mn}_4$ - $(\mu\text{-O}_{\text{hydrazone}})_4$  moieties with eight ligands (Figure 7.5; **L4**), arranged in an approximately parallel manner, with four above and four below a puckered metal pseudoplane (Figure 7.6).

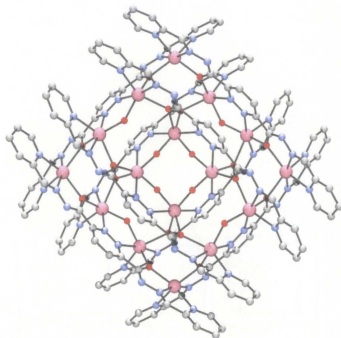


**Figure 7.6:** Ball-and-stick model of an  $\text{Mn}_{16}(\text{L4})_8(\text{OH})_8$  cation [56]; pink = Mn, red = O, grey = C, blue = N.

Each  $\text{Mn}_4-(\mu\text{-O}_{\text{hydrazone}})_4$  subunit was bridged to two adjacent subunits by a combined  $\mu\text{-NN}_{\text{pyridazine}}/\mu\text{-O}$  double bridge, in which the oxygen was exogenous (Figure 7.6; X = OH<sup>-</sup> for example), resulting from the solvent and completing the distorted octahedral coordination spheres of the inner metal ions. Variable temperature magnetic data showed a drop in moment from approximately  $22 \mu_{\text{B}}$  at 300 K (which is slightly lower than the expected spin only moment of  $23.6 \mu_{\text{B}}$  for sixteen  $S' = 5/2$  centres) to approximately  $4 \mu_{\text{B}}$  at 2 K, consistent with the presence of antiferromagnetic coupling. The magnetic data were not modeled due to the enormous matrix calculations that an 80-electron problem would require in order to generate the required spin state/energy profile.

Two new tetratopic pyridazine bis(hydrazone) tetratopic ligands have been synthesized (**2.10** and **2.11**, Figure 7.7 and 7.8, respectively), and form antiferromagnetically coupled, compartmental  $4 \times [2 \times 2]$   $M_{16}$  grids (where  $M = \text{Mn(II)}$ ,  $\text{Co(II)}$  and  $\text{Co(II)/Co(III)}$ ). Based upon the X-ray structural analysis of two  $\text{Mn(II)}_{16}$  grids magnetic exchange models are proposed. These results are discussed here.

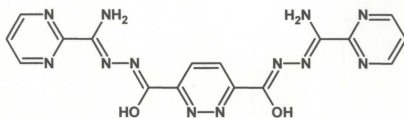


**Figure 7.7:** Tetratopic pyridazine bis(hydrazone) ligand 2pdoapm, **2.10**.

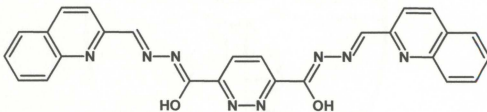


**Figure 7.8:** Tetratopic pyridazine bis(hydrazone) ligand 2pdo56hq, **2.11**.

## 7.2: Experimental:

**Note:** In some cases there is a difference between the most reasonable formula based on the elemental analysis (analytical formula), and that obtained from X-ray crystallography.

The analytical formulae will be used here.

### 7.2.1: Complex synthesis:

**7.2.1.1:**  $[(\text{C}_{16}\text{H}_{12}\text{O}_2\text{N}_{12})_8\text{Mn}_{16}\text{O}_4(\text{OH})_4](\text{PF}_6)_4 \cdot 57\text{H}_2\text{O} \cdot 12\text{CH}_3\text{OH}$  (**7.1**) A solution of  $\text{Mn}(\text{CF}_3\text{SO}_3)_2$  (3 mL of a  $0.091 \text{ g mL}^{-1}$  solution in  $\text{CH}_3\text{OH}$ ; 0.8 mmol) was added to a slurry of 2pdoapm (**2.10**) (0.070 g; 0.17 mmol) in 20 mL of 1:1  $\text{CH}_3\text{CN}:\text{CH}_3\text{OH}$

producing a yellow slurry.  $\text{NaOH}_{(\text{aq})}$  (1 mL of  $1.17 \text{ mol}\cdot\text{L}^{-1}$ ;  $\sim 1 \text{ mmol}$ ) in order to achieve a slightly basic pH ( $\sim 8$ ), turning the reaction solution clear and dark red.  $\text{NH}_4\text{PF}_6$  (0.040 g, 0.25 mmol) was added, and the solution was heated gently (equipped with a condenser) for 24 hours and then filtered. The filtrate was preserved for crystallization. Red needle-like crystals, suitable for X-ray diffraction, formed upon standing after 13 days (0.040 g, 61 % yield). Anal. Calcd (%) for  $[(\text{C}_{16}\text{H}_{12}\text{O}_2\text{N}_{12})_8 \text{Mn}_{16}\text{O}_4 (\text{OH})_4](\text{PF}_6)_4(\text{H}_2\text{O})_{57}(\text{CH}_3\text{OH})_{12}$ ; C, 27.17; H, 4.27; N 21.72; Found (bulk sample) (%): C, 27.20; H, 1.90; N 21.93.

**7.2.1.2:**  $[(2\text{pdoapm-2H})_8\text{Co(II)}_{16}(\text{OH})_8](\text{BF}_4)_8\cdot 19.8\text{H}_2\text{O}$  (**7.2a**) and  $[(2\text{pdoapm-2H})_8\text{Co(II)}_{12}\text{Co(III)}_4(\text{H}_2\text{O})_8](\text{BF}_4)_{20}\cdot 95\text{H}_2\text{O}$  (**7.2b**)  $2\text{pdoapm}$  (**2.10**) (0.12 g, 0.30 mmol) was added to a solution of  $\text{Co}(\text{BF}_4)_2\cdot 6\text{H}_2\text{O}$  (0.21 g; 0.62 mmol) in 20 mL of 1:1  $\text{CH}_3\text{OH}:\text{CH}_3\text{CN}$ . This produced a clear, light orange solution to which 1 mL of  $1.22 \text{ mol}\cdot\text{L}^{-1}$   $\text{NaOH}_{(\text{aq})}$  was added in order to achieve a neutral pH. The resulting dark purple solution was stirred with gentle heating for 18 hours and at room temperature for 6 hours and then filtered. The filtrate was preserved for crystallization. Several red prismatic crystals, suitable for X-ray diffraction, formed upon standing after 22 days. One crystal (**7.2a**) was used for X-ray diffraction. The following day ( $\sim 24$  hours after isolation of **7.2a**) the bulk solution was layered with 3 mL of dichloromethane, which precipitated a dark red powder that was collected by filtration (**7.2b**) (0.26g; 60 % yield). Note that air was not excluded in this procedure. Anal. Calcd (%) for **7.2b**  $[(\text{C}_{16}\text{H}_{14}\text{N}_{12}\text{O}_2)_8\text{Co}_{16}(\text{H}_2\text{O})_8](\text{BF}_4)_{20}(\text{H}_2\text{O})_{95}$ ; C, 19.75; H, 4.11; N 17.27; Found (bulk sample) (%): C, 19.75; H, 1.91; N 17.22. UV-Vis for **7.2b**:  $\lambda_{\text{max}}(\text{CH}_3\text{CN})/\text{nm}$  411 ( $\epsilon/\text{dm}^3 \text{ mol}^{-1} \text{ cm}^{-1}$  19 202).

**7.2.1.3:** (2pdoapm-2H)<sub>8</sub>Co<sub>16</sub>(H<sub>2</sub>O)<sub>8</sub>(BF<sub>4</sub>)<sub>16</sub>·74H<sub>2</sub>O (**7.3**). Note: All reaction steps were performed under an N<sub>2(g)</sub> atmosphere and all solvents were degassed with N<sub>2(g)</sub> prior to use. To a slurry of 2pdoapm, **2.10**, (0.12 g; 0.30 mmol) in 15 mL of 1:1 CH<sub>3</sub>CN:CH<sub>3</sub>OH was added a solution of Co(BF<sub>4</sub>)<sub>2</sub>·6H<sub>2</sub>O (0.21 g; 0.62 mmol) in 6 mL of 1:1 CH<sub>3</sub>CN:CH<sub>3</sub>OH dropwise *via* syringe, producing a clear red-orange solution that turned clear red upon stirring at room temperature for 45 minutes. 1.5 mL of 0.50 mol·L<sup>-1</sup> NaOH<sub>(aq)</sub> (0.75 mmol) was then added dropwise *via* syringe over 12 minutes, turning the reaction solution clear and dark red. This was stirred with gentle heating in a hot water bath for 20 minutes, and then at room temperature for 18 hours. The volume was then reduced under vacuum to 5 mL, and a solution of 3:1 CH<sub>3</sub>OH:(CH<sub>3</sub>CH<sub>2</sub>)<sub>2</sub>O was added *via* syringe. The resulting slurry was stirred at room temperature for one hour and was then filtered under N<sub>2(g)</sub>. 0.11 g (0.016 mmol; 63 % yield) of very dark red, microcrystalline **7.3** was collected. Anal. Calcd (%) for (C<sub>16</sub>H<sub>14</sub>N<sub>12</sub>O<sub>2</sub>)<sub>8</sub>Co<sub>16</sub>(H<sub>2</sub>O)<sub>8</sub>(BF<sub>4</sub>)<sub>16</sub>(H<sub>2</sub>O)<sub>74</sub>; C, 21.77; H, 3.94; N 19.04; Found (bulk sample) (%): C, 21.99; H, 1.92; N 19.07.

**7.2.1.4:** [(2pdo56hq-2H)<sub>8</sub>Mn<sub>16</sub>(OH)<sub>8</sub>](NO<sub>3</sub>)<sub>8</sub>·27H<sub>2</sub>O (**7.4**). Mn(NO<sub>3</sub>)<sub>2</sub>·6H<sub>2</sub>O (0.21 g, 0.73 mmol) was added to a beige slurry of 2pdo56hq, **2.11**, (0.11 g; 0.22 mmol) in 20 mL of 1:1 CH<sub>3</sub>CN:CH<sub>3</sub>OH, producing no change in the appearance of the slurry. NaOH<sub>(aq)</sub> (1 mL of 1.17 mol·L<sup>-1</sup>; ~ 1 mmol) was added in order to achieve a neutral pH (~ 7), turning the reaction mixture cloudy and brown. Upon addition of 5 mL of H<sub>2</sub>O, the solution became clear and brown. The reaction flask was equipped with a condenser, and the reaction was heated gently (approximately 55 °C) for 20 hours and then filtered. The dark

red filtrate was preserved for crystallization. Red crystals, suitable for X-ray analysis, formed upon standing after 3 days (0.060 g, 38 % yield). Anal. Calcd (%) for  $[(C_{26}H_{16}O_2N_8)_8Mn_{16}(OH)_8](NO_3)_8(H_2O)_{27}$ ; C, 43.24; H, 3.31; N 17.46; Found (bulk sample) (%): C, 43.24; H, 3.11; N 17.37.

### 7.2.2: Crystallography

The diffraction intensities of a red, needle crystal of **7.1** having approximate dimensions of  $0.45 \times 0.14 \times 0.10$  mm were collected on a Rigaku Saturn CCD area detector with graphite monochromated Mo-K $\alpha$  radiation at 113(2) K to a maximum  $2\theta$  value of  $61.9^\circ$ . The data were corrected for Lorentz and polarization effects and a correction for secondary extinction [81] was applied. The structure was solved by direct methods [82,83] and expanded using Fourier techniques [84]. Hydrogen atoms were introduced in difference map or calculated positions with isotropic thermal parameters set twenty percent greater than those of their bonding partners. They were refined on the riding model. The Platon [91] Squeeze procedure was applied to recover 423.8 electrons per unit cell in two voids (total volume  $4437.5 \text{ \AA}^3$ ); that is 211.9 electrons per formula unit. Disordered solvent water molecules appeared to be present prior to the application of Squeeze, though a good point atom model could not be achieved for these. The application of Squeeze gave a good improvement in the data statistics and allowed for a full anisotropic refinement of the framework structure and counterions. Two half-occupancy, hexafluorophosphate anions were present in the asymmetric unit; one was disordered and its fluorine atom occupancies reflect this disorder. These contribute a charge of -4 per formula unit. Protons H(25) and H(26) were located on O(5) and O(6),

respectively, in the difference map, making their assignment hydroxide bridges, while no such protons could be located on O(7) and O(8) and are hence presumed to be oxides. Neutral atom scattering factors and anomalous dispersion effects were taken from the usual sources [85-88]. All calculations were performed using the Crystal Structure [89,90] crystallographic software package except for refinement, which was performed using SHELXL-97 [83].

A dark red prismatic crystal of **7.2a** having approximate dimensions of  $0.27 \times 0.19 \times 0.18$  mm was treated similarly to **7.1**. Hydrogen atoms were introduced in calculated positions with isotropic thermal parameters set twenty percent greater than those of their bonding partners. They were refined on the riding model. One disordered half-occupancy tetrafluoroborate was refined isotropically with fluorines held in fixed positions in the last round of least squares in order to achieve convergence. All other non-hydrogen atoms were refined anisotropically. Two other full-occupancy disordered tetrafluoroborate anions are present in the asymmetric unit; the fluorine atom occupancies reflect this disorder. The Platon [91] Squeeze procedure was applied to recover 396.4 electrons per unit cell in one void (total volume  $3552.2 \text{ \AA}^3$ ); that is 198.2 electrons per formula unit. Disordered solvent water molecules appeared to be present prior to the application of Squeeze, though a good point atom model could not be achieved for these. The application of Squeeze gave a good improvement in the data statistics and allowed for a satisfactory refinement of the framework structure and counterions.

A red prismatic crystal of **7.4** having approximate dimensions of  $0.41 \times 0.28 \times 0.28$  mm was treated similarly to **7.1**. Hydrogen atoms were introduced in difference

map (H(33)) or calculated positions with isotropic thermal parameters set twenty percent greater than those of their bonding partners. They were refined on the riding model. The asymmetric unit contains one full-occupancy nitrate anion that was refined anisotropically until the final rounds of least squares, when its thermal parameters and positional coordinates were fixed in order to achieve convergence. The asymmetric unit also contains eight partial occupancy water molecules as lattice solvent. The corresponding protons could not be located in the difference map and were omitted from the model. Atoms O(6) and O(7), each with occupancy equal to  $\frac{1}{2}$ , appear make up a full occupancy hydroxide bridge, hydrogen bonded to the water molecule O(17). No protons were located on the bridging atom O(5) and the species is presumed to be oxide. Abbreviated crystal data for **7.1**, **7.2a** and **7.4** are listed in Tables 7.1 and 7.2.

**Table 7.1:** Summary of crystallographic data for **7.1** and **7.2a**.

	<b>7.1</b>	<b>7.2a</b>
Chemical Formula	$C_{128}H_{142.4}F_{24}N_{96}Mn_{16}O_{45.2}P_4$	$C_{128}H_{143.6}B_8Co_{16}F_{32}N_{96}O_{43.8}$
M	5207.61	5364.92
T(K)	113(2)	113(2)
Crystal System	orthorhombic	orthorhombic
Space Group	Pmmn (#59)	Pmmn (#59)
a (Å)	25.845(3)	25.517(3)
b (Å)	29.547(4)	29.451(3)
c (Å)	16.420(2)	15.8192(16)
$\alpha$ (°)	90.00	90.00
$\beta$ (°)	90.00	90.00
$\gamma$ (°)	90.00	90.00
V (Å <sup>3</sup> )	12539(3)	11888(2)
Z	2	2
D <sub>calc</sub> (g/cm <sup>3</sup> )	1.379	1.499
$\mu$ (MoK $\alpha$ ) (cm <sup>-1</sup> )	8.95	11.90
Reflections Total	56060	93316
Reflections Unique	12815	12830
R <sub>int</sub>	0.0510	0.0658
R <sub>1</sub> ( $I > 2.00\sigma(I)$ )	0.0928	0.0955
wR <sub>2</sub> (All reflections)	0.2793	0.2806

**Table 7.2:** Summary of crystallographic data for 7.4.

	7.4
Chemical Formula	$C_{208}H_{196}Mn_{16}N_{68}O_{68}$
M	5615.26
T(K)	113(2)
Crystal System	tetragonal
Space Group	$P4_21c$ (#114)
a (Å)	22.856(2)
b (Å)	22.856(2)
c (Å)	27.634(3)
$\alpha$ (°)	90.00
$\beta$ (°)	90.00
$\gamma$ (°)	90.00
V (Å <sup>3</sup> )	14436(2)
Z	2
D <sub>calc</sub> (g/cm <sup>3</sup> )	1.292
$\mu$ (MoK $\alpha$ ) (cm <sup>-1</sup> )	7.53
Reflections Total	114457
Reflections Unique	14185
R <sub>int</sub>	0.0574
R <sub>1</sub> ( $I > 2.00\sigma(I)$ )	0.0934
wR <sub>2</sub> (All reflections)	0.2707

### 7.3: Results and Discussion:

**Note:** The crystallographically determined formulae are used herein. Colour code for figures: purple = cobalt, magenta = manganese, grey = carbon, blue = nitrogen, red = oxygen. Crystallographic representations/illustrations were generated using Persistence of Vision Ray Tracer (POV-Ray©) for Windows, version 3.6, with scene description files written by Ortep-3 for Windows (Version 1.08) Copyright© 1997-2003 Louis J. Farrugia.

#### 7.3.1: Description of crystal structures:

##### 7.3.1.1: $[(2\text{pdoapm-2H})_8\text{Mn}_{16}\text{O}_4(\text{OH})_4](\text{PF}_6)_4 \cdot 21.2\text{H}_2\text{O}$ (7.1).

The structure of the cationic fragment of 7.1 and its unit cell and the bifurcated Mn-O core are shown in Figures 7.9a, b and c respectively, and significant bond lengths and angles are listed in Table 7.3.

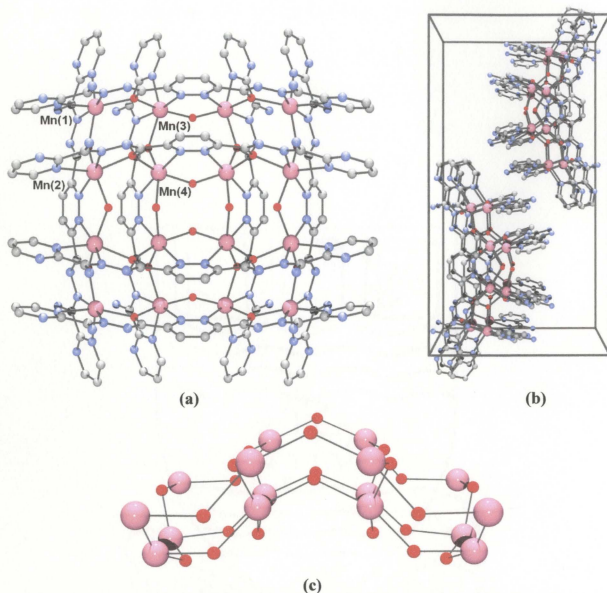


**Figure 7.9:** a) Ball-and-stick depiction of the cationic moiety **7.1**. Hydrogen atoms omitted for clarity. b) The unit cell of **7.1**, looking down the *a*-axis; anions omitted for clarity. c) Bifurcation of the M-O core in **7.1**.

The crystal structure of **7.1** consists of a hexadecanuclear core of six-coordinate Mn(II) ions in an arrangement of four  $[2 \times 2] \text{Mn}_4-(\mu\text{-O}_{\text{hydrazone}})_4$  moieties forming a roughly square cationic framework (Figure 7.9a), with eight 2pdoapm ligands, arranged in two almost parallel groups of four, one group above and the other below a puckered

metal pseudoplane (Figure 7.9c). Each  $\text{Mn}_4(\mu\text{-O}_{\text{hydrazone}})_4$  subunit is bridged to two adjacent subunits by a combined  $\mu\text{-NN}_{\text{pyridazine}}/\mu\text{-O}$  double bridge, in which the oxygen is from an exogenous source (Figure 7.10). The bifurcation of the metal core is expected due to the bending of the ligand arms (end-pieces) relative to the pyridazine central group (Figure 7.5).

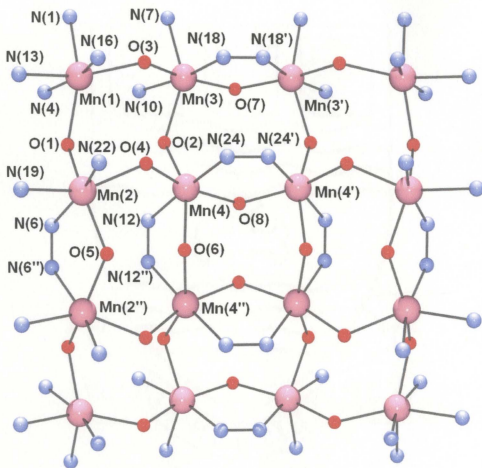


**Figure 7.10:** Ball-and-stick depiction of the core structure of 7.1.

The presence of sixteen Mn(II) centres creates a charge of +32 which must be balanced. Each ligand is presumed to be doubly-deprotonated [55,56] and four hexafluorophosphate anions are present per grid; these account for a charge of -20.

Protons were located on O(5) and O(6) in the difference map, making their assignment hydroxide bridges. No protons could be located on O(7) and O(8) which are therefore assigned as oxides. Together the hydroxides and oxides make up the remaining charge of -12. The formation of hydroxide and oxide is reasonable since base was added in the synthesis.

Mn-Mn distances mediated only by  $\mu$ -O bridges fall in the range 3.7796(14) - 3.9057(14) Å, with Mn-O-Mn angles in the range 119.18(15) - 126.15(18)°, which are slightly less than those observed for other  $\mu$ -O<sub>hydrazone</sub> bridged [2×2] Mn(II)<sub>4</sub> grids (126.5 - 131.6°) [64]. This is in good agreement with previously reported 4×[2×2] Mn(II)<sub>16</sub> grids [55,56] and reasonable in light of the secondary  $\mu$ -O/ $\mu$ -NN bridges connecting the subunits. Distances between manganese centres that are doubly  $\mu$ -O/ $\mu$ -NN bridged fall in the range 3.6860(14) - 3.7690(8) Å, with Mn-O-Mn angles in the range 116.2(2) - 126.9(3)° and Mn-NN-Mn torsion angles of 180.0°. The overall metallic core of 7.1 measures approximately 10.74 × 10.80 Å<sup>2</sup>. Mn(1) has a *cis*-MnN<sub>4</sub>O<sub>2</sub> coordination environment, while Mn(2) and Mn(3) have *mer*-MnN<sub>3</sub>O<sub>3</sub> environments and Mn(4) has a *trans*-MnN<sub>2</sub>O<sub>4</sub> coordination environment. Mn(1), Mn(2) and Mn(3) display long Mn-N distances to the external pyrimidine rings (N(1), N(13), N(19) and N(7), with distances in the range 2.306(4) - 2.380(6) Å), likely due to the stretching of the ligands over the bifurcated metal core, with all other Mn-L distances exhibiting shorter contacts (2.083(3) - 2.289(4) Å).

**Table 7.3:** Selected bond distances (Å) angles (°) and torsion angles (°) for **7.1**.

Mn(1) N(16)	2.139(5)	Mn(3) O(7)	2.083(3)
Mn(1) N(4)	2.140(5)	Mn(3) N(10)	2.135(5)
Mn(1) O(1)	2.188(3)	Mn(3) O(3)	2.189(4)
Mn(1) O(3)	2.192(4)	Mn(3) O(2)	2.213(4)
Mn(1) N(1)	2.306(4)	Mn(3) N(18)	2.255(5)
Mn(1) N(13)	2.380(6)	Mn(3) N(7)	2.314(5)
Mn(2) O(5)	2.107(2)	Mn(4) O(8)	2.155(3)
Mn(2) N(22)	2.169(5)	Mn(4) O(2)	2.156(4)
Mn(2) O(1)	2.184(4)	Mn(4) O(4)	2.174(4)
Mn(2) O(4)	2.209(4)	Mn(4) O(6)	2.191(3)
Mn(2) N(6)	2.306(4)	Mn(4) N(12)	2.279(5)
Mn(2) N(19)	2.359(6)	Mn(4) N(24)	2.289(4)
Mn(2) O(1)	Mn(1) 126.08(17)	Mn(2) N(6)	N(6'') Mn(2'') 180.0
Mn(4) O(2)	Mn(3) 126.15(18)	Mn(3) N(18)	N(18') Mn(3) 180.0
Mn(3) O(3)	Mn(1) 126.15(18)	Mn(4) N(24)	N(24') Mn(4'') 180.0
Mn(4) O(4)	Mn(2) 119.18(15)	Mn(4) N(12)	N(12'') Mn(4'') 180.0
Mn(2) O(5)	Mn(2'') 126.9(3)		
Mn(4) O(6)	Mn(4'') 116.2(2)		
Mn(3) O(7)	Mn(3') 124.4(3)		
Mn(4) O(8)	Mn(4') 120.8(2)		

**7.3.1.2:** [(2pdoapm-2H)<sub>8</sub>Co<sub>16</sub>(OH)<sub>8</sub>](BF<sub>4</sub>)<sub>8</sub>·19.8H<sub>2</sub>O (**7.2a**).

The structure of the cationic fragment of **7.2a**, its unit cell and the bifurcated Co-O core are shown in Figure 7.11a, b and c respectively, and significant bond lengths and angles are listed in Table 7.4.

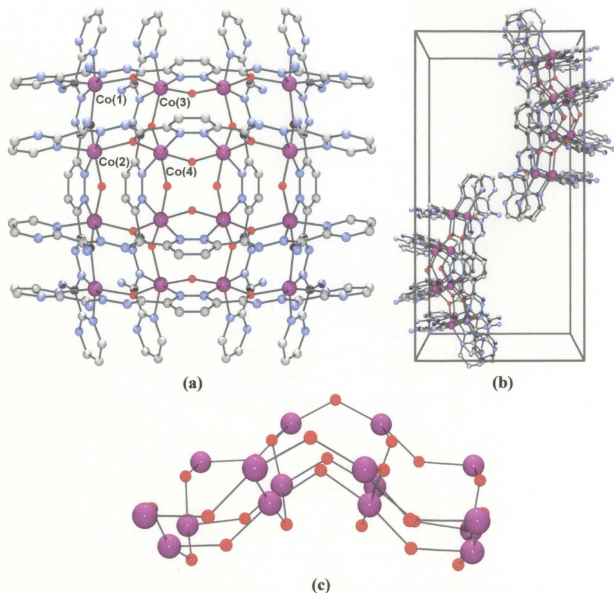


**Figure 7.11:** a) Ball-and-stick depiction of the cationic moiety **7.2a**. Hydrogen atoms omitted for clarity. b) The unit cell of **7.2a**, looking down the *a*-axis; anions omitted for clarity. c) Bifurcation of the M-O core in **7.2a**.

The crystal structure of **7.2a** consists of a core of sixteen distorted octahedral Co(II) ions arranged in four  $[2 \times 2]$   $\text{Co}_4(\mu\text{-O}_{\text{hydrazone}})_4$  squares connected to each other by  $\mu\text{-NN}_{\text{pyridazine}}/\mu\text{-O}$  double bridges forming a cationic framework, with eight  $2\text{pdoapm}$  ligands (Figure 7.11a). The two groups of ligands are arranged in an approximately

parallel manner, with four above and four below the bifurcated metal pseudoplane (Figure 7.11c). The full core structural representation of 7.2a is shown in Figure 7.12.

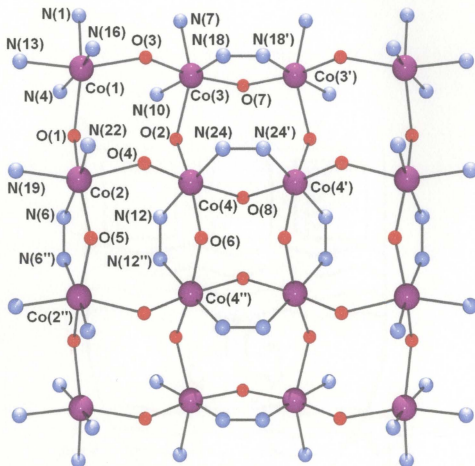


**Figure 7.12:** Ball-and-stick depiction of the core structure of 7.2a.

Each cobalt centre is in the +2 oxidation station based upon BVS calculations (2.28, 2.24, 2.29, 2.25 for Co(1) - Co(4) respectively) [59,93]. For charge balance purposes in the symmetry expanded model, there are sixteen cobalt atoms, for a total charge of +32 and eight tetrafluoroborate anions contributing a charge of -8. Each ligand is presumed to be doubly deprotonated each with a charge of -2 for an additional contribution of -16. While no protons could be located in the difference map for the

bridging atoms O(5-8), these are presumed to be hydroxide ions, contributing an additional total charge of -8 per formula unit; therefore charge balance is achieved.

Co-Co distances mediated only by  $\mu$ -O bridges fall in the range 3.8669(12) - 3.9891(10) Å, with Co-O-Co angles in the range 132.24(17) - 135.64(18)°, while distances between cobalt centres that are doubly  $\mu$ -O/ $\mu$ -NN bridged fall in the range 3.4616(10) - 3.6313(12) Å, with Co-O-Co angles in the range 112.4(2) - 123.8(3)° and Co-NN-Co torsion angles of 180.0°. The overall metallic core for **7.2a** measures approximately  $10.76 \times 10.81 \text{ \AA}^2$ . Co(1) has a *cis*-CoN<sub>4</sub>O<sub>2</sub> coordination environment, while Co(2) and Co(3) have *mer*-CoN<sub>3</sub>O<sub>3</sub> environments and Co(4) has a *trans*-CoN<sub>2</sub>O<sub>4</sub> coordination environment, all with Co-L distances between 2.007(5) - 2.220(6) Å.

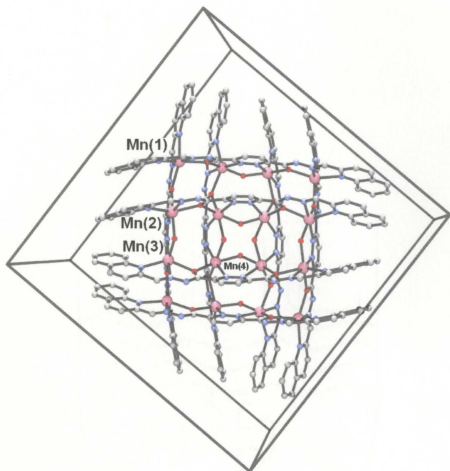
**Table 7.4:** Selected bond distances (Å) angles (°) and torsion angles (°) for **7.2a**.

Co(1) N(16)	2.018(5)	Co(3) N(10)	2.007(5)
Co(1) N(4)	2.018(5)	Co(3) O(7)	2.019(3)
Co(1) O(3)	2.162(4)	Co(3) N(18)	2.096(4)
Co(1) N(1)	2.170(5)	Co(3) O(3)	2.123(4)
Co(1) O(1)	2.179(3)	Co(3) N(7)	2.183(5)
Co(1) N(13)	2.220(6)	Co(3) O(2)	2.183(3)
Co(2) N(22)	2.028(6)	Co(4) O(4)	2.055(4)
Co(2) O(5)	2.058(3)	Co(4) N(12)	2.080(4)
Co(2) N(6)	2.099(4)	Co(4) O(8)	2.083(3)
Co(2) O(1)	2.129(4)	Co(4) O(2)	2.086(3)
Co(2) O(4)	2.162(4)	Co(4) O(6)	2.091(3)
Co(2) N(19)	2.174(7)	Co(4) N(24)	2.102(5)
Co(2) O(1)	Co(1) 135.64(18)	Co(2) N(6)	N(6'') Co(2'') 180.0
Co(4) O(2)	Co(3) 135.34(18)	Co(3) N(18)	N(18'') Co(3'') 180.0
Co(3) O(3)	Co(1) 132.24(17)	Co(4) N(24)	N(24'') Co(4'') 180.0
Co(4) O(4)	Co(2) 132.94(18)	Co(4) N(12)	N(12'') Co(4'') 180.0
Co(2) O(5)	Co(2'') 123.8(3)		
Co(4) O(6)	Co(4'') 114.9(2)		
Co(3) O(7)	Co(3'') 122.6(2)		
Co(4) O(8)	Co(4'') 112.4(2)		

**7.3.1.3:** [(2pdo56hq-2H)<sub>8</sub>Mn<sub>16</sub>O<sub>4</sub>(OH)<sub>4</sub>](NO<sub>3</sub>)<sub>4</sub>•32H<sub>2</sub>O (**7.4**).

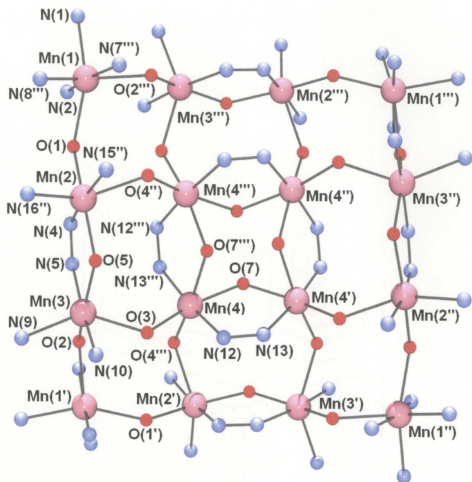
The unit cell of **7.4**, showing the structure of the cationic fragment is shown in

Figure 7.13 and significant bond lengths and angles are listed in Table 7.5.



**Figure 7.13:** Ball-and-stick depiction of the cationic moiety in the unit cell of **7.4**, viewed down the *c*-axis. Hydrogen atoms, solvent, anions and O(6) omitted for clarity.

The crystal structure of **7.4** is similar to that of **7.1** in that it consists of four  $[2 \times 2]$   $\text{Mn}_4(\mu\text{-O}_{\text{hydrzone}})_4$  squares arranged in an approximately square cationic framework (Figure 7.13) connected by  $\mu\text{-NN}_{\text{pyridazine}}/\mu\text{-O}$  double bridges with two groups of four 2pdo56hq ligands arranged in an approximately parallel manner, with one group above and the other below a metal pseudoplane. The core structural representation of **7.4** is shown in Figure 7.14.



**Figure 7.14:** Ball-and-stick depiction of the core structure of **7.4**; O(6) omitted for clarity.

The presence of sixteen Mn(II) centres means that a charge of +32 must be balanced. Each ligand is presumed to be doubly-deprotonated, and four nitrate anions were found per grid, together contributing a charge of -20. O(6) (omitted for clarity from Figure 7.13 and 7.14) and O(7) are each at  $\frac{1}{2}$  occupancy, bonded to the single proton H(33), which was located in the difference map, and together make up a disordered hydroxide bridge, thereby contributing a charge of -4. No protons were located on the bridging atoms O(5) and so these species are presumed to be oxide, contributing a charge of -8 overall, and balancing the charge for the full formula unit.

Mn-Mn distances mediated only by  $\mu$ -O bridges fall in the range 3.9426(13) - 4.0712(14) Å, with Mn-O-Mn angles in the range 124.3(2) - 129.8(2)°, which are again slightly less than those observed for other  $\mu$ -O<sub>hydrazone</sub> bridged [2×2] Mn(II)<sub>4</sub> grids (126.5 - 131.6°) [64]. Distances between manganese centres that are doubly  $\mu$ -O/ $\mu$ -NN bridged fall in the range 3.7086(12) - 3.7638(13) Å, with Mn-O-Mn angles in the range 119.4(5) - 130.8(3)° and Mn-NN-Mn torsion angles of 174.7 and 174.9°. The overall metallic core of **7.4** measures approximately 11.05 × 11.05 Å<sup>2</sup>. Mn(1) has a *cis*-MnN<sub>4</sub>O<sub>2</sub> coordination environment, while Mn(2) and Mn(3) have *mer*-MnN<sub>3</sub>O<sub>3</sub> environments and Mn(4) has a *trans*-MnN<sub>2</sub>O<sub>4</sub> coordination environment. Mn(1), Mn(2) and Mn(3) display long Mn-N distances to the external pyridine-moiety of the quinoline rings (N(1), N(8'''), N(9) and N(16''), with distances in the range 2.286(6) - 2.373(6) Å), likely due to the stretching of the ligands over the metal core, with all other Mn-L distances exhibiting shorter contacts (2.064(5) - 2.306(6) Å).

The ligands of **7.4** are aligned in two approximately parallel groups above and below the metal pseudoplane, with distances between terminal quinoline-pyridine centroids of 3.74 - 3.78 Å, off-set by 20.1 - 54.0°, and terminal quinoline-arene centroids of 3.68 - 3.74 Å, off-set by 13.9 - 54.8° (Figure 7.15, orange arrows). Examination of the extended lattice structure reveals that the aromatic quinoline moieties effectively extending the overall structure in a two-dimensional array, with each grid interlocked with two others through both face-to-face quinoline-arene to quinoline-pyridine interactions (Figure 7.15, green arrow, 3.80 Å, off-set by 33.5°) and perpendicular edge-to-face interactions (Figure 7.15, purple arrows, 3.89 - 3.99 Å).

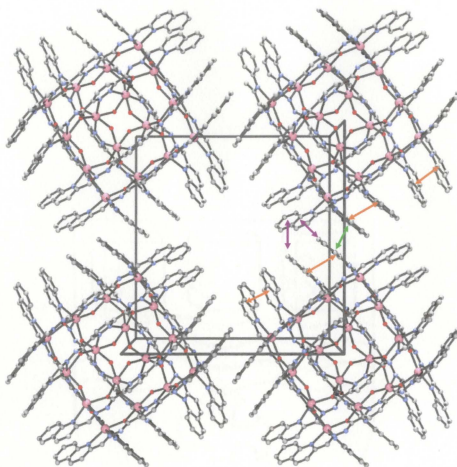


**Figure 7.15:** Ball-and-stick depiction of **7.4**, viewed down the  $c$ -axis ( $0 \leq x \leq 1$ ,  $0 \leq y \leq 1$ ,  $0.75 \leq z \leq 1$ ) showing face-to-face intramolecular (orange arrows), intermolecular (green arrow) and intermolecular edge-to-face (purple arrows)  $\pi$ - $\pi$  interactions.

**Table 7.5:** Selected bond distances (Å) angles (°) and torsion angles (°) for 7.4.

Mn(1) N(7''') 2.150(7)	Mn(3) O(5) 2.077(5)
Mn(1) N(2) 2.176(6)	Mn(3) N(10) 2.185(6)
Mn(1) O(1) 2.250(5)	Mn(3) O(2) 2.214(5)
Mn(1) O(2''') 2.282(5)	Mn(3) O(3) 2.263(5)
Mn(1) N(8''') 2.286(6)	Mn(3) N(5) 2.272(6)
Mn(1) N(1) 2.373(6)	Mn(3) N(9) 2.335(6)
Mn(2) O(5) 2.064(5)	Mn(4) O(7) 2.138(10)
Mn(2) N(15'') 2.183(6)	Mn(4) O(6) 2.144(9)
Mn(2) O(1) 2.215(5)	Mn(4) O(7''') 2.149(10)
Mn(2) N(4) 2.267(6)	Mn(4) O(6''') 2.153(9)
Mn(2) O(4'') 2.302(5)	Mn(4) O(4) 2.193(5)
Mn(2) N(16'') 2.344(6)	Mn(4) O(3) 2.195(5)
	Mn(4) N(12) 2.286(6)
	Mn(4) N(13''') 2.306(6)
Mn(2) O(1) Mn(1) 128.7(2)	
Mn(3''') O(2''') Mn(1) 129.8(2)	
Mn(4) O(3) Mn(3) 124.3(2)	Mn(2) N(4) N(5) Mn(3) 174.9
Mn(4''') O(4'') Mn(2) 126.1(2)	Mn(4) N(12) N(13) Mn(4') 174.7
Mn(2) O(5) Mn(3) 130.8(3)	
Mn(4) O(6) Mn(4') 119.4(5)	
Mn(4) O(7) Mn(4') 119.8(5)	

**7.3.2: Magnetic Properties:**

Compounds 7.1 and 7.4 are Mn(II)<sub>16</sub> grids. As discussed in section 4.3.2, the full matrix calculation on a 45-electron [3×3] Mn(II)<sub>9</sub> problem is not possible because of the immensity of the calculations involved. The same problem arises here in that modeling of the exchange situation cannot be performed in a fully isotropic manner, as this would involve 80 electrons and enormous matrix calculations [55,56]. Therefore, a simpler model that treats the system as a set of four compartmentalized [2×2] Mn<sub>4</sub>-(μ-O<sub>hydrazone</sub>)<sub>4</sub> squares was considered (Figure 7.16).

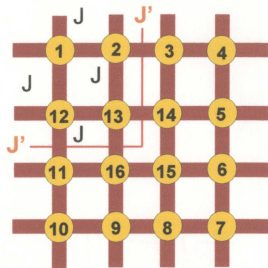


**Figure 7.16:** Magnetic exchange model for a  $4 \times [2 \times 2]$   $M_{16}$  grid.

A Hamiltonian to describe this exchange situation is expressed in equation 7.1.

$$H_{ex} = -J\{S_1 \cdot S_2 + S_2 \cdot S_{13} + S_{13} \cdot S_{12} + S_{12} \cdot S_1\} \quad (7.1)$$

A correction for intramolecular interactions between the  $[2 \times 2]$  subunits *via* the double  $\mu$ -NN<sub>pyridazine</sub>/ $\mu$ -O bridge is included by introducing a molecular field approximation ( $zJ'$ ) [142] into the susceptibility expression (equation 7.2).

$$\chi_{mol} = \frac{N\beta^2 g^2}{3k(T - zJ' \chi_{square})} \frac{\sum S'(S'+1)(2S'+1)e^{-E(S')/kT}}{\sum (2S'+1)e^{-E(S')/kT}} (1 - \rho) + \frac{N\beta^2 g^2 S(S+1)\rho}{3kT} + TIP \quad (7.2)$$

$z$  is the number of adjacent neighbours for each  $[2 \times 2]$  square and  $J'$  is the exchange interaction between adjacent subunits. Variable-temperature magnetic data for 7.1 are shown in Figure 7.17, with a drop in moment from  $21.37 \mu_B$  at 300 K to  $4.63 \mu_B$  at 2 K.

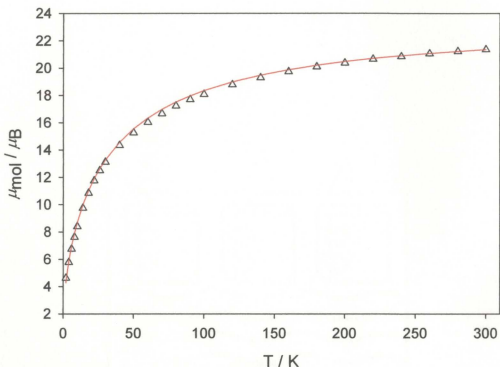


**Figure 7.17:** Variable temperature magnetic data for **7.1**;  $g = 2.0$ ,  $J = -0.04 \text{ cm}^{-1}$ ,  $z = 2$ ,  $J' = -4.0 \text{ cm}^{-1}$ ,  $\rho = 0.014$ ,  $10^2 R = 2.91$ .

The data were fitted to equation 7.2 to give  $g = 2.0$ ,  $J = -0.04 \text{ cm}^{-1}$ ,  $z = 2$ ,  $J' = -4.0 \text{ cm}^{-1}$ ,  $\rho = 0.014$ ,  $10^2 R = 2.91$  ( $R = [\sum(\chi_{\text{obs}} - \chi_{\text{calc}})^2 / \sum \chi_{\text{obs}}^2]^{1/2}$ ). The solid line in Figure 7.17 was calculated with these parameters. The negative sign of both  $J$  and  $J'$  are consistent with the large Mn-O-Mn bond and Mn-NN-Mn torsional angles, leading to the observed antiferromagnetic exchange [28,29,45,70,73,96].

Variable-temperature magnetic data for **7.4** are shown in Figure 7.18, with a drop in moment from  $21.42 \mu_{\text{B}}$  at 300 K to  $4.12 \mu_{\text{B}}$  at 2 K.

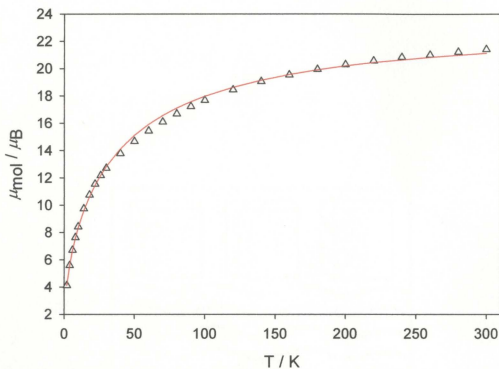


**Figure 7.18:** Variable temperature magnetic data for **7.4**;  $g = 2.0$ ,  $J = -0.35 \text{ cm}^{-1}$ ,  $z = 2$ ,  $J' = -4.25 \text{ cm}^{-1}$ ,  $\rho = 0.019$ ,  $10^2 R = 2.3$ .

The data were fitted to equation 7.2 to give  $g = 2.0$ ,  $J = -0.35 \text{ cm}^{-1}$ ,  $z = 2$ ,  $J' = -4.25 \text{ cm}^{-1}$ ,  $\rho = 0.019$ ,  $10^2 R = 2.3$  ( $R = [\sum(\chi_{\text{obs}} - \chi_{\text{calc}})^2 / \sum \chi_{\text{obs}}^2]^{1/2}$ ). The solid line in Figure 7.18 was calculated with these parameters. The negative sign of both  $J$  and  $J'$  are again consistent with the large Mn-O-Mn bond and Mn-NN-Mn torsional angles, leading to the observed antiferromagnetic behaviour. Despite the  $\pi$ - $\pi$  interactions which organize the grids into an extended lattice motif for **7.4**, no long range magnetic ordering was observed experimentally. It should be noted that for both **7.1** and **7.4**, the approach used to model the magnetic exchange is not rigorous, however, it does provide valuable information about the magnitude of the different exchange couplings in the context of a sensible analysis that is consistent with the X-ray structures.

The X-ray structure of **7.2a** was determined from a single crystal that formed from the solution, while the bulk sample that was collected for magnetic and elemental analysis, **7.2b**, was precipitated from solution 24 hours later. Variable-temperature magnetic data for **7.2b** are shown in Figure 7.19, with a drop in moment from  $15.72 \mu_B$  at 300 K to  $7.54 \mu_B$  at 2 K.

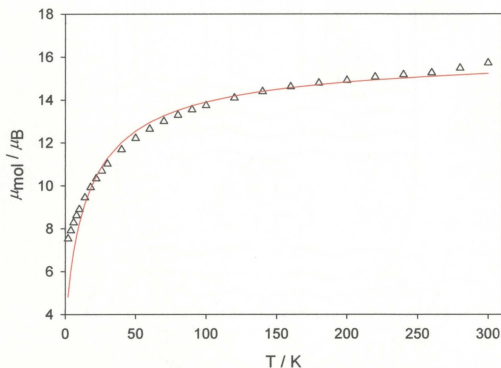


**Figure 7.19:** Variable temperature magnetic data for **7.2b**; solid line calculated with  $g = 2.42$ ,  $J = -0.5 \text{ cm}^{-1}$ ,  $z = 2$ ,  $J' = -1.3 \text{ cm}^{-1}$ ,  $\rho = 0.10$ ,  $\text{TIP} = 800 \times 10^{-6} \text{ cm}^3 \text{ mol}^{-1}$ ,  $10^2 R = 8.38$ .

Typically, the observed magnetic moment per Co(II) centre at 298 K, with orbital contributions is between  $4.3$  and  $5.2 \mu_B$  [147]. Assuming a moment of  $4.8 \mu_B$ , for 16 Co(II) centres, the expected moment at room temperature is  $19.2 \mu_B$ . Further,

extrapolation of the single ion effects from the dinuclear Co(III)/Co(II) complex [(ioap-H)(ioap-2H)Co<sub>2</sub>(H<sub>2</sub>O)<sub>4</sub>](BF<sub>4</sub>)<sub>2</sub> (**3.1**) which contains a single Co(II) centre in an N<sub>2</sub>O<sub>4</sub> coordination sphere, suggests that for a putative Co(II)<sub>16</sub> grid with no exchange, the magnetic moment would scale up to 13.6  $\mu$ B to 18  $\mu$ B in the 2 to 300 K temperature range. Alternately, applying the same reasoning to a putative Co(II)<sub>12</sub>Co(III)<sub>4</sub> grid with no exchange should lead to observed moments between 11.8  $\mu$ B to 15.6  $\mu$ B. Therefore, while the single crystal structure is consistent with all 16 cobalt centres being in the +2 oxidation state, the experimental magnetic data for the bulk sample indicates that some oxidation of the Co(II) centres to diamagnetic Co(III) has taken place. A UV-visible experiment was performed in acetonitrile to confirm the mixed valency of the cobalt cations, however only a single absorption at 411 nm with an extinction coefficient of 19 202 dm<sup>3</sup>mol<sup>-1</sup>cm<sup>-1</sup> was observed. This extinction coefficient far exceeds what would be expected for Laporte forbidden d-d transitions, and is more likely the result of a metal to ligand charge transfer (MLCT). While it is still possible that d-d transitions occurred, the strong MLCT would likely have dominated the absorbance spectrum.

It is not possible to determine directly which cobalt centres are oxidized, however, a reasonable suggestion would be for the more exposed corner sites, with *cis*-CoN<sub>4</sub>O<sub>2</sub> coordination environments. This is consistent with the situation for [3 $\times$ 3] Mn(II)<sub>9</sub> grids, where selective oxidation leads to the corner sites oxidizing to Mn(III) first [30,73,29]. This putative model was therefore tested by assuming Co(III) sites at the corners of the grid (Figure 7.20).

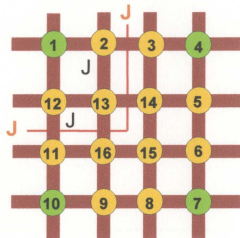


**Figure 7.20:** Magnetic exchange models for a  $4 \times [2 \times 2]$   $\text{Co(II)}_{12}\text{Co(III)}_4$  grid (yellow centres =  $\text{Co(II)}$  with  $S = 3/2$ ; green centres =  $\text{Co(III)}$  with  $S = 0$ ).

Given this situation, **7.2b** can be described as four  $\mu\text{-O}_{\text{hydrazone}}$  bridged trinuclear subunits, with a molecular field correction to account for the interaction between subunits via the double  $\mu\text{-NN}_{\text{pyridazine}}/\mu\text{-O}$  bridges. A Hamiltonian to describe this exchange situation is expressed in equation 7.3.

$$H_{\text{ex}} = -J\{S_2 \cdot S_{13} + S_{13} \cdot S_{12}\} \quad (7.3)$$

A molecular field approximation [142] is introduced into the susceptibility expression in equation 7.4:

$$\chi_{\text{mol}} = \frac{N\beta^2 g^2}{3k(T - zJ' \chi_{\text{trimer}})} \frac{\sum S^i (S^i + 1)(2S^i + 1)e^{-E(S^i)/kT}}{\sum (2S^i + 1)e^{-E(S^i)/kT}} (1 - \rho) + \frac{N\beta^2 g^2 S(S + 1)\rho}{3kT} + \text{TIP} \quad (7.4)$$

Given the enormity of the full matrix calculations for such a model, a full isotropic fit was not attempted. However, a reasonable fit was generated using equation 7.4 with  $g = 2.42$ ,  $J = -0.5 \text{ cm}^{-1}$ ,  $z = 2$ ,  $J' = -1.3 \text{ cm}^{-1}$ ,  $\rho = 0.10$ ,  $\text{TIP} = 800 \times 10^{-6} \text{ cm}^3$

$\text{mol}^{-1}$ ,  $10^2 R = 8.38$  ( $R = [\Sigma(\chi_{\text{obs}} - \chi_{\text{calc}})^2 / \Sigma \chi_{\text{obs}}^2]^{1/2}$ ). The solid line in Figure 7.19 was calculated with these parameters. A good agreement exists above 14 K, but below this temperature the simulation deviates somewhat from the experimental data, likely due to the fact that orbital contributions and zero-field splitting effects have not been accounted for in the exchange model.

The preparation of **7.2** was repeated under a nitrogen atmosphere, resulting in the formation of **7.3**, which is presumed to be a  $4 \times [2 \times 2]$  Co(II)<sub>16</sub> grid, in agreement with the structure of **7.2a**. Its variable-temperature magnetic data are shown in Figure 7.21, with a drop in moment from 17.88  $\mu_{\text{B}}$  at 300 K to 7.28  $\mu_{\text{B}}$  at 2 K.

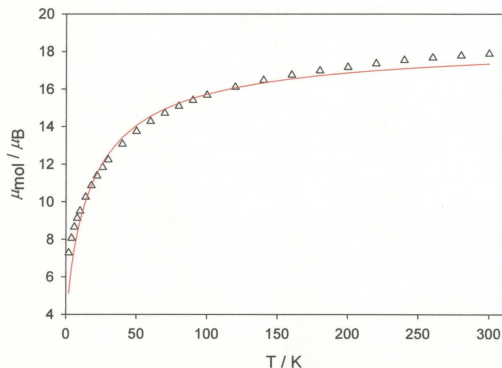


**Figure 7.21:** Variable temperature magnetic data for **7.3**; solid line calculated with  $g = 2.42$ ,  $J = -0.08 \text{ cm}^{-1}$ ,  $z = 2$ ,  $J' = -4.9 \text{ cm}^{-1}$ ,  $\rho = 0.10$ ,  $\text{TIP} = 800 \times 10^{-6} \text{ cm}^3 \text{ mol}^{-1}$ ,  $10^2 R = 7.68$ .

The room temperature moment is much higher than observed for **7.2b**, and is consistent with a  $\text{Co(II)}_{16}$  antiferromagnetically coupled grid, based on the extrapolation at 300 K from **3.2** (*vide supra*). The data were fitted to equation 7.2, with  $g = 2.42$ ,  $J = -0.08 \text{ cm}^{-1}$ ,  $z = 2$ ,  $J' = -4.9 \text{ cm}^{-1}$ ,  $\rho = 0.10$ ,  $\text{TIP} = 800 \times 10^{-6} \text{ cm}^3 \text{ mol}^{-1}$ ,  $10^2R = 7.68$ . The solid line in Figure 7.21 was calculated with these parameters. Again, orbital and zero-field splitting effects have not been included in the magnetic model, and may be the reason for the discrepancy between the experimental and calculated data below 14 K.

#### 7.4: Summary:

$4 \times [2 \times 2]$   $\text{Mn(II)}_{16}$  grids were synthesized by self-assembly reactions between metal salts and 2pdoapm (**2.10**) and 2pdo56hq (**2.11**). These were characterized and found to be structurally similar to previously reported  $\text{Mn(II)}_{16}$  grids [55,56].

The structural characterization of the  $\text{Mn(II)}_{16}$  grids provided the basis for magnetic interpretation and modeling of **7.1** and **7.4**. These grids were treated as compartmental  $[2 \times 2]$   $\text{Mn}_4(\mu\text{-O}_{\text{hydrazone}})_4$  squares with a molecular field correction introduced into the susceptibility expression to account for interactions between the  $[2 \times 2]$  subunits *via* the double  $\mu\text{-NN}_{\text{pyridazine}}/\mu\text{-O}$  bridges.

Intermolecular  $\pi\text{-}\pi$  interactions were observed in the extended lattice motif of **7.4** due to the presence of a quinoline-moiety endpiece. Edge-to-face and face-to-face contacts organized the cations of **7.4** into layers with distances of separation that were consistent with those reported by Janiak [132], though some deviation in the off-set angles was observed. No long-range magnetic ordering was observed despite the extended lattice interactions, though, as discussed in Chapter 6, this is not unexpected due

to the weak nature of  $\pi$ - $\pi$  interactions and long distances between metal centres in neighboring grids.

A  $4 \times [2 \times 2]$   $\text{Co(II)}_{16}$  grid was structurally characterized, however, interpretation of its magnetic properties was hampered by several factors, including the apparent inconsistency between the metal oxidation states in the single crystal of **7.2a** and the bulk sample, **7.2b**. The corner sites of **7.1**, **7.2a** and **7.4** have the same nitrogen-rich *cis*- $\text{MN}_4\text{O}_2$  coordination environment as previously reported  $\text{Mn}_9$  grids that have been shown to be site-specifically sensitive to oxidation [29,30,73], and so it was assumed that these sites were also the most susceptible to oxidation from  $\text{Co(II)}$  to  $\text{Co(III)}$ . An attempt to model the magnetic behaviour of **7.2b** was made based on this assumption. The preparation of **7.2a** was repeated under a nitrogen atmosphere and the magnetic data for this sample, **7.3**, were consistent with the presence of sixteen antiferromagnetically interacting  $\text{Co(II)}$  centres.

## Chapter 8: Homovalent and heterovalent copper complexes from reactions with tetratopic ligands

### 8.1: Preamble:

Tetratopic pyridazine bis(hydrazone) ligands (Figure 8.1) are suitable for use in the synthesis of magnetically active  $4 \times [2 \times 2]$   $M_{16}$  grid-type molecules [55,56], and complexes of this nature with Mn(II), Co(II) and Co(II/III) were discussed in Chapter 7.

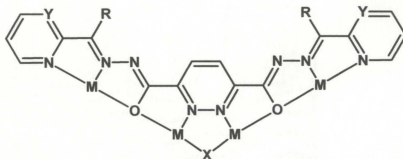


**Figure 8.1:** Tetratopic pyridazine bis(hydrazone) ligands **L1** ( $R = NH_2$ ,  $Y = CH$ ), **L2** ( $R = H$ ,  $Y = CH$ ) and **2pdoapm (2.10)** ( $R = NH_2$ ,  $Y = N$ ), showing metal coordination pockets.

Reaction of **L1** with  $Cu(CH_3COO)_2$  and  $NaBF_4$  lead to the formation of a dodecanuclearcopper(II) grid-like assembly,  $Cu(II)_{12}(L1)_8$  based on an incompletely metalated  $[4 \times 4]$  topology (Figure 8.2) [146].

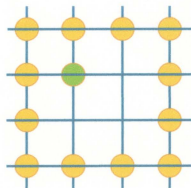
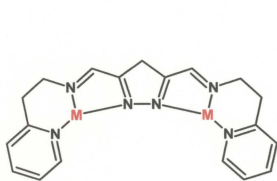


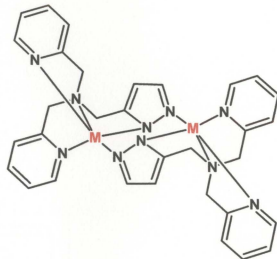
**Figure 8.2:** Representation of a  $\text{Cu(II)}_{12}(\text{L1})_8$  incomplete 'picture frame'; yellow circles = Cu(II), green circle = intercalated  $\text{Na}^+$  ion.

The report for this complex states that while all the Cu(II) centres exhibited axial elongation, the experimental magnetic properties could not be adequately modeled due to the lack crystallographic symmetry, and the possible presence of weak and strong antiferromagnetic coupling, as well as weak to moderate ferromagnetic interactions.

Ligands that incorporate a bis(pyrazolato) moiety exhibit a dinucleating capacity, particularly for Cu(II) metal ions [148-151], and may also prove to be a suitable centre piece for ligands intended to increase  $[n \times n]$  grid nuclearity (where  $n$  is an even integer). For example, de Geest [152] reports an acyclic pyrazolate-containing Schiff-base ligand (Figure 8.3a, **L3**) that leads to the formation of the dinuclear complexes  $[\text{Cu(II)}_2(\text{L3})(\text{H}_2\text{O})_2(\text{CH}_3\text{COO})_3]$  and  $[\text{Cu(II)}_2(\text{L3})(\text{NCS})_2(\text{DMF})]\text{BF}_4$  while Tanase [153] reports the formation of a doubly pyrazolato-bridged dicopper(II) complex,  $[\text{Cu}(\text{L4})_2(\text{ClO}_4)_2 \cdot 2\text{CH}_3\text{CN}]$  from the tripodal ligand **L4** (Figure 8.3b).



(a)



(b)

**Figure 8.3:** The pyrazolate-containing ligands a) **L3** and b) **L4**, each which leads to the formation of dinuclear complexes.

Klinge et al. [154] report a pyrazole-based diamide ligand, (**L5**, Figure 8.4a) that forms  $[2 \times 2]$  (**L5**)<sub>4</sub>M<sub>4</sub> (M = Ni(II) and Cu(II)) and (**L5**)<sub>4</sub>Ni<sub>2</sub>Cu<sub>2</sub> grids (Figure 8.4b). The (**L5**)<sub>4</sub>Cu<sub>4</sub> grid contains copper ions in distorted N<sub>4</sub>O square pyramidal coordination environments, with  $d_{x^2-y^2}$  magnetic ground states and weak antiferromagnetic coupling reported ( $J = -8.2 \text{ cm}^{-1}$ ). A model that explains the observed coupling is discussed based on the overlap of the metal orbitals with pyrazolate-N $\sigma$  orbitals and deviations of the pyrazolate-based perpendicular and coplanar planes with the basal planes of neighboring copper centres, leading to deviations from the expected magnetic orbital orthogonality.

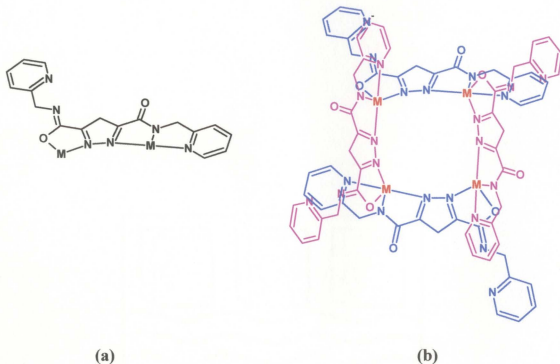


**Figure 8.4:** a) The ligand **L5** which leads to the formation of b)  $[2 \times 2]$  grid-type molecules.

A tetratopic pyrazole bis(hydrazone) ligand, **L6**, has been reported (Figure 8.5a) [56], however, instead of leading to the formation of  $[4 \times 4]$  grids upon reaction with metal salts, as was the case for the analogous pyridazine bis(hydrazone) ligand [55,56], the additional steric constraints of the central pyrazole moiety caused the ligand to twist into its ketonic *syn* conformation (Figure 8.5b), which lead to the formation of a dinuclear Cu(II) complex exhibiting a mixture of five- and six-membered chelate rings.

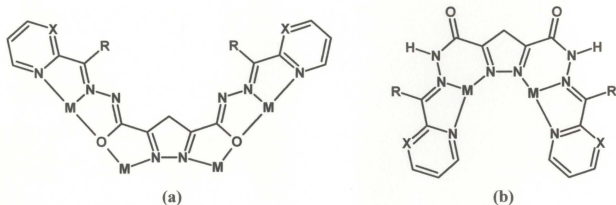


**Figure 8.5:** The ligands **L6** ( $X = \text{CH}$ ,  $R = \text{H}$ ) and **2pyoapm** (**2.9**;  $X = \text{N}$ ,  $R = \text{NH}_2$ ) in a) the tetratopic configuration and b) the dinucleating ketonic *syn* conformation.

The results of reactions between the tetratopic ligands **2pyoapm** (**2.9**; Figure 8.5) and **2pdoapm** (**2.10**; Figure 8.1) with  $\text{Cu(II)}$  salts will be discussed herein. Modeling the magnetic properties of five- and six-coordinate  $\text{Cu(II)}$  complexes is complicated, and the identity and location of ground state magnetic orbitals must be considered when identifying exchange pathways. Particular attention to the orientation of the Jahn-Teller axis is paid in the structural characterizations, and leads to the proposed magnetic models that are presented.

## 8.2: Experimental:

**Note:** In some cases there is a difference between the most reasonable formula based on the elemental analysis (analytical formula), and that obtained from X-ray crystallography. The analytical formulae will be used here.

### 8.2.1: Complex synthesis:

**8.2.1.1:**  $(2\text{pyoapm-H})\text{Cu}_2(\text{ClO}_4)_2(\text{OH})(\text{H}_2\text{O}) \cdot 0.25 \text{CH}_3\text{OH}$  (**8.1**). **2pyoapm** (**2.9**; 0.12 g, 0.30 mmol) was added to a solution of  $\text{Cu}(\text{ClO}_4)_2 \cdot 6\text{H}_2\text{O}$  (0.22 g, 0.59 mmol) in

methanol:acetonitrile:water (10:20:10 mL) producing a clear, green solution. The addition of 5 drops of triethylamine produced a brown solution, which was stirred and heated gently for 18 hours. Upon filtration, a small amount of brown solid was collected and discarded, while the clear green filtrate was kept for crystallization. Blue-green prismatic crystals, suitable for X-ray analysis, formed after the filtrate was left standing for 35 days (yield 0.050 g, 14%). Anal. Calcd (%) for  $(C_{15}H_{13}N_{12}O_2)Cu_2(ClO_4)_2(OH)(H_2O)(CH_3OH)_{0.25}$  (bulk sample): C, 24.03; H, 2.25; N, 22.05. Found (%): C, 24.26; H, 2.03; N, 22.07.

**8.2.1.2:**  $[(2pdoapm-2H)_6(2pdoapm-3H)_2Cu_{16}(O)_2(OH)_4(H_2O)_2](CF_3SO_3)_6 \cdot 66H_2O \cdot 10CH_3OH$  (**8.2**). 2pdoapm (**2.10**; 0.12 g, 0.30 mmol) was added to a solution of  $Cu(CF_3SO_3)_2$  (0.22 g, 0.61 mmol) dissolved in 1:1  $CH_3OH:CH_3CN$  (15 mL). This reaction produced a clear, dark green solution to which aqueous NaOH (4 mL;  $0.65 \text{ mol} \cdot L^{-1}$ ;  $\sim 3 \text{ mmol}$ ) was added to achieve a neutral pH. The resulting dark brown solution was stirred with gentle heating for 24 hours and then filtered. The filtrate was preserved for crystallization. Brown needle-like crystals, suitable for X-ray diffraction, formed upon standing after 12 days (0.030 g, 35% yield). Anal. calcd (%) for  $[(C_{16}H_{12}N_{12}O_2)_6(C_{16}H_{11}N_{12}O_2)_2Cu_{16}(O)_2(OH)_4(H_2O)_2](CF_3SO_3)_6(H_2O)_{66}(CH_3OH)_{10}$ : C, 25.47; H, 4.07; N, 19.81; found: C, 25.24; H, 2.13; N, 19.82.

**8.2.1.3:**  $[(2pdoapm-2H)_8Cu_{16}](CF_3SO_3)_{12} \cdot 24H_2O$  (**8.3**). 2pdoapm (**2.10**; 0.12 g, 0.30 mmol) was added to a solution of  $Cu(CF_3SO_3)_2$  (0.22 g, 0.61 mmol) dissolved in 1:1  $CH_3OH/CH_3CN$  (20 mL). This reaction produced a clear, dark green solution that was stirred with gentle heating for 18 hours. A solution of  $KAg(CN)_2$  (0.06 g, 0.3 mmol) in 5

mL of 1:1 CH<sub>3</sub>OH:H<sub>2</sub>O was then added dropwise over 2 minutes, changing the solution to clear and dark brown. This solution was heated gently in a flask equipped with a condenser, for 48 hours, and for a further 24 hours at room temperature and then filtered. The filtrate was preserved for crystallization. Brown needle-like crystals, suitable for X-ray diffraction, formed upon standing after 4 days (0.090 g, 37 % yield). Anal. calcd (%) for [(C<sub>16</sub>H<sub>12</sub>N<sub>12</sub>O<sub>2</sub>)<sub>8</sub>Cu<sub>16</sub>](CF<sub>3</sub>SO<sub>3</sub>)<sub>12</sub>(H<sub>2</sub>O)<sub>24</sub>: C, 26.00; H, 2.24; N, 20.77; found: C, 26.20; H, 1.76; N, 20.65. UV-Vis:  $\lambda_{\max}(\text{CH}_3\text{CN})/\text{nm}$  402 ( $\epsilon/\text{dm}^3 \text{ mol}^{-1} \text{ cm}^{-1}$  200 192).

### 8.2.2: Crystallography

The diffraction intensities of a light blue, prismatic crystal of **8.1** having approximate dimensions of 0.36 × 0.17 × 0.14 mm were collected on a Rigaku Saturn CCD area detector with graphite monochromated Mo-K $\alpha$  radiation at 113(2) K to a maximum 2 $\theta$  value of 62.5°. The data were corrected for Lorentz and polarization effects and a correction for secondary extinction [81] was applied. The structure was solved by direct methods [82,83] and expanded using Fourier techniques [84]. Hydrogen atoms were introduced in calculated or difference map positions (H(6),H(8), H(19) and H(21)) with isotropic thermal parameters set twenty percent greater than those of their bonding partners. They were refined on the riding model. O(17) and O(30) were refined isotropically, while all other non-hydrogen atoms were refined anisotropically. The model contains two perchlorate anions per formula unit (four are present in the asymmetric unit), of which one is disordered. The occupancy of the corresponding oxygen atoms reflect this disorder. The model also contains 1.8 partial-occupancy water molecules per formula unit as lattice solvent. The occupancy of the oxygen atoms reflect

this partial occupancy. The water protons could not be located in the difference map and hence were omitted from the model. Neutral atom scattering factors and anomalous dispersion effects were taken from the usual sources [85-88]. All calculations were performed using the Crystal Structure [89,90] crystallographic software package except for refinement, which was performed using SHELXL-97 [83].

A brown needle crystal of **8.2** having approximate dimensions of  $0.68 \times 0.15 \times 0.14$  mm was treated similarly to **8.1**. Hydrogen atoms were introduced in difference map (H(4,5,10,11,16,17,22,23 and 25-28) or calculated positions with isotropic thermal parameters set twenty percent greater than those of their bonding partners. They were refined on the riding model, while all other non-hydrogen atoms were refined anisotropically. The Platon [91] Squeeze procedure was applied to recover 427.1 electrons per unit cell in two voids (total volume  $4161.7 \text{ \AA}^3$ ); that is 213.55 electrons per formula unit. Disordered solvent water and acetonitrile appeared to be present prior to the application of Squeeze, though a good point atom model could not be achieved for these. The application of Squeeze gave a good improvement in the data statistics and allowed for a full anisotropic refinement of the framework structure and counterions. Two full-occupancy, disordered triflate anions are present in the asymmetric unit; the occupancies of their oxygen and fluorine atoms reflect this disorder. This leaves an overall charge of -2 missing from the model to achieve charge balance. While the amine protons were all located in the difference map, H(23) appeared significantly lower in the peak list than the other protons. Its occupancy was therefore set to  $\frac{1}{2}$ , which accounts for the charge balance in the symmetry expanded model.

A red-brown prismatic crystal of **8.3** having approximate dimensions of  $0.56 \times 0.45 \times 0.25$  mm was treated similarly to **8.1**. All hydrogen atoms were introduced in calculated positions with isotropic thermal parameters set twenty percent greater than those of their bonding partners. They were refined on the riding model, while all other non-hydrogen atoms in the cationic framework were refined anisotropically. The asymmetric unit contains two triflate anions that were refined anisotropically, except for the carbon atoms C(33) and C(34), which were refined isotropically initially and then also held with fixed thermal parameters in the final round of least squares in order to achieve convergence. The Platon [91] Squeeze procedure was applied to recover 640.9 electrons per unit cell in one void (total volume  $3601.4 \text{ \AA}^3$ ); that is 320.45 electrons per formula unit. An area of disperse electron density was present in the asymmetric unit prior to the application of Squeeze, which is a full occupancy triflate anion, though a good point atom model could not be achieved. This translates to four triflate anions per formula unit (292 electrons). The remaining electron density is attributed to solvent water molecules (28.45 electrons, or 2.8 water molecules). The application of Squeeze gave a good improvement in the data statistics and allowed for a full anisotropic refinement of the cationic framework structure. Abbreviated crystal data for **8.1** - **8.3** are listed in Tables 8.1 and 8.2.

**Table 8.1:** Summary of crystallographic data for **8.1** and **8.2**.

	<b>8.1</b>	<b>8.2</b>
Chemical Formula	C <sub>15</sub> H <sub>16.6</sub> Cl <sub>2</sub> Cu <sub>2</sub> N <sub>12</sub> O <sub>12.8</sub>	C <sub>134</sub> H <sub>144.8</sub> Cu <sub>16</sub> F <sub>18</sub> N <sub>96</sub> O <sub>63.4</sub> S <sub>6</sub>
M	767.77	5665.49
T(K)	113(2)	113(2)
Crystal System	triclinic	orthorhombic
Space Group	P $\bar{1}$ (#2)	Pmmn (#59)
a (Å)	12.180(6)	25.797(2)
b (Å)	14.450(6)	29.199(2)
c (Å)	16.120(7)	16.5920(13)
$\alpha$ (°)	68.36(5)	90.00
$\beta$ (°)	77.37(4)	90.00
$\gamma$ (°)	75.81(5)	90.00
V (Å <sup>3</sup> )	2531(2)	12497.5(18)
Z	4	2
D <sub>calc</sub> (g/cm <sup>3</sup> )	2.013	1.505
$\mu$ (MoK $\alpha$ ) (cm <sup>-1</sup> )	19.83	14.82
Reflections Total	21786	56226
Reflections Unique	9766	12804
R <sub>int</sub>	0.0789	0.0318
R <sub>1</sub> ( <i>I</i> > 2.00 $\sigma$ ( <i>I</i> ))	0.1204	0.0639
wR <sub>2</sub> (All reflections)	0.3189	0.1825

**Table 8.2:** Summary of crystallographic data for **8.3**.

	<b>8.3</b>
Chemical Formula	$C_{140}H_{101.6}Cu_{16}F_{36}N_{96}O_{54.8}S_{12}$
M	6090.75
T(K)	138(2)
Crystal System	tetragonal
Space Group	$P4_2/n$ (#86)
a (Å)	23.579(3)
b (Å)	23.579(3)
c (Å)	22.196(2)
$\alpha$ (°)	90.00
$\beta$ (°)	90.00
$\gamma$ (°)	90.00
V (Å <sup>3</sup> )	12341(2)
Z	2
D <sub>calc</sub> (g/cm <sup>3</sup> )	1.639
$\mu$ (MoK $\alpha$ ) (cm <sup>-1</sup> )	15.63
Reflections Total	26597
Reflections Unique	11965
R <sub>int</sub>	0.0335
R <sub>1</sub> ( $I > 2.00\sigma(I)$ )	0.1133
wR <sub>2</sub> (All reflections)	0.3400

### 8.3: Results and Discussion:

**Note:** The crystallographically determined formulae are used herein. Colour code for figures: green = copper, grey = carbon, blue = nitrogen, red = oxygen, yellow = chlorine. Crystallographic representations/illustrations were generated using Persistence of Vision Ray Tracer (POV-Ray©) for Windows, version 3.6, with scene description files written by Ortep-3 for Windows (Version 1.08) Copyright© 1997-2003 Louis J. Farrugia.

8.3.1: Description of crystal structures and magnetic properties:

#### 8.3.1.1: $[(2\text{pyoapm-H})\text{Cu}(\text{OH})](\text{ClO}_4)_2 \cdot 1.6\text{H}_2\text{O}$ (**8.1**)

The structure of the cationic fragment of **8.1** is shown in Figure 8.6, and significant bond lengths and angles are listed in Table 8.3.

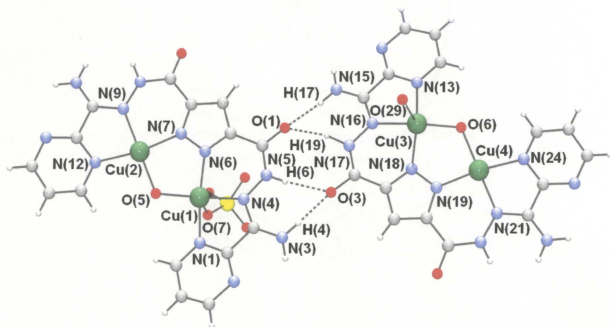


**Figure 8.6:** Ball-and-stick depiction of the cationic moiety **8.1**.

The asymmetric unit of **8.1** contains two  $L_1\text{Cu}(\text{II})_2$  ( $L = 2\text{pyoapm-H}$ ) dinuclear cationic moieties, with ligands in the ketonic *cis* conformation, and the hydrazone oxygens locking the two cations together through hydrogen bonding at the external, non-

coordinated O-N<sub>diazine</sub>-N<sub>amine</sub> groups (Figure 8.6; O(1)-H(17), O(1)-H(16), O(3)-H(6) and O(3)-H(4)). N-O distances fall in the range of 2.765(14)-2.886(11) Å, with four such connections between each dinuclear centre. In each cation the two copper ions are bridged by the central pyrazole group, and by a second, adventitious hydroxide bridge (O(5) and O(6)) and are bound by tridentate N<sub>3</sub> coordination pockets, with a mixture of five- and six-membered chelate rings. In each moiety, one copper (Cu(2) and Cu(4)) is in an entirely ligand based square planar geometry, while the second copper is in a square pyramidal environment, with one long bond to the oxygen of a perchlorate anion (Cu(1) - O(7), 2.263(8) Å), or to a water molecule (Cu(3) - O(29) 2.292(8) Å) with shorter remaining bonds (1.879(7) -1.969(8) Å). Cu-Cu distances are 3.2446(17) Å (Cu(1)-Cu(2)) and 3.2540(17) Å (Cu(2)-Cu(3)), with corresponding Cu-OH-Cu angles of 117.9(3)<sup>o</sup> and 118.7(3)<sup>o</sup> and almost planar Cu -NN<sub>pyrazole</sub>-Cu torsion angles of 172.0<sup>o</sup> and 171.6<sup>o</sup> respectively.

The hydrogen-bonding in **8.1** extends to create flat bifurcated chains of Cu(II)<sub>2</sub> subunits (Figure 8.7). These chains are organized into closely packed layers (Figure 8.8a and b), with separation between layers of approximately 3.9 Å.

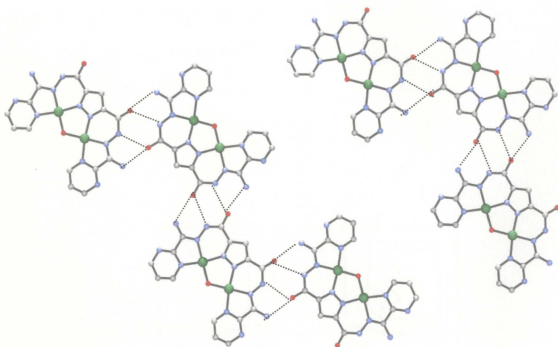


**Figure 8.7:** Bifurcated chains of  $\text{Cu(II)}_2$  subunits in **8.1**.

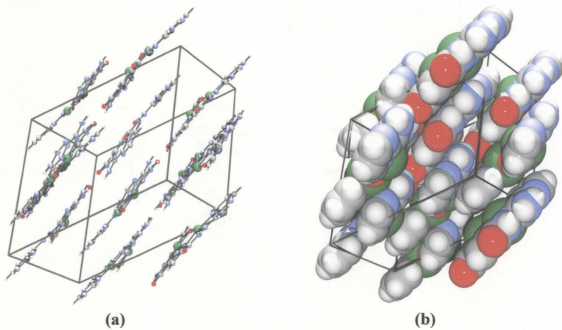


**Figure 8.8:** a) Ball-and-stick model of the unit cell of **8.1**, showing the layered arrangement of cations; b) van der Waals representation showing the close packing between layers.

The variable-temperature magnetic data for compound **8.1** are shown in Figure 8.9, with a drop in moment from 1.81  $\mu_B$  per (Cu(II))<sub>2</sub> at 300 K to 0.46  $\mu_B$  at 2 K.

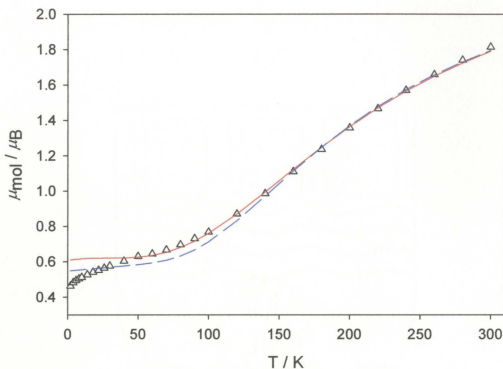


**Figure 8.9:** Variable temperature magnetic data for **8.1**; dashed blue line (dinuclear model)  $g = 2.02(4)$ ,  $J = -357(12) \text{ cm}^{-1}$ ,  $\text{TIP} = 100 \times 10^{-6} \text{ cm}^3 \text{ mol}^{-1}$ ,  $\rho = 0.05$ ,  $\theta = -3.8 \text{ K}$ ,  $10^2 R = 3.8$ ; solid red line (alternating chain model)  $g = 2.07$ ,  $J = -187 \text{ cm}^{-1}$ ,  $\alpha = 0.2$ ,  $\text{TIP} = 50 \times 10^{-6} \text{ cm}^3 \text{ mol}^{-1}$ ,  $\rho = 0.04$ ,  $\theta = -4 \text{ K}$ ,  $10^2 R = 1.6$ .

A Hamiltonian that describes the exchange situation as a simple dinuclear system (with  $S = \frac{1}{2}$  for Cu(II)) is expressed in equation 8.1.

$$H_{ex} = -J\{S_1 \cdot S_2\} \quad (8.1)$$

The data were fitted using MAGMUN4.1 [49] to give  $g = 2.02(4)$ ,  $J = -357(12)$   $\text{cm}^{-1}$ ,  $\text{TIP} = 100 \times 10^{-6} \text{ cm}^3 \text{ mol}^{-1}$ ,  $\rho = 0.05$ ,  $\theta = -3.8 \text{ K}$ ,  $10^2 R = 3.8$  ( $R = [\Sigma(\chi_{\text{obs}} - \chi_{\text{calc}})^2 / \Sigma \chi_{\text{obs}}^2]^{1/2}$ ). The dashed blue line in Figure 8.9 was calculated with these parameters. The sign and magnitude of the coupling constant,  $J$ , is consistent with those reported for similar dinuclear pyrazole-bridged Cu(II) systems (Figure 8.5) [56], however, the model does not produce a good fit below 120 K and gives an unusually low fitted value for  $g$ . For these reasons, and given the significant hydrogen bonding interactions between the dinuclear units that was evident from the structural analysis, an alternating chain model [155,156] was tested. The exchange Hamiltonian for this model is expressed in equation 8.2 (with the exchange coupling defined here as  $2J$ ), and the total spin states ( $S'$ ) and their energies ( $E(S')$ ) were again substituted into the Van Vleck equation (equation 8.2).

$$H_{\text{ex}} = -2[J\{S_i \cdot S_{i+1}\} + \alpha J\{S_{i+1} \cdot S_{i+2}\}] \quad (8.2)$$

The susceptibility equation was derived (see Appendix 2) and the data were fitted to give  $g = 2.07$ ,  $J = -187 \text{ cm}^{-1}$ ,  $\alpha = 0.2$ ,  $\text{TIP} = 50 \times 10^{-6} \text{ cm}^3 \text{ mol}^{-1}$ ,  $\rho = 0.04$ ,  $\theta = -4 \text{ K}$ ,  $10^2 R = 1.6$  ( $R = [\Sigma(\chi_{\text{obs}} - \chi_{\text{calc}})^2 / \Sigma \chi_{\text{obs}}^2]^{1/2}$ ). The solid red line in Figure 8.9 was calculated with these parameters and clearly represents an improvement in the fitting over the simple dinuclear model, especially at lower temperatures. This exchange model should not be considered rigorous, especially in light of the high number of fitted parameters, and the deviation between the experimental data and the fitted line below 40 K, however, it does support the suggestion that the extended hydrogen-bonded structure influences the

overall exchange and provides a pathway for weak magnetic exchange between the dinuclear moieties.

**Table 8.3:** Selected bond distances (Å) angles (°) and torsion angles (°) for **8.1**.

Cu(1) O(5)	1.903(7)	Cu(3) O(6)	1.879(7)
Cu(1) N(6)	1.918(8)	Cu(3) N(18)	1.911(8)
Cu(1) N(1)	1.947(8)	Cu(3) N(13)	1.954(8)
Cu(1) N(4)	1.963(8)	Cu(3) N(16)	1.969(8)
Cu(1) O(7)	2.263(8)	Cu(3) O(29)	2.292(8)
Cu(2) O(5)	1.883(7)	Cu(4) O(6)	1.903(7)
Cu(2) N(7)	1.922(8)	Cu(4) N(19)	1.923(8)
Cu(2) N(12)	1.950(8)	Cu(4) N(24)	1.951(8)
Cu(2) N(9)	1.960(9)	Cu(4) N(21)	1.956(8)
O(1) N(15)	2.881(15)	Cu(1) Cu(2)	3.2446(17)
O(1) N(17)	2.885(12)	Cu(3) Cu(4)	3.2540(17)
O(3) N(3)	2.765(14)		
O(3) N(5)	2.886(11)		
Cu(2) O(5)	Cu(1) 117.9(3)	Cu(1) N(6) N(7)	Cu(2) 172.0
Cu(3) O(6)	Cu(4) 118.7(3)	Cu(3) N(18) N(19)	Cu(4) 171.6

**8.3.1.2:** [(2pdoapm-2H)<sub>6</sub>(2pdoapm-3H)<sub>2</sub>Cu<sub>16</sub>O<sub>2</sub>(OH)<sub>4</sub>(H<sub>2</sub>O)<sub>2</sub>](CF<sub>3</sub>SO<sub>3</sub>)<sub>6</sub>·21.4H<sub>2</sub>O (**8.2**)

The structure of the cationic fragment of **8.2** and its unit cell and the bifurcated Cu-O core are shown in Figure 8.10a, 8.10b and 8.10c respectively, and significant bond lengths and angles are listed in Table 8.4.

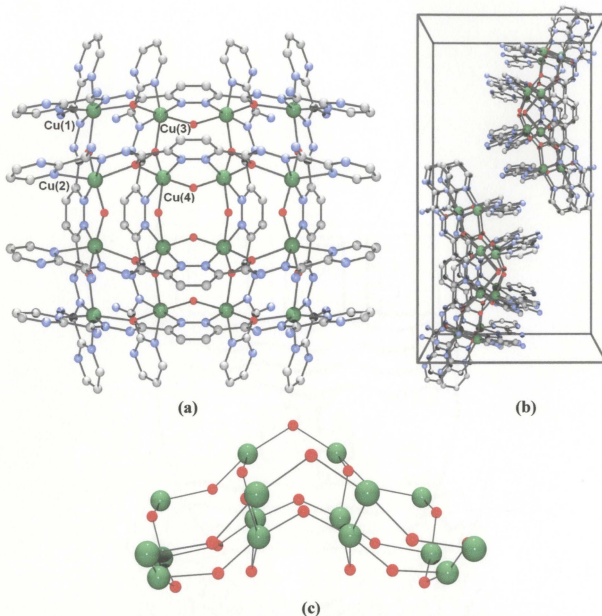


**Figure 8.10:** a) Ball-and-stick depiction of the cationic moiety **8.2**. Hydrogen atoms omitted for clarity. b) The unit cell of **8.2**, looking down the *a*-axis; anions omitted for clarity. c) Bifurcation of the M-O core in **8.2**.

The crystal structure of **8.2** reveals sixteen six-coordinate Cu(II) ions in what can best be described as an arrangement of four  $[2 \times 2]$   $\text{Cu}_4-(\mu\text{-O}_{\text{hydrazone}})_4$  moieties organized into a square cationic framework (Figure 8.10a), with eight 2pdoapm ligands, arranged in

an approximately parallel manner, with four above and four below a puckered (Figure 8.10c) metal pseudoplane. The puckering of the metal core is expected due to the bending of the ligand arms (end-pieces) relative to the pyridazine central group (Figure 8.1). Each  $\text{Cu}_4-(\mu\text{-O}_{\text{hydrazone}})_4$  subunit is bridged to two adjacent subunits by a combined  $\mu\text{-NN}_{\text{pyridazine}}/\mu\text{-O}$  double bridge, in which the oxygen is from an exogenous (solvent) source (Figure 8.11).

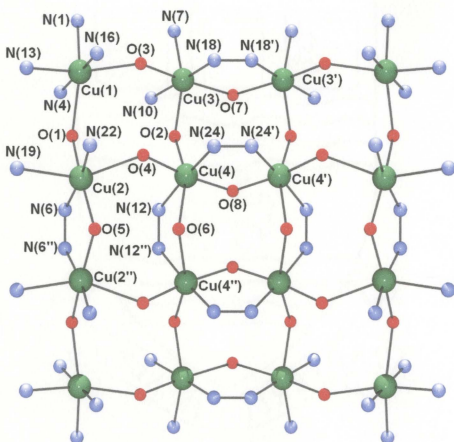


**Figure 8.11:** Ball-and-stick depiction of the core structure of **8.2**.

The presence of sixteen Cu(II) centres means that a cationic charge of +32 must be balanced. Six well-defined lattice triflate ( $\text{CF}_3\text{SO}_3^-$ ) anions are present, and each ligand bears a charge of at least -2 based on the normal loss of protons from the

hydrazone oxygen atoms, accounting for a charge of -22. The identity of the exogenous oxygen bridges must now be considered. Single protons were located in difference map positions on O(5) and O(6), and so these were assigned as hydroxide ions, while two protons were located on O(7) and none were located on O(8), making these a water and an oxide bridge, respectively. These bridges account for an additional charge of -8 per formula unit. Finally, amine protons (H(4,5,10,11,16,17,22 and 23)) were located in difference map positions, however, H(23) was significantly lower in the peak list, and so its occupancy was assigned as one half, accounting for the final charge of -2, required for overall neutrality. The presence of hydroxide and oxide bridges, as well as the partial deprotonation of one of the ligand amine groups is reasonable since hydroxide formation as a bridge in reactions of pyridazine-based ligands is common [157,158] and because base was added during the synthesis of **8.2**.

Cu-Cu distances mediated only by  $\mu$ -O bridges fall in the range 3.9232(7) - 4.1124(7) Å, with Cu-O-Cu angles in the range 131.38(12) - 140.37(15)°, while distances between copper centres that are doubly  $\mu$ -O/ $\mu$ -NN bridged fall in the range 3.3635(7) - 3.7286(7) Å, with Cu-O-Cu angles in the range 96.91(14) - 123.84(19)° and Cu-NN-Cu torsion angles of 180.0°. The overall molecular dimensions for **8.2** involve a square cation approximately  $19 \times 19 \text{ \AA}^2$  with a metallic core measuring  $10.8 \times 11.1 \text{ \AA}^2$ . Figure 8.12 shows the asymmetric unit of **8.2**, a  $[2 \times 2] \text{ Cu}_4-(\mu\text{-O}_{\text{hydrazone}})_4$  moiety, that is reflected by mirror plane symmetry (space group Pmmn) to generate the full grid assembly. Cu(1) has a *cis*- $\text{CuN}_4\text{O}_2$  coordination environment, and exhibits a Jahn-Teller compressed geometry ( $d_{z^2}$  magnetic ground state), as defined by two short axial contacts

to N(4) and N(16) (1.919(4) and 1.932(4) Å), and longer equatorial contacts (2.179(4) - 2.254(3) Å). Cu(2) and Cu(3) have *mer*-CuN<sub>3</sub>O<sub>3</sub> environments, and exhibit Jahn-Teller elongation ( $d_{x^2-y^2}$  magnetic ground states), with long axial contacts to N(19) and O(4) (2.324(3) and 2.467(4) Å) for Cu(2) and to O(3) and O(7) (2.134(4) and 2.250(2) Å) for Cu(3), with shorter remaining equatorial Cu - L distances (1.920(4) - 2.164(4) Å). Cu(4) has a *trans*-CuN<sub>2</sub>O<sub>4</sub> coordination environment and also exhibits Jahn-Teller elongation ( $d_{x^2-y^2}$  magnetic ground state), with long contacts to O(2) and O(6) (2.193(3) and 2.451(2) Å), and shorter remaining Cu - L bond distances (1.9255(18) - 2.080(3) Å).

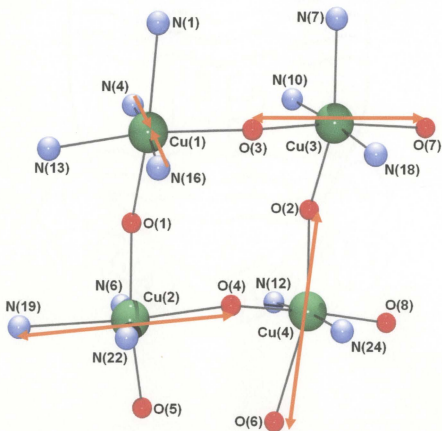


**Figure 8.12:** The asymmetric unit of 8.2; arrows highlight the Jahn-Teller axes.

The orthogonal arrangement of the axially elongated Jahn-Teller axes for Cu(2), Cu(3) and Cu(4) means that only ferromagnetic exchange should be expected between these centres. Since Cu(1) exhibits a  $d_{z^2}$  magnetic ground state, however, some limited antiferromagnetic exchange *via* the  $\mu\text{-O}_{\text{hydrazone}}$  bridge might be expected between Cu(1) and Cu(2).

Bridging between Cu(3)-Cu(3'), Cu(4)-Cu(4'), Cu(4)-Cu(4'') and Cu(2)-Cu(2'') (Figure 8.11) involves a combination of both  $\mu\text{-O}_{\text{hydrazone}}/\mu\text{-NN}_{\text{pyridazine}}$  connections. For these, the Cu(3)-O(7)-Cu(3') and Cu(4)-O(6)-Cu(4'') connections are orthogonal, but the Cu(3)-N(18)-N(18')-Cu(3') and Cu(2)-N(12)-N(12'')-Cu(4'') connections are not, and so antiferromagnetic exchange should dominate the exchange situation between these centres, *via* the  $\mu\text{-NN}_{\text{pyridazine}}$  bridges. The Cu(2)-O(5)-Cu(2''), Cu(2)-N(6)-N(6'')-Cu(2''), Cu(2)-O(8)-Cu(4'), and Cu(4)-N(24)-N(24')-Cu(4') connections are all non-orthogonal, and again antiferromagnetic exchange should be observed, however, between these metal centres, two possible exchange pathways are present, and the magnitude of the exchange may be expected to be larger than between the centres with only one non-orthogonal connection.

The variable temperature magnetic data (molar magnetic moment and susceptibility) for **8.2**, a  $4 \times [2 \times 2]$  Cu(II)<sub>16</sub> grid, are shown in Figure 8.13. The moment drops from  $6.6 \mu_B$  at 300 K to a slight minimum of  $3.7 \mu_B$  around 10 K, before dropping slightly below this temperature, which clearly indicates that the dominant magnetic interactions are antiferromagnetic. Significant residual spin is present in the ground state, and approximates the presence of four uncompensated Cu(II) centres. A change of slope

is observed in the experimental data at approximately 50 K, and suggests that more than one exchange pathway with couplings of significantly different magnitudes are present, which is consistent with the complex bridging connectivities that were revealed from the structure.

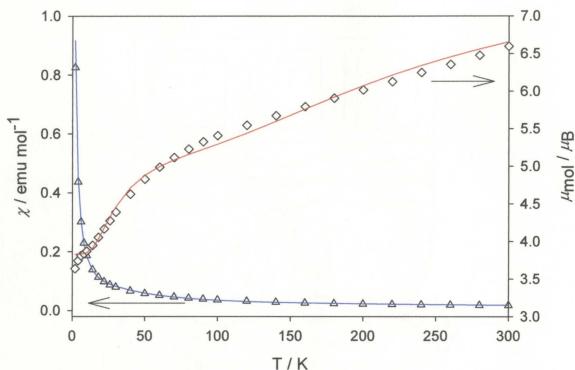


**Figure 8.13:** Variable temperature magnetic data for **8.2**.  $\chi$  represented by triangles;  $\mu$  represented by diamonds; solid lines calculated from fitted values of  $g_{ave} = 2.21$ ,  $J_1 = -45 \text{ cm}^{-1}$ ,  $J_2 = -350 \text{ cm}^{-1}$ ,  $TIP = 800 \times 10^{-6} \text{ cm}^3 \text{ mol}^{-1}$ ,  $10^2 R = 2.3$ .

Figure 8.12 shows the orientation of the elongated Jahn-Teller axis for Cu(2), Cu(3) and Cu(4) leading to  $d_{x^2-y^2}$  magnetic ground states and magnetic orbital orthogonality. Each of the  $[2 \times 2]$  subunits has these orthogonal connections (between Cu(2) - Cu(4), Cu(4) - Cu(3), and Cu(3) - Cu(1)) with the possibility of very weak antiferromagnetic coupling between Cu(1) ( $d_{z^2}$  magnetic ground state) and Cu(2) via the

non-orthogonal connection. It will be assumed that on the basis of the strong, experimentally observed antiferromagnetic exchange, however, that this weak exchange is negligible and that the corner Cu(1) sites is effectively magnetically isolated.

Next, the connections between the  $[2 \times 2]$  subunits *via* the  $\mu$ -O and  $\mu$ -NN bridges must be considered by taking into account the orthogonality situation and the molecular symmetry. A spin-exchange model that represents these contributions is shown in Figure 8.14.

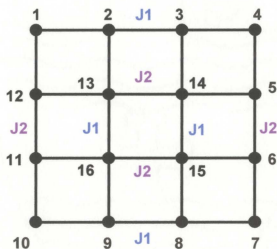


**Figure 8.14:** A spin-exchange model for 8.2; J1 = antiferromagnetic coupling *via* pyridazine  $\mu$ -NN only; J2 = antiferromagnetic coupling *via* both  $\mu$ -NN and  $\mu$ -O bridges.

This model can be divided into four magnetic groups, some of which contribute significantly to the observed variable temperature data, while others do not. First, the four corner sites, 1, 4, 7 and 10 (Figure 8.14) are considered to be isolated centres, thus representing Curie contributions. Second, the connections 2-13, 3-14, 5-14, 6-15, 8-15, 9-16, 11-16, and 12-13 are orthogonal (Figure 8.12 and 8.14), and any resulting weak ferromagnetic exchange will be overshadowed by much stronger antiferromagnetic

exchange components. Next, the connections between 2-3, 14-15, 8-9 and 13-16 consist of double  $\mu$ -NN/ $\mu$ -O bridges (Figure 8.11 and 8.14). The orbital connections *via* the  $\mu$ -O pathways are orthogonal, while those *via* the  $\mu$ -NN pathway are non-orthogonal (Figure 8.12) and should contribute significantly to the observed antiferromagnetic exchange. This exchange coupling is represented by the term J1 (Figure 8.14). Finally, the connections between 5-6, 11-12, 13-14 and 15-16 also consist of double  $\mu$ -NN/ $\mu$ -O bridges (Figure 8.11 and 8.14), however, here both pathways are non-orthogonal, and should contribute significantly to the overall antiferromagnetic exchange. These double bridges are assigned one exchange coupling constant, J2 (Figure 8.14), which encompasses the contribution *via* both the  $\mu$ -NN and  $\mu$ -O pathways, and is therefore expected to be significantly larger in magnitude than J1. The exchange can therefore be modeled as the sum of four dinuclear terms and one tetranuclear term, as defined by the exchange Hamiltonian given in equation 8.3.

$$H_{ex} = -J1\{S_2 \cdot S_3 + S_8 \cdot S_9\} - J2\{S_5 \cdot S_6 + S_{11} \cdot S_{12}\} - [J1\{S_{13} \cdot S_{16} + S_{14} \cdot S_{15}\} + J2\{S_{13} \cdot S_{14} + S_{15} \cdot S_{16}\}] \quad (8.3)$$

Exchange equations were written for the dinuclear and tetranuclear components which were then factored and combined with a Curie correction for the four isolated corner sites and a correction for TIP (see Appendix 2). The experimental data were then fitted to the susceptibility expression to give  $g_{ave} = 2.21$ ,  $J1 = -45 \text{ cm}^{-1}$ ,  $J2 = -350 \text{ cm}^{-1}$ ,  $TIP = 800 \times 10^{-6} \text{ cm}^3 \text{ mol}^{-1}$ ,  $10^2 R = 2.3$  and the solid lines in Figure 8.13 were calculated with these values. As predicted from the model the magnitude of J2 is significantly

larger than that of  $J_1$ , and both values are in agreement with magnetic couplings reported for compounds with similar exchange pathways. As a comparison, the dinuclear complex  $[\text{Cu}_2(\text{PPD})\text{Cl}_4]$  [159], exhibits magnetic exchange *via* a single pyridazine bridge, with an exchange coupling of  $-65 \text{ cm}^{-1}$ , in agreement with the magnitude and the exchange environment for  $J_1$  in this model. For compounds with double  $\mu\text{-NN}_{\text{pyridazine}}/\mu\text{-OH}$  bridges between Cu(II) centres, antiferromagnetic exchange coupling with magnitudes between  $375\text{-}450 \text{ cm}^{-1}$  have been reported [157,158], also in agreement with the magnitude and the exchange environment for  $J_2$  in this model.

A final piece of experimental evidence that supports the proposed model comes from the magnetization data which show a rise to a value of  $4.4 \text{ N}\beta$  at 5 T (Figure 8.15), with no evidence for saturation. The profile is consistent for a ground-state system with the sum of four independent  $S=1/2$  centres (Figure 8.15; solid line), corresponding to the four isolated corner sites in **8.2**.

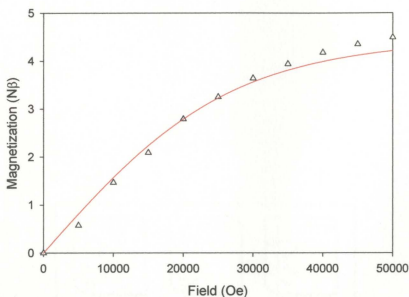


**Figure 8.15:** Variable field magnetization data for **8.2**;  $g = 2.21$ ,  $T = 2$  K,  $S' = 4 \times \frac{1}{2}$ .

**Table 8.4:** Selected bond distances (Å) angles ( $^{\circ}$ ) and torsion angles ( $^{\circ}$ ) for **8.2**.

Cu(1) N(16)	1.919(4)	Cu(3) N(10)	1.920(4)			
Cu(1) N(4)	1.932(4)	Cu(3) N(18)	2.040(4)			
Cu(1) N(13)	2.179(4)	Cu(3) O(2)	2.098(3)			
Cu(1) N(1)	2.223(4)	Cu(3) O(3)	2.134(4)			
Cu(1) O(3)	2.237(4)	Cu(3) N(7)	2.164(4)			
Cu(1) O(1)	2.254(3)	Cu(3) O(7)	2.250(2)			
Cu(2) O(5)	1.9459(18)	Cu(4) O(8)	1.9255(18)			
Cu(2) N(22)	1.990(3)	Cu(4) O(4)	1.979(3)			
Cu(2) N(6)	2.004(3)	Cu(4) N(24)	1.993(3)			
Cu(2) O(1)	2.042(3)	Cu(4) N(12)	2.080(3)			
Cu(2) O(4)	2.324(3)	Cu(4) O(2)	2.193(3)			
Cu(2) N(19)	2.467(4)	Cu(4) O(6)	2.451(2)			
Cu(2) O(1)	Cu(1)	139.96(14)	Cu(2) N(6)	N(6'')	Cu(2'')	180.0
Cu(3) O(2)	Cu(4)	139.44(14)	Cu(4) N(12)	N(12'')	Cu(4'')	180.0
Cu(3) O(3)	Cu(1)	140.37(15)	Cu(3) N(18)	N(18')	Cu(3')	180.0
Cu(4) O(4)	Cu(2)	131.38(12)	Cu(4) N(24)	N(24')	Cu(4')	180.0
Cu(2) O(5)	Cu(2'')	123.84(19)				
Cu(4) O(6)	Cu(4'')	96.91(14)				
Cu(3) O(7)	Cu(3')	111.92(18)				
Cu(4) O(8)	Cu(4')	121.00(19)				

### 8.3.1.3: $[(2\text{pdoapm}-2\text{H})_8\text{Cu}_{16}](\text{CF}_3\text{SO}_3)_{12}\cdot 2.8\text{H}_2\text{O}$ (**8.3**)

The structure of the cationic fragment of **8.3** and its unit cell are shown in Figures 8.16a and 8.16b respectively, and significant bond lengths and angles are listed in Table 8.5.

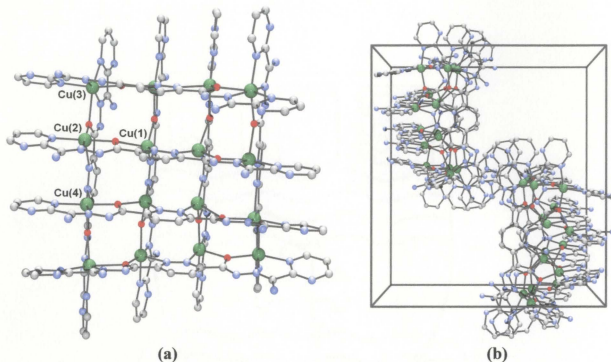


**Figure 8.16:** a) Ball-and-stick depiction of the cationic moiety **8.3**. Hydrogen atoms omitted for clarity. b) The unit cell of **8.3**, looking down the a-axis; anions omitted for clarity.

The structure of **8.3** is similar to that of **8.2** in that it reveals eight ligands encompassing sixteen copper ions in an arrangement of four  $[2 \times 2]$   $\text{Cu}_4-(\mu\text{-O}_{\text{hydrazone}})_4$  moieties. No exogenous oxygen atoms are present, however, and instead each  $\text{Cu}_4-(\mu\text{-O}_{\text{hydrazone}})_4$  subunit is bridged to two adjacent subunits by  $\mu\text{-NN}_{\text{pyridazine}}$  bridges only (Figure 8.17). During the experimental preparation, base was omitted, but instead  $\text{KAg}(\text{CN})_2$  was added. This was done in an attempt to replace the adventitious secondary

bridging oxygen atoms, present in **8.2**, with  $\text{Ag}(\text{CN})_2^-$  anions that could possibly then link two grids together via a  $\text{Cu}_{\text{grid A}}-\text{N}-\text{C}-\text{Ag}-\text{C}-\text{N}-\text{Cu}_{\text{grid B}}$  motif. Instead, however, this resulted in an unusual redox reaction and the formation of a mixed oxidation state  $\text{Cu}(\text{II})_{12}\text{Cu}(\text{I})_4$  grid (*vide infra*). The absence of secondary oxygen bridges may therefore be the result, aided by the ability of copper to adopt coordination numbers of 4, 5 and 6, negating the requirement for extra ligands to fill vacant coordination sites.

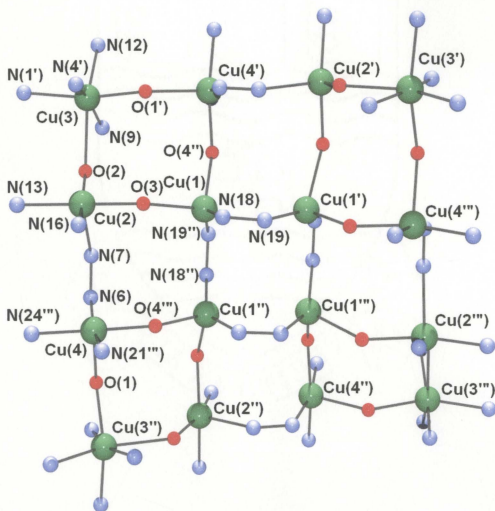


**Figure 8.17:** Ball-and-stick depiction of the core structure of **8.3**.

Cu-Cu distances mediated by  $\mu$ -O bridges fall in the range 3.8999(13) - 3.9943(13) Å, with Cu-O-Cu angles in the range 131.1(3) - 140.1(3)<sup>o</sup>, while distances between copper centres that are  $\mu$ -NN bridged fall in the range 3.3171(13) - 3.8575(13) Å, with Cu-NN-Cu torsion angles of 165.6 and 173.8<sup>o</sup>. The metallic core dimensions for **8.2** are approximately 10.92 × 10.92 Å<sup>2</sup>.

Figure 8.18 depicts a quarter of the metallic grid core, and clearly shows the coordination environment of the four unique copper centres. Cu(1) and its symmetry related counterparts are four-coordinate with N<sub>2</sub>O<sub>2</sub> environments and distorted tetrahedral geometry (L-Cu(1)-L angles 71.5(2) - 145.5(2)<sup>o</sup>). Cu(2), Cu(4) and their symmetry related centres have N<sub>3</sub>O<sub>2</sub> coordination environment and slightly distorted square-pyramidal geometries ( $\tau_{\text{Cu}(2)} = 0.13$ ;  $\tau_{\text{Cu}(4)} = 0.12$  [94]), while Cu(3) and its symmetry related atoms are distorted octahedral and *cis*-CuN<sub>4</sub>O<sub>2</sub> coordinated. BVS values [92] for Cu(2), Cu(3) and Cu(4) are 1.39, 1.42, 1.45 respectively, while for Cu(1) the value is 0.65. While these numbers do not agree with expected integer values, the large difference between Cu(1) and the other copper atoms clearly reflects the presence of different metal oxidation states. Comparable values for corner, side and centre six-coordinate sites in **4.6**, a [3×3] Cu(II)<sub>9</sub> grid, are 1.40, 1.38 and 1.30 respectively and therefore, Cu(2), Cu(3) and Cu(4) are assigned an oxidation state of +2, while Cu(1) is in the +1 oxidation state. The assignment of Cu(1) as +1 is also consistent with the unusual tetrahedral geometry observed for these centres. This gives a charge of +28 from the metal ions that must be balanced. Each ligand is presumed to have the normal charge of

-2, and twelve well-defined  $\text{CF}_3\text{SO}_3^-$  anions are present, therefore the overall charge is balanced in agreement with the assignment of the metal oxidation states.

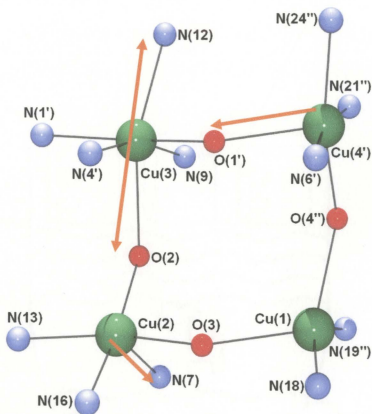


**Figure 8.18:** One-quarter of the cationic core of **8.3**; arrows highlight the Jahn-Teller axes.

Cu(2) and Cu(4) exhibit Jahn-Teller elongation ( $d_{x^2-y^2}$  magnetic ground states), with long axial contacts to N(7) (2.296(6) Å) and O(1) (2.213(6) Å) with shorter remaining equatorial Cu - L distances (1.890(7) - 2.047(7) Å). Cu(3) also exhibits Jahn-Teller elongation ( $d_{x^2-y^2}$  magnetic ground state), with long contacts to O(2) and N(12) (2.340(5) - 2.386(7) Å), and shorter remaining Cu - L bond distances (1.918(7) - 2.061(6)

Å). The connections between Cu(2), Cu(3) and Cu(4) are orbitally orthogonal and should therefore lead to ferromagnetic spin exchange.

The hydrolysis of  $\text{Ag}(\text{CN})_2^-$ , followed by the copper mediated oxidation of  $\text{CN}^-$  to  $\text{OCN}^-$  by air may explain the observed presence of Cu(I) [160-162]. A UV-visible experiment was performed in acetonitrile to confirm the mixed valency of the copper cations, however only a single absorption at 402 nm with an extinction coefficient of  $200\,192\text{ dm}^3\text{ mol}^{-1}\text{ cm}^{-1}$  was observed. This extinction coefficient far exceeds what would be expected for Laporte forbidden d-d transitions, and is more likely the result of a metal to ligand charge transfer (MLCT). While it is still possible that d-d transitions occurred, the strong MLCT would likely have dominated the absorbance spectrum.

A  $\text{Cu}(\text{II})_{15}\text{Cu}(\text{I})_{17}$  cluster that formed the primary building unit of a metal-organic framework has been reported [163], in which the presence and ratio of the metal ions was supported by magnetic measurements and by X-ray photoelectron spectroscopy (XPS). While an XPS experiment was not performed for **8.3**, the variable-temperature magnetic data were collected and are shown in Figure 8.19. A drop in moment from  $7.1\ \mu_{\text{B}}$  at 300 K to  $6.4\ \mu_{\text{B}}$  at 30 K is present, suggestive of the possible presence antiferromagnetic exchange component, followed by a rise to  $6.9\ \mu_{\text{B}}$  at 2 K, indicative of the presence of ferromagnetic exchange as well.

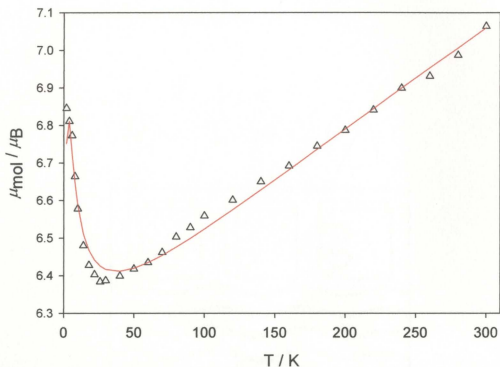


**Figure 8.19:** Variable temperature magnetic data for **8.3**;  $g = 2.072$ ,  $J = 4.23 \text{ cm}^{-1}$ ,  $z = 2$ ,  $J' = -0.08 \text{ cm}^{-1}$ ,  $\text{TIP} = 1200 \times 10^{-6} \text{ cm}^3 \text{ mol}^{-1}$ ,  $\rho = 0.02$ ,  $10^2 R = 0.636$ .

The four diamagnetic Cu(I) ions will not contribute to the observed magnetic properties and are unlikely to act as a conduit for magnetic exchange across the grid between distant Cu(II) ions. Examination of the outer square framework of the grid, consisting of twelve Cu(II) ions (Figure 8.17 and 8.18) shows that all of the bridging connections between adjacent metal centres are orbitally orthogonal and should therefore lead to ferromagnetic exchange between  $\mu$ -O bridged centres based on a comparison to Cu(II)<sub>4</sub> and Cu(II)<sub>9</sub> grids with the same magnetic ground states, orbital alignment and similar large M-O-M bond angles [59,63,66,69,71,96]. The long, three bond,  $\mu$ -NN<sub>pyridazine</sub> bridges (N6-N7) are also not expected to contribute significantly to the exchange situation, therefore a magnetic model consisting of four  $\mu$ -O<sub>hydrazone</sub> bridged

trinuclear subunits, with a molecular field correction to account for the interaction between subunits *via* the  $\mu$ -NN<sub>pyridazine</sub> bridge was considered. This model is shown in Figure 8.20.

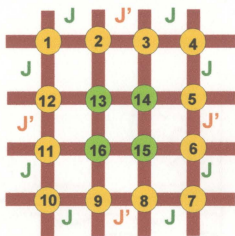


**Figure 8.20:** Magnetic exchange model for 8.3. Yellow circles represent Cu(II) ( $S = 1/2$ ) centres and green circles represent Cu(I) ( $S = 0$ ) centres.

A Hamiltonian to describe this exchange situation is expressed in equation 8.4.

$$H_{ex} = -J\{S_2 \cdot S_{13} + S_{13} \cdot S_{12}\} \quad (8.4)$$

A molecular field approximation [142] is introduced into the susceptibility expression in equation 8.5:

$$\chi_{mol} = \frac{N\beta^2 g^2}{3k(T - zJ' \chi_{trimer})} \frac{\sum S'(S'+1)(2S'+1)e^{-E(S')/kT}}{\sum (2S'+1)e^{-E(S')/kT}} (1 - \rho) + \frac{N\beta^2 g^2 S(S+1)\rho}{3kT} + TIP \quad (8.5)$$

The data were fitted to equation 8.5 (see Appendix 2) to give  $g = 2.072$ ,  $J = 4.23 \text{ cm}^{-1}$ ,  $z = 2$ ,  $J' = -0.08 \text{ cm}^{-1}$ ,  $TIP = 1200 \times 10^{-6} \text{ cm}^3 \text{ mol}^{-1}$ ,  $\rho = 0.02$ ,  $10^2 R = 0.636$ . The solid line in Figure 8.19 was obtained with these parameters, and the positive sign and

magnitude of the exchange coupling  $J$  is consistent with other ferromagnetically dominated Cu(II) grid systems [59,63,66,69,71,96]. TIP is expected to contribute significantly in such an array of twelve Cu(II) centres, and accounts for the rise in moment from 30 K to 300 K, that was observed experimentally.

Magnetization data as a function of field at 2 K show a rise to 10.7 N $\beta$  units at 5 T (Figure 8.21). The dashed blue line in Figure 8.21 was calculated using the appropriate Brillouin function for a ground state of  $S' = 12/2$ . This is the expected ground state if the outer Cu(II)<sub>12</sub> square was treated as a simple, alternating chain of orthogonally connected centres. The experimental data does not appear to agree with that situation, but instead appears to approach the calculated (red) line for an  $S' = 4 \times 3/2$  ground state, more consistent with the proposed model used to fit the variable temperature data.

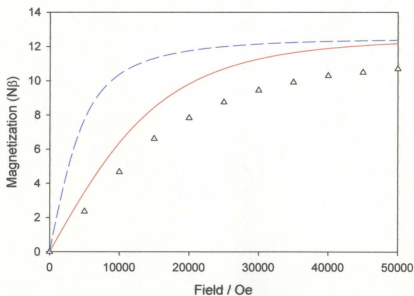


**Figure 8.21:** Variable field magnetization data for **8.3**; solid red line calculated for  $g = 2.072$ ,  $S' = 4 \times 3/2$ ,  $T = 2$  K and dashed blue line calculated for  $g = 2.072$ ,  $S' = 12/2$ ,  $T = 2$  K using the appropriate Brillouin function.

**Table 8.5:** Selected bond distances (Å) angles (°) and torsion angles (°) for **8.3**.

Cu(1) N(18)	2.107(8)	Cu(3) N(4')	1.918(7)
Cu(1) N(19'')	2.161(7)	Cu(3) N(9)	1.978(7)
Cu(1) O(4''')	2.286(5)	Cu(3) O(1')	2.021(5)
Cu(1) O(3)	2.348(5)	Cu(3) N(1')	2.061(6)
		Cu(3) O(2)	2.340(5)
		Cu(3) N(12)	2.386(7)
Cu(2) N(16)	1.890(7)	Cu(4) O(4''')	1.952(6)
Cu(2) O(2)	1.941(5)	Cu(4) N(6)	2.013(6)
Cu(2) O(3)	1.982(6)	Cu(4) N(24''')	2.014(7)
Cu(2) N(13)	2.047(7)	Cu(4) N(21''')	1.903(7)
Cu(2) N(7)	2.296(6)	Cu(4) O(1)	2.213(6)
Cu(3) O(1)	Cu(4) 140.1(3)	Cu(2) N(7) N(6)	Cu(4) 165.6
Cu(2) O(2)	Cu(3) 131.1(3)	Cu(1) N(18) N(19)	Cu(1') 173.8
Cu(2) O(3)	Cu(1) 134.4(3)		
Cu(4) O(4)	Cu(1) 134.7(3)		

#### 8.4: Summary:

Results of the reactions between tetratopic ligands 2pyoapm (**2.9**) and 2pdoapm (**2.10**) with Cu(II) salts were presented and their magneto-structural relationships discussed. For **8.1**, the steric constraint associated with a central dinucleating pyrazole moiety of 2pyoapm (**2.9**) leads to the adoption of a ketonic *syn* conformation by the ligand, and produced a hydrogen bonded Cu(II)<sub>2</sub> network based on dinuclear subunits. Strong antiferromagnetic coupling was expected based on the non-orthogonal overlap of the magnetic orbitals and the large Cu-O-Cu and Cu-NN<sub>pyrazole</sub>-Cu angles. The experimental temperature dependent magnetic data, however, could not be adequately modeled using a simple dinuclear approach. Based on the structurally characterized presence of extensive hydrogen bonding between Cu(II) dimers (Figure 8.7), an

alternating chain model was used to describe the exchange situation, leading to a much better fit of the experimental data.

Compound **8.2** was a  $2 \times [4 \times 4]$  Cu(II)<sub>16</sub> grid, that was isostructural with **7.1** and **7.2a**. The experimental magnetic data were typical of intramolecular antiferromagnetic exchange, with a change in slope in the moment as a function of temperature plot, suggestive of at least two exchange constants with significantly different magnitudes. Although the structure revealed a complicated network of magnetic exchange pathways, the identification of the Jahn-Teller axes, and a combination of orthogonal and non-orthogonal orbital connections, allowed for a fairly simple magnetic model to be devised. An excellent fit to the experimental data was achieved, with coupling constants that agreed with literature precedent. A magnetization study provided further evidence that the proposed model was valid.

The report of an incomplete Cu(II)<sub>12</sub>(L1)<sub>8</sub> (L1; Figure 8.1) picture frame complex, based on a  $[4 \times 4]$  topology [146], differs from the fully metalated  $2 \times [4 \times 4]$  Cu(II)<sub>16</sub> grid reported here (**8.2**), likely due to the addition of base (NaOH) in the preparation of **8.2**, leading to deprotonation of the ligand, **2.10**. In the preparation of **8.3**, base was also omitted, but instead KAg(CN)<sub>2</sub> was added. This resulted in an unusual redox reaction and the formation of the mixed oxidation state Cu(II)<sub>12</sub>Cu(I)<sub>4</sub> grid. While multiple exchange pathways were again present for **8.3**, the presence of four diamagnetic Cu(I) centres helped to simplify the task of proposing a magnetic model. Structural characterization lead to the observation of magnetic orbital orthogonality between Cu(II) centres that were  $\mu$ -O<sub>hydrazone</sub> bridged, while the three bond Cu-NN<sub>pyradizine</sub>-Cu connection

was too long to be considered magnetically significant. These structural interpretations lead to a magnetic model that gave fitted parameters agreeing well with the experimental data.

## Chapter 9: General Conclusions

Metallo-supramolecular  $[n \times n]$   $M_n$  transition metal grid arrays (with  $n = 2, 3$  and  $4$ ) were synthesized by self-assembly reactions with new ditopic imidazole hydrazone, tritopic picolinic dihydrazone and tetratopic pyridazine bis(hydrazone) ligands.

Mono-, di-, trinuclear,  $[2 \times 2]$   $M_4$  grid and trigonal-bipyramidal clusters formed by self-assembly reactions with the ditopic ligands **2.2** and **2.3** and were discussed in Chapter 3. These results demonstrated the dynamic and variable nature of the coordination process, and illustrated the effects of the available ligand conformational options, the influence of steric congestion by ligand substituents, and the thermodynamic stability of the  $[2 \times 2]$  grid arrangement in the nickel and copper cases. The structural results from **3.1-3.8** suggest a possible route to the self-assembly of  $[2 \times 2]$   $M_4$  grid and trigonal-bipyramidal architectures.

$[3 \times 3]$   $M_9$  ( $M = \text{Mn(II)}, \text{Co(II)}, \text{Cu(II)}$  and  $\text{Zn(II)}$ ) grids synthesized by self-assembly reactions between  $\text{MX}_2$  salts and 2pmoap (**2.4**; Chapter 4) were characterized structurally and all exhibited the same  $[\text{M}_9-(\mu\text{-O})_{12}]$  core framework. In reactions where the metal nitrate salt was used, the  $\text{Zn(II)}_9$ ,  $\text{Mn(II)}_9$  and  $\text{Cu(II)}_9$  complexes (**4.1**, **4.2** and **4.5**, respectively) were found to be isostructural, crystallizing in the tetragonal space group  $I4_1/acd$  (#142), with extremely similar lattice parameters. Similarly,  $[3 \times 3]$   $\text{Mn(II)}_5\text{Cu(II)}_4$ ,  $\text{Mn(II)}_5\text{Zn(II)}_4$  and  $\text{Mn(II)Cu(II)}_8$  heterobimetallic grids (**5.2**, **5.1** and **5.4**, respectively) produced with 2pmoap and  $\text{M(NO}_3)_2$  salts and were found to be isostructural with the homometallic grids, all crystallizing in the  $I4_1/acd$  space group (Chapter 5).

The structural characterizations of these [3×3] grids formed the basis for magnetic interpretation and modeling and the Mn(II)<sub>9</sub> and Cu(II)<sub>9</sub> cases deserve particular attention. In the Mn(II)<sub>9</sub> case (4.2), large, similar Mn-O-Mn bridging angles lead to antiferromagnetic exchange between metal centres throughout the grid, while in the Cu(II)<sub>9</sub> cases (4.5 and 4.6), the effect of large Cu-O-Cu bridging angles for the ring of eight metal centres was negated by the presence of Jahn-Teller distortions leading to magnetic orbital orthogonality and dominant ferromagnetic exchange. For the Cu(II)<sub>9</sub> grids, a second magnetic effect, due to the presence of a d<sub>z<sup>2</sup></sub> Jahn-Teller distortion for the central Cu(II) ion, lead to antiferromagnetic exchange between the central Cu(II) ion and the side metal sites. Jahn-Teller distortions were also present, and characterized structurally, in the Cu(II) containing heterobimetallic grids (5.2 and 5.4), resulting in a ferrimagnetic magnetic profile for 5.2.

Chapter 6 reported [3×3] Mn(II)<sub>9</sub>, Cu(II)<sub>9</sub> and Co(II)<sub>5</sub>Co(III)<sub>4</sub> grids synthesized by self-assembly reactions between metal salts and ligands with quinoline-type endpieces (2po45nq (2.7) and 2po34nq (2.8)). A Cu(II)<sub>9</sub> grid and a Mn(II)<sub>9</sub> grid (6.4 and 6.6, respectively) were structurally characterized and their intramolecular properties (structure and magnetism) were found to be similar to those previously reported for ferromagnetically dominated Cu(II)<sub>9</sub> and antiferromagnetic Mn(II)<sub>9</sub> grids. This was despite the presence of intermolecular edge-to-face and face-to-face π-π interactions between terminal quinoline moieties of adjacent grids, leading to long-range structural motifs. The absence of any detectable long range magnetic ordering is sensible in light of

the weak nature of  $\pi$ - $\pi$  interactions and the long distances between metal centres in neighboring grids, with no direct bridging connections.

Three isostructural  $4 \times [2 \times 2]$   $M(\text{II})_{16}$  ( $M = \text{Mn}(\text{II}), \text{Co}(\text{II})$  and  $\text{Cu}(\text{II})$ ) grids were synthesized by self-assembly reactions between metal salts and 2pdoapm (**2.10**). All three crystallized in the orthorhombic space group  $Pm\bar{m}n$  (#59), with very similar lattice parameters, as presented in Chapters 7 and 8. Interpretation of the magnetic properties of the  $\text{Co}_{16}$  grid was complicated by the apparent inconsistency between the metal oxidation states in the single crystal of **7.2a** and the bulk sample, **7.2b**. The preparation was repeated under  $\text{N}_{2(g)}$ , leading to a bulk material with experimental magnetic data consistent with the presence of 16  $\text{Co}(\text{II})$  centres. The magnetic properties of the  $\text{Mn}(\text{II})_{16}$  and  $\text{Co}(\text{II})_{16}$  grids were modeled as compartmental  $[2 \times 2]$   $M_4-(\mu\text{-O}_{\text{hydrazone}})_4$  squares with a molecular field correction introduced into the susceptibility expression to account for interactions between the  $[2 \times 2]$  subunits *via* the double  $\mu\text{-NN}_{\text{pyridazine}}/\mu\text{-O}$  bridges. The structure of the  $\text{Cu}(\text{II})_{16}$  grid revealed a complicated network of magnetic exchange pathways, however, the characterization of Jahn-Teller axes leading to a combination of orthogonal and non-orthogonal orbital connections, allowed for a fairly simple magnetic model to be devised.

Finally, several unique and unexpected results worthy of special mention were reported in this thesis. An antiferromagnetic  $3 \times [1 \times 3]$   $\text{Mn}(\text{II})_9$  rectangle (**6.2**) was synthesized using a tritopic ligand with a quinoline-type endpiece (2po56hq; **2.5**). The magnetic properties of **6.2** were successfully modeled using a linear triad to represent the  $\mu\text{-O}_{\text{hydrazone}}$  bridged  $\text{Mn}(\text{II})$  centres, with a molecular field correction to account for the

interaction between triads *via* the  $\mu$ -NN<sub>diazine</sub> bridges. The first antiferromagnetic [3×3] Cu(II)<sub>9</sub> grid was reported (**6.3**), also from a tritopic ligand with a quinoline-type endpiece (2po56nq; **2.6**). Each Cu(II) centre exhibited axial compression and a d<sub>z</sub><sup>2</sup> magnetic ground state, leading to antiferromagnetic coupling *via* to the large Cu-O-Cu bridging angles between both the ions in the ring and between the central ion and its neighbors.

Reactions between tetratopic ligands 2pyoapm (**2.9**) and 2pdoapm (**2.10**) with Cu(II) salts also lead to two unusual results. For **8.1**, the steric constraint associated with a central dinucleating pyrazole moiety of 2pyoapm (**2.9**) lead to the adoption of a ketonic *syn* conformation by the ligand, and produced a hydrogen bonded Cu(II)<sub>2</sub> network based on dinuclear subunits. In the preparation of **8.3**, a Cu<sub>16</sub> grid, base was omitted, and instead a solution of KAg(CN)<sub>2</sub> was added. This resulted in an unusual redox reaction and the formation of a mixed oxidation state Cu(II)<sub>12</sub>Cu(I)<sub>4</sub> grid. While multiple exchange pathways were again present for **8.3**, the presence of four diamagnetic Cu(I) centres and magnetic orbital orthogonality between the remaining Cu(II) centres, lead to a simple magnetic model.

### References:

- [1] E. Fischer, *Ber. Deutsch. Chem. Gesell.*, **1894**, 27, 2985.
- [2] Nobel Web. (2008). The Nobel Prize in Chemistry 1902. In *The Official Web Site of the Nobel Foundation*.. Retrieved June 14, 2006, from [http://nobelprize.org/nobel\\_prizes/chemistry/laureates/1902/index.html](http://nobelprize.org/nobel_prizes/chemistry/laureates/1902/index.html).
- [3] Nobel Web. (2008). The Nobel Prize in Chemistry 1987. In *The Official Web Site of the Nobel Foundation*.. Retrieved June 14, 2006, from [http://nobelprize.org/nobel\\_prizes/chemistry/laureates/1987/index.html](http://nobelprize.org/nobel_prizes/chemistry/laureates/1987/index.html).
- [4] J.-M. Lehn (Nobel lecture), *Angew. Chem., Int. Ed.*, **1988**, 27, 89.
- [5] J.-M. Lehn, *Science*, **1993**, 260, 1762.
- [6] J. W. Steed, J. L. Atwood, (2000). Chapter 1: Concepts: What is Supramolecular Chemistry?. In *Supramolecular Chemistry*. (pp. 2-3) New York: John Wiley & Sons, Ltd.
- [7] S. Leininger, B. Olenyuk, P. J. Stang, *Chem. Rev.*, **2000**, 100, 853.
- [8] R. E. P. Winpenny, *Dalton Trans.*, **2002**, 1.
- [9] R. Sessoli, H.-L. Tsai, A. R. Schake, S. Wang, J. B. Vincent, K. Folting, D. Gatteschi, G. Christou, D. N. Hendrickson, *J. Am. Chem. Soc.*, **1993**, 115, 1804.
- [10] J. C. Goodwin, R. Sessoli, D. Gatteschi, W. Wernsdorfer, A. K. Powell, S. L. Heath., *J. Chem. Soc., Dalton Trans.*, **2000**, 1835.
- [11] A. M. Ako, I. J. Hewitt, V. Mereacre, R. Clerac, W. Wernsdorfer, C. E. Anson, A. K. Powell, A.K. *Angew. Chem., Int. Ed.*, **2006**, 45, 4926.

- [12] G. Aromi, A. R. Bell, M. Helliwell, J. Raftery, S. J. Teat, G. A. Timco, O. Roubeau, R. E. P. Winpenny, *Chem. Eur. J.*, **2003**, *9*, 3024.
- [13] M. Shanmugam, G. Chastanet, T. Mallah, R. Sessoli, S. J. Teat, G. A. Timco, R. E. P. Winpenny, *Chem. Eur. J.*, **2006**, 8777.
- [14] J. van Slageren, R. Sessoli, D. Gatteschi, A. A. Smith, M. Helliwell, R. E. P. Winpenny, A. Cornia, A.-L. Barra, A. G. M. Jansen, E. Rentschler, G. A. Timco, *Chem. Eur. J.*, **2002**, *8*, 277.
- [15] J. Overgaard, B. B. Iversen, S. P. Palii, G. A. Timco, N. V. Gerbeleu, F. K. Larsen, *Chem. Eur. J.*, **2002**, *8*, 2775.
- [16] F. K. Larsen, E. J. L. McInnes, H. El Mkami, J. Overgaard, S. Piligkos, G. Rajaraman, E. Rentschler, A. A. Smith, G. M. Smith, V. Boote, M. Jennings, G. A. Timco, R. E. P. Winpenny, *Angew. Chem., Int. Ed.*, **2003**, *42*, 101.
- [17] G. A. Timco, A. S. Batsanov, F. K. Larsen, C. A. Muryn, J. Overgaard, S. J. Teat, R. E. P. Winpenny, *Chem. Commun.*, **2005**, 3649.
- [18] E. Breuning, G. S. Hanan, F. J. Romero-Salguero, A. M. Garcia, P. N. W. Baxter, J.-M. Lehn, E. Wegelius, K. Rissanen, H. Nierengarten, A. van Dorsseleer, *Chem. Eur. J.*, **2002**, *8*, 3458.
- [19] J. Rojo, J.-M. Lehn, G. Baum, D. Fenske, O. Waldmann, P. Müller, *Eur. J. Inorg. Chem.*, **1999**, 517.
- [20] G. S. Hanan, D. Volkmer, U. S. Schubert, J.-M. Lehn, G. Baum and D. Fenske, *Angew. Chem., Int. Ed.*, **1997**, *36*, 1842.

- [21] P. N. W. Baxter, J.-M. Lehn, J. Fischer, M.-T. Youinou, *Angew. Chem., Int. Ed.*, **1994**, *33*, 2284.
- [22] A. M. Garcia, F. J. Romero-Salguero, D. M. Bassani, J.-M. Lehn, G. Baum, D. Fenske, *Chem. Eur. J.*, **1999**, *6*, 1803.
- [23] M. Barboiu, G. Vaughan, R. Graff, J.-M. Lehn, *J. Am. Chem. Soc.*, **2003**, *125*, 10257.
- [24] Intel. (April 29, 2005). In *Excerpts from A Conversation with Gordon Moore: Moore's Law*. Retrieved October 23, 2006, from [ftp://download.intel.com/museum/Moores\\_Law/VideoTranscripts/Excepts\\_A\\_Conversation\\_with\\_Gordon\\_Moore.pdf](ftp://download.intel.com/museum/Moores_Law/VideoTranscripts/Excepts_A_Conversation_with_Gordon_Moore.pdf).
- [25] M. Ruben, J. Rojo, F. J. Romero-Salguero, L. H. Uppadine, J.-M. Lehn, *Angew. Chem. Int. Ed.*, **2004**, *43*, 3644.
- [26] N. C. Seeman. *Sci. Am. Reports*, **2007**, *17*, 30.
- [27] P. Vettiger, M. Despont, U. Drechsler, U. Dürig, W. Haberle, M. I. Lutwyche, H. E. Rothuizen, R. Stutz, R. Widmer, G. K. Binnig. *IBM J. Res. Develop.*, **2000**, *44*, 323.
- [28] V. A. Milway, T. S. M. Abedin, V. Niel, T. L. Kelly, L. N. Dawe, S. K. Dey, D. W. Thompson, D. O. Miller, M. S. Alam, P. Müller, L. K. Thompson, *Dalton Trans.*, **2006**, 2835.
- [29] L. K. Thompson, T. L. Kelly, L. N. Dawe, H. Grove, M. T. Lemaire, J. A. K. Howard, E. C. Spencer, C. J. Matthews, S. T. Onions, S. J. Coles, P. N. Horton, M. B. Hursthouse, M. E. Light, *Inorg. Chem.*, **2004**, *43*, 7605.

- [30] L. Zhao, C. J. Matthews, L. K. Thompson, S. L. Heath, *Chem. Commun.*, **2000**, 265.
- [31] O. Waldmann, H. U. Gudel, T. L. Kelly, L. K. Thompson, *Inorg. Chem.*, **2006**, *45*, 3295.
- [32] E. M. Rumberger, S. J. Shah, C. C. Beedle, L. N. Zakharov, A. L. Rheingold, D. N. Hendrickson, *Inorg. Chem.*, **2005**, *44*, 2742.
- [33] F. Meier, J. Levy, D. Loss, *Phys. Rev. B.*, **2003**, *68*, 134417-1.
- [34] A. Earnshaw, (1968). *Introduction to Magnetochemistry*. New York: Academic Press.
- [35] See for example: (a) C.E. Housecroft, A.G. Sharpe, (2005). *Inorganic Chemistry*. 2<sup>nd</sup> Ed. Toronto: Prentice Hall. (b) J.E. Huheey, E.A. Keiter, R.L. Keiter, (1993). *Inorganic Chemistry: Principles of Structure and Reactivity*. 4th Ed. New York: Harper Collins College Publishers. (c) R. S. Drago, (1992). *Physical Methods for Chemists*. 2<sup>nd</sup> Ed. Gainesville: Surfside Scientific Publishers.
- [36] Special Focus on Orbital Physics Issue, *New J. Phys.*, **2004**, *6*.
- [37] W. Geertsma, D. Khomskii, *Phys. Rev. B.*, **1996**, *54*, 3011.
- [38] T. Moriya, *Phys. Rev.*, **1960**, *120*, 91.
- [39] P. W. Anderson, *Phys. Rev.*, **1959**, *115*, 2.
- [40] P. W. Anderson, *Phys. Rev.*, **1950**, *79*, 350.
- [41] J. B. Goodenough, A. Wold, R. J. Arnott, N. Menyuk, *Phys. Rev.*, 1961, *124*, 373.
- [42] F. E. Mabbs, D. J. Machin.(1973). Chapter 7: The magnetic properties of polynuclear transition metal complexes: Superexchange. In *Magnetism and transition metal complexes*. (pp. 174-175) New York: Halsted Press.

- [43] R.L. Martin.(1968) Chapter 9: Metal-Metal Interaction in Paramagnetic Clusters. In E. A. V. Ebsworth, A. G. Maddock and A. G. Sharpe (Eds.), *New pathways in inorganic chemistry*. (pp. 175-231). London: Cambridge United Press.
- [44] L. K. Thompson, Z. Xu, A. E. Goeta, J. A. K. Howard, H. J. Clase, D. O. Miller, *Inorg. Chem.*, **1998**, *37*, 3217.
- [45] Z. Xu, L. K. Thompson, D. O. Miller, H. J. Clase, J. A. K. Howard, A. E. Goeta, *Inorg. Chem.*, **1998**, *37*, 3620.
- [46] V. H. Crawford, H. W. Richardson, J. R. Wasson, D. J. Hodson, W. E. Hatfield, *Inorg. Chem.*, **1976**, *15*, 2107.
- [47] K. S. Murray, *Adv. Inorg. Chem.*, **1995**, *43*, 261.
- [48] K. Kambe, *J. Phys. Soc. Jpn.*, **1950**, *5*, 48.
- [49] MAGMUN4.1/OW01.exe is available as a combined package free of charge from the authors (<http://www.ucs.mun.ca/~lthomp/magmun>). MAGMUN has been developed by Dr. Zhiqiang Xu (Memorial University), and OW01.exe by Dr. O. Waldmann. We do not distribute the source codes. The programs may be used only for scientific purposes, and economic utilization is not allowed. If either routine is used to obtain scientific results, which are published, the origin of the programs should be quoted.
- [50] O. Kahn, (1993). Chapter 2: Molecules Containing a Unique Magnetic Center without First-Order Orbital Momentum: Magnetization. In *Molecular Magnetism*. (pp. 10-12) New York: VCH Publishers, Inc.

- [51] J. Rojo, F. J. Romero-Salguero, J.-M. Lehn, G. Baum, D. Fenske, *Eur. J. Inorg. Chem.*, **1999**, 1421.
- [52] E. Breuning, M. Ruben, J.-M. Lehn, F. Renz, Y. Garcia, V. Ksenofontov, P. Gutlich, E. Wegelius, K. Rissanen, *Angew. Chem., Int. Ed.*, **2000**, *39*, 2504.
- [53] E. Breuning, U. Ziener, J.-M. Lehn, E. Wegelius, K. Rissanen, *Eur. J. Inorg. Chem.*, **2001**, 1515.
- [54] S. T. Onions, A. M. Frankin, P. N. Horton, M. B. Hursthouse, C. J. Matthews, *Chem. Comm.*, **2003**, 2864.
- [55] S. K. Dey, L. K. Thompson, L. N. Dawe, *Chem. Comm.*, **2006**, *47*, 4967.
- [56] S. K. Dey, T. S. M. Abedin, L. N. Dawe, S. S. Tandon, J. L. Collins, L. K. Thompson, A. V. Postnikov, M. S. Alam, P. Müller, *Inorg. Chem.*, **2007**, *46*, 7767.
- [57] L. N. Dawe, L. K. Thompson, *Angew. Chem., Int. Ed.*, **2007**, *46*, 7440.
- [58] C. J. Matthews, K. Avery, Z. Xu, L. K. Thompson, L. Zhao, D. O. Miller, K. Biradha, K. Poirier, M. J. Zaworotko, C. Wilson, A. E. Goeta, J. A. K. Howard, *Inorg. Chem.*, **1999**, *38*, 5266.
- [59] L. K. Thompson, C. J. Matthews, L. Zhao, Z. Xu, D. O. Miller, C. Wilson, M. A. Leech, J. A. K. Howard, S. L. Heath, A. G. Whittaker, R. E. P. Winpenny, *J. Solid State Chem.*, **2001**, *159*, 308.
- [60] Z. Xu, L. K. Thompson, C. J. Matthews, D. O. Miller, A. E. Goeta, J. A. K. Howard, *Inorg. Chem.*, **2001**, *40*, 2446.

- [61] C. J. Matthews, L. K. Thompson, S. R. Parsons, Z. Xu, D. O. Miller, S. L. Heath, *Inorg. Chem.*, **2001**, *40*, 4448.
- [62] Z. Xu, L. K. Thompson, D. O. Miller, *J. Chem. Soc., Dalton Trans.*, **2002**, 2462.
- [63] H. Grove, T. J. Kelly, L. K. Thompson, L. Zhao, Z. Xu, T. S. M. Abedin, D. O. Miller, A. E. Goeta, C. Wilson, J. A. K. Howard, *Inorg. Chem.*, **2004**, *43*, 4278.
- [64] L. N. Dawe, T. S. M. Abedin, T. L. Kelly, L. K. Thompson, D. O. Miller, L. Zhao, C. Wilson, M. A. Leech, J. A. K. Howard, *J. Mater. Chem.*, **2006**, *16*, 2645.
- [65] C. J. Matthews, Z. Xu, S. K. Mandal, L. K. Thompson, K. Biradha, K. Poirier, M. J. Zaworotko, *Chem. Commun.*, **1999**, 347.
- [66] L. Zhao, Z. Xu, L. K. Thompson, S. L. Heath, D. O. Miller, M. Ohba, *Angew. Chem., Int. Ed.*, **2000**, *39*, 3114.
- [67] O. Waldmann, R. Koch, S. Schromm, P. Müller, L. Zhao, L. K. Thompson, *Chem. Phys. Lett.*, **2000**, *332*, 73.
- [68] O. Waldmann, L. Zhao, L. K. Thompson, *Phys. Rev. Lett.*, **2002**, *88*, 066401.
- [69] L. Zhao, Z. Xu, L. K. Thompson, D. O. Miller, *Polyhedron*, **2001**, *20*, 1359.
- [70] L. K. Thompson, L. Zhao, Z. Xu, D. O. Miller, W. M. Reiff, *Inorg. Chem.*, **2003**, *42*, 128.
- [71] Z. Xu, L. K. Thompson, D. O. Miller, *Polyhedron*, **2002**, *21*, 1715.
- [72] L. K. Thompson, *Coord. Chem. Rev.*, **2002**, *233-234*, 193.
- [73] L. Zhao, Z. Xu, H. Grove, V. A. Milway, L. N. Dawe, T. S. M. Abedin, L. K. Thompson, T. L. Kelly, R. G. Harvey, D. O. Miller, L. Weeks, J. G. Shapter, K. J. Pope, *Inorg. Chem.*, **2004**, *43*, 3812.

- [74] L. K. Thompson, O. Waldmann, Z. Xu, *Coord. Chem. Rev.*, **2005**, 249, 2677.
- [75] L. N. Dawe, T. S. M. Abedin, L. K. Thompson, *Dalton Trans.*, **2008**, 1661.
- [76] L. Weeks, L. K. Thompson, J. G. Shapter, K. J. Pope, Z. Xu, *J. Microsc.*, **2003**, 212, 102.
- [77] C. A. Hunter, J. K. M. Sanders. *J. Am. Chem. Soc.*, **1990**, 112, 5525.
- [78] G. H. Spencer, Jr., P. C. Cross, K. B. Wiberg, *J. Chem. Phys.*, **1961**, 35, 1939.
- [79] S. Sueur, M. Lagrenee, F. Abraham, C. Bremard, *J. Heterocycl. Chem.*, **1987**, 24, 1285.
- [80] Personal communication with Clare Maloney, Canadian Microanalytical Service, Ltd. October 11, 2007.
- [81] A. C. Larson. (1970) *Crystallographic Computing*, (pp. 291-294) F.R. Ahmed, ed. Munksgaard: Copenhagen. (Equation 22, with V replaced by the cell volume)
- [82] SIR92: A. Altomare, G. Cascarano, C. Giacovazzo, A. Guagliardi, M. Burla, G. Polidori, M. Camalli, *J. Appl. Cryst.*, **1994**, 27, 435.
- [83] SHELX97: Sheldrick, G.M. (1997).
- [84] DIRDIF99: P. T. Beurskens, G. Admiraal, G. Beurskens, W. P. Bosman, R. de Gelder, R. Israel, J. M. M. Smits. (1999). The DIRDIF-99 program system, Technical Report of the Crystallography Laboratory, University of Nijmegen, The Netherlands.
- [85] D. T. Cromer, J. T. Waber. (1974). *International Tables for X-ray Crystallography, Vol. IV*, The Kynoch Press: Birmingham, England, Table 2.2 A.

- [86] J. A. Ibers, W. C. Hamilton. *Acta Crystallogr.*, **1964**, *17*, 781.
- [87] D. C. Creagh, W. J. McAuley. (1992) *International Tables for Crystallography*, Vol C, (pp. 219-222). A. J.C. Wilson, ed., Kluwer Academic Publishers: Boston, Table 4.2.6.8.
- [88] D.C. Creagh, J.H. Hubbell. (1992) *International Tables for Crystallography*, Vol C, (pp. 200-206) A. J. C. Wilson, ed., Kluwer Academic Publishers: Boston, Table 4.2.4.3.
- [89] CrystalStructure 3.7.0: Crystal Structure Analysis Package, Rigaku and Rigaku/MSC (2000-2005). 9009 New Trails Dr. The Woodlands TX 77381 USA.
- [90] CRYSTALS Issue 10: D. J. Watkin, C. K. Prout, J. R. Carruthers, P. W. Betteridge. (1996) Chemical Crystallography Laboratory, Oxford, UK.
- [91] A. L. Spek, *J.Appl.Cryst.*, **2003**, *36*, 7.
- [92] (a) G. J. Palenik, *Inorg. Chem.*, **1997**, *36*, 122. (b) M. O'Keefe, N. E. Brese, *J. Am. Chem. Soc.*, **1991**, *113*, 3226.
- [93] V. Niel, V. A. Milway, L. N. Dawe, H. Grove, S. S. Tandon, T. S. M. Abedin, T. L. Kelley, E. C. Spencer, J. A. K. Howard, J. L. Collins, D. O. Miller, L. K. Thompson, *Inorg. Chem.*, **2008**, *47*, 176.
- [94] A.W. Addison, T. N. Rao, J. Reedijk, J. van Rijn, G.C. Verschoor, *J. Chem. Soc. Dalton Trans.*, **1984**, 1349.
- [95] S. Roy, T. N. Mandal, A. K. Barik, S. Pal, R. J. Butcher, M. S. El Fallah, J. Tercero, S. K. Kar, *Dalton Trans.*, **2007**, 1229.

- [96] V. A. Milway, V. Niel, T. S. M. Abedin, Z. Xu, L. K. Thompson, H. Grove, D. O. Miller and S. R. Parsons, *Inorg. Chem.*, **2004**, *43*, 1874.
- [97] O. Waldmann, L. Zhao, L. K. Thompson, *Phys. Rev. Lett.*, **2002**, *88*, 066401.
- [98] T. Guidi, S. Carretta, P. Santini, E. Livioti, N. Magnani, C. Mondelli, O. Waldmann, L. K. Thompson, L. Zhao, C. D. Frost, G. Amoretti, R. Caciuffo, *Phys. Rev. B*, **2004**, *69*, 104432.
- [99] M. Ruben, J. -M. Lehn, P. Müller, *Chem. Soc. Rev.*, **2006**, *11*, 1056.
- [100] S. S. Tandon, L. N. Dawe, V. A. Milway, J. L. Collins, L. K. Thompson, *Dalton Trans.*, **2007**, 1948.
- [101] O. Kahn, (1993). Chapter 12: Magnetic Long-Range Ordering in Molecular Compounds: Design of Molecular-Based Magnets. In *Molecular Magnetism*. (pp. 287-332) New York: VCH Publishers, Inc.
- [102] J. S. Miller, *Dalton Trans.*, **2006**, 2742.
- [103] H. Oshio, O. Tamada, H. Onodera, T. Ito, T. Ikoma, S. Tero-Kubota, *Inorg. Chem.*, **1999**, *38*, 5686.
- [104] M. Pascu, F. Lloret, N. Avarvari, M. Julve, M. Andruh, *Inorg. Chem.*, **2004**, *43*, 5189.
- [105] F. Karadas, E. J. Schelter, A. V. Prosvirin, J. Basca and K.R. Dunbar, *Chem. Commun.*, **2005**, 1414.
- [106] M. Koikawa, M. Ohba, T. Tokii, *Polyhedron*, **2005**, *24*, 2257.
- [107] H. Oshio, M. Nihei, A. Yoshida, H. Nojiri, M. Nakano, A. Yamaguchi, Y. Karaki, H. Ishimoto, *Chem. Eur. J.*, **2005**, *11*, 843.

- [108] T. Kobayashi, T. Yamaguchi, H. Ohta, Y. Sunatsuki, M. Kojima, N. Re, M. Nonoyamac, N. Matsumoto, *Chem. Commun.*, **2006**, 1950.
- [109] D. Li, S. Parkin, G. Wang, G. T. Yee, S. M. Holmes, *Inorg. Chem.*, **2006**, *45*, 2773.
- [110] W.-G. Wang, A.-J. Zhou, W.-X. Zhang, M.-L. Tong, X.-M. Chen, M. Nakano, C. C. Beedle, D. N. Hendrickson, *J. Am. Chem. Soc.*, **2007**, *129*, 1014.
- [111] O. Kahn, J. Galy, Y. Journaux, J. Jaud, I. Morgenstern-Badarau, *J. Am. Chem. Soc.*, **1982**, *104*, 2165.
- [112] V. Baron, B. Gillon, O. Plantevin, A. Cousson, C. Mathoniere, O. Kahn, A. Grand, L. Ohrstrom, B. Delley, *J. Am. Chem. Soc.*, **1996**, *118*, 11822.
- [113] D. G. McCollum, G. P. A. Yap, A.L. Rheingold, B. Bosnich, *J. Am. Chem. Soc.*, **1996**, *118*, 1365.
- [114] M. Cantuel, F. Gumy, J.-C. G. Bunzli, C. Piguet, *Dalton Trans.*, **2006**, 2647.
- [115] R. Ruiz, M. Julve, J. Faus, F. Lloret, M.C. Munoz, Y. Journaux, C. Bois, *Inorg. Chem.* **1997**, *36*, 3434.
- [116] O. Kahn, *Acc. Chem. Res.*, **2000**, *33*, 647.
- [117] H. Oshio, M. Nihei, S. Koizumi, T. Shiga, H. Nojiri, M. Nakano, N. Shirakawa, M. Akatsu, *J. Am. Chem. Soc.*, **2005**, *127*, 4568.
- [118] Y. Sunatsuki, H. Shimada, T. Matsuo, M. Nakamura, F. Kai, N. Matsumoto, N. Re, *Inorg. Chem.* **1998**, *37*, 5566.
- [119] F. Karadas, E. J. Schelter, A. V. Prosvirin, J. Bacsá, K. R. Dunbar, *Chem. Commun.*, **2005**, 1414.

- [120] S. R. Parsons, L. K. Thompson, S. K. Dey, C. Wilson, J. A. K. Howard, *Inorg. Chem.*, **2006**, *45*, 8832.
- [121] Program OWXISG <pack3> © Oliver Waldmann. Release 21.11.2006.
- [122] J. W. Steed, J. L. Atwood, (2000). Chapter 1: Concepts: Nature of Supramolecular Interactions. In *Supramolecular Chemistry*. (pp. 19-30) New York: John Wiley & Sons, Ltd.
- [123] F. J. M. Hoeben, P. Jonkheijm, E. W. Meijer, A. P. H. J. Schenning, *Chem. Rev.*, **2005**, *105*, 1491.
- [124] L. Brammer, *Chem. Soc. Rev.*, **2004**, *33*, 476.
- [125] V. A. Milway, T. S. M. Abedin, L. K. Thompson, D. O. Miller, *Inorg. Chim. Acta*, **2006**, *359*, 2700.
- [126] C. G. Claessens, J. F. Stoddart, *J. Phys. Org. Chem.*, **1997**, *10*, 254.
- [127] E. A. Meyer, R. K. Castellano, F. Diederich, *Angew. Chem., Int. Ed.*, **2003**, *42*, 1210.
- [128] M. J. Hannon, *Chem. Soc. Rev.*, **2007**, *36*, 280.
- [129] S. Mizyed, P.E. Georghiou, M. Bancu, B. Cuadra, A. K. Rai, P. Cheng, L. T. Scott, *J. Am. Chem. Soc.*, **2001**, *123*, 12770.
- [130] P. E. Georghiou, A. H. Tran, S. Mizyed, M. Bancu, L. T. Scott, *J. Org. Chem.*, **2005**, *70*, 6158.
- [131] A. Sygula, F. R. Fronczek, R. Sygula, P. W. Rabideau, M. M. Olmstead, *J. Am. Chem. Soc.*, **2007**, *129*, 3842.
- [132] C. Janiak, *J. Chem. Soc., Dalton Trans.*, **2000**, 3885.

- [133] C.A. Hunter, J.K.M. Sanders, *J. Am. Chem. Soc.*, **1990**, *112*, 5525.
- [134] C. A. Hunter, *Chem. Soc. Rev.*, **1994**, *23*, 101.
- [135] E.-il Kim, S. Paliwal, C. S. Wilcox, *J. Am. Chem. Soc.*, **1998**, *120*, 11192.
- [136] M. O. Sinnokrot, C. D. Sherrill, *J. Am. Chem. Soc.*, **2004**, *126*, 7690.
- [137] D. Dobrzynska, L. B. Jerzykiewicz, *J. Am. Chem. Soc.*, **2004**, *126*, 11118.
- [138] D. Dobrzynska, L. B. Jerzykiewicz, J. Jezierska, M. Duczmal, *Cryst. Growth Des.*, **2005**, *5*, 1945.
- [139] S. R. Halper, S. M. Cohen, *Inorg. Chem.*, **2005**, *44*, 4139.
- [140] Y. Mikata, H. So, A. Yamashita, A. Kawamura, M. Mikuriya, K. Fukui, A. Ichimura, S. Yano, *Dalton Trans.*, **2007**, 3330.
- [141] D. Prema, A.V. Wiznycia, B. M. T. Scott, J. Hilborn, J. Desper, C. J. Levy, *Dalton Trans.*, **2007**, 4788.
- [142] O. Kahn. (1993). Section 2.6: Intermolecular Interactions. In *Molecular Magnetism*. (pp. 26-29) New York: VCH Publishers, Inc.
- [143] J. W. Steed, J. L. Atwood. (2000). Chapter 2: The Supramolecular Chemistry of Life: Biochemical Self-Assembly. In *Supramolecular Chemistry*. (pp. 82-83) New York: John Wiley & Sons, Ltd.
- [144] P. N. W. Baxter, J.-M. Lehn, G. Baum, D. Fenske. *Chem. Eur. J.*, **2000**, *6*, 4510.
- [145] L. K. Thompson, C. J. Matthews, L. Zhao, C. Wilson, M. A. Leech, J. A. K. Howard. *J. Chem. Soc., Dalton Trans.*, **2001**, 2258.
- [146] C. J. Matthews, S. T. Onions, G. Morata, M. Bosch Salvia, M. R. J. Elsegood, D. J. Price. *Chem. Commun.*, **2003**, 320.

- [147] A. Earnshaw, (1968). Chapter 3: Transition Metal Complexes. In *Introduction to Magnetochemistry*. (pp. 34) New York: Academic Press.
- [148] T. Kamiyuki, H. Okawa, N. Matsumoto, S. Kida. *J. Chem. Soc., Dalton Trans.*, **1990**, 195.
- [149] P. Matsushima, H. Hamada, K. Watanabe, M. Koikawa, T. Tokii, *J. Chem. Soc., Dalton Trans.*, **1999**, 971.
- [150] E. Spodine, A. M. Atria, J. Valenzuela, J. Jalocha, J. Manzur, A. M. Garcia, M. T. Garland, O. Pena, J. Y. Saillard, *J. Chem. Soc., Dalton Trans.*, **1999**, 3029.
- [151] M. K. Ehlert, S. J. Rettig, A. Storr, R. C. Thompson, J. Trotter, *Can. J. Chem.* **1992**, *70*, 2161.
- [152] D. J. de Geest, A. Noble, B. Moubaraki, K. S. Murray, D. S. Larsen, S. Brooker, *Dalton Trans.*, **2007**, 467.
- [153] S. Tanase, I. A. Koval, E. Bouwman, R. de Gelder, J. Reedijk, *Inorg. Chem.*, **2005**, *44*, 7860.
- [154] J. Klingele (née Hausmann), A. I. Prikhod'ko, G. Leibelng, S. Demeshko, S. Dechert, F. Meyer, *Dalton Trans.*, **2007**, 2003.
- [155] W. Duffy, K. P. Barr, *Phys. Rev.*, 1968, *165*, 647.
- [156] J. W. Hall, W. E. Marsh, R. R. Weller, W. E. Hatfield, *Inorg. Chem.*, **1981**, *20*, 1033.
- [157] L. K. Thompson, T. C. Woon, D. B. Murphy, E. J. Gabe, F. L. Lee, Y. Le Page, *Inorg. Chem.*, **1985**, *24*, 4719.
- [158] L. K. Thompson, S. K. Mandal, E. J. Gabe, F. L. Lee, *Inorg. Chem.*, **1987**, *26*, 657.

- [159] S. K. Mandal, L. K. Thompson, E. J. Gabe, F. L. Lee, *Inorg. Chem.*, **1987**, *26*, 2384.
- [160] J. K. Beattie, G. A. Polyblank, *Aus. J. Chem.*, **1995**, *48*, 861.
- [161] Q. F. Zhou, Q. Wang, Zheng Xu, *Materials Letters*, **2003**, *57*, 1915.
- [162] M. Sarla, M. Pandit, D.K. Tyagi, J.C. Kapoor, *J. Hazardous Materials*, **2004**, *116*, 49.
- [163] J. He, J.-X. Zhang, C.-K. Tsang, Z. Xu, Y.-G. Yin, D. Li, S.-W. Ng, *Inorg. Chem.*, **2008**, *47*, 7948.

## Appendix 1: Vector coupling approach to magnetic modelling:

### A1.1: Dinuclear compounds:

The coupling in dinuclear complexes may be approached by the Kambe [48] approach.

The Hamiltonian to describe a dinuclear complex (with the exchange coupling expressed as  $2J$ ) is:

$$H_{ex} = -2J_{12}(S_1 \cdot S_2) \quad (A1.1)$$

We will now define

$$S' = S_1 + S_2 \quad (A1.2)$$

Squaring and rearranging equation A1.2 gives

$$(S_1 + S_2)^2 = (S' \cdot S') = 2S(S+1) + 2(S_1 \cdot S_2) \quad (A1.3)$$

$$2(S_1 \cdot S_2) = (S' \cdot S') - 2S(S+1) \quad (A1.4)$$

which can be substituted back into equation A1.1 to give:

$$H_{ex} = -J_{12}[(S' \cdot S') - S(S+1)] \quad (A1.5)$$

This is now a general form of the Hamiltonian suitable for addressing dinuclear clusters.

Note:  $S' = (S_1 + S_2) \dots |S_1 - S_2|$  in integer steps, therefore  $(S' \cdot S')$  will have  $[S'(S'+1)]$  eigenvalues.

Therefore energies for this system are expressed in equation (A1.6) as:

$$E(S') = -J[S'(S'+1) - 2S(S+1)] \quad (A1.6)$$

Which may now be substituted into the modified Van Vleck expression in order to evaluate magnetic susceptibility as a function of temperature. Note that the degeneracy  $\omega(S') = 1$  for dinuclear clusters.:

$$\chi M = \frac{N\beta^2 g^2}{3k(T-\theta)} \frac{\sum S'(S'+1)(2S'+1)\Omega(S')e^{-E(S')/kT}}{\sum (2S'+1)\Omega(S')e^{-E(S')/kT}} (1-\rho) + \quad (A1.7)$$

$$\frac{N\beta^2 g^2 S(S+1)\rho}{3kT} + TIP$$

Magnetic susceptibility as a function of temperature may now be evaluated.

While a closed-form of the equation can be obtained by manually, by calculating the spin states and energies and then substituting those into the Van Vleck equation, a different approach can also be used to evaluate this problem. A Turbo Basic v. 1.0© (1987; Borland International, Inc.) routine that evaluates the numerator and denominator of the Van Vleck equation separately for each possible energy state by a series of nested loops, and then sums and recombines these to generate a complete susceptibility profile as a function of temperature, can be employed. Figure A1.1 gives the core of this program. S is an input required from the user, which is then defined to be equal to S<sub>1</sub>, and S<sub>2</sub>.

Evaluate:

Espin=0: muo# = 0: muu# = 0

J1=J1/1.4388

Sstar = S1 + S2

For SK = Sstar to abs(S1-S2) step -1

if SK<0, then SK=-SK

a = SK\*(SK+1)

b= 1+(2\*SK)

Sp=S\*(S+1)

term1= J1\*(a-2\*Sp)

Espin = term1

Espin = Espin/T

top# = (a\*b)\*(e^Espin)

bot# = b\*(e^Espin)

muo# = muo# +top#

muu# = muu# +bot#

next SK

chi = muo#/muu#

chi=chi\*const\*g\*g/(3\*(T-th))

chi=chi\*(1-ro)+TIP+ro\*const\*g\*g\*S\*(S+1)/(3\*T)

J1=J1\*1.4388

Return

**Figure A1.1:** The core of a Turbo Basic routine for evaluating susceptibility as a function of temperature for a homometallic dinuclear system.

### A1.2: Trinuclear Compounds:

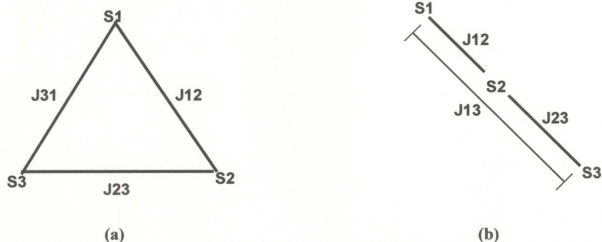


**Figure A1.2:** General scheme for the coupling in a) an equilateral triangle and b) a linear triad of spin centers.

The Hamiltonian to describe either of these cases (with the exchange coupling defined as  $2J$ ) is:

$$H_{\alpha} = -2[J_{12}(S_1 \cdot S_2) + J_{23}(S_2 \cdot S_3) + J_{31}(S_3 \cdot S_1)] \quad (\text{A1.8})$$

Letting  $J = J_{12} = J_{23}$ ;  $\alpha J = J_{31}$

$$H_{\alpha} = -2J[(S_1 \cdot S_2) + (S_2 \cdot S_3) + \alpha(S_3 \cdot S_1)] \quad (\text{A1.9})$$

Two summations are now defined in equations A1.10 and A1.11:

$$S' = S_1 + S_2 + S_3 \quad (\text{A1.10})$$

and

$$S^* = S_3 + S_1 \quad (\text{A1.11})$$

Squaring equation A1.10 leads to:

$$(S_1 + S_2 + S_3)^2 = (S' \cdot S') = 3S(S+1) + 2(S_1 \cdot S_2) + 2(S_2 \cdot S_3) + 2(S_3 \cdot S_1) \quad (\text{A1.12})$$

Which can be rearranged to give equation A1.13.

$$2(S_1 \cdot S_2) + 2(S_2 \cdot S_3) = (S' \cdot S') - 3S(S+1) - 2(S_3 \cdot S_1) \quad (\text{A1.13})$$

Squaring equation A1.11 leads to:

$$(S_3 + S_1)^2 = (S^* \cdot S^*) = 2S(S+1) + 2(S_3 \cdot S_1) \quad (\text{A1.14})$$

Which can be rearranged to give equation A1.15.

$$2(S_3 \cdot S_1) = (S^* \cdot S^*) - 2S(S+1) \quad (\text{A1.15})$$

Equations A1.13 and A1.15 can now be substituted back into equation A1.9 to give:

$$H_{ex} = -J(S' \cdot S') - 3S(S+1) - (S^* \cdot S^*) + 2S(S+1) + \alpha\{(S^* \cdot S^*) - 2S(S+1)\} \quad (\text{A1.16})$$

Gathering terms leads to equation A1.17, which is a general form of a Hamiltonian suitable for addressing either an equilateral triangle or a linear triad.

$$\begin{aligned} H_{ex} &= -J\{(S' \cdot S') - (S^* \cdot S^*) - S(S+1)\} + \alpha\{(S^* \cdot S^*) - 2S(S+1)\} \\ &= -J[(S' \cdot S') - (1-\alpha)(S^* \cdot S^*) - (1+2\alpha)S(S+1)] \end{aligned} \quad (\text{A1.17})$$

Note that  $S^* = (S_3 + S_1) \dots |S_3 - S_1|$  in integer steps, therefore  $(S^* \cdot S^*)$  will have  $[S^*(S^*+1)]$  eigenvalues and  $S' = (S^* + S) \dots |S^* - S|$  in integer steps, therefore  $(S' \cdot S')$  will have  $[S'(S'+1)]$  eigenvalues.

Finally, for an equilateral triangle where  $J_{31} = J_{12} = J_{23} = J, \therefore \alpha = 1$  the Hamiltonian (A1.17) simplifies to:

$$H_{ex} = -J[(S' \cdot S') - 3S(S+1)] \quad (\text{A1.18})$$

with energies:

$$E = -J[S'(S'+1) - 3S(S+1)] \quad (\text{A1.19})$$

And for a linear triad with a negligible 1-3 interaction  $J_{12} = J_{23} = J; J_{31} \approx 0 \therefore \alpha \approx 0$  and the Hamiltonian (A1.17) simplifies to:

$$H_{\alpha} = -J[(S' \cdot S') - (S^* \cdot S^*) - (S(S+1))] \quad (\text{A1.20})$$

with energies:

$$E = -J[S'(S'+1) - S^*(S^*+1) - S(S+1)] \quad (\text{A1.21})$$

For either case the energies may now be substituted into the modified Van Vleck expression (equation A1.7) in order to evaluate magnetic susceptibility as a function of temperature. While a closed-form of the equation can be obtained by manually calculating the spin states and energies and then substituting those into the Van Vleck equation, a different approach can also be used to evaluate this problem. A Turbo Basic v. 1.0© (1987; Borland International, Inc.) routine that evaluates the numerator and denominator of the Van Vleck equation separately for each possible energy state by a series of nested loops, and then sums and recombines these to generate a complete susceptibility profile as a function of temperature, can be employed. Figure A1.3 gives the core of this program for an equilateral triangle expression. S is an input required from the user, which is then defined to be equal to  $S_1, S_2$  and  $S_3$ .

```

Evaluate:
Espin=0: muo# = 0: muu# = 0
J1=J1/1.4388
Sstar = S1 + S2
For SK = Sstar to abs(S1-S2) step -1
  hi=SK+S3: lo = SK-S3
  if lo<0 then lo=-lo
  if hi<lo then swap hi,lo
    For ST = hi to lo step -1
      a = ST*(ST+1)
      d= 1+(2*ST)
      Sp=S*(S+1)
      term1= J1*(a-3*Sp)
      Espin = term1
      Espin = Espin/T
      top# = (a*d)*(e^Espin)
      bot# = d*(e^Espin)
      muo# = muo# +top#
      muu# = muu# +bot#
    Next ST
  next SK
chi = muo#/muu#
chi=chi*const*g*g/(3*(T-th))
chi=chi*(1-ro)+TIP+ro*const*g*g*S*(S+1)/(3*T)
J1=J1*1.4388
Return

```

**Figure A1.3:** The core of a Turbo Basic routine for evaluating susceptibility as a function of temperature for an equilateral triangle.

### A1.3: Tetranuclear Compounds:

A general tetranuclear exchange model is illustrated in Figure A1.4.

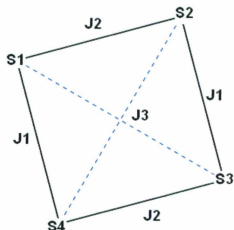


**Figure A1.4:** General scheme for the coupling in a tetranuclear complex.

A general Hamiltonian to describe this exchange situation is:

$$H_{ex} = -2J1(S_2 \cdot S_3 + S_1 \cdot S_4) - 2J2(S_1 \cdot S_2 + S_3 \cdot S_4) - 2J3(S_1 \cdot S_3 + S_2 \cdot S_4) \quad (\text{A1.22})$$

We will now define

$$S' = S_1 + S_2 + S_3 + S_4 \quad (\text{A1.23})$$

Squaring equation A1.23 gives:

$$(S_1 + S_2 + S_3 + S_4)^2 = (S' \cdot S') = 4S(S+1) + 2(S_1 \cdot S_2) + 2(S_1 \cdot S_3) + 2(S_4 \cdot S_1) + 2(S_2 \cdot S_3) + 2(S_2 \cdot S_4) + 2(S_3 \cdot S_4) \quad (\text{A1.24})$$

Which can be rearranged to give equation A1.25.

$$2(S_2 \cdot S_3 + S_4 \cdot S_1) = (S' \cdot S') - 2[(S_1 \cdot S_2) + (S_1 \cdot S_3) + (S_2 \cdot S_4) + (S_3 \cdot S_4) + 2S(S+1)] \quad (\text{A1.25})$$

The following will also be defined, squared and rearranged:

$$S^{**} = S_1 + S_2 \quad (\text{A1.26})$$

$$(S_1 + S_2)^2 = (S^{**} \cdot S^{**}) = 2S(S+1) + 2(S_1 \cdot S_2) \quad (\text{A1.27})$$

$$2(S_1 \cdot S_2) = (S^{**} \cdot S^{**}) - 2S(S+1) \quad (\text{A1.28})$$

$$S^{++} = S_3 + S_4 \quad (\text{A1.29})$$

$$(S_3 + S_4)^2 = (S^{++} \cdot S^{++}) = 2S(S+1) + 2(S_3 \cdot S_4) \quad (\text{A1.30})$$

$$2(S_3 \cdot S_4) = (S^{++} \cdot S^{++}) - 2S(S+1) \quad (\text{A1.31})$$

$$S^* = S_1 + S_3 \quad (\text{A1.32})$$

$$(S_1 + S_3)^2 = (S^* \cdot S^*) = 2S(S+1) + 2(S_1 \cdot S_3) \quad (\text{A1.33})$$

$$2(S_1 \cdot S_3) = (S^* \cdot S^*) - 2S(S+1) \quad (\text{A1.34})$$

$$S^+ = S_2 + S_4 \quad (\text{A1.35})$$

$$(S_2 + S_4)^2 = (S^+ \cdot S^+) = 2S(S+1) + 2(S_2 \cdot S_4) \quad (\text{A1.36})$$

$$2(S_2 \cdot S_4) = (S^+ \cdot S^+) - 2S(S+1) \quad (\text{A1.37})$$

Substituting equations A1.28, A1.31, A1.34 and A1.37 into A1.25 gives:

$$2(S_4 \cdot S_1 + S_2 \cdot S_3) = (S^+ \cdot S^+) - (S^{**} \cdot S^{**}) + 2S(S+1) - (S^{++} \cdot S^{++}) + 2S(S+1) - (S^* \cdot S^*) + 2S(S+1) - (S^+ \cdot S^+) + 2S(S+1) - 4S(S+1) \quad (\text{A1.38})$$

Gathering terms and dividing by 2 gives equation A1.39:

$$S_4 \cdot S_1 + S_2 \cdot S_3 = \frac{1}{2}(S^+ \cdot S^+) - \frac{1}{2}(S^{**} \cdot S^{**}) - \frac{1}{2}(S^+ \cdot S^+) - \frac{1}{2}(S^{**} \cdot S^{**}) - \frac{1}{2}(S^{++} \cdot S^{++}) + 2S(S+1) \quad (\text{A1.39})$$

A new, general exchange Hamiltonian for tetranuclear clusters may now be defined:

$$H_{ex} = -J1(S^+(S^++1) - S^{**}(S^{**}+1) - S^{++}(S^{++}+1) - S^+(S^++1) - S^*(S^*+1) - J2[S^{++}(S^{++}+1) + S^{**}(S^{**}+1)] - J3[S^*(S^*+1) + S^+(S^++1) - 4S(S+1)] \quad (\text{A1.40})$$

The general tetranuclear Hamiltonian can be simplified to represent specific cases. If  $J_3 = 0$ , then the model represents a rectangular system with no cross coupling.

The exchange Hamiltonian for this system is:

$$H_{ex} = -J_1(S'(S'+1) - S^{**}(S^{**}+1) - S^{++}(S^{++}+1) - S^+(S^++1) - S^*(S^*+1) - J_2[S^{**}(S^{**}+1) + S^{++}(S^{++}+1)]) \quad (A1.41)$$

For a square with cross coupling,  $J_1 = J_2$  and the exchange Hamiltonian becomes:

$$H_{ex} = -J_1[S'(S'+1) - S^*(S^*+1) - S^+(S^++1)] - J_3[S^*(S^*+1) + S^+(S^++1) - 4S(S+1)] \quad (A1.42)$$

For a square without cross coupling, the exchange Hamiltonian becomes:

$$H_{ex} = -J_1(S'(S'+1) - S^*(S^*+1) - S^+(S^++1)) \quad (A1.43)$$

Finally, if  $J_1 = J_2 = J_3$ , the model can represent a tetrahedron:

$$H_{ex} = -J_1(S'(S'+1) - 4S(S+1)) \quad (A1.44)$$

Again, simple computer programs can be written to model magnetic data using these expressions.

## Appendix 2: Magnetic models, turbo basic routines, OW01.ini files, and spk files:

### A2.1.1: Simple Dinuclear Complexes - 8.1

The exchange Hamiltonian for a simple dinuclear compound is:

$$H_{ex} = -J\{S_1 \cdot S_2\}$$

The input OW01.ini file for a Cu(II)<sub>2</sub> complex is:

```
Spins: 1 1
Couplings: 12
Strengths: -1
Output: Cu2
```

And the \*.spk file generated by OW01.exe is:

```
MDA 01.00 SPK 00
#PROGRAM:
  Program OW0L, (c) Oliver Waldmann, Version 11.5.01
#HAMILTONIAN:
  Heisenberg Hamiltonian
#SYSTEM:
  Spins = 1/2 1/2
  Couplings = 1-2
#PARAMETER:
  Strengths = -1
  Emin = -0.75
#COMMENT:
  sorted spektrum with classification
#DATA:          ←(Column one is the relative energy, and column two is 2 Sz)
0               0      0
1               2      0
```

### A2.1.2: Dinuclear Complexes by an alternating chain model - 8.1

The exchange Hamiltonian for an alternating chain [155,156] model of hydrogen bonded dinuclear compounds is:

$$H_{ex} = -2\{J\{S_i \cdot S_{i+1}\} + \alpha J\{S_{i+1} \cdot S_{i+2}\}\}$$

The experimental data is fitted to the susceptibility expression by non-linear regression using a TurboBasic routine with the following "core":

```
*****
*** Calculation of mu (eff)
*****
Evaluate:
xx# = -J1/kk/T
term1 = -0.12587+0.22752*al
term2 = 0.019111-0.13307*al+0.50967*al^2-1.3167*al^3+1.0081*al^4
term3 = 0.10772+1.4192*al
term4 = -0.0028521-0.42346*al+2.1953*al^2-0.82412*al^3
term5 = 0.37754-0.067022*al+6.9805*al^2-21.678*al^3+15.838*al^4
chi = (con * g * g)/(T-
th)*(0.25+term1*xx#+term2*xx#^2)/(1+term3*xx#+term4*xx#^2+term5*xx#^3)
rub = (con * g * g * S * (S + 1) * alpha) / (3 * kk * T)
chi=(chi*(1-alpha)) + rub + tip
chi=2*chi
RETURN
```

The constants are defined as:

```
'N = 6.02205 * (10 ^ 23)
'beta = 9.27408 * (10 ^ -24)
'e = 2.7182818284#
'k = 1.38066 * (10 ^ -23)
con = 0.37513
kk=0.69503
S = 0.5
```

The values that are fitted by this routine, and their initial values are:

```
th = 0
J = 0
rho = 0
alpha = 0
J1 = -1
J2 = -1
g = 2
```

## A2.2: Trinuclear Complexes - 3.2

The exchange Hamiltonian for a trinuclear compound with  $J = J12 = J23$  and with  $J13$  assumed to be negligible is:

$$H_{ex} = -J(S_1 \cdot S_2 + S_2 \cdot S_3)$$

The input OW01.ini file for a  $Mn(II)_3$  complex is:

```
Spins: 5 5 5
Couplings: 12 23
Strengths: -1 -1
Output: Mn3
```

And the \*.spk file generated by OW01.exe is:

MDA 01.00 SPK 00

#PROGRAM:

Program OW0L, (c) Oliver Waldmann, Version 11.5.01

#HAMILTONIAN:

Heisenberg Hamiltonian

#SYSTEM:

Spins = 5/2 5/2 5/2

Couplings = 1-2 2-3

#PARAMETER:

Strengths = -1 -1

Emin = -15

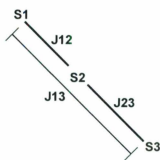
#COMMENT:

sorted spektrum with classification

#DATA:

0	5	0
2.5	3	0
3.5	7	0
5	5	1
5	1	0
6.5	3	1
8	1	1
8	9	0
8.5	7	1
9	5	2
9.5	3	2
11.5	3	3
12	5	3
12.5	7	2

←Note the non-zero ground state associated with the odd number of spins present in the cluster.



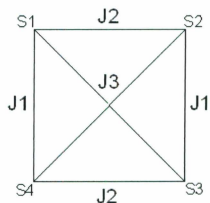
13	9	1
13.5	11	0
14	5	4
15	5	5
15.5	7	3
17	9	2
17.5	7	4
18.5	11	1
20	9	3
20	13	0
22.5	11	2
25	13	1
27.5	15	0

Note: Clearly, with increasing numbers of magnetic centres and exchange pathways the number of non-degenerate spin states becomes significantly larger. For this reason, all of the data contained within the \*.spk files will not be given for further examples, however, these are all contained on the disk of magnetic and crystallographic data.

### A2.3: Tetranuclear Complexes - 3.3, 3.4, 3.5 and 3.7

The exchange Hamiltonian for a tetranuclear compound with  $J = J_1 = J_2$  and  $J_3$  assumed to be negligible is:

$$H_{ex} = -J(S_1 \cdot S_2 + S_2 \cdot S_3 + S_3 \cdot S_4 + S_1 \cdot S_4)$$

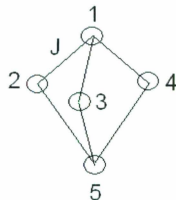


The input OW01.ini file for a Ni(II) <sub>4</sub> complex is:	The input OW01.ini file for a Cu(II) <sub>4</sub> complex is:
Spins: 2 2 2 2 Couplings: 12 23 34 41 Strengths: -1 -1 -1 -1 Output: Ni4	Spins: 1 1 1 1 Couplings: 12 23 34 41 Strengths: -1 -1 -1 -1 Output: Cu4
And the abbreviated *.spk file generated by OW01.exe is:	And the abbreviated *.spk file generated by OW01.exe is:
<pre>#SYSTEM:   Spins = 2/2 2/2 2/2 2/2   Couplings = 1-2 2-3 3-4 4-1 #PARAMETER:   Strengths = -1 -1 -1 -1   Emin = -6 #DATA: 0      0      0 1      2      0 3      4      0 3      2      1 3      2      2 4      0      1 5      4      1 5      4      2 etc...</pre>	<pre>#SYSTEM:   Spins = 1/2 1/2 1/2 1/2   Couplings = 1-2 2-3 3-4 4-1 #PARAMETER:   Strengths = -1 -1 -1 -1   Emin = -2 #DATA: 0      0      0 1      2      0 2      0      1 2      2      1 2      2      2 3      4      0</pre>

#### A2.4: Pentanuclear Clusters - 3.8

The exchange Hamiltonian for a pentanuclear cluster is:

$$H_{\alpha} = -J(S_1 \cdot S_3 + S_4 \cdot S_3 + S_5 \cdot S_3 + S_1 \cdot S_2 \\ + S_5 \cdot S_2 + S_4 \cdot S_2)$$



The input OW01.ini file for an Mn(II)<sub>5</sub> complex is:

```
Spins: 5 5 5 5 5
Couplings: 12 23 14 52 53 54
Strengths: -1 -1 -1 -1 -1
Output: Mn5
```

And the \*.spk file generated by OW01.exe is:

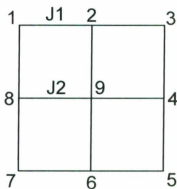
```
MDA 01.00 SPK 00
#PROGRAM:
  Program OW0L, (c) Oliver Waldmann, Version 11.5.01
#HAMILTONIAN:
  Heisenberg Hamiltonian
#SYSTEM:
  Spins = 5/2 5/2 5/2 5/2 5/2
  Couplings = 1-2 1-3 1-4 5-2 5-3 5-4
#PARAMETER:
  Strengths = -1 -1 -1 -1 -1
  Emin = -42.5000000000002
#COMMENT:
  sorted spektrum with classification
#DATA:
0          5      0
3.5       7      0
5         3      0
5         3      1
7.5       5      1
7.5       5      2
8         9      0
8.5       7      1
10        1      0
10        1      1
10        1      2
11        7      2
etc...
```

### A2.5: [3×3] M(II)<sub>9</sub> Grids

The exchange Hamiltonian for an isotropic [3×3] M<sub>9</sub> grid

is:

$$H_{ex} = -J1\{S_1 \cdot S_2 + S_2 \cdot S_3 + S_3 \cdot S_4 + S_4 \cdot S_5 + S_5 \cdot S_6 \\ + S_6 \cdot S_7 + S_7 \cdot S_8 + S_1 \cdot S_8\} \\ - J2\{S_2 \cdot S_9 + S_4 \cdot S_9 + S_6 \cdot S_9 + S_8 \cdot S_9\}$$



#### A2.5.1: [3×3] Co(II)<sub>9</sub> Grids - 4.3

If it is assumed that  $J=J1=J2$  and that orbital contributions can be ignored, then the input OW01.ini file for a Co(II)<sub>9</sub> grid complex is:

```
Spins: 3 3 3 3 3 3 3 3 3
Couplings: 12 23 34 45 56 67 78 81 29 49 69 89
Strengths: -1 -1 -1 -1 -1 -1 -1 -1 -1 -1 -1
Output: Co(II)9
```

And the \*.spk file generated by OW01.exe is:

```
MDA 01.00 SPK 00
#PROGRAM:
  Program OW0L, (c) Oliver Waldmann, Version 11.5.01
#HAMILTONIAN:
  Heisenberg Hamiltonian
#SYSTEM:
  Spins = 3/2 3/2 3/2 3/2 3/2 3/2 3/2 3/2 3/2
  Couplings = 1-2 2-3 3-4 4-5 5-6 6-7 7-8 8-1 2-9 4-9 6-9 8-9
#PARAMETER:
  Strengths = -1 -1 -1 -1 -1 -1 -1 -1 -1 -1 -1
  Emin = -32.084208489536
#COMMENT:
  sorted spektrum with classification
#DATA:
0          3          0
1.502661438 5          0
2.354198636 1          0
2.354198636 1          1
etc...     ← There are 30 276 non-degenerate spin states for this system!
```

### A2.5.2: [3×3] Cu(II)<sub>9</sub> Grids - 4.5, 4.6, 6.3 and 6.4

For [3×3] Cu(II)<sub>9</sub> grids J1 and J2 are not equal in magnitude, and for 4.5, 4.6 and 6.4 the couplings are also not equal in sign (that is, J1 is ferromagnetic while J2 is antiferromagnetic). An input OW01.ini file for a Cu(II)<sub>9</sub> grid complex with both ferro- and antiferromagnetic contributions is:

```
Spins: 1 1 1 1 1 1 1 1 1
Couplings: 12 23 34 45 56 67 78 81 29 49 69 89
Strengths: -0.1 -0.1 -0.1 -0.1 -0.1 -0.1 -0.1 -0.1 0.1 1 1 1 1
Output: Cu(II)9
```

And the \*.spk file generated by OW01.exe is:

```
MDA 01.00 SPK 00
#PROGRAM:
  Program OW0L, (c) Oliver Waldmann, Version 11.5.01
#HAMILTONIAN:
  Heisenberg Hamiltonian
#SYSTEM:
  Spins = 1/2 1/2 1/2 1/2 1/2 1/2 1/2 1/2 1/2
  Couplings = 1-2 2-3 3-4 4-5 5-6 6-7 7-8 8-1 2-9 4-9 6-9 8-9
#PARAMETER:
  Strengths = -0.1 -0.1 -0.1 -0.1 -0.1 -0.1 -0.1 -0.1 0.1 1 1 1 1
  Emin = -1.30136333119542
#COMMENT:
  sorted spektrum with classification
#DATA:
0          1      0
0.06499966915    3      0
0.141364005      3      1
0.141364005      3      2
0.1536708092     3      3
0.172625541      5      0
0.2489343583     5      1
0.2520729535     5      2
0.2520729535     5      3
0.2833504458     5      4
etc...
```

Note: If, for example, MAGMUN4.1 returns a fitted  $J = 10$ , then  $J_1 = 1 \text{ cm}^{-1}$  and  $J_2 = -10 \text{ cm}^{-1}$ . Since these values are determined from a fixed ratio, the fitted values from the non-linear regression are not rigorous, however, they are sensible in light of the structural analysis.

### A2.5.3: [3×3] Cu(II)<sub>8</sub>Mn(II)<sub>1</sub> Grid - 5.4

A similar approach as that used for the [3×3] Cu(II)<sub>9</sub> grids may be employed where J1 and J2 are not equal in magnitude or sign and the identity of the central ion is not the same as those in the ring. The input OW01.ini file for a Cu(II)<sub>8</sub>Mn(II)<sub>1</sub> grid complex with both ferro- and antiferromagnetic contributions is:

```
Spins: 1 1 1 1 1 1 1 1 5
Couplings: 12 23 34 45 56 67 78 81 29 49 69 89
Strengths: -0.2 -0.2 -0.2 -0.2 -0.2 -0.2 -0.2 -0.2 -0.2 1 1 1 1
Output: Cu(II)9
```

And the \*.spk file generated by OW01.exe is:

```
MDA 01.00 SPK 00
#PROGRAM:
  Program OW0L, (c) Oliver Waldmann, Version 11.5.01
#HAMILTONIAN:
  Heisenberg Hamiltonian
#SYSTEM:
  Spins = 1/2 1/2 1/2 1/2 1/2 1/2 1/2 1/2 5/2
  Couplings = 1-2 2-3 3-4 4-5 5-6 6-7 7-8 8-1 2-9 4-9 6-9 8-9
#PARAMETER:
  Strengths = 0.2 0.2 0.2 0.2 0.2 0.2 0.2 0.2 -1 -1 -1 -1
  Emin = -7.24002235653721
#COMMENT:
  sorted spektrum with classification
#DATA:
0          3      0
0.09165342133    1      0
0.09165342133    1      1
0.09601322388    1      2
0.2282804404     1      3
0.2360949702     1      4
0.2722473489     3      1
0.2722473489     3      2
0.2759967665     3      3
0.2937650477     5      0
1.664840164      7      0
1.697778044      5      1
1.697778044      5      2
etc...
```

**A2.5.4: [3×3] Mn(II)<sub>9</sub> Grids - 4.2, 6.6**

An isotropic spin Hamiltonian would involve 45 electrons and an enormous matrix calculation. Instead the experimental data is fitted to a model based upon the Fisher approach [73,74], defined by the following susceptibility expressions:

$$\chi_{mol} = \left( \frac{8 \times \chi_{Mn} + 1.094 \times g^2}{T - \theta} \right) \times (1 - \rho) + \left( \frac{1.094 \times g^2}{T} \right) \times \rho + TIP$$

$$u = \coth \left[ \frac{JS(S+1)}{kT} \right] - \left[ \frac{kT}{JS(S+1)} \right]$$

$$\chi_{Mn} = \frac{Ng^2 \beta^2 S(S+1)(1+u)}{3kT(1-u)}$$

Non-linear regression is used to treat the susceptibility expression using a TurboBasic routine with the following "core":

```
*****
*** Calculation of mu (cff)
*****
Evaluate:
term0 = J1 * S * (S + 1) / kk
term1 = T / term0
term2 = term0 / T
term3# = EXP(term2) + EXP(-term2)
term6# = EXP(term2) - EXP(-term2)
term3 = term3# / term6#
u = term1 - term3
term4 = S * (S + 1)
term5 = (1 - u) / (1 + u)
chi = con * g * g * term4 * term5 / (3 * kk * (T - th))
term7 = (2 * J2 * chi) / (con * g * g)
bot = 1 - term7
chi = chi / bot
rub = (con * g * g * S * (S + 1) * alpha) / (3 * kk * T)
chi = (chi * (1 - alpha)) + rub + tip
chi = chi * 8
chi = chi + (con * g * g * S1 * (S1 + 1)) / (3 * kk * T)
```

'J = J / 1.439; J2 = J2 / 1.439  
RETURN

The constants are defined as:

'N = 6.02205 \* (10 ^ 23)  
'beta = 9.27408 \* (10 ^ -24)  
'e = 2.71828182846#  
'k = 1.38066 \* (10 ^ -23)  
con = 0.37513  
kk=0.69503

The values that are fitted by this routine, and  
their initial values are:

th = 0  
J = 0  
'rho = 0  
alpha = 0  
J1 = -1  
J2 = -1  
g = 2

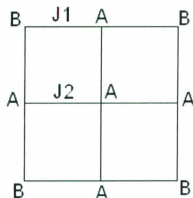
Additionally, the spin sates for the atoms in the outer ring (S) and for the atom in the  
centre position (S1) must be entered. For the case where all ions are Mn(II), S = S1 = 2.5  
(ie. 5/2).

### A2.6: [3×3] A<sub>5</sub>B<sub>4</sub> Grids

The exchange Hamiltonian for an isotropic [3×3] M<sub>9</sub> grid is:

$$H_{ex} = -J1\{S_1 \cdot S_2 + S_2 \cdot S_3 + S_3 \cdot S_4 + S_4 \cdot S_5 + S_5 \cdot S_6 + S_6 \cdot S_7 + S_7 \cdot S_8 + S_8 \cdot S_9\} \\ - J2\{S_2 \cdot S_9 + S_4 \cdot S_9 + S_6 \cdot S_9 + S_8 \cdot S_9\}$$

#### A2.6.1: [3×3] Mn(II)<sub>5</sub>Cu(II)<sub>4</sub> and Co(II)<sub>5</sub>Co(III)<sub>4</sub> Grids - 5.2



Both Mn(II)<sub>5</sub>Cu(II)<sub>4</sub> and Co(II)<sub>5</sub>Co(III)<sub>4</sub> grids can be treated by this model. In one case A=Co(II) and B=Co(III), while in the other A = Mn(II) and B = Cu(II). Here, the input OW01.ini file for the Mn(II)<sub>5</sub>Cu(II)<sub>4</sub> grid, with J = J1 = J2 is shown (Co(II)<sub>5</sub>Co(III)<sub>4</sub> case can be found on the disk of Magnetic and Crystallographic data).

Spins: 1 5 1 5 1 5 1 5 5

Couplings: 12 23 34 45 56 67 78 81 29 49 69 89

Strengths: -1 -1 -1 -1 -1 -1 -1 -1 -1 -1

Output: Mn5Cu4

And the \*.spk file generated by OW01.exe is:

MDA 01.00 SPK 00

#PROGRAM:

Program OW0L, (c) Oliver Waldmann, Version 11.5.01

#HAMILTONIAN:

Heisenberg Hamiltonian

#SYSTEM:

Spins = 1/2 5/2 1/2 5/2 1/2 5/2 1/2 5/2 5/2

Couplings = 1-2 2-3 3-4 4-5 5-6 6-7 7-8 8-1 2-9 4-9 6-9 8-9

#PARAMETER:

Strengths = -1 -1 -1 -1 -1 -1 -1 -1 -1 -1

Emin = -39.1468936196929

#COMMENT:

sorted spektrum with classification

#DATA:

0	11	0	←Theoretical ground state is S'=11/2
3.193490698	9	0	←Next lowest lying spin state is S'=9/2
3.193490698	9	1	
etc...			

### A2.6.2: [3x3] Mn(II)<sub>5</sub>Ni(II)<sub>4</sub> Grid - 5.3

If the metal ion A = Mn(II) and B = Ni(II) and J=J1=J2 then the number of spin states exceeds the number of lines than can be read by MAGMUN4.1. Oliver Waldmann's OW1L.exe reduced symmetry program [121] must instead be employed. The input OW1L.ini file for this Mn(II)<sub>5</sub>Ni(II)<sub>4</sub> grid is:

```
Spins: 2 5 2 5 2 5 5
Couplings: 12 23 34 45 56 67 78 81 29 49 69 89
Strengths: -1 -1 -1 -1 -1 -1 -1 -1 -1 -1 -1
Couplingscheme: 15x37xx26x48xxx9x
Symmetryelements:
123456789
567812349
781234569
345678129
765432189
321876549
543218769
187654329
Symmetrygroup: D4
Output: Mn5Ni4
```

Here, it is the output \*.eig file that must be used to generate a magnetic simulation. The \*.eig file generated by OW1L.exe is:

```
MDA 01.00 EIG 01
#PROGRAM:
Program OW1L, (c) Oliver Waldmann, Version 4.6.03
#HAMILTONIAN:
Heisenberg Hamiltonian
#SYSTEM:
Spins = 2/2 5/2 2/2 5/2 2/2 5/2 2/2 5/2 5/2
Couplings = 1-2 2-3 3-4 4-5 5-6 6-7 7-8 8-1 2-9 4-9 6-9 8-9
Couplingscheme: 1 5 x 3 7 x x 2 6 x 4 8 x x x 9 x
Symmetrygroup: D4
#PARAMETER:
Strengths = -1 -1 -1 -1 -1 -1 -1 -1 -1 -1 -1
Symmetryelements:
1 2 3 4 5 6 7 8 9
5 6 7 8 1 2 3 4 9
7 8 1 2 3 4 5 6 9
3 4 5 6 7 8 1 2 9
7 6 5 4 3 2 1 8 9
```

```

3 2 1 8 7 6 5 4 9
5 4 3 2 1 8 7 6 9
1 8 7 6 5 4 3 2 9
#COMMENT:
energies
#DATA:      ← The data is not in a format that can be read by a text based program
etc...
```

The \*.eig file is then input into the program owXisg.exe, where values of g, J, TIP, and  $\theta$  can be entered by the user, and a \*.mxi file is generated with the calculated  $\chi$ ,  $\chi T$  and  $\mu_{\text{eff}}$  values over a specified temperature range. The \*.mxi file for this example follows.

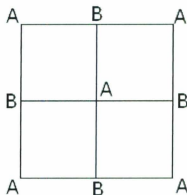
```

#MDA OWXISG ASC
#PROGRAM:
  Program OWXISG (pack3), (c) Oliver Waldmann, Release 21.11.2006
#HAMILTONIAN:
  Spin Hamiltonian with Jij
#SYMMETRY:
  No
#DIAGONALIZATION:
  Diagonalization: QR
#SYSTEM:
  Si: 2/2 5/2 2/2 5/2 2/2 5/2 2/2 5/2 5/2
  CJij: 1-2 2-3 3-4 4-5 5-6 6-7 7-8 8-1 2-9 4-9 6-9 8-9
  Jij: -1 -1 -1 -1 -1 -1 -1 -1 -1 -1 -1
#PARAMETER:
  Emin: -50.6931
  EIG: ni4mn5a.eig
  J: 3
  g: 2.17
  xi0: 0.00075      ← TIP
  theta: 0.05
  T: 2>300/3
#COMMENT:
  magnetic susceptibility
#DATAFORMAT:
  T (K) Xi (emu/mol) XiT (emu K/mol) mu_eff
#DATA:
2      4.79926      9.59851      8.76288
5      2.1228      10.614      9.21478
8      1.54069      12.3255     9.92997
11     1.25852      13.8437     10.5238
etc... to a max value of
299    0.0970991    29.0326     15.2401
```

Note that this method of data treatment does not regress the experimental data, but does allow the user to rapidly compare plots of experimental data and calculated values for a variety of manually input  $g$ ,  $J$ ,  $TIP$  and  $\theta$  values.

**A2.6.3:**  $[3 \times 3]$   $Mn(II)_5Zn(II)_4$ - 5.1

The substitution pattern here is slightly different than in the previous examples. Here,  $A=Mn(II)$  ( $S=5/2$ ) and  $B=Zn(II)$  ( $S=0$ ). The exchange here is expected to be weak, long-range antiferromagnetic coupling between  $Mn(II)$  centres *via* the intervening  $Zn(II)$  sites. An exchange Hamiltonian to describe this situation is:



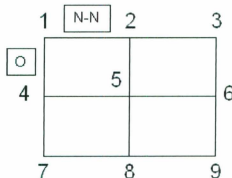
$$H_{ex} = -J(S_1 \cdot S_7 + S_1 \cdot S_9 + S_1 \cdot S_3 + S_5 \cdot S_7 + S_5 \cdot S_9 + S_5 \cdot S_3)$$

This is equivalent to the exchange situation described for a normal pentanuclear  $Mn(II)_5$  cluster (Section A2.4).

A2.7:  $3 \times [1 \times 3]$  Mn(II)<sub>9</sub> - 6.2

$3 \times [1 \times 3]$  Mn(II)<sub>9</sub> rectangular grids cannot be treated by full matrix calculations because of the immensity of the calculations involved. Instead, this is treated by three, linear trinuclear subunits with a molecular field correction to account for nearest neighbor interactions. An exchange Hamiltonian to express this situation is:

$$H_{ex} = -J\{S_1 \cdot S_4 + S_4 \cdot S_7\}$$



And the susceptibility expression

$$\text{is: } \chi_{mol} = \frac{N\beta^2 g^2}{3k(T - zJ' \chi_{trimer})} \frac{\sum S'(S'+1)(2S'+1)e^{-E(S')/kT}}{\sum (2S'+1)e^{-E(S')/kT}} (1 - \rho) + \frac{N\beta^2 g^2 S(S+1)\rho}{3kT} + TIP$$

Non-linear regression is used to treat the susceptibility expression using a TurboBasic routine with the following "core":

```

*****
**Calc. of mu (eff)
*****
Evaluate:
Espin=0: muo#= 0: muu# = 0
J=J/1.4388
J1=J1/1.4388
'Sstar = S1 + S2 + S3
'Splus = S3 + S1
For SK = (S3 + S1) to ABS(S3 - S1) step -1
'if SK<0 then SK=0
For SL = (SK + S2) to ABS(SK - S2) step -1
    a = SL*(SL+1)
    b = 1+(2*SL)
    c = SK*(SK+1)
    d = S*(S + 1)
    term1= J*(a-c-d)+J1*(c-2*d)
    Espin = term1
    Espin = Espin/T
    top# = (a*b)*(e^Espin)
    bot# = b*(e^Espin)
    muo# = muo# +top#
    muu# = muu# +bot#

```

```

next SL
next SK
chi = muo#/muo#
th=zz*J2*chi
chi=chi*const*g*g/(3*(T-th))
chi=chi*(1-ro)+TIP+ro*const*g*g*S*(S+1)/(3*T)
chi=chi*3
J1=J1*1.4388
J=J*1.4388
Return

```

The constants are defined as:

```

'N = 6.02205 * (10 ^ 23)
'beta = 9.27408 * (10 ^ -24)
'e = 2.71828182846#
'k = 1.38066 * (10 ^ -23)
const=0.3751349

```

The values that are fitted by this routine, and their initial values are:

```

g=2
theta = 0
Jcm = 0
rho = 0
alpha = 0
J=-1

```

Additionally, the spin states (S1) for the atoms must be the same and must be entered, as well as the number of nearest neighbors in the extended structure (zz). In this example S1 = 2.5 (that is 5/2) and zz = 1.333 (that is 4/3).

### A2.8: 4x[2x2] M<sub>16</sub> grids - 7.1, 7.3, 7.4

[4x4] M(II)<sub>16</sub> grids (M = Mn and Co) cannot be treated by full matrix calculations because of the immensity of the calculations involved. Instead, they are treated as a set of four compartmentalized [2x2] M<sub>4</sub>-(μ-O<sub>hydrazone</sub>)<sub>4</sub> squares with a molecular field correction to account for nearest neighbor interactions *via* the double μ-NN<sub>pyridazine</sub>/μ-O bridges. An exchange Hamiltonian to express this situation is:

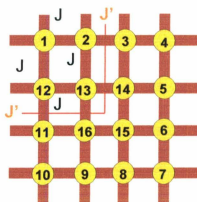
$$H_{ex} = -J\{S_1 \cdot S_2 + S_2 \cdot S_{13} + S_{13} \cdot S_{12} + S_{12} \cdot S_1\}$$

And the susceptibility expression is:

$$\chi_{mol} = \frac{N\beta^2 g^2}{3k(T - zJ' \chi_{square})} \frac{\sum S^i(S^i+1)(2S^i+1)e^{-E(S^i)/kT}}{\sum (2S^i+1)e^{-E(S^i)/kT}} (1 - \rho) + \frac{N\beta^2 g^2 S(S+1)\rho}{3kT} + TIP$$

Non-linear regression is used to treat the susceptibility expression using a TurboBasic routine with the following "core":

```
*****
**Calc. of mu (eff)
*****
Evaluate:
S=S1:S2=S1:S3=S1:S4=S1
Espin=0: mu=0: muo= 0: muu= 0 : muc=0
J1=J1/1.438
J2=J2/1.438
Sstar = S1 + S3
Splus = S2 + S4
For SK = Sstar to 0 step -1
For SL = Splus to 0 step -1
  hi=SK+SL: lo = SK-SL
  if lo<0 then lo=-lo
  if hi<lo then swap hi,lo
  For ST = hi to lo step -1
    a = ST*(ST+1)
    b = SK*(SK+1)
    c = SL*(SL+1)
    d = 1+(2*ST)
    Sp=S*(S+1)
    term1 = J1*(a-b-c)
```



```

        Espin = term1
        Espin = Espin/T
        top = (a*d)*(e^Espin)
        bot = d*(e^Espin)
        muo = muo +top
        muu = muu +bot
    Next ST
next SL
next SK
chi = muo/muu
chi=chi*const*g*g/(3*T-z*J2*chi)
'chi=chi/10
chi=chi*(1-ro)+TIP+ro*const*g*g*S*(S+1)/(3*T)
chi=chi*4
J1=J1*1.438
J2=J2*1.438
Return

```

The constants are defined as:

```

N = 6.02205 * (10 ^ 23)
beta = 9.27408 * (10 ^ -24)
e = 2.71828182846
k = 1.38066 * (10 ^ -23)
const=0.375134

```

The values that are fitted by this routine, and their initial values are:

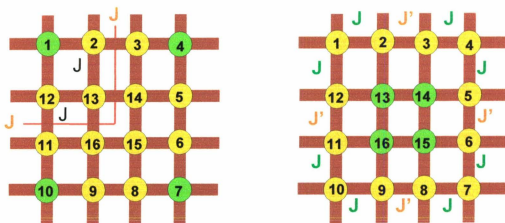
```

g=2
theta = 0
J2 = -5
rho = 0
alpha = 0
J=-1

```

Additionally, the spin states (S1) for the atoms must be the same and must be entered, as well as the number of nearest neighbors in the extended structure (z). For both Mn(II)<sub>16</sub> and Co(II)<sub>16</sub>, z=2, while S1 = 2.5 (that is 5/2) and S1 = 1.5 (that is 3/2), respectively.

A2.9:  $4 \times [2 \times 2]$   $M_{16}$  grids with four diamagnetic centres - 7.2b, 8.3



Both **7.2b**, a  $\text{Co(II)}_2\text{Co(III)}_4$  grid, and **8.3**, a  $\text{Cu(II)}_2\text{Cu(I)}_4$  grid, have one diamagnetic centre in each of the four compartmental  $[2 \times 2]$   $M_4$ - $(\mu\text{-O}_{\text{hydrazone}})_4$  squares. Therefore, these grids may be treated as four trinuclear subunit with a molecular field correction to account for nearest neighbor interactions *via* the double  $\mu\text{-NN}_{\text{pyridazine}}/\mu\text{-O}$  bridges. An exchange Hamiltonian to express this situation is:

$$H_{ex} = -J\{S_2 \cdot S_{13} + S_{13} \cdot S_{12}\}$$

And the susceptibility expression is:

$$\chi_{mol} = \frac{N\beta^2 g^2}{3k(T - zJ' \chi_{trimer})} \frac{\sum S'(S'+1)(2S'+1)e^{-E(S')/kT}}{\sum (2S'+1)e^{-E(S')/kT}} (1 - \rho) + \frac{N\beta^2 g^2 S(S+1)\rho}{3kT} + TIP$$

Non-linear regression is used to treat the susceptibility expression using a TurboBasic routine with the following "core":

```
*****
***(Calc. of mu (eff)
*****
Evaluate:
Espin=0: muo#= 0: muu# = 0
J=J/1.4388
J1=J1/1.4388
'Sstar = S1 + S2 + S3
'Splus = S3 + S1
For SK = (S3 + S1) to ABS(S3 - S1) step -1
'if SK<0 then SK=0
```

```

For SL = (SK + S2) to ABS(SK - S2) step -1
  a = SL*(SL+1)
  b = 1+(2*SL)
  c = SK*(SK+1)
  d = S*(S + 1)
  term1= J*(a-c-d)+J1*(c-2*d)
  Espin = term1
  Espin = Espin/T
  top# = (a*b)*(e^Espin)
  bot# = b*(e^Espin)
  muo# = muo# +top#
  muu# = muu# +bot#
next SL
next SK
chi = muo#/muu#
th=zz*J2*chi
chi=chi*const*g*g/(3*(T-th))
chi=chi*(1-ro)+TIP+ro*const*g*g*S*(S+1)/(3*T)
chi=chi*4
J1=J1*1.4388
J=J*1.4388
Return

```

The constants are defined as:

```

'N = 6.02205 * (10 ^ 23)
'beta = 9.27408 * (10 ^ -24)
'e = 2.71828182846#
'k = 1.38066 * (10 ^ -23)
const=0.3751349

```

The values that are fitted by this routine, and their initial values are:

```

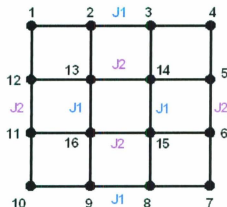
g=2
theta = 0
Jcm = 0
rho = 0
alpha = 0
J=-1

```

Additionally, the spin states (S1) for the atoms must be the same and must be entered, as well as the number of nearest neighbors in the extended structure (zz). In both of these cases, zz = 2, while S1 = 1.5 (that is 3/2) for **7.2b**, a Co(II)<sub>12</sub>Co(III)<sub>4</sub> grid, and S1 = 0.5 (that is 1/2) for **8.3**, a Cu(II)<sub>12</sub>Cu(I)<sub>4</sub> grid.

## A2.10: 4x[2x2] Cu(II)<sub>16</sub> grid - 8.2

The 4x[2x2] Cu(II)<sub>16</sub> grid (8.2) consists of a several different exchange pathways that were discussed in Chapter 8. Simply put, the corners sites, 1, 4, 7, and 10 do not participate in any magnetic exchange with their nearest neighbors and act as Curie centres. The exchange pathways denoted by J1 consist of antiferromagnetic coupling *via* pyridazine  $\mu$ -NN while those denoted by J2 consist of antiferromagnetic coupling *via* both  $\mu$ -NN and  $\mu$ -O bridges. An exchange Hamiltonian to express this situation is:



$$H_{ex} = -J1\{S_2 \cdot S_3 + S_8 \cdot S_9\} - J2\{S_5 \cdot S_6 + S_{11} \cdot S_{12}\} - \\ [J1\{S_{13} \cdot S_{16} + S_{14} \cdot S_{15}\} + J2\{S_{13} \cdot S_{14} + S_{15} \cdot S_{16}\}]$$

Non-linear regression is used to treat the susceptibility expression and to correct for the Curie centres, using a TurboBasic routine with the following "core":

```
*****
*** Calculation of chi
*****
Evaluate:
k = .69503
ff# = (j2 ^ 2 + j1 ^ 2 - j2 * j1) ^ .5
gg# = EXP(ff# / k / T)
hh# = EXP((j1 + ff#) / k / T)
jj# = EXP((j2 + ff#) / k / T)
kk# = EXP((j1 + j2 + ff#) / k / T)
ll# = 6 * gg# + 6 * hh# + 6 * jj# + 30 * kk#
mm# = 1 + gg# ^ 2 + 3 * gg# + 3 * hh# + 3 * jj# + 5 * kk#
pp = .12505 * g ^ 2 / T * (ll# / mm#)
f1# = exp(-j1/k/T)
chi1 = (2 * g ^ 2 * .125045 / (T) * (1 + f1# / 3) ^ -1)
f2# = exp(-j2/k/T)
chi2 = (2 * g ^ 2 * .125045 / (T) * (1 + f2# / 3) ^ -1)
chi3 = pp
chi4 = 0.37513 * g ^ 2 / T
chi = (2 * chi1 + 2 * chi2 + chi3 + chi4) * (1 - alpha) + tip + .093784 * g ^ 2 / T * alpha
RETURN
```

The constants are defined as:

$N = 6.02205 * (10^{23})$   
 $\text{beta} = 9.27408 * (10^{-24})$   
 $e = 2.71828182846$   
 $k = 1.38066 * (10^{-23})$   
 $\text{con} = N * \text{beta} * \text{beta} / k$

The values that are fitted by this routine, and their initial values are:

$g = 2$   
 $\text{theta} = 0$   
 $J_{\text{cm}} = 0$   
 $\text{rho} = 0$   
 $\text{alpha} = 0$

### Appendix 3: Expanded structural data:

#### A3.1: [(ioap-H)(ioap-2H)Co<sub>2</sub>(H<sub>2</sub>O)<sub>4</sub>](BF<sub>4</sub>)<sub>2</sub>(H<sub>2</sub>O)<sub>2.75</sub> (3.1)

##### A. Crystal Data

Empirical Formula	C <sub>22</sub> H <sub>34.50</sub> B <sub>2</sub> Co <sub>2</sub> F <sub>8</sub> N <sub>12</sub> O <sub>8.75</sub>
Formula Weight	898.56
Crystal Color, Habit	brown, prism
Crystal Dimensions	0.28 × 0.12 × 0.10 mm
Crystal System	triclinic
Lattice Type	Primitive
Detector Position	40.00 mm
Pixel Size	0.137 mm
Lattice Parameters	a = 9.882(2) Å b = 14.623(3) Å c = 14.928(4) Å α = 107.465(3) ° β = 107.784(3) ° γ = 95.447(4) ° V = 1917.6(8) Å <sup>3</sup>
Space Group	P1̄ (#2)
Z value	2
Dcalc	1.556 g/cm <sup>3</sup>
F000	913
μ(MoKα)	9.64 cm <sup>-1</sup>

##### B. Intensity Measurements

Detector	Rigaku Saturn
Goniometer	Rigaku AFC8
Radiation	MoKα (λ = 0.71070 Å) graphite monochromated
Detector Aperture	70 mm × 70 mm
Data Images	780 exposures
ω oscillation Range (χ=0.0, φ=0.0)	-15.0 - 15.0°
Exposure Rate	100.0 sec./°
Detector Swing Angle	15.11°
ω oscillation Range (χ=45.0, φ=180.0)	-75.0 - 105.0°
Exposure Rate	100.0 sec./°

Detector Swing Angle	15.11°
$\omega$ oscillation Range ( $\chi=54.0$ , $\phi=0.0$ )	-75.0 - 105.0°
Exposure Rate	100.0 sec./°
Detector Swing Angle	15.11°
Detector Position	40.00 mm
Pixel Size	0.137 mm
$2\theta_{\max}$	61.8°
No. of Reflections Measured	Total: 18471 Unique: 7865 ( $R_{\text{int}} = 0.0453$ )
Corrections	Lorentz-polarization Absorption (trans. factors: 0.8491 - 0.9356) Secondary Extinction (coefficient: 0.0021(15))

### C. Structure Solution and Refinement

Structure Solution	Direct Methods (SIR92)
Refinement	Full-matrix least-squares on $F^2$
Function Minimized	$\sum w (F_o^2 - F_c^2)^2$
Least Squares Weights	$w = 1 / [ \sigma^2(F_o^2) + (0.1591 \cdot P)^2 + 4.5988 \cdot P ]$ where $P = (\text{Max}(F_o^2, 0) + 2F_c^2)/3$
$2\theta_{\max}$ cutoff	53.0°
Anomalous Dispersion	All non-hydrogen atoms
No. Observations (All reflections)	7865
No. Variables	552
Reflection/Parameter Ratio	14.25
Residuals: $R_1$ ( $I > 2.00\sigma(I)$ )	0.0988
Residuals: $R$ (All reflections)	0.1092
Residuals: $wR_2$ (All reflections)	0.2902
Goodness of Fit Indicator	1.077
Max Shift/Error in Final Cycle	0.000
Maximum peak in Final Diff. Map	1.33 e-/Å <sup>3</sup>
Minimum peak in Final Diff. Map	-1.13 e-/Å <sup>3</sup>

**A3.2: [(ioap)<sub>2</sub>(ioap-H)<sub>2</sub>Mn<sub>3</sub>(H<sub>2</sub>O)<sub>2</sub>](NO<sub>3</sub>)<sub>4</sub>(H<sub>2</sub>O) (3.2)****A. Crystal Data**

Empirical Formula	C <sub>44</sub> H <sub>52</sub> Mn <sub>3</sub> N <sub>28</sub> O <sub>19</sub>
Formula Weight	1441.96
Crystal Color, Habit	orange, prism
Crystal Dimensions	0.32 × 0.21 × 0.16 mm
Crystal System	triclinic
Lattice Type	Primitive
Detector Position	39.90 mm
Pixel Size	0.137 mm
Lattice Parameters	a = 10.7348(13) Å b = 13.6851(18) Å c = 23.480(3) Å α = 88.283(5) ° β = 80.327(5) ° γ = 86.514(5) ° V = 3393.4(7) Å <sup>3</sup>
Space Group	P $\bar{1}$ (#2)
Z value	2
D <sub>calc</sub>	1.411 g/cm <sup>3</sup>
F <sub>000</sub>	1478
μ(MoKα)	6.34 cm <sup>-1</sup>

**B. Intensity Measurements**

Detector	Rigaku Saturn
Goniometer	Rigaku AFC8
Radiation	MoKα (λ = 0.71070 Å) graphite monochromated
Detector Aperture	70 mm × 70 mm
Data Images	780 exposures
ω oscillation Range (χ=0.0, φ=0.0)	-15.0 - 15.0°
Exposure Rate	104.0 sec./°
Detector Swing Angle	15.10°
ω oscillation Range (χ=45.0, φ=180.0)	-75.0 - 105.0°
Exposure Rate	104.0 sec./°
Detector Swing Angle	15.10°
ω oscillation Range (χ=54.0, φ=0.0)	-75.0 - 105.0°

Exposure Rate	104.0 sec./ <sup>o</sup>
Detector Swing Angle	15.10 <sup>o</sup>
Detector Position	39.90 mm
Pixel Size	0.137 mm
2 $\theta$ <sub>max</sub>	61.9 <sup>o</sup>
No. of Reflections Measured	Total: 34286
	Unique: 15289 (R <sub>int</sub> = 0.038)
Corrections	Lorentz-polarization
	Absorption
	(trans. factors: 0.8627 - 0.9334)
	Secondary Extinction
	(coefficient: 0.0055(14))

### C. Structure Solution and Refinement

Structure Solution	Direct Methods (SHELX97)
Refinement	Full-matrix least-squares on F <sup>2</sup>
Function Minimized	$\Sigma w (F_o^2 - F_c^2)^2$
Least Squares Weights	$w = 1 / [ \sigma^2(F_o^2) + (0.1519 \cdot P)^2 + 0.0000 \cdot P ]$
	where $P = (Max(F_o^2, 0) + 2F_c^2)/3$
2 $\theta$ <sub>max</sub> cutoff	55.0 <sup>o</sup>
Anomalous Dispersion	All non-hydrogen atoms
No. Observations (All reflections)	15289
No. Variables	705
Reflection/Parameter Ratio	21.69
Residuals: R1 (I > 2.00 $\sigma$ (I))	0.0738
Residuals: R (All reflections)	0.0881
Residuals: wR2 (All reflections)	0.2393
Goodness of Fit Indicator	1.042
Max Shift/Error in Final Cycle	0.001
Maximum peak in Final Diff. Map	0.95 e-/ $\text{Å}^3$
Minimum peak in Final Diff. Map	-0.51 e-/ $\text{Å}^3$

**A3.3: [(ioap-H)<sub>4</sub>Ni<sub>4</sub>(CF<sub>3</sub>SO<sub>3</sub>)(H<sub>2</sub>O)<sub>3</sub>](CF<sub>3</sub>SO<sub>3</sub>)<sub>2</sub>(PF<sub>6</sub>) (3.3)****A. Crystal Data**

Empirical Formula	C <sub>47</sub> F <sub>15</sub> N <sub>24</sub> Ni <sub>4</sub> O <sub>16</sub> S <sub>3</sub> PH <sub>50</sub>
Formula Weight	1854.10
Crystal Color, Habit	brown, prism
Crystal Dimensions	0.61 × 0.49 × 0.22 mm
Crystal System	trigonal
Lattice Type	R-centered
Detector Position	40.02 mm
Pixel Size	0.137 mm
Lattice Parameters	a = 42.677(3) Å c = 22.0593(15) Å V = 34795(4) Å <sup>3</sup>
Space Group	R $\bar{3}$ (#148)
Z value	18
D <sub>calc</sub>	1.593 g/cm <sup>3</sup>
F <sub>000</sub>	16884
μ(MoKα)	11.70 cm <sup>-1</sup>

**B. Intensity Measurements**

Detector	Rigaku Saturn
Goniometer	Rigaku AFC8
Radiation	MoKα (λ = 0.71070 Å) graphite monochromated
Detector Aperture	70 mm × 70 mm
Data Images	910 exposures
ω oscillation Range (χ=0.0, φ=0.0)	-75.0 - 105.0°
Exposure Rate	70.0 sec./°
Detector Swing Angle	15.11°
ω oscillation Range (χ=0.0, φ=90.0)	-75.0 - 90.0°
Exposure Rate	70.0 sec./°
Detector Swing Angle	15.11°
ω oscillation Range (χ=0.0, φ=180.0)	-55.0 - 55.0°
Exposure Rate	70.0 sec./°
Detector Swing Angle	15.11°
Detector Position	40.02 mm
Pixel Size	0.137 mm

$2\theta_{\max}$	61.8°
No. of Reflections Measured	Total: 130730
	Unique: 16011 ( $R_{\text{int}} = 0.0337$ )
Corrections	Lorentz-polarization
	Absorption
	(trans. factors: 0.5944 - 0.8270)

### C. Structure Solution and Refinement

Structure Solution	Direct Methods (SHELX97)
Refinement	Full-matrix least-squares on $F^2$
Function Minimized	$\Sigma w (F_o^2 - F_c^2)^2$
Least Squares Weights	$w = 1 / [ \sigma^2(F_o^2) + (0.1504 \cdot P)^2 + 215.7550 \cdot P ]$
	where $P = (\text{Max}(F_o^2, 0) + 2F_c^2) / 3$
$2\theta_{\max}$ cutoff	53.0°
Anomalous Dispersion	All non-hydrogen atoms
No. Observations (All reflections)	16011
No. Variables	959
Reflection/Parameter Ratio	16.70
Residuals: R1 ( $I > 2.00\sigma(I)$ )	0.0883
Residuals: R (All reflections)	0.0925
Residuals: wR2 (All reflections)	0.2520
Goodness of Fit Indicator	1.089
Max Shift/Error in Final Cycle	0.002
Maximum peak in Final Diff. Map	1.62 e <sup>-</sup> /Å <sup>3</sup>
Minimum peak in Final Diff. Map	-1.61 e <sup>-</sup> /Å <sup>3</sup>

**A3.4:** [(ioap-H)<sub>4</sub>Cu<sub>4</sub>](NO<sub>3</sub>)<sub>4</sub>(CH<sub>3</sub>CN)<sub>4</sub> (3.4)

## A. Crystal Data

Empirical Formula	C <sub>52</sub> H <sub>56</sub> Cu <sub>4</sub> N <sub>32</sub> O <sub>16</sub>
Formula Weight	1639.45
Crystal Color, Habit	green, prism
Crystal Dimensions	0.37 × 0.30 × 0.25 mm
Crystal System	tetragonal
Lattice Type	I-centered
Detector Position	39.97 mm
Pixel Size	0.137 mm
Lattice Parameters	a = 18.9374(11) Å c = 18.2748(11) Å V = 6553.8(7) Å <sup>3</sup>
Space Group	I4 <sub>1</sub> /a (#88)
Z value	4
D <sub>calc</sub>	1.661 g/cm <sup>3</sup>
F <sub>000</sub>	3344
μ(MoKα)	13.73 cm <sup>-1</sup>

## B. Intensity Measurements

Detector	Rigaku Saturn
Goniometer	Rigaku AFC8
Radiation	MoKα (λ = 0.71070 Å) graphite monochromated
Detector Aperture	70 mm × 70 mm
Data Images	690 exposures
ω oscillation Range (χ=0.0, φ=0.0)	-75.0 - 105.0°
Exposure Rate	46.0 sec./°
Detector Swing Angle	15.06°
ω oscillation Range (χ=30.0, φ=180.0)	-75.0 - 90.0°
Exposure Rate	46.0 sec./°
Detector Swing Angle	15.06°
Detector Position	39.97 mm
Pixel Size	0.137 mm
2θ <sub>max</sub>	61.9°
No. of Reflections Measured	Total: 29320 Unique: 3757 (R <sub>int</sub> = 0.027)

Corrections

Lorentz-polarization Absorption  
(trans. factors: 0.7720 - 0.8541)

### C. Structure Solution and Refinement

Structure Solution

Direct Methods (SHELX97)

Refinement

Full-matrix least-squares on  $F^2$

Function Minimized

$\sum w (F_o^2 - F_c^2)^2$

Least Squares Weights

$w = 1 / [ \sigma^2(F_o^2) + (0.0575 \cdot P)^2 + 10.6681 \cdot P ]$

where  $P = (\text{Max}(F_o^2, 0) + 2F_c^2) / 3$

$2\theta_{\text{max}}$  cutoff

55.0°

Anomalous Dispersion

All non-hydrogen atoms

No. Observations (All reflections)

3757

No. Variables

236

Reflection/Parameter Ratio

15.92

Residuals: R1 ( $I > 2.00\sigma(I)$ )

0.0403

Residuals: R (All reflections)

0.0409

Residuals: wR2 (All reflections)

0.1070

Goodness of Fit Indicator

1.107

Max Shift/Error in Final Cycle

0.001

Maximum peak in Final Diff. Map

0.58 e<sup>-</sup>/Å<sup>3</sup>

Minimum peak in Final Diff. Map

-0.52 e<sup>-</sup>/Å<sup>3</sup>

**A3.5:** [(ioap-H)<sub>4</sub>Cu<sub>4</sub>](PF<sub>6</sub>)<sub>2.5</sub>(CF<sub>3</sub>SO<sub>3</sub>)<sub>1.5</sub>(H<sub>2</sub>O)<sub>2</sub>(CH<sub>3</sub>CN)<sub>3.5</sub> (**3.5**)

## A. Crystal Data

Empirical Formula	C <sub>52.50</sub> H <sub>58.50</sub> Cu <sub>4</sub> F <sub>19.50</sub> N <sub>27.50</sub> O <sub>10.50</sub> P <sub>2.50</sub> S <sub>1.50</sub>
Formula Weight	1992.89
Crystal Color, Habit	green, prism
Crystal Dimensions	0.35 × 0.14 × 0.10 mm
Crystal System	orthorhombic
Lattice Type	Primitive
Detector Position	40.00 mm
Pixel Size	0.137 mm
Lattice Parameters	a = 26.4718(15) Å b = 20.6212(13) Å c = 29.8235(18) Å V = 16280.1(17) Å <sup>3</sup>
Space Group	Pbca (#61)
Z value	8
D <sub>calc</sub>	1.626 g/cm <sup>3</sup>
F <sub>000</sub>	8024
μ(MoKα)	12.32 cm <sup>-1</sup>

## B. Intensity Measurements

Detector	Rigaku Saturn
Goniometer	Rigaku AFC8
Radiation	MoKα (λ = 0.71070 Å) graphite monochromated
Detector Aperture	70 mm × 70 mm
Data Images	390 exposures
ω oscillation Range (χ=0.0, φ=0.0)	-30.0 - 30.0°
Exposure Rate	90.0 sec./°
Detector Swing Angle	15.10°
ω oscillation Range (χ=45.0, φ=90.0)	-75.0 - 60.0°
Exposure Rate	90.0 sec./°
Detector Swing Angle	15.10°
Detector Position	40.00 mm
Pixel Size	0.137 mm
2θ <sub>max</sub>	62.0°

No. of Reflections Measured	Total: 75953
Corrections	Unique: 16823 ( $R_{int} = 0.0451$ ) Lorentz-polarization Absorption (trans. factors: 0.7089 - 0.9024)

### C. Structure Solution and Refinement

Structure Solution	Direct Methods (SHELX97)
Refinement	Full-matrix least-squares on $F^2$
Function Minimized	$\Sigma w (F_o^2 - F_c^2)^2$
Least Squares Weights	$w = 1 / [ \sigma^2(F_o^2) + (0.1303 \cdot P)^2 + 72.9980 \cdot P ]$ where $P = (\text{Max}(F_o^2, 0) + 2F_c^2)/3$
$2\theta_{max}$ cutoff	53.0 $^\circ$
Anomalous Dispersion	All non-hydrogen atoms
No. Observations (All reflections)	16823
No. Variables	1127
Reflection/Parameter Ratio	14.93
Residuals: R1 ( $I > 2.00\sigma(I)$ )	0.0922
Residuals: R (All reflections)	0.1035
Residuals: wR2 (All reflections)	0.2593
Goodness of Fit Indicator	1.118
Max Shift/Error in Final Cycle	0.001
Maximum peak in Final Diff. Map	2.14 e $^-/\text{Å}^3$
Minimum peak in Final Diff. Map	-1.06 e $^-/\text{Å}^3$

**A3.6:** [Cu(ioapm)(ClO<sub>4</sub>)(CH<sub>3</sub>CN)](ClO<sub>4</sub>) (3.6)

## A. Crystal Data

Empirical Formula	C <sub>12</sub> H <sub>14</sub> Cl <sub>2</sub> CuN <sub>8</sub> O <sub>9</sub>
Formula Weight	548.74
Crystal Color, Habit	green, platelet
Crystal Dimensions	0.36 × 0.32 × 0.10 mm
Crystal System	monoclinic
Lattice Type	Primitive
Detector Position	39.89 mm
Pixel Size	0.137 mm
Lattice Parameters	a = 7.6317(6) Å b = 9.1727(7) Å c = 28.531(3) Å β = 93.058(2) ° V = 1994.4(3) Å <sup>3</sup>
Space Group	P2 <sub>1</sub> /c (#14)
Z value	4
D <sub>calc</sub>	1.827 g/cm <sup>3</sup>
F <sub>000</sub>	1108.00
μ(MoKα)	14.300 cm <sup>-1</sup>

## B. Intensity Measurements

Detector	Rigaku Saturn
Goniometer	Rigaku AFC8
Radiation	MoKα (λ = 0.71070 Å) graphite monochromated
Detector Aperture	70 mm × 70 mm
Data Images	680 exposures
ω oscillation Range (χ=0.0, φ=0.0)	15.0 - 75.0°
Exposure Rate	34.0 sec./°
Detector Swing Angle	15.06°
ω oscillation Range (χ=0.0, φ=180.0)	-75.0 - 105.0°
Exposure Rate	34.0 sec./°
Detector Swing Angle	15.06°
ω oscillation Range (χ=30.0, φ=90.0)	-50.0 - 50.0°
Exposure Rate	34.0 sec./°

Detector Swing Angle	15.06°
Detector Position	39.89 mm
Pixel Size	0.137 mm
2 $\theta$ <sub>max</sub>	61.8°
No. of Reflections Measured	Total: 18304
	Unique: 5449 (R <sub>int</sub> = 0.025)
Corrections	Lorentz-polarization
	Absorption
	(trans. factors: 0.3103 - 0.5308)
	Secondary Extinction
	(coefficient: 2.20000e-003)

### C. Structure Solution and Refinement

Structure Solution	Direct Methods (SIR92)
Refinement	Full-matrix least-squares on F <sup>2</sup>
Function Minimized	$\Sigma w (F_o^2 - F_c^2)^2$
Least Squares Weights	$w = 1 / [ \sigma^2(F_o^2) + (0.0772 \cdot P) + 1.9592 \cdot P ]$
	where $P = (\text{Max}(F_o^2, 0) + 2F_c^2) / 3$
2 $\theta$ <sub>max</sub> cutoff	61.8°
Anomalous Dispersion	All non-hydrogen atoms
No. Observations (All reflections)	5449
No. Variables	345
Reflection/Parameter Ratio	15.79
Residuals: R1 (I > 2.00σ(I))	0.0502
Residuals: R (All reflections)	0.0525
Residuals: wR2 (All reflections)	0.1387
Goodness of Fit Indicator	1.061
Max Shift/Error in Final Cycle	0.001
Maximum peak in Final Diff. Map	0.92 e-/Å <sup>3</sup>
Minimum peak in Final Diff. Map	-0.59 e-/Å <sup>3</sup>

**A3.7: [Cu<sub>4</sub>(ioapm-H)<sub>4</sub>](ClO<sub>4</sub>)<sub>4</sub>·3 H<sub>2</sub>O (3.7)****A. Crystal Data**

Empirical Formula	C <sub>46</sub> H <sub>49</sub> Cl <sub>4</sub> Cu <sub>4</sub> N <sub>31</sub> O <sub>20</sub>
Formula Weight	1752.08
Crystal Color, Habit	green, prism
Crystal Dimensions	0.72 × 0.17 × 0.11 mm
Crystal System	monoclinic
Lattice Type	C-centered
Detector Position	39.86 mm
Pixel Size	0.137 mm
Lattice Parameters	a = 22.912(9) Å b = 21.105(7) Å c = 18.184(7) Å β = 128.679(7) <sup>o</sup> V = 6864(4) Å <sup>3</sup>
Space Group	C2/c (#15)
Z value	4
D <sub>calc</sub>	1.695 g/cm <sup>3</sup>
F <sub>000</sub>	3544
μ(MoKα)	14.71 cm <sup>-1</sup>

**B. Intensity Measurements**

Detector	Rigaku Saturn
Goniometer	Rigaku AFC8
Radiation	MoKα (λ = 0.71070 Å) graphite monochromated
Detector Aperture	70 mm × 70 mm
Data Images	776 exposures
ω oscillation Range (χ=0.0, φ=0.0)	-75.0 - 105.0 <sup>o</sup>
Exposure Rate	30.0 sec./ <sup>o</sup>
Detector Swing Angle	15.19 <sup>o</sup>
ω oscillation Range (χ=0.0, φ=180.0)	-75.0 - 105.0 <sup>o</sup>
Exposure Rate	30.0 sec./ <sup>o</sup>
Detector Swing Angle	15.19 <sup>o</sup>
ω oscillation Range (χ=30.0, φ=0.0)	44.0 - 72.0 <sup>o</sup>
Exposure Rate	30.0 sec./ <sup>o</sup>

Detector Swing Angle	15.19°
Detector Position	39.86 mm
Pixel Size	0.137 mm
2θ <sub>max</sub>	62.0°
No. of Reflections Measured	Total: 10270
	Unique: 37116 (R <sub>int</sub> = 0.082)
Corrections	Lorentz-polarization
	Absorption
	(trans. factors: 0.6225 - 0.8358)
	Secondary Extinction
	(coefficient: 0.00010(12))

### C. Structure Solution and Refinement

Structure Solution	Direct Methods (SHELX97)
Refinement	Full-matrix least-squares on F <sup>2</sup>
Function Minimized	$\Sigma w (F_o^2 - F_c^2)^2$
Least Squares Weights	$w = 1 / [ \sigma^2(F_o^2) + (0.1466 \cdot P)^2 + 53.5329 \cdot P ]$
	where $P = (Max(F_o^2, 0) + 2F_c^2)/3$
2θ <sub>max</sub> cutoff	62.0°
Anomalous Dispersion	All non-hydrogen atoms
No. Observations (All reflections)	9417
No. Variables	471
Reflection/Parameter Ratio	19.99
Residuals: R1 (I > 2.00σ(I))	0.1101
Residuals: R (All reflections)	0.1217
Residuals: wR2 (All reflections)	0.2986
Goodness of Fit Indicator	1.133
Max Shift/Error in Final Cycle	0.000
Maximum peak in Final Diff. Map	1.49 e <sup>-</sup> /Å <sup>3</sup>
Minimum peak in Final Diff. Map	-1.88 e <sup>-</sup> /Å <sup>3</sup>

**A3.8: [Mn<sub>5</sub>(ioapm-H)<sub>6</sub>](ClO<sub>4</sub>)<sub>4</sub>·2.5H<sub>2</sub>O (3.8)**

## A. Crystal Data

Empirical Formula	C <sub>60</sub> H <sub>74</sub> N <sub>42</sub> O <sub>29</sub> Cl <sub>4</sub> Mn <sub>5</sub>
Formula Weight	2264.01
Crystal Color, Habit	red, prism
Crystal Dimensions	0.20 × 0.20 × 0.20 mm
Crystal System	monoclinic
Lattice Type	Primitive
Detector Position	44.89 mm
Pixel Size	0.137 mm
Lattice Parameters	a = 16.8375(19) Å b = 23.483(3) Å c = 23.610(3) Å β = 96.970(3) ° V = 9266.1(18) Å <sup>3</sup>
Space Group	P2 <sub>1</sub> /n (#14)
Z value	4
D <sub>calc</sub>	1.623 g/cm <sup>3</sup>
F000	4612
μ(MoKα)	8.77 cm <sup>-1</sup>

## B. Intensity Measurements

Detector	Rigaku Saturn
Goniometer	Rigaku AFC8
Radiation	MoKα (λ = 0.71070 Å) graphite monochromated
Detector Aperture	70 mm x 70 mm
Data Images	340 exposures
ω oscillation Range (χ=0.0, φ=0.0)	-80.0 - 90.0°
Exposure Rate	120.0 sec./°
Detector Swing Angle	10.12°
Detector Position	44.89 mm
Pixel Size	0.137 mm
2θ <sub>max</sub>	54.8°

No. of Reflections Measured

Total: 32353

Corrections

Unique: 16107 ( $R_{\text{int}} = 0.0312$ )

Lorentz-polarization

Absorption

(trans. factors: 0.6677 - 1.000)

### C. Structure Solution and Refinement

Structure Solution

Direct Methods (SHELX97)

Refinement

Full-matrix least-squares on  $F^2$

Function Minimized

$\Sigma w (F_o^2 - F_c^2)^2$

Least Squares Weights

$w = 1 / [ \sigma^2(F_o^2) + (0.1745 \cdot P)^2$

$+ 25.0992 \cdot P ]$

where  $P = (\text{Max}(F_o^2, 0) + 2F_c^2)/3$

$2\theta_{\text{max}}$  cutoff

54.8°

Anomalous Dispersion

All non-hydrogen atoms

No. Observations (All reflections)

16107

No. Variables

1222

Reflection/Parameter Ratio

13.18

Residuals:  $R1$  ( $I > 2.00\sigma(I)$ )

0.0979

Residuals:  $R$  (All reflections)

0.1096

Residuals:  $wR2$  (All reflections)

0.2906

Goodness of Fit Indicator

1.062

Max Shift/Error in Final Cycle

0.000

Maximum peak in Final Diff. Map

1.48 e<sup>-</sup>/Å<sup>3</sup>

Minimum peak in Final Diff. Map

-2.48 e<sup>-</sup>/Å<sup>3</sup>

**A3.9: [(2pmoap-2H)<sub>6</sub>Zn<sub>9</sub>](NO<sub>3</sub>)<sub>6</sub>·15.5H<sub>2</sub>O (4.1)****A. Crystal Data**

Empirical Formula	C <sub>102</sub> H <sub>109</sub> N <sub>72</sub> O <sub>45.50</sub> Zn <sub>9</sub>
Formula Weight	3659.94
Crystal Color, Habit	yellow, prism
Crystal Dimensions	0.39 × 0.35 × 0.24 mm
Crystal System	tetragonal
Lattice Type	I-centered
Detector Position	39.77 mm
Pixel Size	0.137 mm
Lattice Parameters	a = 27.668(4) Å c = 38.890(7) Å V = 29770(8) Å <sup>3</sup>
Space Group	I4 <sub>1</sub> /acd (#142)
Z value	8
D <sub>calc</sub>	1.633 g/cm <sup>3</sup>
F <sub>000</sub>	14872
μ(MoKα)	15.28 cm <sup>-1</sup>

**B. Intensity Measurements**

Detector	Rigaku Saturn
Goniometer	Rigaku AFC8
Radiation	MoKα (λ = 0.71070 Å) graphite monochromated
Detector Aperture	70 mm x 70 mm
Data Images	720 exposures
ω oscillation Range (χ=0.0, φ=0.0)	-75.0 - 105.0°
Exposure Rate	80.0 sec./°
Detector Swing Angle	15.28°
ω oscillation Range (χ=45.0, φ=90.0)	-75.0 - 105.0°
Exposure Rate	80.0 sec./°
Detector Swing Angle	15.28°
Detector Position	39.77 mm
Pixel Size	0.137 mm
2θ <sub>max</sub>	62.2°

No. of Reflections Measured	Total: 104796
Corrections	Unique: 6545 ( $R_{int} = 0.0584$ ) Lorentz-polarization Absorption (trans. factors: 0.6804 - 0.7898)
C. Structure Solution and Refinement	
Structure Solution	Direct Methods (SHELX97)
Refinement	Full-matrix least-squares on $F^2$
Function Minimized	$\Sigma w (F_o^2 - F_c^2)^2$
Least Squares Weights	$w = 1 / [ \sigma^2(F_o^2) + (0.1762 \cdot P)^2 + 210.7963 \cdot P ]$ where $P = (\text{Max}(F_o^2, 0) + 2F_c^2)/3$
$2\theta_{max}$ cutoff	50.0°
Anomalous Dispersion	All non-hydrogen atoms
No. Observations (All reflections)	6545
No. Variables	540
Reflection/Parameter Ratio	12.12
Residuals: R1 ( $I > 2.00\sigma(I)$ )	0.1275
Residuals: R (All reflections)	0.1318
Residuals: wR2 (All reflections)	0.3481
Goodness of Fit Indicator	1.253
Max Shift/Error in Final Cycle	0.000
Maximum peak in Final Diff. Map	1.42 e <sup>-</sup> /Å <sup>3</sup>
Minimum peak in Final Diff. Map	-0.52 e <sup>-</sup> /Å <sup>3</sup>

**A3.10:** [(2pmoap-2H)<sub>6</sub>Mn<sub>9</sub>](NO<sub>3</sub>)<sub>6</sub>·28H<sub>2</sub>O (**4.2**)

## A. Crystal Data

Empirical Formula	C <sub>102</sub> H <sub>134</sub> Mn <sub>9</sub> N <sub>72</sub> O <sub>58</sub>
Formula Weight	3791.07
Crystal Color, Habit	red, chip
Crystal Dimensions	0.23 × 0.20 × 0.17 mm
Crystal System	tetragonal
Lattice Type	I-centered
Detector Position	40.02 mm
Pixel Size	0.137 mm
Lattice Parameters	a = 27.9255(13) Å c = 40.217(2) Å V = 31362(3) Å <sup>3</sup>
Space Group	I4 <sub>1</sub> /acd (#142)
Z value	8
D <sub>calc</sub>	1.606 g/cm <sup>3</sup>
F <sub>000</sub>	15512
μ(MoKα)	8.09 cm <sup>-1</sup>

## B. Intensity Measurements

Detector	Rigaku Saturn
Goniometer	Rigaku AFC8
Radiation	MoKα (λ = 0.71070 Å) graphite monochromated
Detector Aperture	70 mm × 70 mm
Data Images	690 exposures
ω oscillation Range (χ=0.0, φ=0.0)	-75.0 - 105.0°
Exposure Rate	74.0 sec./°
Detector Swing Angle	15.07°
ω oscillation Range (χ=30.0, φ=90.0)	-75.0 - 90.0°
Exposure Rate	74.0 sec./°
Detector Swing Angle	15.07°
Detector Position	40.02 mm
Pixel Size	0.137 mm
2θ <sub>max</sub>	61.9°

No. of Reflections Measured

Total: 151450

Corrections

Unique: 11887 ( $R_{\text{int}} = 0.059$ )

Lorentz-polarization

Absorption

(trans. factors: 0.8901 - 0.9176)

### C. Structure Solution and Refinement

Structure Solution

Direct Methods (SHELX97)

Refinement

Full-matrix least-squares on  $F^2$

Function Minimized

$\Sigma w (F_o^2 - F_c^2)^2$

Least Squares Weights

$w = 1 / [ \sigma^2(F_o^2) + (0.0942 \cdot P)^2 + 214.6007 \cdot P ]$

where  $P = (\text{Max}(F_o^2, 0) + 2F_c^2)/3$

$2\theta_{\text{max}}$  cutoff

61.9°

Anomalous Dispersion

All non-hydrogen atoms

No. Observations (All reflections)

11887

No. Variables

532

Reflection/Parameter Ratio

22.34

Residuals:  $R_1$  ( $I > 2.00\sigma(I)$ )

0.1278

Residuals:  $R$  (All reflections)

0.1356

Residuals:  $wR_2$  (All reflections)

0.3049

Goodness of Fit Indicator

1.348

Max Shift/Error in Final Cycle

0.000

Maximum peak in Final Diff. Map

1.01 e<sup>-</sup>/Å<sup>3</sup>

Minimum peak in Final Diff. Map

-0.89 e<sup>-</sup>/Å<sup>3</sup>

**A3.11: [(2pmoap-2H)<sub>6</sub>Co<sub>9</sub>](NO<sub>3</sub>)<sub>6</sub>·2CH<sub>3</sub>CN·11H<sub>2</sub>O (4.3)**

## A. Crystal Data

Empirical Formula	C <sub>106</sub> H <sub>106</sub> Co <sub>9</sub> N <sub>74</sub> O <sub>41</sub>
Formula Weight	3602.87
Crystal Color, Habit	red, prism
Crystal Dimensions	0.64 × 0.60 × 0.53 mm
Crystal System	orthorhombic
Lattice Type	F-centered
Detector Position	40.03 mm
Pixel Size	0.137 mm
Lattice Parameters	a = 39.369(3) Å b = 39.416(3) Å c = 39.411(3) Å V = 61157(8) Å <sup>3</sup>
Space Group	Fddd (#70)
Z value	16
D <sub>calc</sub>	1.565 g/cm <sup>3</sup>
F <sub>000</sub>	29296
μ(MoKα)	10.51 cm <sup>-1</sup>

## B. Intensity Measurements

Detector	Rigaku Saturn
Goniometer	Rigaku AFC8
Radiation	MoKα (λ = 0.71070 Å) graphite monochromated
Detector Aperture	70 mm × 70 mm
Data Images	720 exposures
ω oscillation Range (χ=0.0, φ=0.0)	-75.0 - 105.0°
Exposure Rate	90.0 sec./°
Detector Swing Angle	15.12°
ω oscillation Range (χ=54.0, φ=0.0)	-75.0 - 105.0°
Exposure Rate	90.0 sec./°
Detector Swing Angle	15.12°
Detector Position	40.03 mm
Pixel Size	0.068 mm
2θ <sub>max</sub>	62.0°

No. of Reflections Measured	Total: 133536
	Unique: 15853 ( $R_{\text{int}} = 0.0415$ )
Corrections	Lorentz-polarization
	Absorption
	(trans. factors: 0.5634 - 0.7400)

### C. Structure Solution and Refinement

Structure Solution	Direct Methods (SHELX97)
Refinement	Full-matrix least-squares on $F^2$
Function Minimized	$\Sigma w (F_o^2 - F_c^2)^2$
Least Squares Weights	$w = 1 / [ \sigma^2(F_o^2) + (0.1532 \cdot P)^2 + 480.5058 \cdot P ]$
	where $P = (\text{Max}(F_o^2, 0) + 2F_c^2)/3$
$2\theta_{\text{max}}$ cutoff	53.0°
Anomalous Dispersion	All non-hydrogen atoms
No. Observations (All reflections)	15853
No. Variables	1092
Reflection/Parameter Ratio	14.52
Residuals: R1 ( $I > 2.00\sigma(I)$ )	0.0988
Residuals: R (All reflections)	0.1065
Residuals: wR2 (All reflections)	0.2877
Goodness of Fit Indicator	1.185
Max Shift/Error in Final Cycle	0.002
Maximum peak in Final Diff. Map	1.35 e <sup>-</sup> /Å <sup>3</sup>
Minimum peak in Final Diff. Map	-0.52 e <sup>-</sup> /Å <sup>3</sup>

**A3.12: [(pmpoapCOO)Cu](NO<sub>3</sub>) (4.4)**

## A. Crystal Data

Empirical Formula	C <sub>12</sub> H <sub>9</sub> CuN <sub>7</sub> O <sub>6</sub>
Formula Weight	410.79
Crystal Color, Habit	blue, irregular
Crystal Dimensions	0.20 × 0.19 × 0.18 mm
Crystal System	monoclinic
Lattice Type	Primitive
Detector Position	40.03 mm
Pixel Size	0.137 mm
Lattice Parameters	a = 8.6190(18) Å b = 9.1399(17) Å c = 18.120(4) Å β = 94.220(5) ° V = 1423.6(5) Å <sup>3</sup>
Space Group	P2 <sub>1</sub> /n (#14)
Z value	4
D <sub>calc</sub>	1.917 g/cm <sup>3</sup>
F <sub>000</sub>	828
μ(MoKα)	15.89 cm <sup>-1</sup>

## B. Intensity Measurements

Detector	Rigaku Saturn
Goniometer	Rigaku AFC8
Radiation	MoKα (λ = 0.71070 Å) graphite monochromated
Detector Aperture	70 mm × 70 mm
Data Images	1208 exposures
ω oscillation Range (χ=0.0, φ=0.0)	-60.0 - 0.0°
Exposure Rate	60.0 sec./°
Detector Swing Angle	15.06°
ω oscillation Range (χ=45.0, φ=180.0)	-75.0 - 105.0°
Exposure Rate	60.0 sec./°
Detector Swing Angle	15.06°
ω oscillation Range (χ=54.0, φ=90.0)	-44.0 - 80.0°
Exposure Rate	60.0 sec./°

Detector Swing Angle	15.06°
$\omega$ oscillation Range ( $\chi=0.0$ , $\phi=90.0$ )	15.0 - 75.0°
Exposure Rate	60.0 sec./°
Detector Swing Angle	15.06°
$\omega$ oscillation Range ( $\chi=54.0$ , $\phi=180.0$ )	-75.0 - 105.0°
Exposure Rate	60.0 sec./°
Detector Swing Angle	15.06°
Detector Position	40.03 mm
Pixel Size	0.137 mm
2 $\theta$ <sub>max</sub>	61.6°
No. of Reflections Measured	Total: 21924 Unique: 3280 ( $R_{int} = 0.0273$ )
Corrections	Lorentz-polarization Absorption (trans. factors: 0.7709 - 0.9025)

### C. Structure Solution and Refinement

Structure Solution	Direct Methods (SHELX97)
Refinement	Full-matrix least-squares on $F^2$
Function Minimized	$\Sigma w (F_o^2 - F_c^2)^2$
Least Squares Weights	$w = 1 / [ \sigma^2(F_o^2) + (0.0487 \cdot P)^2 + 2.9610 \cdot P ]$ where $P = (\text{Max}(F_o^2, 0) + 2F_c^2)/3$
2 $\theta$ <sub>max</sub> cutoff	55.0°
Anomalous Dispersion	All non-hydrogen atoms
No. Observations (All reflections)	3280
No. Variables	236
Reflection/Parameter Ratio	13.90
Residuals: R1 ( $I > 2.00\sigma(I)$ )	0.0405
Residuals: R (All reflections)	0.0411
Residuals: wR2 (All reflections)	0.0998
Goodness of Fit Indicator	1.043
Max Shift/Error in Final Cycle	0.000
Maximum peak in Final Diff. Map	1.01 e <sup>-</sup> /Å <sup>3</sup>
Minimum peak in Final Diff. Map	-0.68 e <sup>-</sup> /Å <sup>3</sup>

**A3.13:** [(2pmoap-2H)<sub>6</sub>Cu<sub>9</sub>](NO<sub>3</sub>)<sub>6</sub>·20.5H<sub>2</sub>O (4.5)

## A. Crystal Data

Empirical Formula	C <sub>102</sub> H <sub>119</sub> Cu <sub>9</sub> N <sub>72</sub> O <sub>50.50</sub>
Formula Weight	3733.43
Crystal Color, Habit	brown, prism
Crystal Dimensions	0.51 × 0.24 × 0.19 mm
Crystal System	tetragonal
Lattice Type	I-centered
Detector Position	40.00 mm
Pixel Size	0.137 mm
Lattice Parameters	a = 27.841(2) Å c = 38.298(3) Å V = 29686(4) Å <sup>3</sup>
Space Group	I4 <sub>1</sub> /acd (#142)
Z value	8
D <sub>calc</sub>	1.671 g/cm <sup>3</sup>
F <sub>000</sub>	15200
μ(MoKα)	13.72 cm <sup>-1</sup>

## B. Intensity Measurements

Detector	Rigaku Saturn
Goniometer	Rigaku AFC8
Radiation	MoKα (λ = 0.71070 Å) graphite monochromated
Detector Aperture	70 mm × 70 mm
Data Images	360 exposures
ω oscillation Range (χ=45.0, φ=0.0)	-75.0 - 105.0°
Exposure Rate	80.0 sec./°
Detector Swing Angle	15.15°
Detector Position	40.00 mm
Pixel Size	0.137 mm
2θ <sub>max</sub>	62.0°
No. of Reflections Measured	Total: 60270 Unique: 7277 (R <sub>int</sub> = 0.0403)
Corrections	Lorentz-polarization Absorption (trans. factors: 0.6946 - 0.8228)

### C. Structure Solution and Refinement

Structure Solution	Direct Methods (SHELX97)
Refinement	Full-matrix least-squares on $F^2$
Function Minimized	$\Sigma w (F_o^2 - F_c^2)^2$
Least Squares Weights	$w = 1 / [ \sigma^2(F_o^2) + (0.1812 \cdot P)^2 + 194.6936 \cdot P ]$ where $P = (\text{Max}(F_o^2, 0) + 2F_c^2)/3$
$2\theta_{\text{max}}$ cutoff	52.0°
Anomalous Dispersion	All non-hydrogen atoms
No. Observations (All reflections)	7277
No. Variables	537
Reflection/Parameter Ratio	13.55
Residuals: R1 ( $I > 2.00\sigma(I)$ )	0.1055
Residuals: R (All reflections)	0.1115
Residuals: wR2 (All reflections)	0.3060
Goodness of Fit Indicator	1.147
Max Shift/Error in Final Cycle	0.001
Maximum peak in Final Diff. Map	2.01 e <sup>-</sup> /Å <sup>3</sup>
Minimum peak in Final Diff. Map	-1.30 e <sup>-</sup> /Å <sup>3</sup>

**A3.14:**  $[\text{Cu}_9(2\text{pmoap}-2\text{H})_2(2\text{pmoap}-\text{H})_4](\text{ClO}_4)_{10} \cdot 13.2\text{H}_2\text{O}$  (4.6)

## A. Crystal Data

Empirical Formula	$\text{C}_{102}\text{H}_{108.40}\text{Cl}_{10}\text{Cu}_9\text{N}_{66}\text{O}_{65.20}$
Formula Weight	4228.43
Crystal Color, Habit	brown, prism
Crystal Dimensions	$0.17 \times 0.11 \times 0.09$ mm
Crystal System	tetragonal
Lattice Type	Primitive
Detector Position	39.97 mm
Pixel Size	0.137 mm
Lattice Parameters	$a = 20.9857(14)$ Å $c = 17.3731(12)$ Å $V = 7651.1(9)$ Å <sup>3</sup>
Space Group	$P4_2/n$ (#86)
Z value	2
D <sub>calc</sub>	1.835 g/cm <sup>3</sup>
F <sub>000</sub>	4270.00
$\mu(\text{MoK}\alpha)$	15.173 cm <sup>-1</sup>

## B. Intensity Measurements

Detector	Rigaku Saturn
Goniometer	Rigaku AFC8
Radiation	MoK $\alpha$ ( $\lambda = 0.71070$ Å) graphite monochromated
Detector Aperture	70 mm $\times$ 70 mm
Data Images	690 exposures
$\omega$ oscillation Range ( $\chi=0.0$ , $\phi=0.0$ )	$-75.0 - 105.0^\circ$
Exposure Rate	60.0 sec./ $^\circ$
Detector Swing Angle	15.05 $^\circ$
$\omega$ oscillation Range ( $\chi=0.0$ , $\phi=90.0$ )	$-75.0 - 90.0^\circ$
Exposure Rate	60.0 sec./ $^\circ$
Detector Swing Angle	15.05 $^\circ$
Detector Position	39.97 mm
Pixel Size	0.137 mm
2 $\theta$ <sub>max</sub>	61.9 $^\circ$

No. of Reflections Measured

Total: 75957

Corrections

Unique: 10853 ( $R_{int} = 0.053$ )

Lorentz-polarization

Absorption

(trans. factors: 0.7611 - 0.8280)

Secondary Extinction

(coefficient: 0.00010(12))

### C. Structure Solution and Refinement

Structure Solution

Direct Methods (SHELX97)

Refinement

Full-matrix least-squares on  $F^2$

Function Minimized

$\sum w (F_o^2 - F_c^2)^2$

Least Squares Weights

$w = 1 / [ \sigma^2(F_o^2) + (0.0910 \cdot P)^2 + 23.3167 \cdot P ]$

where  $P = (\text{Max}(F_o^2, 0) + 2F_c^2)/3$

$2\theta_{max}$  cutoff

61.9 $^\circ$

Anomalous Dispersion

All non-hydrogen atoms

No. Observations (All reflections)

10853

No. Variables

567

Reflection/Parameter Ratio

19.14

Residuals:  $R_1$  ( $I > 2.00\sigma(I)$ )

0.1023

Residuals:  $R$  (All reflections)

0.1127

Residuals:  $wR_2$  (All reflections)

0.2479

Goodness of Fit Indicator

1.254

Max Shift/Error in Final Cycle

0.000

Maximum peak in Final Diff. Map

1.16  $e^-/\text{\AA}^3$

Minimum peak in Final Diff. Map

-1.40  $e^-/\text{\AA}^3$

**A3.15:** [(2pmoap-2H)<sub>6</sub>Mn<sub>5</sub>Zn<sub>4</sub>](NO<sub>3</sub>)<sub>6</sub>·14H<sub>2</sub>O (**5.1**)

## A. Crystal Data

Empirical Formula	C <sub>102</sub> H <sub>106</sub> Mn <sub>5</sub> N <sub>72</sub> O <sub>42</sub> Zn <sub>4</sub>
Formula Weight	3548.63
Crystal Color, Habit	orange, prism
Crystal Dimensions	0.20 × 0.20 × 0.20 mm
Crystal System	tetragonal
Lattice Type	I-centered
Detector Position	39.96 mm
Pixel Size	0.137 mm
Lattice Parameters	a = 27.958(3) Å c = 39.801(4) Å V = 31112(5) Å <sup>3</sup>
Space Group	I4 <sub>1</sub> /acd (#142)
Z value	8
D <sub>calc</sub>	1.515 g/cm <sup>3</sup>
F <sub>000</sub>	14424
μ(MoKα)	10.94 cm <sup>-1</sup>

## B. Intensity Measurements

Detector	Rigaku Saturn
Goniometer	Rigaku AFC8
Radiation	MoKα (λ = 0.71070 Å) graphite monochromated
Detector Aperture	70 mm × 70 mm
Data Images	540 exposures
ω oscillation Range (χ=0.0, φ=0.0)	-45.0 - 75.0°
Exposure Rate	120.0 sec./°
Detector Swing Angle	15.08°
ω oscillation Range (χ=54.0, φ=0.0)	-75.0 - 75.0°
Exposure Rate	120.0 sec./°
Detector Swing Angle	15.08°
Detector Position	39.96 mm
Pixel Size	0.137 mm
2θ <sub>max</sub>	62.0°

No. of Reflections Measured

Total: 96366

Corrections

Unique: 7665 ( $R_{\text{int}} = 0.0992$ )

Lorentz-polarization

(trans. factors: 0.8324 - 0.9111)

Secondary Extinction

(coefficient: 0.00002(2))

### C. Structure Solution and Refinement

Structure Solution

Direct Methods (SHELX97)

Refinement

Full-matrix least-squares on  $F^2$

Function Minimized

$\Sigma w (F_o^2 - F_c^2)^2$

Least Squares Weights

$w = 1 / [ \sigma^2(F_o^2) + (0.1062 \cdot P)^2 + 291.2670 \cdot P ]$

where  $P = (\text{Max}(F_o^2, 0) + 2F_c^2)/3$

$2\theta_{\text{max}}$  cutoff

52.0°

Anomalous Dispersion

All non-hydrogen atoms

No. Observations (All reflections)

7665

No. Variables

465

Reflection/Parameter Ratio

16.48

Residuals:  $R_1$  ( $I > 2.00\sigma(I)$ )

0.1168

Residuals:  $R$  (All reflections)

0.1292

Residuals:  $wR_2$  (All reflections)

0.2855

Goodness of Fit Indicator

1.187

Max Shift/Error in Final Cycle

0.001

Maximum peak in Final Diff. Map

2.18  $e^-/\text{\AA}^3$

Minimum peak in Final Diff. Map

-0.84  $e^-/\text{\AA}^3$

**A3.16:** [(2pmoap-2H)<sub>6</sub>Mn<sub>5</sub>Cu<sub>4</sub>](NO<sub>3</sub>)<sub>6</sub>·24H<sub>2</sub>O (**5.2**)

## A. Crystal Data

Empirical Formula	C <sub>102</sub> H <sub>126</sub> Cu <sub>4</sub> Mn <sub>5</sub> N <sub>72</sub> O <sub>54</sub>
Formula Weight	3753.44
Crystal Color, Habit	brown, chunk
Crystal Dimensions	0.20 × 0.20 × 0.20 mm
Crystal System	tetragonal
Lattice Type	I-centered
Detector Position	40.03 mm
Pixel Size	0.137 mm
Lattice Parameters	a = 27.6101(16) Å c = 40.319(2) Å V = 30736(3) Å <sup>3</sup>
Space Group	I4 <sub>1</sub> /acd (#142)
Z value	8
D <sub>calc</sub>	1.622 g/cm <sup>3</sup>
F <sub>000</sub>	15320
μ(MoKα)	10.47 cm <sup>-1</sup>

## B. Intensity Measurements

Detector	Rigaku Saturn
Goniometer	Rigaku AFC8
Radiation	MoKα (λ = 0.71070 Å) graphite monochromated
Detector Aperture	70 mm × 70 mm
Data Images	360 exposures
ω oscillation Range (χ=0.0, φ=0.0)	-75.0 - 105.0°
Exposure Rate	50.0 sec./ <sup>o</sup>
Detector Swing Angle	15.07°
Detector Position	40.03 mm
Pixel Size	0.137 mm
2θ <sub>max</sub>	61.9°
No. of Reflections Measured	Total: 77008 Unique: 11442 (R <sub>int</sub> = 0.0407)

Corrections

Lorentz-polarization

Absorption

(trans. factors: 0.7734 - 0.8241)

Secondary Extinction

(coefficient: 0.00008(3))

### C. Structure Solution and Refinement

Structure Solution

Direct Methods (SHELX97)

Refinement

Full-matrix least-squares on  $F^2$

Function Minimized

$\Sigma w (F_o^2 - F_c^2)^2$

Least Squares Weights

$w = 1 / [ \sigma^2(F_o^2) + (0.1304 \cdot P)^2 + 92.4439 \cdot P ]$

where  $P = (\text{Max}(F_o^2, 0) + 2F_c^2) / 3$

$2\theta_{\text{max}}$  cutoff

61.9°

Anomalous Dispersion

All non-hydrogen atoms

No. Observations (All reflections)

11442

No. Variables

556

Reflection/Parameter Ratio

20.58

Residuals: R1 ( $I > 2.00\sigma(I)$ )

0.1009

Residuals: R (All reflections)

0.1128

Residuals: wR2 (All reflections)

0.2837

Goodness of Fit Indicator

1.219

Max Shift/Error in Final Cycle

0.001

Maximum peak in Final Diff. Map

1.33 e<sup>-</sup>/Å<sup>3</sup>

Minimum peak in Final Diff. Map

-0.81 e<sup>-</sup>/Å<sup>3</sup>

**A3.17:** [(2pmoap-2H)<sub>6</sub>Mn<sub>1</sub>Cu<sub>8</sub>](NO<sub>3</sub>)<sub>6</sub>·15H<sub>2</sub>O (5.4)

## A. Crystal Data

Empirical Formula	C <sub>102</sub> H <sub>120</sub> Cu <sub>8</sub> MnN <sub>72</sub> O <sub>45</sub>
Formula Weight	3637.83
Crystal Color, Habit	brown, chunk
Crystal Dimensions	0.30 × 0.30 × 0.15 mm
Crystal System	tetragonal
Lattice Type	I-centered
Detector Position	59.83 mm
Pixel Size	0.137 mm
Lattice Parameters	a = 27.889(3) Å c = 39.039(4) Å V = 30365(5) Å <sup>3</sup>
Space Group	14 <sub>1</sub> /acd (#142)
Z value	8
D <sub>calc</sub>	1.591 g/cm <sup>3</sup>
F <sub>000</sub>	14824
μ(MoKα)	12.80 cm <sup>-1</sup>

## B. Intensity Measurements

Detector	Rigaku Saturn
Goniometer	Rigaku AFC8
Radiation	MoKα (λ = 0.71070 Å) graphite monochromated
Detector Aperture	70 mm × 70 mm
Data Images	406 exposures
ω oscillation Range (χ=0.0, φ=0.0)	-50.0 - 63.0°
Exposure Rate	120.0 sec./°
Detector Swing Angle	10.09°
ω oscillation Range (χ=45.0, φ=0.0)	0.0 - 90.0°
Exposure Rate	120.0 sec./°
Detector Swing Angle	10.09°
Detector Position	59.83 mm
Pixel Size	0.137 mm
2θ <sub>max</sub>	46.4°

No. of Reflections Measured

Total: 36621

Corrections

Unique: 4959 ( $R_{\text{int}} = 0.0296$ )

Lorentz-polarization

Absorption

(trans. factors: 0.7997 - 1.0000)

### C. Structure Solution and Refinement

Structure Solution

Direct Methods (SHELX97)

Refinement

Full-matrix least-squares on  $F^2$

Function Minimized

$\Sigma w (F_o^2 - F_c^2)^2$

Least Squares Weights

$w = 1 / [ \sigma^2(F_o^2) + (0.2000 \cdot P)^2 + 0.0000 \cdot P ]$

where  $P = (\text{Max}(F_o^2, 0) + 2F_c^2)/3$

$2\theta_{\text{max}}$  cutoff

46.4°

Anomalous Dispersion

All non-hydrogen atoms

No. Observations (All reflections)

4959

No. Variables

542

Reflection/Parameter Ratio

9.15

Residuals: R1 ( $I > 2.00\sigma(I)$ )

0.1079

Residuals: R (All reflections)

0.1126

Residuals: wR2 (All reflections)

0.3702

Goodness of Fit Indicator

1.801

Max Shift/Error in Final Cycle

0.003

Maximum peak in Final Diff. Map

1.37 e<sup>-</sup>/Å<sup>3</sup>

Minimum peak in Final Diff. Map

-1.19 e<sup>-</sup>/Å<sup>3</sup>

**A3.18:** (2po56hq+2H)(BF<sub>4</sub>)<sub>2</sub>(CH<sub>3</sub>OH)<sub>1</sub>(H<sub>2</sub>O)<sub>1</sub> (**6.1**)

## A. Crystal Data

Empirical Formula	C <sub>28</sub> H <sub>27</sub> B <sub>2</sub> F <sub>8</sub> N <sub>7</sub> O <sub>4</sub>
Formula Weight	699.17
Crystal Color, Habit	colorless, prism
Crystal Dimensions	0.48 × 0.20 × 0.20 mm
Crystal System	triclinic
Lattice Type	Primitive
Detector Position	40.03 mm
Pixel Size	0.137 mm
Lattice Parameters	a = 9.1217(8) Å b = 10.1336(8) Å c = 17.6705(19) Å α = 77.640(8) ° β = 82.793(9) ° γ = 68.011(6) ° V = 1477.6(2) Å <sup>3</sup>
Space Group	P1̄ (#2)
Z value	2
D <sub>calc</sub>	1.571 g/cm <sup>3</sup>
F <sub>000</sub>	716
μ(MoKα)	1.39 cm <sup>-1</sup>

## B. Intensity Measurements

Detector	Rigaku Saturn
Goniometer	Rigaku AFC8
Radiation	MoKα (λ = 0.71070 Å) graphite monochromated
Detector Aperture	70 mm × 70 mm
Data Images	1070 exposures
ω oscillation Range (χ=0.0, φ=0.0)	-75.0 - 105.0°
Exposure Rate	60.0 sec./°
Detector Swing Angle	15.08°
ω oscillation Range (χ=45.0, φ=0.0)	-75.0 - 90.0°
Exposure Rate	60.0 sec./°
Detector Swing Angle	15.08°

$\omega$ oscillation Range ( $\chi=54.0$ , $\phi=90.0$ )	-75.0 - 73.0 <sup>o</sup>
Exposure Rate	60.0 sec./ <sup>o</sup>
Detector Swing Angle	15.08 <sup>o</sup>
$\omega$ oscillation Range ( $\chi=54.0$ , $\phi=180.0$ )	-54.0 - -12.0 <sup>o</sup>
Exposure Rate	60.0 sec./ <sup>o</sup>
Detector Swing Angle	15.08 <sup>o</sup>
Detector Position	40.03 mm
Pixel Size	0.137 mm
2 $\theta_{\max}$	61.8 <sup>o</sup>
No. of Reflections Measured	Total: 20929
	Unique: 6703 (R <sub>int</sub> = 0.0308)
Corrections	Lorentz-polarization
	Absorption
	(trans. factors: 0.9597 - 0.9873)

### C. Structure Solution and Refinement

Structure Solution	Direct Methods (SHELX97)
Refinement	Full-matrix least-squares on F <sup>2</sup>
Function Minimized	$\Sigma w (F_o^2 - F_c^2)^2$
Least Squares Weights	$w = 1 / [ \sigma^2(F_o^2) + (0.0821 \cdot P)^2 + 0.7465 \cdot P ]$
	where P = (Max(F <sub>o</sub> <sup>2</sup> , 0) + 2F <sub>c</sub> <sup>2</sup> )/3
2 $\theta_{\max}$ cutoff	55.0 <sup>o</sup>
Anomalous Dispersion	All non-hydrogen atoms
No. Observations (All reflections)	6703
No. Variables	444
Reflection/Parameter Ratio	15.10
Residuals: R1 ( $I > 2.00\sigma(I)$ )	0.0647
Residuals: R (All reflections)	0.0714
Residuals: wR2 (All reflections)	0.1741
Goodness of Fit Indicator	1.094
Max Shift/Error in Final Cycle	0.001
Maximum peak in Final Diff. Map	0.87 e <sup>-</sup> /Å <sup>3</sup>
Minimum peak in Final Diff. Map	-0.55 e <sup>-</sup> /Å <sup>3</sup>

**A3.19:** [(2po56hq-2H)<sub>6</sub>Mn<sub>9</sub>](ClO<sub>4</sub>)<sub>6</sub> (**6.2**)

## A. Crystal Data

Empirical Formula	C <sub>162</sub> H <sub>102</sub> Cl <sub>6</sub> Mn <sub>9</sub> N <sub>42</sub> O <sub>36</sub>
Formula Weight	3920.01
Crystal Color, Habit	red, prism
Crystal Dimensions	0.20 × 0.20 × 0.20 mm
Crystal System	monoclinic
Lattice Type	Primitive
Detector Position	39.92 mm
Pixel Size	0.137 mm
Lattice Parameters	a = 20.908(4) Å b = 27.102(4) Å c = 32.492(5) Å β = 98.239(4) ° V = 18222(5) Å <sup>3</sup>
Space Group	P2 <sub>1</sub> /n (#14)
Z value	4
D <sub>calc</sub>	1.429 g/cm <sup>3</sup>
F <sub>000</sub>	7932
μ(MoKα)	7.72 cm <sup>-1</sup>

## B. Intensity Measurements

Detector	Rigaku Saturn
Goniometer	Rigaku AFC8
Radiation	MoKα (λ = 0.71070 Å) graphite monochromated
Detector Aperture	70 mm × 70 mm
Data Images	720 exposures
ω oscillation Range (χ=0.0, φ=0.0)	-75.0 - 105.0°
Exposure Rate	150.0 sec./°
Detector Swing Angle	15.21°
ω oscillation Range (χ=54.0, φ=0.0)	-75.0 - 105.0°
Exposure Rate	150.0 sec./°
Detector Swing Angle	15.21°
Detector Position	39.92 mm
Pixel Size	0.137 mm
2θ <sub>max</sub>	62.2°

No. of Reflections Measured

Total: 137797

Corrections

Unique: 37263 ( $R_{\text{int}} = 0.0513$ )

Lorentz-polarization

Absorption

(trans. factors: 0.6309 - 1.000)

### C. Structure Solution and Refinement

Structure Solution

Direct Methods (SHELX97)

Refinement

Full-matrix least-squares on  $F^2$

Function Minimized

$\Sigma w (F_o^2 - F_c^2)^2$

Least Squares Weights

$w = 1 / [ \sigma^2(F_o^2) + (0.1111 \cdot P)^2 + 25.5808 \cdot P ]$

where  $P = (\text{Max}(F_o^2, 0) + 2F_c^2)/3$

$2\theta_{\text{max}}$  cutoff

55.0°

Anomalous Dispersion

All non-hydrogen atoms

No. Observations (All reflections)

37263

No. Variables

2297

Reflection/Parameter Ratio

16.22

Residuals:  $R_1$  ( $I > 2.00\sigma(I)$ )

0.0936

Residuals:  $R$  (All reflections)

0.1268

Residuals:  $wR_2$  (All reflections)

0.2597

Goodness of Fit Indicator

1.044

Max Shift/Error in Final Cycle

0.001

Maximum peak in Final Diff. Map

0.94  $e^-/\text{\AA}^3$

Minimum peak in Final Diff. Map

-0.69  $e^-/\text{\AA}^3$

**A3.20:**  $[(2\text{po}56\text{nq}-2\text{H})_6\text{Cu}_9](\text{BF}_4)_6 \cdot 6.4\text{H}_2\text{O}$  (**6.3**)

## A. Crystal Data

Empirical Formula	$\text{C}_{162}\text{H}_{126.80}\text{B}_6\text{Cu}_9\text{F}_{24}\text{N}_{54}\text{O}_{18.40}$
Formula Weight	4217.07
Crystal Color, Habit	red, prism
Crystal Dimensions	$0.60 \times 0.49 \times 0.41$ mm
Crystal System	triclinic
Lattice Type	Primitive
Detector Position	39.94 mm
Pixel Size	0.137 mm
Lattice Parameters	$a = 15.604(3)$ Å $b = 23.136(4)$ Å $c = 26.411(5)$ Å $\alpha = 93.403(4)^\circ$ $\beta = 100.014(5)^\circ$ $\gamma = 90.626(5)^\circ$ $V = 9371(3)$ Å <sup>3</sup>
Space Group	$\bar{P}1$ (#2)
Z value	2
D <sub>calc</sub>	1.494 g/cm <sup>3</sup>
F <sub>000</sub>	4262
$\mu(\text{MoK}\alpha)$	10.99 cm <sup>-1</sup>

## B. Intensity Measurements

Detector	Rigaku Saturn
Goniometer	Rigaku AFC8
Radiation	MoK $\alpha$ ( $\lambda = 0.71070$ Å) graphite monochromated
Detector Aperture	70 mm $\times$ 70 mm
Data Images	780 exposures
$\omega$ oscillation Range ( $\chi=0.0$ , $\phi=0.0$ )	-15.0 - 15.0°
Exposure Rate	240.0 sec./°
Detector Swing Angle	15.20°
$\omega$ oscillation Range ( $\chi=45.0$ , $\phi=0.0$ )	-75.0 - 105.0°
Exposure Rate	240.0 sec./°
Detector Swing Angle	15.20°

$\omega$ oscillation Range ( $\chi=54.0$ , $\phi=180.0$ )	-75.0 - 105.0 <sup>o</sup>
Exposure Rate	240.0 sec./ <sup>o</sup>
Detector Swing Angle	15.20 <sup>o</sup>
Detector Position	39.94 mm
Pixel Size	0.137 mm
$2\theta_{\max}$	62.0 <sup>o</sup>
No. of Reflections Measured	Total: 81553
	Unique: 33798 ( $R_{\text{int}} = 0.0445$ )
Corrections	Lorentz-polarization
	Absorption
	(trans. factors: 0.6374 - 0.7964)

### C. Structure Solution and Refinement

Structure Solution	Patterson Methods (DIRDIF99 ORIENT)
Refinement	Full-matrix least-squares on $F^2$
Function Minimized	$\Sigma w (F_o^2 - F_c^2)^2$
Least Squares Weights	$w = 1 / [ \sigma^2(F_o^2) + (0.2000 \cdot P)^2 + 0.0000 \cdot P ]$
	where $P = (\text{Max}(F_o^2, 0) + 2F_c^2)/3$
$2\theta_{\max}$ cutoff	51.0 <sup>o</sup>
Anomalous Dispersion	All non-hydrogen atoms
No. Observations (All reflections)	33798
No. Variables	2306
Reflection/Parameter Ratio	14.66
Residuals: R1 ( $I > 2.00\sigma(I)$ )	0.0987
Residuals: R (All reflections)	0.1153
Residuals: wR2 (All reflections)	0.3167
Goodness of Fit Indicator	1.154
Max Shift/Error in Final Cycle	0.001
Maximum peak in Final Diff. Map	3.24 e <sup>-</sup> /Å <sup>3</sup>
Minimum peak in Final Diff. Map	-1.94 e <sup>-</sup> /Å <sup>3</sup>

**A3.21:** [(2po45nq-2H)<sub>6</sub>Cu<sub>8.5</sub>](CF<sub>3</sub>SO<sub>3</sub>)<sub>1.4</sub>(PF<sub>6</sub>)<sub>3.6</sub>·3H<sub>2</sub>O (**6.4**)

## A. Crystal Data

Empirical Formula	C <sub>163.40</sub> H <sub>120</sub> Cu <sub>8.50</sub> F <sub>25.80</sub> N <sub>54</sub> O <sub>19.20</sub> P <sub>3.60</sub> S <sub>1.40</sub>
Formula Weight	4333.79
Crystal Color, Habit	brown, prism
Crystal Dimensions	0.39 × 0.38 × 0.28 mm
Crystal System	tetragonal
Lattice Type	Primitive
Detector Position	39.92 mm
Pixel Size	0.137 mm
Lattice Parameters	a = 20.580(3) Å c = 22.970(4) Å V = 9729(3) Å <sup>3</sup>
Space Group	P4 <sub>2</sub> /n (#86)
Z value	2
D <sub>calc</sub>	1.479 g/cm <sup>3</sup>
F <sub>000</sub>	4374.2
μ(MoKα)	10.53 cm <sup>-1</sup>

## B. Intensity Measurements

Detector	Rigaku Saturn
Goniometer	Rigaku AFC8
Radiation	MoKα (λ = 0.71070 Å) graphite monochromated
Detector Aperture	70 mm × 70 mm
Data Images	720 exposures
ω oscillation Range (χ=0.0, φ=0.0)	-75.0 - 105.0°
Exposure Rate	140.0 sec./°
Detector Swing Angle	15.16°
ω oscillation Range (χ=45.0, φ=0.0)	-75.0 - 105.0°
Exposure Rate	140.0 sec./°
Detector Swing Angle	15.16°
Detector Position	39.92 mm
Pixel Size	0.137 mm
2θ <sub>max</sub>	62.1°

No. of Reflections Measured	Total: 75221
Corrections	Unique: 9535 ( $R_{int} = 0.0410$ )
	Lorentz-polarization
	Absorption
	(trans. factors: 0.7165 - 0.8284)

### C. Structure Solution and Refinement

Structure Solution	Direct Methods (SHELX97)
Refinement	Full-matrix least-squares on $F^2$
Function Minimized	$\Sigma w (F_o^2 - F_c^2)^2$
Least Squares Weights	$w = 1 / [ \sigma^2(F_o^2) + (0.2000 \cdot P)^2 + 0.0000 \cdot P ]$
	where $P = (\text{Max}(F_o^2, 0) + 2F_c^2) / 3$
$2\theta_{max}$ cutoff	52.0°
Anomalous Dispersion	All non-hydrogen atoms
No. Observations (All reflections)	9535
No. Variables	722
Reflection/Parameter Ratio	13.21
Residuals: $R1$ ( $I > 2.00\sigma(I)$ )	0.1174
Residuals: $R$ (All reflections)	0.1232
Residuals: $wR2$ (All reflections)	0.3717
Goodness of Fit Indicator	1.683
Max Shift/Error in Final Cycle	0.001
Maximum peak in Final Diff. Map	2.79 $e^-/\text{Å}^3$
Minimum peak in Final Diff. Map	-1.46 $e^-/\text{Å}^3$

**A3.22:** [(2po34nq-2H)<sub>6</sub>Mn<sub>9</sub>](CF<sub>3</sub>SO<sub>3</sub>)<sub>3</sub>(NO<sub>3</sub>)<sub>3</sub>(H<sub>2</sub>O)<sub>3.8</sub> (6.6)

## A. Crystal Data

Empirical Formula	C <sub>163</sub> H <sub>121.60</sub> F <sub>9</sub> N <sub>57</sub> O <sub>33.80</sub> S <sub>3</sub> Mn <sub>9</sub>
Formula Weight	4181.12
Crystal Color, Habit	red, prism
Crystal Dimensions	0.68 × 0.36 × 0.35 mm
Crystal System	triclinic
Lattice Type	Primitive
Detector Position	39.86 mm
Pixel Size	0.137 mm
Lattice Parameters	a = 20.514(5) Å b = 20.643(4) Å c = 25.948(6) Å α = 90.917(4) ° β = 108.365(7) ° γ = 90.517(7) ° V = 10426(4) Å <sup>3</sup>
Space Group	P $\bar{1}$ (#2)
Z value	2
D <sub>calc</sub>	1.332 g/cm <sup>3</sup>
F <sub>000</sub>	4246
μ(MoKα)	6.41 cm <sup>-1</sup>

## B. Intensity Measurements

Detector	Rigaku Saturn
Goniometer	Rigaku AFC8
Radiation	MoKα (λ = 0.71070 Å) graphite monochromated
Detector Aperture	70 mm × 70 mm
Data Images	780 exposures
ω oscillation Range (χ=0.0, φ=0.0)	-15.0 - 15.0°
Exposure Rate	90.0 sec./°
Detector Swing Angle	15.29°
ω oscillation Range (χ=45.0, φ=0.0)	-75.0 - 105.0°
Exposure Rate	90.0 sec./°

Detector Swing Angle	15.29°
$\omega$ oscillation Range ( $\chi=54.0$ , $\phi=180.0$ )	-75.0 - 105.0°
Exposure Rate	90.0 sec./°
Detector Swing Angle	15.29°
Detector Position	39.86 mm
Pixel Size	0.137 mm
$2\theta_{\max}$	62.1°
No. of Reflections Measured	Total: 97528
	Unique: 42546 ( $R_{\text{int}} = 0.0576$ )
Corrections	Lorentz-polarization
	Absorption
	(trans. factors: 0.9287 - 0.9695)

### C. Structure Solution and Refinement

Structure Solution	Patterson Methods (DIRDIF99 ORIENT)
Refinement	Full-matrix least-squares on $F^2$
Function Minimized	$\sum w (F_o^2 - F_c^2)^2$
Least Squares Weights	$w = 1 / [ \sigma^2(F_o^2) + (0.1637 \cdot P)^2 + 0.0000 \cdot P ]$
	where $P = (\text{Max}(F_o^2, 0) + 2F_c^2) / 3$
$2\theta_{\max}$ cutoff	53.0°
Anomalous Dispersion	All non-hydrogen atoms
No. Observations (All reflections)	42546
No. Variables	2207
Reflection/Parameter Ratio	19.28
Residuals: $R_1$ ( $I > 2.00\sigma(I)$ )	0.0889
Residuals: $R$ (All reflections)	0.1171
Residuals: $wR_2$ (All reflections)	0.2794
Goodness of Fit Indicator	1.004
Max Shift/Error in Final Cycle	0.001
Maximum peak in Final Diff. Map	1.46 e-/Å <sup>3</sup>
Minimum peak in Final Diff. Map	-0.54 e-/Å <sup>3</sup>

**A3.23:**  $[(2\text{pdoapm-2H})_8\text{Mn}_{16}\text{O}_4(\text{OH})_4](\text{PF}_6)_4 \cdot 21.2\text{H}_2\text{O}$  (7.1)

## A. Crystal Data

Empirical Formula	$\text{C}_{128}\text{H}_{142.40}\text{F}_{24}\text{Mn}_{16}\text{N}_9\text{O}_{45.20}\text{P}_4$
Formula Weight	5207.61
Crystal Color, Habit	red, needle
Crystal Dimensions	$0.45 \times 0.14 \times 0.10$ mm
Crystal System	orthorhombic
Lattice Type	Primitive
Detector Position	39.97 mm
Pixel Size	0.137 mm
Lattice Parameters	$a = 25.845(3)$ Å $b = 29.547(4)$ Å $c = 16.420(2)$ Å $V = 12539(3)$ Å <sup>3</sup>
Space Group	Pmmn (#59)
Z value	2
D <sub>calc</sub>	1.379 g/cm <sup>3</sup>
F <sub>000</sub>	5240
$\mu(\text{MoK}\alpha)$	8.95 cm <sup>-1</sup>

## B. Intensity Measurements

Detector	Rigaku Saturn
Goniometer	Rigaku AFC8
Radiation	MoK $\alpha$ ( $\lambda = 0.71070$ Å) graphite monochromated
Detector Aperture	70 mm $\times$ 70 mm
Data Images	390 exposures
$\omega$ oscillation Range ( $\chi=0.0$ , $\phi=0.0$ )	-15.0 - 45.0°
Exposure Rate	180.0 sec./°
Detector Swing Angle	15.14°
$\omega$ oscillation Range ( $\chi=0.0$ , $\phi=90.0$ )	-75.0 - 60.0°
Exposure Rate	180.0 sec./°
Detector Swing Angle	15.14°
Detector Position	39.97 mm
Pixel Size	0.137 mm
2 $\theta_{\text{max}}$	61.9°

No. of Reflections Measured

Total: 56060

Corrections

Unique: 12815 ( $R_{\text{int}} = 0.0510$ )  
Lorentz-polarization  
Absorption  
(trans. factors: 0.8144 - 0.9450)

### C. Structure Solution and Refinement

Structure Solution

Direct Methods (SHELX97)

Refinement

Full-matrix least-squares on  $F^2$

Function Minimized

$\Sigma w (F_o^2 - F_c^2)^2$

Least Squares Weights

$w = 1 / [ \sigma^2(F_o^2) + (0.1427 \cdot P)^2 + 20.7219 \cdot P ]$

where  $P = (\text{Max}(F_o^2, 0) + 2F_c^2) / 3$

$2\theta_{\text{max}}$  cutoff

52.0°

Anomalous Dispersion

All non-hydrogen atoms

No. Observations (All reflections)

12815

No. Variables

716

Reflection/Parameter Ratio

17.90

Residuals:  $R_1$  ( $I > 2.00\sigma(I)$ )

0.0928

Residuals:  $R$  (All reflections)

0.1208

Residuals:  $wR_2$  (All reflections)

0.2793

Goodness of Fit Indicator

1.070

Max Shift/Error in Final Cycle

0.000

Maximum peak in Final Diff. Map

1.04 e<sup>-</sup>/Å<sup>3</sup>

Minimum peak in Final Diff. Map

-0.42 e<sup>-</sup>/Å<sup>3</sup>

**A3.24:** [(2pdoapm-2H)<sub>8</sub>Co<sub>16</sub>(OH)<sub>8</sub>](BF<sub>4</sub>)<sub>8</sub>·19.8H<sub>2</sub>O (**7.2a**)

## A. Crystal Data

Empirical Formula	C <sub>128</sub> H <sub>143.60</sub> B <sub>8</sub> Co <sub>16</sub> F <sub>32</sub> N <sub>96</sub> O <sub>43.80</sub>
Formula Weight	5364.92
Crystal Color, Habit	Dark red, prism
Crystal Dimensions	0.27 × 0.19 × 0.18 mm
Crystal System	orthorhombic
Lattice Type	Primitive
Detector Position	39.97 mm
Pixel Size	0.137 mm
Lattice Parameters	a = 25.517(3) Å b = 29.451(3) Å c = 15.8192(16) Å V = 11888(2) Å <sup>3</sup>
Space Group	Pmmn (#59)
Z value	2
D <sub>calc</sub>	1.499 g/cm <sup>3</sup>
F <sub>000</sub>	5388
μ(MoKα)	11.90 cm <sup>-1</sup>

## B. Intensity Measurements

Detector	Rigaku Saturn
Goniometer	Rigaku AFC8
Radiation	MoKα (λ = 0.71070 Å) graphite monochromated
Detector Aperture	70 mm × 70 mm
Data Images	646 exposures
ω oscillation Range (χ=0.0, φ=0.0)	-75.0 - 105.0°
Exposure Rate	170.0 sec./°
Detector Swing Angle	15.12°
ω oscillation Range (χ=54.0, φ=180.0)	-55.0 - 88.0°
Exposure Rate	170.0 sec./°
Detector Swing Angle	15.12°
Detector Position	39.97 mm
Pixel Size	0.137 mm
2θ <sub>max</sub>	62.0°

No. of Reflections Measured

Total: 93316

Corrections

Unique: 12830 ( $R_{\text{int}} = 0.0658$ )

Lorentz-polarization

Absorption

(trans. factors: 0.7795 - 0.8804)

### C. Structure Solution and Refinement

Structure Solution

Direct Methods (SHELX97)

Refinement

Full-matrix least-squares on  $F^2$

Function Minimized

$\Sigma w (F_o^2 - F_c^2)^2$

Least Squares Weights

$w = 1 / [ \sigma^2(F_o^2) + (0.1464 \cdot P)^2 + 27.2928 \cdot P ]$

where  $P = (\text{Max}(F_o^2, 0) + 2F_c^2)/3$

$2\theta_{\text{max}}$  cutoff

53.0°

Anomalous Dispersion

All non-hydrogen atoms

No. Observations (All reflections)

12830

No. Variables

726

Reflection/Parameter Ratio

17.67

Residuals:  $R_1$  ( $I > 2.00\sigma(I)$ )

0.0955

Residuals:  $R$  (All reflections)

0.1072

Residuals:  $wR_2$  (All reflections)

0.2806

Goodness of Fit Indicator

1.142

Max Shift/Error in Final Cycle

0.001

Maximum peak in Final Diff. Map

1.37  $e^-/\text{\AA}^3$

Minimum peak in Final Diff. Map

-0.90  $e^-/\text{\AA}^3$

**A3.25:** [(2pd056hq-2H)<sub>8</sub>Mn<sub>16</sub>O<sub>4</sub>(OH)<sub>4</sub>](NO<sub>3</sub>)<sub>4</sub>·32H<sub>2</sub>O (7.4)

## A. Crystal Data

Empirical Formula	C <sub>208</sub> H <sub>196</sub> Mn <sub>16</sub> N <sub>68</sub> O <sub>68</sub>
Formula Weight	5615.26
Crystal Color, Habit	red, prism
Crystal Dimensions	0.41 × 0.28 × 0.28 mm
Crystal System	tetragonal
Lattice Type	Primitive
Detector Position	39.91 mm
Pixel Size	0.137 mm
Lattice Parameters	a = 22.856(2) Å c = 27.634(3) Å V = 14436(2) Å <sup>3</sup>
Space Group	P $\bar{4}$ 2 <sub>1</sub> c (#114)
Z value	2
D <sub>calc</sub>	1.292 g/cm <sup>3</sup>
F <sub>000</sub>	5728
μ(MoKα)	7.53 cm <sup>-1</sup>

## B. Intensity Measurements

Detector	Rigaku Saturn
Goniometer	Rigaku AFC8
Radiation	MoKα (λ = 0.71070 Å) graphite monochromated
Detector Aperture	70 mm × 70 mm
Data Images	720 exposures
ω oscillation Range (χ=0.0, φ=0.0)	-75.0 - 105.0°
Exposure Rate	170.0 sec./°
Detector Swing Angle	15.18°
ω oscillation Range (χ=54.0, φ=0.0)	-75.0 - 105.0°
Exposure Rate	170.0 sec./°
Detector Swing Angle	15.18°
Detector Position	39.91 mm
Pixel Size	0.137 mm
2θ <sub>max</sub>	62.0°

No. of Reflections Measured	Total: 114457
Corrections	Unique: 14185 ( $R_{\text{int}} = 0.0574$ ) Lorentz-polarization Absorption (trans. factors: 0.8172 - 0.9105) Secondary Extinction (coefficient: 0.0036(4))
C. Structure Solution and Refinement	
Structure Solution	Direct Methods (SHELX97)
Refinement	Full-matrix least-squares on $F^2$
Function Minimized	$\Sigma w (F_o^2 - F_c^2)^2$
Least Squares Weights	$w = 1 / [ \sigma^2(F_o^2) + (0.1802 \cdot P)^2 + 22.4926 \cdot P ]$ where $P = (\text{Max}(F_o^2, 0) + 2F_c^2) / 3$
$2\theta_{\text{max}}$ cutoff	52.0°
Anomalous Dispersion	All non-hydrogen atoms
No. Observations (All reflections)	14185
No. Variables	827
Reflection/Parameter Ratio	17.15
Residuals: R1 ( $I > 2.00\sigma(I)$ )	0.0934
Residuals: R (All reflections)	0.0946
Residuals: wR2 (All reflections)	0.2707
Goodness of Fit Indicator	1.111
Max Shift/Error in Final Cycle	0.001
Maximum peak in Final Diff. Map	1.11 e <sup>-</sup> /Å <sup>3</sup>
Minimum peak in Final Diff. Map	-0.68 e <sup>-</sup> /Å <sup>3</sup>

**A3.26: [(2pyoapm-H)Cu(OH)](ClO<sub>4</sub>)<sub>2</sub>·1.6H<sub>2</sub>O (8.1)**

## A. Crystal Data

Empirical Formula	C <sub>15</sub> H <sub>16.60</sub> Cl <sub>2</sub> Cu <sub>2</sub> N <sub>12</sub> O <sub>12.80</sub>
Formula Weight	767.77
Crystal Color, Habit	Light blue, prism
Crystal Dimensions	0.36 × 0.17 × 0.14 mm
Crystal System	triclinic
Lattice Type	Primitive
Detector Position	39.40 mm
Pixel Size	0.137 mm
Lattice Parameters	a = 12.180(6) Å b = 14.450(6) Å c = 16.120(7) Å α = 68.36(5) ° β = 77.37(4) ° γ = 75.81(5) ° V = 2530.7(20) Å <sup>3</sup>
Space Group	P1̄ (#2)
Z value	4
D <sub>calc</sub>	2.015 g/cm <sup>3</sup>
F <sub>000</sub>	1540
μ(MoKα)	19.83 cm <sup>-1</sup>

## B. Intensity Measurements

Detector	Rigaku Saturn
Goniometer	Rigaku AFC8
Radiation	MoKα (λ = 0.71070 Å) graphite monochromated
Detector Aperture	70 mm × 70 mm
Data Images	770 exposures
ω oscillation Range (χ=0.0, φ=0.0)	45.0 - 75.0°
Exposure Rate	90.0 sec./°
Detector Swing Angle	15.55°
ω oscillation Range (χ=45.0, φ=0.0)	-75.0 - 90.0°
Exposure Rate	90.0 sec./°
Detector Swing Angle	15.55°

$\omega$ oscillation Range ( $\chi=54.0$ , $\phi=90.0$ )	-75.0 - 73.0 $^{\circ}$
Exposure Rate	90.0 sec./ $^{\circ}$
Detector Swing Angle	15.55 $^{\circ}$
$\omega$ oscillation Range ( $\chi=54.0$ , $\phi=180.0$ )	-54.0 - -12.0 $^{\circ}$
Exposure Rate	90.0 sec./ $^{\circ}$
Detector Swing Angle	15.55 $^{\circ}$
Detector Position	39.40 mm
Pixel Size	0.137 mm
$2\theta_{\max}$	62.5 $^{\circ}$
No. of Reflections Measured	Total: 21786 Unique: 9766 ( $R_{\text{int}} = 0.0789$ )
Corrections	Lorentz-polarization Absorption (trans. factors: 0.6837 - 0.8732)

### C. Structure Solution and Refinement

Structure Solution	Direct Methods (SHELX97)
Refinement	Full-matrix least-squares on $F^2$
Function Minimized	$\Sigma w (F_o^2 - F_c^2)^2$
Least Squares Weights	$w = 1 / [ \sigma^2(F_o^2) + (0.1279 \cdot P)^2 + 18.4632 \cdot P ]$ where $P = (\text{Max}(F_o^2, 0) + 2F_c^2)/3$
$2\theta_{\max}$ cutoff	52.0 $^{\circ}$
Anomalous Dispersion	All non-hydrogen atoms
No. Observations (All reflections)	9766
No. Variables	829
Reflection/Parameter Ratio	11.78
Residuals: R1 ( $I > 2.00\sigma(I)$ )	0.1204
Residuals: R (All reflections)	0.1388
Residuals: wR2 (All reflections)	0.3189
Goodness of Fit Indicator	1.144
Max Shift/Error in Final Cycle	0.000
Maximum peak in Final Diff. Map	1.43 e-/ $\text{\AA}^3$
Minimum peak in Final Diff. Map	-1.05 e-/ $\text{\AA}^3$

**A3.27:** [(2pdoapm-2H)<sub>6</sub>(2pdoapm-3H)<sub>2</sub>Cu<sub>16</sub>O<sub>2</sub>(OH)<sub>4</sub>(H<sub>2</sub>O)<sub>2</sub>](CF<sub>3</sub>SO<sub>3</sub>)<sub>6</sub>·21.4H<sub>2</sub>O (**8.2**)

## A. Crystal Data

Empirical Formula	C <sub>134</sub> H <sub>144.80</sub> Cu <sub>16</sub> F <sub>18</sub> N <sub>96</sub> O <sub>63.40</sub> S <sub>6</sub>
Formula Weight	5665.49
Crystal Color, Habit	brown, needle
Crystal Dimensions	0.68 × 0.15 × 0.14 mm
Crystal System	orthorhombic
Lattice Type	Primitive
Detector Position	45.01 mm
Pixel Size	0.137 mm
Lattice Parameters	a = 25.797(2) Å b = 29.199(2) Å c = 16.5920(13) Å V = 12497.5(18) Å <sup>3</sup>
Space Group	Pmmn (#59)
Z value	2
D <sub>calc</sub>	1.505 g/cm <sup>3</sup>
F <sub>000</sub>	5700
μ(MoKα)	14.82 cm <sup>-1</sup>

## B. Intensity Measurements

Detector	Rigaku Saturn
Goniometer	Rigaku AFC8
Radiation	MoKα (λ = 0.71070 Å) graphite monochromated
Detector Aperture	70 mm × 70 mm
Data Images	450 exposures
ω oscillation Range (χ=0.0, φ=0.0)	-70.0 - 20.0°
Exposure Rate	120.0 sec./°
Detector Swing Angle	20.10°
ω oscillation Range (χ=54.0, φ=180.0)	-36.3 - 98.8°
Exposure Rate	120.0 sec./°
Detector Swing Angle	20.10°
Detector Position	45.01 mm
Pixel Size	0.137 mm
2θ <sub>max</sub>	62.7°

No. of Reflections Measured	Total: 56226
Corrections	Unique: 12804 ( $R_{int} = 0.0318$ ) Lorentz-polarization Absorption (trans. factors: 0.6534 - 0.8847) Secondary Extinction (coefficient: 0.00006(8))

### C. Structure Solution and Refinement

Structure Solution	Direct Methods (SHELX97)
Refinement	Full-matrix least-squares on $F^2$
Function Minimized	$\Sigma w (F_o^2 - F_c^2)^2$
Least Squares Weights	$w = 1 / [ \sigma^2(F_o^2) + (0.1003 \cdot P)^2 + 36.4907 \cdot P ]$ where $P = (\text{Max}(F_o^2, 0) + 2F_c^2)/3$
$2\theta_{max}$ cutoff	52.0°
Anomalous Dispersion	All non-hydrogen atoms
No. Observations (All reflections)	12804
No. Variables	741
Reflection/Parameter Ratio	17.28
Residuals: R1 ( $I > 2.00\sigma(I)$ )	0.0639
Residuals: R (All reflections)	0.0707
Residuals: wR2 (All reflections)	0.1825
Goodness of Fit Indicator	1.037
Max Shift/Error in Final Cycle	0.001
Maximum peak in Final Diff. Map	1.24 e <sup>-</sup> /Å <sup>3</sup>
Minimum peak in Final Diff. Map	-1.16 e <sup>-</sup> /Å <sup>3</sup>

**A3.28:** [(2pdoapm-2H)<sub>8</sub>Cu<sub>16</sub>](CF<sub>3</sub>SO<sub>3</sub>)<sub>12</sub>·2.8H<sub>2</sub>O (**8.3**)

## A. Crystal Data

Empirical Formula	C <sub>140</sub> H <sub>101.60</sub> Cu <sub>16</sub> F <sub>36</sub> N <sub>96</sub> O <sub>54.80</sub> S <sub>12</sub>
Formula Weight	6090.75
Crystal Color, Habit	red-brown, prism
Crystal Dimensions	0.56 × 0.45 × 0.25 mm
Crystal System	tetragonal
Lattice Type	Primitive
Detector Position	40.01 mm
Pixel Size	0.137 mm
Lattice Parameters	a = 23.579(3) Å c = 22.196(2) Å V = 12341(2) Å <sup>3</sup>
Space Group	P4 <sub>2</sub> /n (#86)
Z value	2
D <sub>calc</sub>	1.639 g/cm <sup>3</sup>
F <sub>000</sub>	6064
μ(MoKα)	15.63 cm <sup>-1</sup>

## B. Intensity Measurements

Detector	Rigaku Saturn
Goniometer	Rigaku AFC8
Radiation	MoKα (λ = 0.71070 Å) graphite monochromated
Detector Aperture	70 mm × 70 mm
Data Images	184 exposures
ω oscillation Range (χ=0.0, φ=90.0)	-10.0 - 82.0°
Exposure Rate	180.0 sec./°
Detector Swing Angle	15.15°
Detector Position	40.01 mm
Pixel Size	0.137 mm
2θ <sub>max</sub>	61.8°

No. of Reflections Measured

Total: 26597

Corrections

Unique: 11965 ( $R_{\text{int}} = 0.0335$ )

Lorentz-polarization

Absorption

(trans. factors: 0.6241 - 0.7983)

Secondary Extinction

(coefficient: 0.0033(6))

### C. Structure Solution and Refinement

Structure Solution

Direct Methods (SHELX97)

Refinement

Full-matrix least-squares on  $F^2$

Function Minimized

$\sum w (F_o^2 - F_c^2)^2$

Least Squares Weights

$w = 1 / [ \sigma^2(F_o^2) + (0.2000 \cdot P)^2 + 0.0000 \cdot P ]$

where  $P = (\text{Max}(F_o^2, 0) + 2F_c^2)/3$

$2\theta_{\text{max}}$  cutoff

52.0°

Anomalous Dispersion

All non-hydrogen atoms

No. Observations (All reflections)

11965

No. Variables

663

Reflection/Parameter Ratio

18.05

Residuals:  $R_1$  ( $I > 2.00\sigma(I)$ )

0.1133

Residuals:  $R$  (All reflections)

0.1334

Residuals:  $wR_2$  (All reflections)

0.3400

Goodness of Fit Indicator

1.245

Max Shift/Error in Final Cycle

0.000

Maximum peak in Final Diff. Map

3.47  $e^-/\text{\AA}^3$

Minimum peak in Final Diff. Map

-0.89  $e^-/\text{\AA}^3$



Louise N. Dawe

Doctoral Thesis: *Love and*

Self-  
2,3,4

43504-07

